UNIVERSITÀ
DEGLI STUDI
FIRENZE

DOTTORATO DI RICERCA IN
FISICA E ASTRONOMIA

CICLO XXXIV

COORDINATORE Prof. D'Alessandro Raffaello

GRMHD simulations of thick accretion disks in the Event Horizon Telescope era: the role of the mean-field dynamo mechanism

Settore Scientifico Disciplinare FIS/05

Dottorando
Dott. Tomei Niccolò
Niccolò Tomei
(firma)

Tutore
Prof. Del Zanna Luca
Luca Del Zanna
(firma)

Coordinatore
Prof. D'Alessandro Raffaello
Raffaello D'Alessandro
(firma)

Anni 2018/2021

Abstract

The recent imaging of the M87 black hole at millimetre wavelengths by the Event Horizon Telescope Collaboration has triggered a renewed interest in numerical models for the accretion of magnetized plasma in the regime of general relativistic magnetohydrodynamics (GRMHD). We have investigated, for the first time by means of non-ideal axisymmetric GRMHD simulations, the mean-field dynamo process operating in thick accretion disks around black holes, in the fully non-linear regime. Combined with the differential rotation of the disk, the dynamo process is able to produce an exponential growth of any initial seed magnetic field up to the values required to explain the observations,when the instability tends to saturate even in the absence of artificial quenching effects. Before reaching the final saturation stage we observe a secondary regime of exponential growing, where the magnetic field increases more slowly due to accretion, which is modifying the underlying equilibrium. In the stationary state characterized by the saturation of the magnetic field growth, the dynamo is able to remove the angular momentum and trigger the accretion. Finally, we show that it is possible to reproduce the main diagnostics present in the literature by starting from very unfavorable initial configurations, such as a purely toroidal magnetic field with negligible magnetization. In parallel, we present the contribution to the code Comparison Project that aims to compare ideal GRMHD solutions for the evolution of a magnetized accretion flow in two distinct regimes where turbulence is promoted by the magnetorotational instability.

List of publications

- O. Porth and EHT-Collaboration, The Event Horizon General Relativistic Magnetohydrodynamic Code Comparison Project. *The Astrophysical Journal Supplement Series*, 243(2), 26 Aug. 2019
- N. Tomei, L. Del Zanna, M. Bugli and N. Bucciantini, General relativistic magnetohydrodynamic dynamo in thick accretion discs: fully non-linear simulations. *Monthly Notices of the Royal Astronomical Society*, 491:2346–2359, Jan. 2020
- N. Tomei, L. Del Zanna, M. Bugli and N. Bucciantini, Are GRMHD Mean-Field Dynamo Models of Thick Accretion Disks SANE? *Universe*, 7(8), 259, Jul. 2021
- H. Olivares and EHT-Collaboration, The Event Horizon General Relativistic Magnetohydrodynamic Code Comparison Project: Magnetically Arrested Disks, in prep.

Contents

Chapter 1

Introduction

The baryonic matter of the Universe is found almost entirely in the form of plasma, or ionized gas where the moving charges interact with each other through the self-generated currents and the related magnetic fields within a highly conductive material. The energy contained in the plasma in terms of the magnetic field is usually comparable to the kinetic and/or thermal energy of the plasma itself, and many violent observed phenomena are attributable to the sudden release of magnetic energy, for example flares (Moore et al., 2001), coronal mass ejections (Antiochos et al., 1999) small-scale heating events that maintain the high temperatures of the corona (Heyvaerts and Priest, 1984; Longcope and Tarr, 2015) produced by magnetic reconnection, gamma-ray bursts (Kumar and Zhang, 2015; MAGIC-Collaboration, 2019), the huge flares observed in gamma rays in neutron stars (Thompson and Duncan, 1995; Palmer et al., 2005), the relativistic jets in active galactic nuclei (AGN) (Asada and Nakamura, 2012; Lister et al., 2016; Walker et al., 2018; Qian et al., 2018; Nakamura et al., 2018).

Since the Universe may not have formed magnetized, a natural question one needs to answer is what processes can lead to a weak magnetic field, from zero initial fields. Battery-like mechanisms, where separation of charges induce the presence of electric fields produced by kinetic effects (Biermann, 1951; Weibel, 1959; Fried, 1959), are needed to create primordial extragalactic fields (Kronberg, 1994), which may be amplified to higher values by plasma advection, rotation and collapse to values appropriate for stellar magnetism (Mestel, 1999), up to $B \sim 10^{12}$ G, the field of a standard neutron star, a value required to power the surrounding young supernova remnant, when present, as recognized even before the actual discovery of pulsars (Pacini, 1967). Most of these batteries lead to field strengths much weaker than the observed field. So some way of amplifying the field is required. This is probably accomplished by the conversion of kinetic energy into magnetic energy, a process generally referred to as a dynamo. The basic principles of the dynamo can be well understood by linear theory, however, since all astrophysical dynamos develop in a regime in where the fields are dynamically important, kinematic theory cannot be considered complete. In recent years, our understanding of the nonlinear properties of dynamo is greatly improved. This is due in large part to the use of new high-resolution numerical simulations that produced further steps forward in the analytical approach.

Magnetic fields of small scale and large scale components are observed in various astrophysical settings. While the small scale field could always be explained by turbulence and convection that shreds and concentrates the field into isolated flux bundles, large scale components are more difficult

to describe comprehensively from a theoretical point of view. The Sun has a large-scale magnetic field with intensity peaks of ~ 2 kG that manifests itself in sunspots variable in number over a period of ~ 11 year cycle and migrating towards the equator and the poles from the mid latitudes but it has also a turbulent component in the deeper convection zone (Galloway and Weiss, 1981; Stenflo, 1988, 1994; Spruit and van Ballegooijen, 1982). Cyclic variations in the magnetic field with average intensity up to 2 kG are also observed in late-type stars who have outer convection zones with magnetic fields whose strength tends to increase with their angular velocity (Baliunas et al., 1995; Johns-Krull et al., 1999).

A system of gas rotating around a central object is extremely frequent in any astrophysical context. In AGNs, Faraday rotation measure maps (Zavala and Taylor, 2003) and theoretical motivations suggest that such environments must be magnetized. The near-horizon emission from low-luminosity active galactic nuclei is produced by synchrotron radiation that peaks from the radio through the far infrared and it may be produced either in the accretion flow (Narayan et al., 1995), the jet (Falcke et al., 1993), or both (Yuan et al., 2002). These astrophysical sources have masses in the range $10^6 - 10^9 M_\odot$, reside at centers of our and other galaxies and are the most powerful steady energy sources known in the universe with their brightness can be up to 100 times greater than brightness of an ordinary galaxy. In fact, in falling through the steep gravitational potential of supermassive black hole (BH), roughly 10% of the accreted rest-mass energy may be converted into radiation. Thus accretion is a process that can be considerably more efficient than many other commonly invoked mechanism in astrophysics (e.g. nuclear fusion). To explain the high accretion rates required to justify emissions from these high-energy sources, some physical mechanism is required to transport angular momentum outwards. In this context, magnetic fields are the key to explain how disks can get rid of their angular momentum through the magnetorotational instability (MRI) (Balbus and Hawley, 1991, 1998). The presence of large-scale magnetic fields is also required to explain how Poynting-dominated relativistic jets may be launched due to rotational energy extraction inside the ergosphere (Blandford and Znajek, 1977; McKinney and Gammie, 2004), though even the rotation of the disk itself is known to be able to drive centrifugally driven polar outflows (Blandford and Payne, 1982). We observe that, while disks around protostars are formed in already magnetized environments, in AGNs the magnetic field may either be dragged in from large radii or it may be regenerated locally by dynamo action.

In a wider context, large scale magnetic field can be seen inside galaxies and clusters of galaxies. In galaxies, the existence of magnetic fields is mainly proven by radio observations of synchrotron emission. The latter also depends on the numerical density of electrons and therefore it is usually assumed that the energy density of the particles and the field are at the equipartition. In spiral galaxies with this assumption it is derived that the mean equipartition strength of the magnetic field varies in range $4-15$ μG (Beck, 2004). Polarized radiation maps also show that these fields are ordered over several kpc (Laing, 1981). Structures of this type can be described in dynamo models by modes of different azimuthal and vertical symmetry (Ruzmaikin et al., 1988). Ordered magnetic fields with intensities similar to those observed in spirals are detected in irregular galaxies while there is little evidence on the nature of magnetizing matter in elliptical galaxies. Finally, there is evidence, again coming mainly from radio observations, of magnetic fields of $\sim (0.1 - 10)$ μG in clusters of galaxies (Allen et al., 2001; Taylor et al., 2001; Feretti, 2002), the largest bound system in the Universe. Faraday rotation studies indicate they have coherence scale in the range $5 - 10$

kpc (Taylor and Perley, 1993; Enßlin and Vogt, 2003; Vogt and Enßlin, 2003). These fields, if they are not maintained by some mechanism, will evolve following the decay of MHD turbulence that we can estimate to occur in an Alfvén time $\sim 10^8$ yr, much less than the age of the cluster. Also in these context is therefore possible for a dynamo mechanism to come into action.

In most cases an amplification of the magnetic fields may occur also by instabilities capable of converting kinetic energy into magnetic energy. Under certain conditions, within the ideal magnetohydrodynamical regime (MHD), both Kelvin–Helmoltz and Rayleigh–Taylor instabilities are able to provide such effect, and these have been studied also in the relativistic environment of Pulsar Wind Nebulae (Bucciantini et al., 2004; Bucciantini and Del Zanna, 2006). A very efficient and ideal process is the MRI mentioned above that provide a local mechanism, efficient for a wide range of magnetic field strength, which leads to a growth on dynamical time-scales of linear perturbations and naturally develops MHD turbulence. The only necessary condition for its onset is the presence of a differentially rotating fluid threaded by a weak magnetic field. In the context of the accretion disk MRI has been studied by both analytical and numerical studies, both through local shearing box simulations and global models; while the former consider a small slice of plasma, the latter evolve the system in its entirety. Both approaches are useful because they allow to obtain local information on the growth and saturation of instability and global effects such as interaction with other phenomena. About the latter, we can mention the work Bugli et al. (2018), where the interaction between MRI and the fluid, nonaxisymmetric Papaloizou-Pringle instability (PPI) (Papaloizou and Pringle, 1984) has been investigated. Three-dimensional general relativistic magnetohydrodynamics (GRMHD) simulations show that in a magnetized torus around a Schwarzschild black hole, PPI large-scale modes are suppressed by the development of MRI, which is then to be considered the main driver for accretion on to supermassive black.

However, in typical astrophysical plasmas, the amplification of the magnetic field is a non-ideal process due to the non-linear coupling of small-scale velocity and magnetic field fluctuations, possibly caused by the MRI. The result of this correlation leads to the creation of an electromotive force capable of amplifying magnetic fields. This process is known as mean-field dynamo (Moffatt, 1978; Krause and Raedler, 1980; Cowling, 1981; Roberts and Soward, 1992; Brandenburg and Subramanian, 2005) and has been applied to a large number of astrophysical contexts, from the Sun to explain the 11 year cycle (Parker, 1955), to cosmological fields (Kulsrud et al., 1997). Anticipating some details that will be discussed later, in axisymmetric and differentially rotating systems, the combined action of turbulent coupling and differential rotation supports the amplification of magnetic fields according to the mechanism known as $\alpha - \Omega$ dynamo. As far as compact objects are concerned, this dynamo may be responsible for the amplification of fields up to $B \sim 10^{14-15}$ G in magnetars during the proto-neutron star phase. If the initial rotation period is less than 1ms, the field can be amplified either by differential rotation, magnetic instabilities, and the dynamo effects described above (Duncan and Thompson, 1992; Bonanno et al., 2003; Burrows et al., 2007; Obergaulinger et al., 2014; Guilet and Müller, 2015; Mösta et al., 2015; Raynaud et al., 2020; Reboul-Salze et al., 2020). The intense magnetic fields that form can be so strong to cause quadrupolar deformations in the star, that in some cases are able to radiate gravitational waves (Dall'Osso et al., 2009; Pili et al., 2017) and guide relativistic outflows capable of powering gamma-ray bursts (Usov, 1992; Bucciantini et al., 2009; Metzger et al., 2011; Bucciantini et al., 2012; Pili et al., 2016). Certainly amplification and supplying of the magnetic field plays a key role in the accretion around the black

holes of AGNs. From a theoretical point of view it is believed that disks are threaded by magnetic fields allowing MRI to operate, leading to a redistribution of angular momentum and to MHD turbulence. MRI works for both ordered and disordered fields, though this mechanism alone is inefficient in compensating the turbulent decay if the initial fields are too weak or too incoherent (Bhat et al., 2017). In these cases a genuine dynamo process would be actually needed to amplify the initial fields to higher values. Amplification of magnetic fields due to a mean-field dynamo and/or MRI is also important in other scenarios of high-energy astrophysics, like neutron star mergers (Rezzolla et al., 2011; Giacomazzo et al., 2015)) and tidal disruption events (Sądowski et al., 2016; Bonnerot et al., 2017).

Currently, GRMHD simulations of MRI-induced accretion on to rotating black holes are being receiving considerable attention due to the success of the Event Horizon Telescope (EHT) collaboration, capable of imaging the emission and the shadow around the event horizon of a black hole for the very first time (EHT-Collaboration, 2019c). The comparison between data and numerical models has allowed to infer the main physical quantities of the compact object (EHT-Collaboration, 2019e). The observed source has been the nucleus of the elliptical galaxy M87, but research is ongoing for the main target Sgr A*, the compact radio source located at the centre of our Milky Way. The most recent study on polarized emission of M87* (EHT-Collaboration, 2021b) has made it possible to obtain more precise estimates of the quantities of interest as well as to direct attention to an accretion model characterized by a high magnetization that creates a highly turbulent environment, so a turbulent dynamo mechanism can fit perfectly into this context.

The aim of this thesis work is to provide an alternative numerical accretion modelling to the ideal one in which the initial magnetic field has a well-defined poloidal structure and an intensity not exactly negligible. The $\alpha - \Omega$ dynamo allows us to investigate the possibility of producing poloidal field necessary for the development of MRI and the launch of jets even starting from the most unfavorable condition, that is an initial toroidal field with extremely lower magnetization than those used in ideal GRMHD simulations. The numerical tool we chose is the ECHO code (Del Zanna et al., 2007) updated from its original version to include non-ideal effects such as resistivity and a mean-field dynamo mechanism (Bucciantini and Del Zanna, 2013). The first study is due to Bugli et al. (2014) that characterized the exponential growth of the magnetic field under the action of the $\alpha - \Omega$ dynamo in accretion disks with the hypothesis of kinematic regime, i.e. evolving only Maxwell's equations. In Tomei et al. (2020) we generalize Bugli's work by investigating the completely self-consistent and non-linear regime (dynamic regime) during the accretion phase. The linear growth of the fields cannot reasonably continue for an arbitrarily long time, and it is expected to be quenched naturally by the feedback on the disk. Our goal is to see how the transition to the non-linear phase occurs, to investigate the interplay with MRI, and the effect of accretion on the dynamo process itself, for a given disk model and a variety of dynamo parameters. Once the saturation was characterized, we studied more rigorously the possibility of reproducing with our model the physical quantities of observational interest by making a precise comparison with the recent literature (Tomei et al., 2021).

At the same time we participated with our ECHO code in the Code Comparison project (Porth and EHT-Collaboration (2019), Olivares et al. in prep.) with the aim to provide support to the EHT collaboration for the creation of ideal GRMHD libraries that allow us to make a comparison with the observations. Some standard accretion problems are studied by different codes in order to

test which techniques are the most effective. The convergence on the results obtained represents a point of reference and synthesis in the vast world of numerical simulations of accretion disks and can allow the development of more accurate models such as the case of the mean-field dynamo.

The thesis work is organized as follows: in Chapter 2 we present the relevant aspect of the theory of the accretion disks around black holes including the mean-field dynamo mechanism. Then we introduce the GRMHD formalism and the disk models used in our simulations in Chapter 3 while Chapter 4 describes the structure of the code ECHO. In Chapter 5 we discuss the results of the ideal simulations of the first part of the Code Comparison Project. We also present some preliminary results obtained relating to the second part. In Chapter 6 we present and discuss the first global results of the mean-field dynamo GRMHD simulations in accretion disks. Finally, we present conclusions and future developments in Chapter 7.

Chapter 2

Some aspects of the theory of the thick accretion disks

The study of the complexity that characterizes the accretion disks around black requires both theoretical models and simulations. Following the review of Abramowicz and Fragile (2013) we can schematize that three generic types of physical processes occur in black hole accretion disks:

- dynamic processes (gravity, pressure and rotation forces) that develop on a time scale of $t_{\rm dyn} \sim 1/\Omega_{\rm disk}$ where $\Omega_{\rm disk}$ is a typical value of the angular velocity;
- thermal processes with a characteristic time-scale $t_{\rm th} \sim c_s^2/\nu\Omega_{\rm disk}^2$ where c_s the sound speed and ν is the kinematic viscosity;
- viscous processes with a characteristic time-scale $t_{\rm vis} \sim R_{\rm disk}^2/\nu$ where $R_{\rm disk}$is the radial distance from the black hole.

Typically, one accepts that $t_{\rm dyn} \ll t_{\rm th} \ll t_{\rm vis}$ and it is therefore reasonable to consider only the dynamic structure of the disk as a first approximation. Depending on the importance of each of the components that contribute to the dynamic structure, we can classify discs into the following classes:

- Thin Disk: they are fully supported by the Keplerian rotation and the contribution due to the pressure is negligible. The geometric structure and the kinematics are greatly influenced by the dynamics: the vertical height is much smaller than the radial extension and the rotation speed is highly supersonic. The low radial velocity implies that advection is an inefficient energy transport mechanism and accretion rate is small, $\dot{M} \sim 10^{-1}\dot{M}_{\rm Edd}$, with $\dot{M}_{\rm Edd} = 10L_{\rm Edd}/c^2$ Eddington rate where $L_{\rm Edd}$ is the Eddington luminosity, that is the maximum value of an accreting source's luminosity beyond which the outgoing radiation pressure is strong enough to counteract the gravitational force. We specify that here, in the definition of Eddington rate $\dot{M}_{\rm Edd}$, we are assuming that the accretion disk has a nominal radiative efficiency of 10%.
- Thick Disk: in these disks the radial pressure gradients are no longer negligible they contribute significantly to the disk support and therefore the vertical size of the disk increases significantly. Mass accretion can be very high, $\dot{M} \gg \dot{M}_{\rm Edd}$ although they are radiatively inefficient due to the lack of an efficient radiative cooling mechanism.

- Advection Dominated Accretion Flow (ADAF): geometrically thick accretion flows (for this reason often included in the literature in the generic category of "thick disks"), characterized by a large pressure and a low rotation speed so that the accretion is similar to a Bondi accretion. Energy transport is dominated by advection and radiative cooling is negligible so that efficiency is very low. Mass accretion rate is very low, $\dot{M} \ll \dot{M}_{\rm Edd}$

The accretion of EHT targets, SgrA* and M87*, occurs at very low Eddington rate, respectively $\dot{M}/\dot{M}_{\rm Edd} \lesssim 10^{-6}$ (Marrone et al., 2007) and $\dot{M}/\dot{M}_{\rm Edd} \lesssim 10^{-5}$ (Kuo et al., 2014), and therefore they can be modeled as ADAF disks. The renewed interest in these sources, due to the recent observations of EHT, has pushed the community of numerical codes to study ever more refined ADAF modeling. In this chapter we make an overview of some general aspects concerning the accretion theory including in particular the Advection Dominated Accretion Flow theory (more details in the reviews of Narayan and McClintock (2008); Yuan and Narayan (2014)), while in Chapters 5 and 6 we show some of our numerical simulations of two configurations belonging to this regime.

2.1 One-dimensional equilibrium models and radiation

2.1.1 The self-similar solutions

ADAFs were formally introduced in the Newtonian limit by Narayan and Yi (1994, 1995a,b) followed by Chen et al. (1995); Abramowicz et al. (1995). In order to describe the key properites of ADAFs consider first a generic steady axisymmetric non-magnetized accretion flow in the Newtonian limit and get the fundamental equations of conservation of mass, radial momentum, angular momentum and energy following the works of Pringle (1981) and Yuan and Narayan (2014).

In a cylindrical coordinate system (R, z, ϕ) centered on the black hole of mass M, we consider a annulus of the disk located at a distance of R, having thickness ΔR, mid-plane density ρ and surface density $\Sigma = \int_{z_0}^{z} \rho {\rm d}z$. The mass contained in the ring is ${\rm d}M = 2\pi R \Delta R \Sigma$ and its angular momentum is ${\rm d}L = 2\pi R \Delta R \Sigma R^2 \Omega$, where $\Omega(R)$ is the angular velocity. The rate of change of the mass of the annulus is equal to the net flow of matter into it from neighboring annuli

$$\frac{\partial M}{\partial t} = \frac{{\rm d}M(R) - {\rm d}M(R + \Delta R)}{\Delta t}. \tag{2.1}$$

We can rewrite the expression as

$$\frac{\partial}{\partial t}(2\pi R \Delta R \Sigma) = (v_R 2\pi R \Sigma)_R - (v_R 2\pi R \Sigma)_{R+\Delta R}, \tag{2.2}$$

where $v_R = \Delta R/\Delta t$ is the radial velocity. Then taking the limit for $\Delta R \to 0$ by it becomes

$$R\frac{\partial \Sigma}{\partial t} + \frac{\partial}{\partial R}(R \Sigma v_R) = 0. \tag{2.3}$$

From Eq.(2.3) we get the conservation of the mass in a steady axisymmetric flow taking $\partial/\partial t = 0$,

$$\frac{\partial}{\partial R}(R \Sigma v_R) = 0. \tag{2.4}$$

Similarly conservation of angular momentum for the annulus yield the equation

$$\frac{\partial}{\partial t}(2\pi R^3 \Delta R \Sigma \Omega) = (2\pi R^3 \Delta R \Sigma \Omega)_R - (2\pi R^3 \Delta R \Sigma \Omega)_{R+\Delta R} + \Delta G, \tag{2.5}$$

with G momentum of the viscous force which can be written as $G = 2\pi R \nu \Sigma R(\partial\Omega/\partial R)R$ where $\nu\Sigma R(\partial\Omega/\partial R)$ is the viscous force per unit of length. The kinematic viscosity coefficient ν is usually parameterized with the Shakura and Sunyaev (1973) prescription:

$$\nu = \alpha_{\rm ss} c_s H, \tag{2.6}$$

where the dimensionless parameter $\alpha_{\rm ss}$ is the Shakura-Sunyaev parameter and H is the vertical scale height. Taking the limit $\Delta R \to 0$ in Eq. (2.5), we get the conservation law of the angular momentum for a steady flow

$$v_R \frac{\partial}{\partial R}(\Omega R^2) = \frac{1}{R\Sigma}\frac{\partial}{\partial R}\left(R^3 \Sigma \nu \frac{\partial \Omega}{\partial R}\right). \tag{2.7}$$

Conservation law of radial momentum can be easily obtained in a reference frame co-rotating with the plasma. In a steady flow we get

$$v_R \frac{\partial}{\partial R} v_R = \Omega^2 R - \Omega_k^2 R - \frac{1}{\rho}\frac{\partial(\rho c_s^2)}{\partial R}, \tag{2.8}$$

where the contributions on the right side are due respectively to the centrifugal force, the Keplerian gravitational potential (Ω_K is the Keplerian angular velocity) and the pressure gradient. In the last term we considered the expression of the isothermal of the sound speed, $c_s = \sqrt{p/\rho}$.
Finally, conservation energy reads

$$\rho T\left(\frac{\partial s}{\partial t} + v_R \frac{\partial s}{\partial R}\right) = q_+ - q_-, \tag{2.9}$$

where s is the specific entropy, T is the temperature and q_+ and q_- are the rates of energy gain and loss per unit volume respectively. In particular q_+ represents the energy per unit of time and volume dissipated due to the viscous effects and it is given by

$$q_+ = \frac{G}{2\pi R H}\frac{\partial G}{\partial \Omega} = R^2 \nu \rho \left(\frac{\partial \Omega}{\partial R}\right)^2, \tag{2.10}$$

where the vertical scale height can be expressed as $H = \Sigma/\rho$. The rate of energy losses q_- is the cooling rate per unit volume. It is usually customary to define a parameter f that indicates the fraction of advected energy: it is written as $f = (q_+ - q_-)/q_+$. Obviously, the quantity $1 - f$ represents the fraction of radiated energy. Again, in the stationary case Eq. (2.9) reads

$$\rho T v_R \frac{\partial s}{\partial R} = R^2 \nu \rho \left(\frac{\partial \Omega}{\partial R}\right)^2 - q_- \equiv f q_+. \tag{2.11}$$

Eqs.(2.4),(2.7),(2.8),(2.11) are general and can be referred to all accretion models. Note, however, that Eq. (2.4) implies the mass accretion rate, defined as $\dot{M} = 4\pi R \Sigma v_R$, is independent of radius. While this may be a reasonable approximation for a thin disk wind, a more general discussion

must include the possibility that the system produces outflows, causing the mass accretion rate to decrease with decreasing radius. Therefore, assuming a power-law variation for simplicity, it is useful to generalize equation as

$$\dot{M} = \dot{M}_{\rm BH}\left(\frac{R}{R_S}\right)^{s_o}, \tag{2.12}$$

where $R_S = 2GM/c^2$ is the Schwarzschild radius of the black hole, $\dot{M}_{\rm BH} = \dot{M}(R_S)$ is the mass accretion rate evaluated at $R = R_S$ and $s_o < 1$ is a measure of the strength of the outflow (Blandford and Begelman, 1999).

The ADAF regime is defined when radiative cooling can be neglected as opposed to heat advection, $f \to 1$ and the accretion flow is underluminous $\dot{M}_{\rm BH} \ll \dot{M}_{\rm Edd}$ or equivalently $\eta \equiv L/(\dot{M}_{\rm BH}c^2) \ll 0.1$, where η is the radiative efficiency and L is the luminosity. The first self-similar solutions are obtained by Narayan and Yi (1994) for arbitrary viscosity parameter $\alpha_{\rm ss}$ and adiabatic index γ_a and assuming $s_o = 0$. A more recent version of the self-similar solution including outflows ($s_o \neq 0$) and magnetic field is due to Yuan et al. (2012):

$$v_R \approx -1.1 \times 10^{-10}\,\alpha_{\rm ss}\, r^{-1/2}\,{\rm cm^{-1}\,s^{-1}}, \tag{2.13}$$

$$\Omega \approx 2.9 \times 10^{4}\, m^{-1} r^{-3/2}\,{\rm s^{-1}}, \tag{2.14}$$

$$c_s^2 \approx 1.4 \times 10^{20}\, r^{-1}\,{\rm cm^2\,s^{-2}}, \tag{2.15}$$

$$n_e \approx 6.3 \times 10^{19}\, \alpha_{\rm ss}^{-1/2}\, \dot{m}_{\rm BH}\, r^{-3/2+s}\,{\rm cm^{-3}}, \tag{2.16}$$

$$B \approx 6.5 \times 10^{8}\, (1+\beta)^{-1/2}\, \alpha_{\rm ss}\, m^{-1/2}\, \dot{m}_{\rm BH}^{1/2}\, r^{-5/4+s/2}\,{\rm G}, \tag{2.17}$$

$$p \approx 1.7 \times 10^{16}\, \alpha_{\rm ss}^{-1}\, m^{-1}\, \dot{m}_{\rm BH}\, r^{-5/2+s}\,{\rm g\,cm^{-1}\,s^{-2}} \tag{2.18}$$

where $m = M/M_\odot$, $\dot{m} = \dot{M}/\dot{M}_{\rm Edd}$, $r = R/R_S$. Again with $\dot{m}_B H$ we have indicated $\dot{m}$ evaluated at $R = R_S$.

The self-similar solutions reveal the key properties of ADAFs that are:

- The accretion rate and the luminosity are lower than the typical values of thin disks.
- The sound speed is comparable to the Keplerian velocity, $c_s \sim v_K$, which means that the temperature of the plasma is nearly virial, $T \sim (10^{12}/R)$ K, consistently with the fact that there is no cooling.
- Due to the high pressure the vertical height of the disc becomes comparable to the radius, $H \sim R$.
- The strong radial pressure support causes the angular velocity to become sub-Keplerian, $\Omega < \Omega_K$.

- The radial velocity is high and consequently the accretion is very fast, only a few free-fall times.
- The high radial velocity in a geometrically thick disk causes the density to be low for the accretion rate to be sub-Eddington.
- The accreting gas in an ADAF has a positive Bernoulli parameter, defined as the sum of the kinetic energy, potential energy and enthalpy (Narayan and Yi, 1994). Since the parameter is conserved in an adiabatic flow, then, if it is positive, it is possible to imagine that the gas can somehow flow adiabatically outwards and reach infinity with a positive net energy. Therefore, winds, jets and other outflows may originate in ADAFs.
- Since the gas is heated but non efficiently cools, the entropy increases with the decreasing of the radius. ADAFs can therefore transport energy via convection.

The regime described by these properties is sometimes referred to as a RIAF (radiatively inefficient accretion flow), however, in this discussion, we adopt the term ADAF.

The ADAF disk is a pressure dominated gas where the temperature can approach 10^{12} K at small radii from the black hole. For such a hot accreting gas not to radiate effectively it is customary to allow the ions and electron to have different temperatures (Narayan and Yi, 1995b). In fact the gravitational energy is mainly transferred to ions that radiate ineffectively. This energy could be exchanged with electrons through Coulomb interactions but in a very hot and low-density plasma these interactions are slow. The ions therefore have an almost virial temperature while the electrons are much colder. Typical ADAF temperatures scaling for protons and electrons are

$$T_i \sim 10^{12}\mathrm{K}, \quad T_e \sim \min(T_i, 10^{9-11}\mathrm{K}) \tag{2.19}$$

Obviously it is crucial to know the precise form of the electron and proton distributions in order to be able to compare the theoretical spectra with those observed. Mahadevan and Quataert (1997) studied the energy distributions of the two species in ADAFs for normal mass accretion rates. They showed that electrons can efficiently exchange energy both by Coulomb collisions and by absorption and emission of synchrotron photons and therefore can thermalize; the electron energy distribution may thus be Maxwellian for the bulk of the electrons, but power-law for a small population of electrons at higher energies. Coulomb collisions are far too inefficient to thermalize the ions, so ions retain whatever energy distribution they acquire through viscous dissipation and heating. Early work on two-temperature ADAFs assumed that viscous heating acts primarily on the ions. We can define a parameter δ that denotes the fraction of the viscously energy that directly heats electrons: Narayan and Yi (1995b) took $\delta = 0$ while Esin et al. (1997) assumed $\delta = m_e/m_i \sim 10^{-3}$. However, the existence of neither a two-temperature plasma, nor a radiatively inefficient accretion flow requires such a small value of δ. By modeling astrophysical observations of Sgr A* and other brighter sources, some constraints have been obtained on its value. Actually we can say that δ is probably in the range 0.1-0.5. The work of Sharma et al. (2007) showed that $\delta \sim (T_e/T_i)^{1/2}/3$. At large radii, where the plasma can be considered one-temperature, the formula gives $\delta \sim 0.3$, while in the inner region, where the plasma is two-temperature, it gives $\delta \sim 0.01 - 0.1$. Taking these

properties into account, the energy equation (2.11) can be replaced by two coupled equations

$$\rho v \frac{de_i}{dR} - q^{p,c} = (1-\delta)q^+ - q^{ie}, \tag{2.20}$$

$$\rho v \frac{de_e}{dR} - q^{e,c} = \delta q^+ + q^{ie} - q^-, \tag{2.21}$$

where e_i, e_e are the internal energies of ions and electrons per unit mass of the gas; $q^{i,c}$, $q^{e,c}$ are the compression works done per unit volume; q^{ie} is the rate of transfer of thermal energy from ions to electrons via Coulomb collisions.

2.1.2 Global models and emissivity function

The self-similar solution presented above allows to understand the main properties of an ADAF but, being scale-free, it is not appropriate near the inner or outer boundary of the flow. Therefore, one must use global solutions especially for calculating the radiation spectrum, since most of the radiation comes from the inner region. A global model is obtained by solving the equations presented in 2.1.1 numerically. The main parameters of global models are:

- BH mass, M;
- accretion rate, $\dot{M}_{BH}$;
- viscosity parameter, $\alpha_{\rm ss}$;
- beta plasma $\beta = p_{\rm gas}/p_{\rm mag}$
- adiabatic index, γ_a;
- viscous heating parameter, δ;
- advection parameter, f;
- the wind parameter s_o;

Actually, most of these parameters are constrained: M is usually known through observations, δ is discussed in 2.1.1, $\alpha_{\rm ss}$, β, s_o are obtained from numerical simulations, while f can be obtained self-consistently (Narayan and Yi, 1995b; Esin et al., 1997; Yuan et al., 2003); $\dot{M}_{\rm BH}$ is a free parameter which can however be fitted to observations of luminosity or spectrum of a source. The numerical solution allows to obtain the radial distribution of the quantities v, Ω, c_s, ρ, T_p, T_e, $p_{\rm gas}$, $p_{\rm mag}$. These global solutions agree with the self-similar solutions away from the boundaries, confirming their validity (Narayan et al., 1997; Chen et al., 1997).

The fully general relativistic version of the global problem has been solved by many authors: the first attempts are due to Abramowicz et al. (1996), but the first satisfactory solutions are found in subsequent works by Abramowicz et al. (1997); Beloborodov et al. (1997); Gammie and Popham (1998). The results show agreement with the Newtonian approximation for $R > 10R_s$, while the effects of the Kerr metric are significant in the inner region.

Global models allow us to reproduce the spectrum of the sources. In a gas as hot as that of ADAF disks, the dominant radiative processes are synchrotron emission and bremsstrahlung, modified by

Comptonization. In order to explain the observed spectra Narayan (1996) first proposed a model based on the transition from thin disk to ADAF that occurs starting from a certain transition radius, $R_{\rm tr}$: in the outer part is the thin disk, while for $R < R_{\rm tr}$ the thin disk is truncated and the region is occupied by an ADAF. The transition radius depends on $\dot{m}_{\rm BH}$ with the thin disk truncated at $R_{\rm tr} \sim 10^3 - 10^4 R_S$ when $\dot{m}_{\rm BH} < 10^{-3}$. In general, the spectrum of a source is produced by the black body contribution of the outer thin disk and by the comptonized synchrotron and bremsstrahlung contributions of the ADAF in the inner region. In addition, the presence of a jet with non-thermal electrons can enhance radio and infrared emission and smooth the inverse Compton bumps.

A useful expression for the emissivity produced by ultrarelativistic thermal electrons emitting synchrotron radiation was provided by Leung et al. (2011). Let us consider a population of eletctrons described by a phase space distribution function $f = {\rm d}n_e {\rm d}\Gamma {\rm d}\Omega_p$, where Γ is the Lorentz factor and ${\rm d}\Omega_p$ is the solid angle element in the moments space. The total emissivity per unit of frequency of this distribution can be defined as

$$j_\nu = \int {\rm d}^3 p f \eta_\nu, \tag{2.22}$$

where

$$\eta_\nu = \frac{{\rm d}E}{{\rm d}\nu {\rm d}t {\rm d}\Omega_p} \tag{2.23}$$

is the emissivity per unit of frequency for a single electron. The function distribution relative to a population of thermal electrons is given by

$$f = \frac{n_e}{4\pi\Theta_e} \frac{\Gamma(\Gamma^2-1)^{1/2}}{K_2(1/\Theta_e)} \exp\left(-\frac{\Gamma}{\Theta_e}\right), \tag{2.24}$$

where $\Theta_e = KT_e/(m_e c^2)$ and K_2 is a modified Bessel function of the second kind. In the ultrarelativistic regime, $\Gamma \gg 1$ and $\Theta_e \gg 1$, we can use the approximation $K_2(1/\Theta_e) \simeq 2\Theta_e^2$ and Eq. (2.24) becomes

$$f \simeq \frac{n_e \Gamma^2}{8\pi\Theta_e^3} \exp\left(-\frac{\Gamma}{\Theta_e}\right). \tag{2.25}$$

The integral is evaluated using a standard approximation

$$\int {\rm d}\Omega_p \eta_\nu \simeq \frac{\sqrt{3} e^3 B \sin\theta}{m_e c^2} F\left(\frac{\nu}{\nu_{\rm cr}}\right), \tag{2.26}$$

where

$$\nu_{cr} = (3/2)\nu_c \sin\theta \Gamma^2, \tag{2.27}$$

ν_c is the electron cyclotron frequency $eB/(2\pi m_e c)$ and the synchrotron function is defined as

$$F(x) = x \int_x^\infty {\rm d}t K_{5/3}(t), \tag{2.28}$$

with the following asymptotic limits

$$F(x) = \begin{cases} 2^{2/3}\Gamma(2/3)x^{1/3} + O(x) & \text{for } x \ll 1, \\ \left(\frac{\pi x}{2}\right)^{1/2} \exp(-x)(1 + O(x^{-1})) & \text{for } x \gg 1. \end{cases} \tag{2.29}$$

In Eqs.(2.28)-(2.29) we put $x = \nu/\nu_s$ where the threshold frequency ν_s is defined as

$$\nu_s = (2/9)\nu_c \Theta_e^2 \sin\theta. \tag{2.30}$$

In simulations of Chapters 5 and 6 we study the high-frequency limit ($\nu \gg \nu_s$) of the thermal synchrotron emissivity. In this regime the integrand of (2.22) is proportional to $\exp(-\Gamma/\Theta_e - \nu/\nu_{\rm cr})$, where now $\nu_{\rm cr} \sim \Gamma^2$, so the peak emission is from electrons with $\Gamma \sim [\nu\Theta_e/(\nu_c \sin\theta)]^{1/3}$. The emissivity per unit frequency results

$$j_\nu \simeq n_e \frac{\sqrt{2}\pi e^2 \nu_s}{6\Theta_e^2 c} X \exp\left(-X^{1/3}\right). \tag{2.31}$$

where $X = \nu/\nu_s$. The emission obtained by integrating Eq. (2.31) over the volume also allow to get a feeling for the predictive power of variability in a turbulent regime.

2.2 Disk dynamics from numerical simulations

Self-similar solutions and global models permit to capture the physics underlying the ADAF accretion problem. For greater realism, numerical magnetohydrodynamic simulations are the only way since they allow to understand the three-dimensional structure of accretion flow and the fundamental role played by the magnetic field. Among these we distinguish between local simulations (shearing box), where a small area of the disk is considered, and global simulations that allow a more complete description of the accretion.

Here we describe one of the most studied phenomena through local simulations, namely magnetorotational instability. At the level of global simulations we focus on the description of the ADAF accretion in the two best-known regimes: SANE (Standard And Normal Evolution) and MAD (Magnetically Arrested Disk).

2.2.1 Magnetorotational instability

A key process of the accretion disks that must be studied through numerical simulations because of its non-linearity is undoubtedly the magnetorotational instability (MRI). It is a fundamental mechanism that allows the transport of angular momentum and can acts also as an effective dynamo. It was first studied by Chandrasekhar (1960) in plasma physics but rediscovered in the context of accretion disks by Balbus and Hawley (1991, 1998).

This ideal instability arises due to the action of a magnetic field in a system subject to differential rotation and can lead to large scale mixing and turbulence very quickly ($t_{\rm MRI} \propto 1/\Omega$). The conditions necessary for MRI to develop are:

- weak poloidal magnetic field;
- disk with differential rotation and angular momentum increasing outwards.

To understand how MRI works, we can think of a mechanical analogy. Let us consider two fluid elements connected by a spring in a differential rotation system such as the one shown in the Figure 2.1. In this model, the force produced by the magnetic field is schematized by the elastic force. Intuitively the spring force is a stabilizing force but if differential rotation is present then it can lead

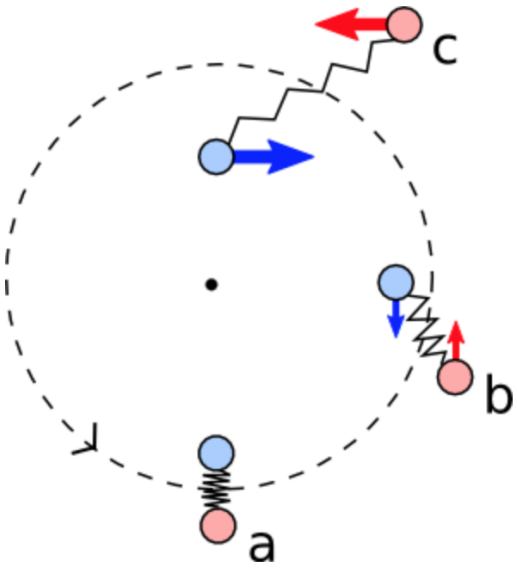

Figure 2.1: Mechanical analogy showing the growth of MRI due to differential rotation.

to instability. To see it, suppose that the two particles are in a configuration like the one shown at the time "a" of the Figure 2.1. Differential rotation increases the displacement between the two particles because the inner particle rotates faster than the outer one. Therefore, the magnetic tension increases and the inner particle is slowed down while the outer one accelerates. By slowing down, the inner particle loses angular momentum and is forced to orbit at smaller radii, while the outer particle moves outward (times "b" and "c"). This mechanism does not stop until the particles are completely separated. However, it is important to point out that the magnetic field must not be excessively strong otherwise the particles can only oscillate around their initial positions.

From the simulations of MRI, we can estimate the viscosity parameter $\alpha_{\rm ss}$ and observe that there is a discrepancy between the numerical results and the observations. The outbursts of the Soft X-ray Transients and the dwarf novae accretion disks suggest, e.g., a value of the viscosity parameter of $\alpha_{ss} \sim 0.1 - 0.4$ (Dubus et al., 2001; Schreiber et al., 2003, 2004), while numerical shearing-box simulations of MRI give lower values $\alpha_{ss} \sim 0.01 - 0.1$ (Davis et al., 2010; Guan and Gammie, 2011; Simon et al., 2012; Hawley et al., 2013). The main limitations of these simulations concern the impossibility of generating large-scale magnetic structures, both due to limited computational resources and the limitations imposed by boundaries conditions (King et al., 2007). More recently, some studies have tried to investigate possible mechanisms capable of producing a higher viscosity parameter. Among them, Held and Latter (2018) showed that convection can effectively transport angular momentum outward in disks and its interaction with the MRI, which is capable of being a source of convection, could lead to an increase of an order of magnitude in the value of the viscosity parameter (Held and Latter, 2021).

2.2.2 Global simulations: Standard And Normal Evolution and Magnetically Arrested Disks

The first global MHD simulations in which the black hole was modeled via a pseudo-Newtonian potential showed similar results to those of the shearing box simulations in terms of MRI-driven turbulence development. Recently, simulations are carried out by general relativistic MHD (GRMHD)

codes that provide a better description of phenomena near the black hole. We discuss now the most important features of the problem resulting from the simulations.

Since we focus on the targets of EHT, SgrA* and M87*, where the accretion rate is very sub Eddington and the radiative cooling timescale becomes longer than the accretion timescale, purely non-radiative GRMHD simulations ignoring cooling can be used to model the data. We specify that radiative cooling is certainly negligible for SgrA* (Dibi et al., 2012), while it is probably not for M87* (Chael et al., 2019).

The general morphology of thick disks derived from simulations is separated into the components shown in Figure 2.2:

- the disk, which contains the bound matter;
- the evacuated funnel extending from the polar caps of the black hole;
- jet sheath, which is the remaining outflowing matter.

The blue line in Figure 2.2 demarcate the bound/unbound transition defined via the Bernoulli criterion for which the relativistic hydrodynamic parameter is defined as $Be = -hu_t - 1$ (Novikov and Thorne, 1973) but here the geometric parameter, $Be = -u_t - 1$, has been adopted so as to have $u_t < -1$ in the unbound region characterized by having $Be > 0$. The red contour demarcates the funnel boundary, $\sigma = 1$, where $\sigma = B^2/(\rho c^2)$ is the magnetization, and the green contour the equipartition $\beta = 1$, which is close to the bound/unbound line along the disk boundary. In McKinney and Gammie (2004) a disk corona was also introduced for the material with $1 < \beta < 3$; however, as this choice is arbitrary, there is no compelling reason to label the corona as a separate entity in the ADAF scenario. Between the evacuated funnel demarcated by the funnel wall (red) and the bound disk material (blue), there is a strip of outflowing material often also referred to as the jet sheath: this flow emerges as plasma from the disk and it is driven against the centrifugal barrier by magnetic and thermal pressure.

In ADAF accretion a key role is played by horizon penetrating magnetic flux $\Phi_{\rm BH}$ normalized by the accretion rate $\dot{M}$, $\phi = \Phi_{\rm BH}/\sqrt{\dot{M}}$. Tchekhovskoy et al. (2012) showed that a maximum for the magnetic flux, $\phi_{\rm max}$ exists depending only mildly on black hole spin, but somewhat on the disk scale height, with taller disks being able to hold more magnetic flux. This parameter defines the two accretion regimes:

- if $\phi < \phi_{\rm max}$ the regime is known as SANE acronym that stands for standard and normal evolution (Narayan et al., 2012; Sądowski et al., 2013);
- if $\phi \sim \phi_{\rm max}$ the regime is kwown as MAD acronym that stands for magnetically arrested disk (Bisnovatyi-Kogan and Ruzmaikin, 1976; Narayan et al., 2003)).

In the first, magnetic fields are present but are not very intense and are largely absorbed by the black hole. In the second mode of accretion the magnetic field is much more intense and the black hole is not able to absorb everything that is transported over great distances. For this reason, a bottleneck is created in the disk due to which the magnetic field accumulates and generates a pressure high enough to significantly dampen the accretion rate, even managing to stop it temporarily.

One of the first quantitative comparisons between MAD and SANE was made by Sądowski et al. (2013). The authors consider a initial torus of gas threaded either by multiple and counterorientated,

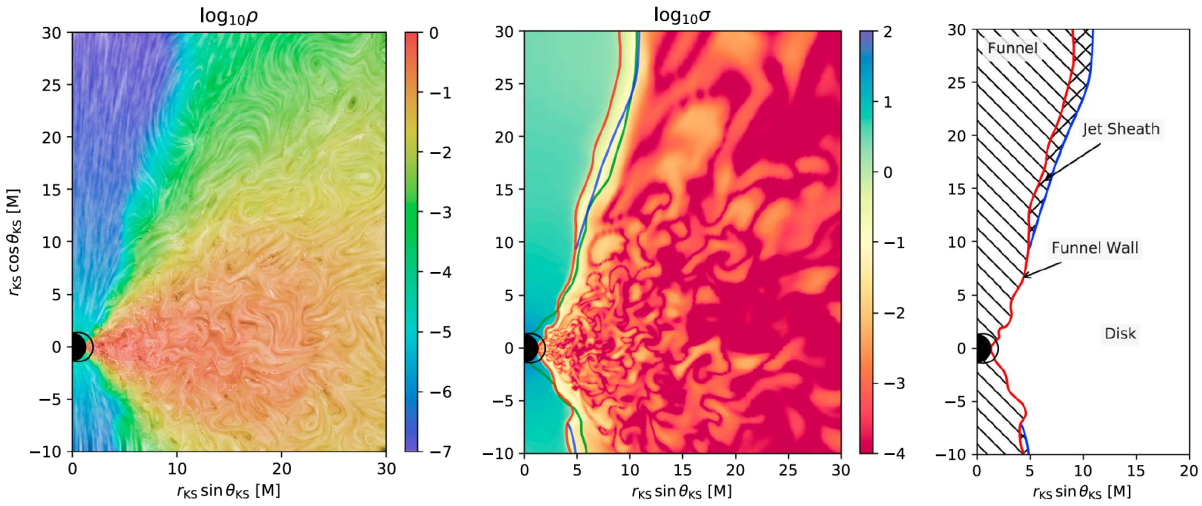

Figure 2.2: Views of the radiatively inefficient turbulent black hole accretion problem against the Kerr–Schild coordinates obtained from a simulation with BHAC (Porth et al., 2017). The black hole horizon is the black disk and the ergosphere is shown as a black contour. Left: logarithmic rest-frame density and rendering of the magnetic field structure using line-integral convolution, showing the ordered field in the funnel region and turbulence in the disk. Center: the logarithm of the magnetization. The magnetized funnel is demarcated by $\sigma = 1$, (red lines), the disk is indicated by $\beta = 1$ (green lines), and the geometric Bernoulli criterion ($u_t = -1$) is given by the blue solid line in the region outside of the funnel. Right: schematic of the main components. Figure of Porth and EHT-Collaboration (2019).

or single poloidal magnetic field loops for SANE and MAD models, respectively. The upper panel of Left Figure 2.3 shows the mass accretion rate $\dot{M}$ and the bottom panel shows the evolution of the magnetic flux ϕ_B where the solid and dotted lines correspond to MAD and SANE models, respectively. While there is no clear difference between MAD and SANE in terms of mass accretion rate, we can see how in the MAD runs the magnetic flux at the horizon always remains around a value that corresponds to the maximum allowed and is higher than SANE runs. An important feature of the ADAF concerns the development of powerful jets according to the Blandford Znajek model (Blandford and Znajek, 1977) which predicts that the magnetic field lines threading a black hole can extract its the rotational energy. Right Figure 2.3 shows the radial profile of efficiency of the accretion flow (red lines), i.e. the energy that flows out to infinity normalized by the net mass accretion rate, and the contributions of jet and wind. We see that SANE run has an efficiency of a few per cent whereas the MAD run has a much larger efficiency greater than 50 per cent. Due to the greater magnetic flux, the jets observed in the MAD models are therefore considerably more powerful than those of the SANE disks.

To build an emission model it is necessary to provide the electronic temperature (T_e) which is not evolved in the simulations. We said that we expect that the electrons and protons in plasma around the black hole are thermally decoupled. To account for the unresolved electron physics in GRMHD simulations, detailed calculations of electron temperatures have been presented by some authors (Ressler et al., 2015; Sądowski et al., 2017). It is found that thermal conductivity does not have a significant effect on the electron temperatures. The most significant effect on electron temperatures is imposed by a model of plasma heating resulting in a proton to electron temperature ratio depending on the local plasma magnetization. This physics can be schematized by the formula

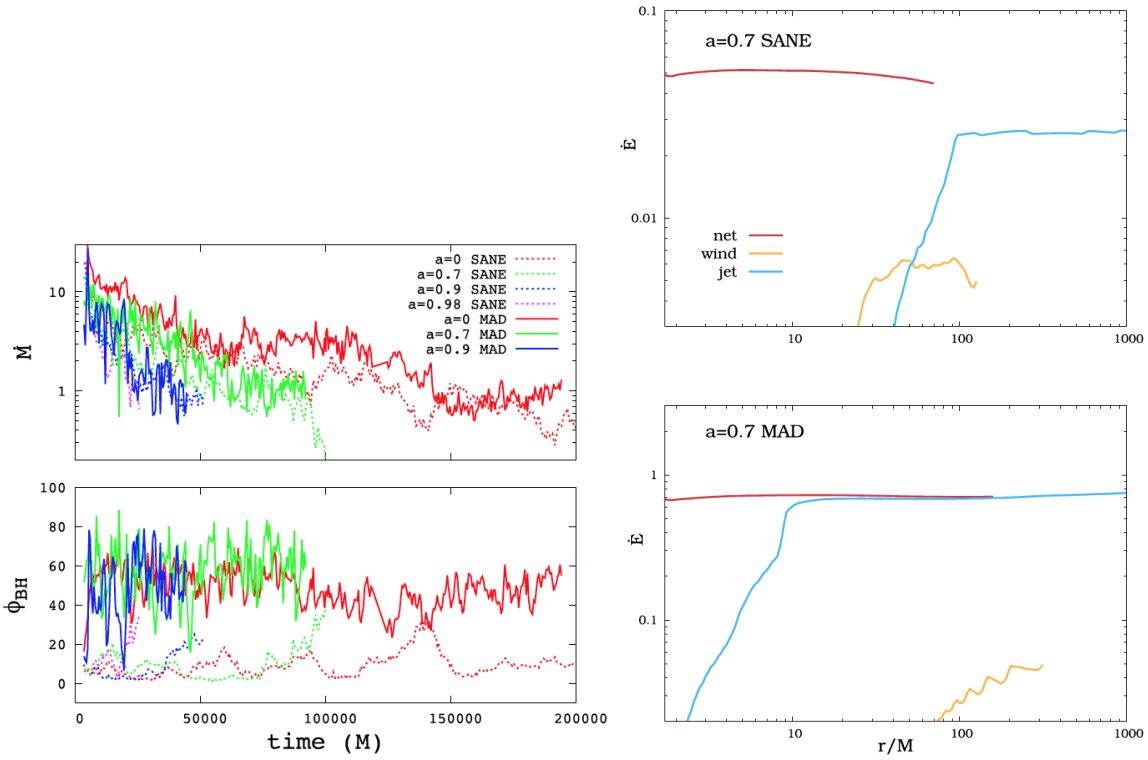

Figure 2.3: Left: temporal evolution of the accretion rate into the BH (top) and magnetic flux at the BH horizon (bottom) for SANE (dotted lines) and MAD (solid lines) models with different BH spins. Right: radial profiles of the energy flux for SANE (top) and MAD (bottom) models. Figures of Sądowski et al. (2013).

(Mościbrodzka et al., 2016):

$$\frac{T_i}{T_e} = R_{\rm high}\frac{\beta^2}{1+\beta^2} + \frac{1}{1+\beta^2}, \tag{2.32}$$

where $R_{\rm high}$ is a free parameter which corresponds to the ratio, T_i/T_e, in the high beta regions of the disk and it is chosen based on model fitting to the observational broadband Spectral Energy Distribution data. In contrast, in the highly magnetized regions of the jet, beta is small and $T_i/T_e \sim 1$. The electron temperature T_e is obtained from the equation (2.32) once the proton temperature T_p has been computed from the simulations. In particular there are several advanced temperature models for the SANE models, while the temperatures of the MAD disks are much more uncertain.

GRMHD simulations also allow to obtain information on variability as explained in Porth and EHT-Collaboration (2019). Indeed, it is known that in Sgr A*, episodic flares are detected in X-ray and nearinfrared (NIR) on a roughly daily basis and a low-level continuous variability is present in NIR and radio. While the nature of the strong coincident X-ray and IR flares is most likely associated with discrete events of particle heating or acceleration, weaker IR flares could also be caused by lensed thermal plasma in the turbulent accretion flow, and flares in the submillimeter band can be attributed solely to turbulent fluctuations in the accretion flow. On short timescales (below the characteristic timescales $\tau \sim 4$ hr in IR and $\tau \sim 8$ hr in submillimeter), the continuous variability is well described by a red-noise spectrum with power-law slope of ~ 2. For low-luminosity AGN, it is found that the submillimeter characteristic timescale is consistent with a linear dependence on the black hole mass as would be expected for optically thin emission in radiatively inefficient

general relativistic models. Hence, in M87, the variability with its characteristic timescale of -45^{+61}_{-24} days can be obtained by scaling the Sgr A* result. More recently, the M87 data processed by the EHT collaboration indicate intrinsic variability of compact structure on a timescale of days confirming the previous results. To obtain detailed information on the timing scale of the variability, a rigorous general relativistic radiative transfer calculation (GRRT) would be required that allows the reconstruction of the photon trajectory in a curved space-time. In Chapter 5 an approximate optically thin light curve is calculated as a volume integral of the emissivity defined by Eq. (2.31) and a study is carried out to confirm that the variability is described by a power-law slope of ~ 2.

2.3 First Event Horizon Telescope results

The goodness of a model is certainly measured by a comparison with observations. The models that predict dynamical and radiative properties of hot, magnetized, thick accretion disks are matched with observational data by:

- fitting the synthetic broadband (radio-X-ray) spectral energy distribution to the fluxes observed at various bands;
- modeling radio images at millimeter and radio wavelengths.

Recently, a big step forward in modeling techniques has been made thanks to observations of the EHT which has mapped the central compact radio source M87* ($M \sim 6.2 \cdot 10^9\ M_\odot$, $D \sim 16.9$ Mpc) at a wavelength of 1.3 mm (230 GHz) allowing to reconstruct the event-horizon-scale images of the supermassive black hole. Here we show the main observational results obtained by EHT and what they implied in the GRMHD modeling of thick accretion disks. The EHT is a Very Long Baseline Interferometery (VLBI) experiment that directly measures the visibilities, i.e. the Fourier components, of the radio brightness distribution on the sky. The EHT array that collected the first data in 2017 is made by eight stations placed in six geographic locations. As the Earth rotates, each telescope pair in the network samples many spatial frequencies creating a virtual telescope that spans nearly the full diameter of the Earth. Image reconstruction from EHT data using the radio interferometry approach took about two years and in April 2019 the images of M87* (Figure 2.4) were presented in a series of papers, EHT-Collaboration (2019a,b,c,d,e,f). The compact source shows a central dark hole with a bright ring arising at $\sim 5r$ because of strong gravitational lensing. The observed peak brightness temperature is $T_{b,pk} \sim 6 \cdot 10^9$ K which is consistent with past VLBI measurements at 230 GHz and the total flux density in the image is in the range $0.2 - 1.2$ Jy. We can infer orders of magnitude of the quantities of interest by assuming $n_e \sim n_p$, $T_i = 3T_e$, $\beta \sim 1$:

$$n_e \sim 2.9 \cdot 10^4\ \mathrm{cm}^{-3}, \tag{2.33}$$

$$B \sim 4.9\ \mathrm{G}, \tag{2.34}$$

$$T_e \sim 6.25 \cdot 10^{10}\ \mathrm{K}, \tag{2.35}$$

$$\dot{m} \sim 2.0 \cdot 10^{-5}. \tag{2.36}$$

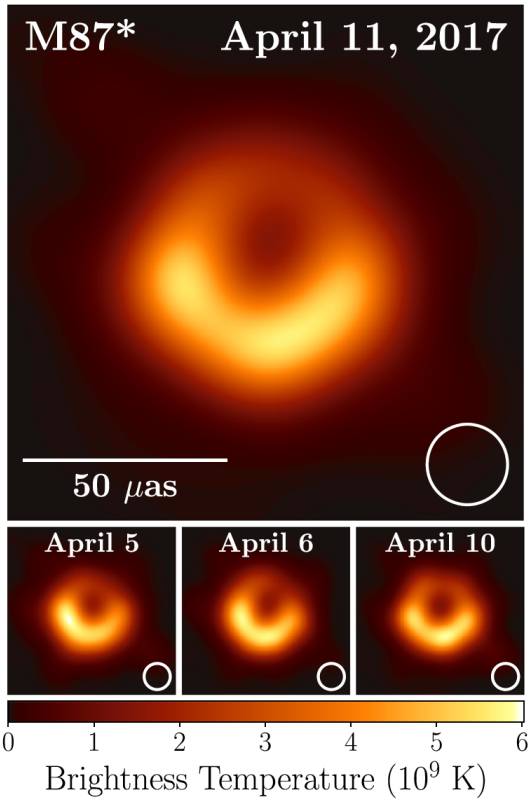

Figure 2.4: First EHT image of M87* from observations on April 2017.

A model can be made by assuming that M87 contains a turbulent, magnetized accretion flow surrounding a Kerr black hole. Several different codes evolved matching initial conditions using the equations of ideal GRMHD to generate a simulation Library. All simulations were initialized with a weakly magnetized torus of plasma orbiting in the equatorial plane of the black hole and driven to a turbulent state by the MRI. The two key physical parameters were the black hole spin a and the normalized magnetic flux ϕ, that discriminates the SANE regime from MAD. The next step was the creation of a large Image Library of synthetic images using the general relativistic ray-tracing. In this phase, other free parameters were added: the observer inclination i and the orientation of the observer through the position angle PA and the parameter $R_{\rm high}$ of Eq. (2.32).
The main results obtained can be summarized as follows:

- the observed image is consistent with expectations for the shadow of a Kerr black hole as predicted by the theory of the general relativity;
- if the black hole spin axis is aligned with the large-scale jet, then the asymmetry implies that the black hole spin is pointing away from Earth;
- models in the simulation library of non-spinning black holes are not consistent with the observations as they do not produce sufficiently powerful jets.

A further step forward in understanding the phenomenon of accretion was certainly made with the study of the polarized image presented in 2021 in two papers EHT-Collaboration (2021a,b). The polarimetric image obtained by processing the 2017 data shows a characteristic azimuthal pattern with a region of higher polarization in the southwestern part of the ring, where the linear

polarization fraction is $\lesssim 10\%$. As it is known that synchrotron radiation should have a polarization of 70%, it is thought that the polarization structure of M87* can be significantly influenced by two factors:

- turbulent magnetic fields;
- internal Faraday rotation.

Faraday rotation is the phenomenon of the rotation of the polarization plane depending on the intensity of the magnetic field along the direction of propagation of the light beam. This process can lead to some degree of depolarization depending on the scale on which it develops. It is reasonable to assume that there is an external Faraday rotation due to the accretion bulk which does not produce any depolarization. On the other hand, the possible presence of an internal Faraday rotation, i.e. localized in the emission region, would lead to a significant decrease in the observed polarization fraction. It can be shown that, given n_e, T_e and B from (2.33)-(2.35), the optical depth $\tau_{\rho V}$ to Faraday rotation at $\sim 5r$ results $\tau_{\rho V} \simeq 5.2 > 2\pi$, indicating that Faraday rotation internal to the emission region is an important effect and could thus explain the depolarization observed in M87*. The constraint on $\tau_{\rho V}$, combined with the two constraints coming from the observations from 2017 on the optical depth ($\tau < 1$) and on the observed flux ($0.2 < F_\nu < 1.2$ Jy), allows to obtain a much more precise estimate of the physical quantities of interest:

$$10^{10} \lesssim T_e \lesssim 1.2 \cdot 10^{10} \text{ K}, \tag{2.37}$$

$$1 \lesssim B \lesssim 30 \text{ G}, \tag{2.38}$$

$$10^4 \lesssim n_e \lesssim 10^7 \text{ cm}^{-3}. \tag{2.39}$$

The importance of the last two papers of the EHT collaboration is also due to the almost definitive confirmation that the accretion in thick disks develops preferably following the physics of the MAD regime rather than that of the SANE. Indeed, the magnetic field in the MAD models is very strong and is capable of not being advected with the flux. This fact allows the formation of an intense poloidal component which generates an azimuthal polarization pattern. Conversely, in SANE disks the magnetic field, being weaker, follows the accretion flow and the resulting polarization pattern tends to have a dominant radial component. The analysis that led to this interpretation involved the comparison between observations and several images from the simulation library carried out by varying the parameters listed above. By crossing the constraints imposed by the polarization pattern with the jet power, only 15 MAD models with $a \neq 0$ and no SANE survive the selection.

2.4 Mean-field dynamo in accretion disks

The simulations employed by the EHT community and for the code comparison tests all rely on initial magnetic fields with pressure which is one hundredth of the kinetic pressure. This value corresponds to a subdominant field, but it is not far from the value needed to reproduce both the dynamics needed to launch the polar jets and the non-thermal synchrotron emission. A more natural

scenario would be the one in which a very low initial field is evolved and amplified by some kind of dynamo process, so to reach self-consistently the correct threshold for MRI to induce accretion and to reproduce the correct dynamical and emission properties.

The first relativistic models for mean-field dynamo effects in thick disks around Kerr black holes were proposed more than two decades ago (Khanna and Camenzind, 1996; Brandenburg, 1996) whereas the first implementation within a full GRMHD scheme (even including radiation) is due to Sądowski et al. (2015), where the dynamo action in accretion discs was parametrized using the results of local shearing box simulations of MRI, leading to the addition of both poloidal and toroidal magnetic field components. Interestingly, the 2D axisymmetric simulations with the mentioned dynamo recipes were able to produce the same kind of fields obtained in 3D simulations without artificial terms, where the turbulent dynamo is fully operative. The first rigorous treatment of the dynamo effects within (resistive) GRMHD was presented by Bucciantini and Del Zanna (2013) later applied to the physics of accretion discs by Bugli et al. (2014) where the evolution of magnetic fields was studied by in axisymmetry and in the kinematic regime, that is by solving Maxwell equations alone not considering the feedback on the disk's plasma.

Here, we briefly introduce the classical theory of mean-field dynamo starting from the limit of the laminar approach to show the need to assume the presence of turbulence. Generalization in the context of GRMHD is described in Chapter 3, while Chapter 6 shows the first numerical studies of the GRMHD dynamo in accretion disks in dynamic regime.

2.4.1 Limits of the laminar dynamo theory

The operational definition given by Moffatt (1978) states that a velocity field of a fluid is acting as a dynamo if it is able to maintain a finite magnetic energy density for $t \to \infty$. However, there are a number of theorems that exclude the possibility of dynamo action in a series of particular symmetries. Among these the most famous is certainly Cowling's anti-dynamo theorem (Cowling, 1976) elegantly illustrated by Boyd and Sanderson (2003). Using a simple argument he showed that no axisymmetric magnetic field can be maintained stationary through the dynamo action of axisymmetric currents. In the case that he considered both the flow and the field lines are in a meridional plane through the axis of symmetry. In any such plane the field lines must be closed curves enclosing at least one neutral line as shown in Figure 2.5. Let us consider the Ohm's law for a resistive plasma and integrate it around this line (from now we use units $G = c = 1$ and make use of the Lorentz-Heaviside notation for the electromagnetic quantities). We get

$$\begin{aligned} \eta \oint \boldsymbol{J} \cdot \mathrm{d}\boldsymbol{l} &= \oint \boldsymbol{E} \cdot \mathrm{d}\boldsymbol{l} + \oint (\boldsymbol{U} \times \boldsymbol{B}) \cdot \mathrm{d}\boldsymbol{l} \\ &= \int (\boldsymbol{\nabla} \times \boldsymbol{E}) \cdot \mathrm{d}\boldsymbol{S} = - \int \frac{\partial \boldsymbol{B}}{\partial t} \cdot \mathrm{d}\boldsymbol{S} = 0 \end{aligned} , \tag{2.40}$$

where η is the resistivity, $\boldsymbol{J}$ is the current density, $\boldsymbol{U}$ is the velocity of the plasma and $\boldsymbol{E}$ and $\boldsymbol{B}$ are the electric and magnetic fields. The integral of the convection term vanishes on account of the fact that $\boldsymbol{B} = 0$ along the neutral line and the final integral vanishes because of the stationarity. But (2.40) implies that $J_\phi = 0$ which is clearly incompatible with Ampere's law and the contradiction proves the theorem. The physical interpretation of the theorem is that while the convection term can

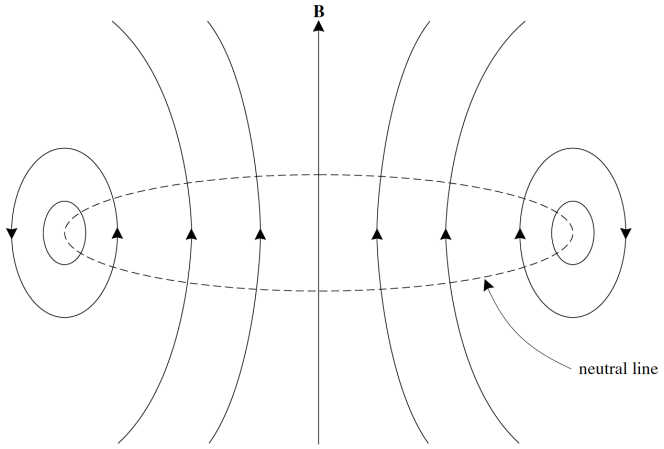

Figure 2.5: Geometry of field lines in Cowling's theorem (Boyd and Sanderson, 2003).

transport the field lines in the meridional plane it cannot create new field lines to replace those that diffuse through the plasma and disappear at the neutral point. The proof of Cowling's theorem can be extended to include an azimuthal component of the magnetic field. In this case $(\boldsymbol{U} \times \boldsymbol{B}) \cdot \mathrm{d}\boldsymbol{l} = 0$ on the neutral line since $\boldsymbol{B}$ and $\mathrm{d}\boldsymbol{l}$ are parallel. The conclusion is that although a system such as an accretion disk around a black hole (but also a star or planet) may have a dominant axially symmetric dipole field at its surface, the magnetic field within the body must be considerably more complicated if it is to be maintained by dynamo action. In the most general terms, as shown in the next paragraph, differential rotation and turbulent convection are required.

2.4.2 Turbulent mean-field dynamo theory

Let us consider a classical plasma in a flat space-time. We assume a velocity field $\boldsymbol{U}$ and a magnetic field $\boldsymbol{B}$ that have a large-scale average component and a small-scale variable component:

$$\boldsymbol{U} = \boldsymbol{U}_0 + \boldsymbol{u}, \tag{2.41}$$

$$\boldsymbol{B} = \boldsymbol{B}_0 + \boldsymbol{b}, \tag{2.42}$$

where $\boldsymbol{u}$ and $\boldsymbol{b}$ are the stochastic fluctuations with zero time average on an intermediate scale. The classical induction equation is defined by

$$\frac{\partial \boldsymbol{B}}{\partial t} + \boldsymbol{\nabla} \times (\boldsymbol{U} \times \boldsymbol{B}) = \eta \nabla^2 \boldsymbol{B}. \tag{2.43}$$

Substituting the expressions (2.41) and (2.42) in the equation (2.43) we get

$$\frac{\partial}{\partial t}(\boldsymbol{B}_0 + \boldsymbol{b}) = \boldsymbol{\nabla} \times [(\boldsymbol{U}_0 + \boldsymbol{u}) \times (\boldsymbol{B}_0 + \boldsymbol{b})] + \eta \nabla^2 (\boldsymbol{B}_0 + \boldsymbol{b}). \tag{2.44}$$

The induction equation (2.44) may be separated into its mean and fluctuating parts:

$$\frac{\partial \boldsymbol{B}_0}{\partial t} = \boldsymbol{\nabla} \times (\boldsymbol{U}_0 \times \boldsymbol{B}_0) + \boldsymbol{\nabla} \times \boldsymbol{\mathcal{E}} + \eta \nabla^2 \boldsymbol{B}_0, \tag{2.45}$$

$$\frac{\partial \boldsymbol{b}}{\partial t} = \boldsymbol{\nabla} \times (\boldsymbol{U}_0 \times \boldsymbol{b}) + \nabla \times (\boldsymbol{u} \times \boldsymbol{B}_0) + \boldsymbol{\nabla} \times \mathcal{G} + \eta \nabla^2 \boldsymbol{b} \tag{2.46}$$

where

$$\boldsymbol{\mathcal{E}} = \langle \boldsymbol{u} \times \boldsymbol{b} \rangle, \tag{2.47}$$

$$\boldsymbol{\mathcal{G}} = \boldsymbol{u} \times \boldsymbol{b} - \langle \boldsymbol{u} \times \boldsymbol{b} \rangle \tag{2.48}$$

The contribution of fluctuations to the large-scale evolution of the magnetic field is clearly understood: a macroscopic electromotive force $\boldsymbol{\mathcal{E}}$ which can greatly influence the magnetic field is induced. In order to build a theory of mean field dynamo it is necessary to express $\boldsymbol{\mathcal{E}}$ in terms of known quantities and statistical properties of the fluctuations. The term $\nabla \times (\boldsymbol{u} \times \boldsymbol{B}_0)$ in Eq. (2.46) acts as a source term generating the fluctuating field $\boldsymbol{b}$. If we suppose that $\boldsymbol{b} = 0$ at some initial instant $t = 0$ then the linearity of Eq. (2.46) guarantees that the fields $\boldsymbol{b}$ and $\boldsymbol{B}_0$ are linearly related. It follows that the fields $\boldsymbol{\mathcal{E}}$ and $\boldsymbol{B}_0$ are likewise linearly related, and since the spatial scale of $\boldsymbol{B}_0$ is by assumption large we may reasonably anticipate that this relationship may be developed as a rapidly convergent series of the form

$$\mathcal{E}_i = \alpha_{ij} B_{0j} + \beta_{ijk} \frac{\partial B_{0j}}{\partial x_k} + \gamma_{ijkl} \frac{\partial^2 B_{0j}}{\partial x_k \partial x_l} + ... \tag{2.49}$$

where the coefficients α_{ij}, β_{ijk}, ... depends on $\boldsymbol{U}_0$, $\boldsymbol{u}$ and η. We specify that terms involving time derivatives $\partial \boldsymbol{B}_0 / \partial t$, $\partial^2 \boldsymbol{B}_0 / \partial t^2$ may also appear in the expression for $\boldsymbol{\mathcal{E}}$. Such terms may however always be replaced by terms involving only space derivatives by means of Eq. (2.45).
Let us first consider the zero-order term

$$\mathcal{E}_i^{(0)} = \alpha_{ij} B_{0j}. \tag{2.50}$$

The tensor α_{ij} can be decoupled in its symmetric and antisymmetric part as $\alpha_{ij} = \alpha_{ij}^{(s)} - \epsilon_{ijk} a_k$, where $a_k = -1/2 \epsilon_{lmk} \alpha_{lm}$ and ϵ_{ijk} is the Levi-Civita antisymmetric symbol. If we insert this expression for α_{ij} into Eq. (2.49) we obtain

$$\mathcal{E}_i^{(0)} = \alpha_{ij}^{(s)} B_{0j} + (\boldsymbol{a} \times \boldsymbol{B}_0)_i \tag{2.51}$$

The effect of the antisymmetric component $\boldsymbol{a}$ is to introduce a correction to the mean flow velocity $\boldsymbol{U}_0$ and lead to an effective velocity $\boldsymbol{U}_0 + \boldsymbol{a}$. However, this contribution can usually be neglected in the situations of interest for us. The role of the symmetric component $\alpha_{ij}^{(s)}$ can be understood if we assume $\boldsymbol{u}$ to be isotropic and homogeneous. In this case also α_{ij} is isotropic, hence we can set

$$\alpha_{ij} = \alpha \delta_{ij}, \tag{2.52}$$

$$\boldsymbol{a} = 0, \tag{2.53}$$

where the scalar parameter α derives from the statistical properties of the velocity fluctuations. Inserting Eq. (2.52) into Eq. (2.50) we obtain

$$\boldsymbol{\mathcal{E}}^{(0)} = \alpha \boldsymbol{B}_0, \tag{2.54}$$

which inserted into Ohm's equation $\boldsymbol{E} = -\boldsymbol{U} \times \boldsymbol{B} + \eta \boldsymbol{J}$ leads to a contribution to the current density equal to

$$\boldsymbol{J}^{(0)} = \frac{1}{\eta} \boldsymbol{\mathcal{E}}^{(0)} = \frac{\alpha}{\eta} \boldsymbol{B}_0. \tag{2.55}$$

This expression reveals the existence of an electric current parallel to the mean magnetic field, which is in strong contrast with the usual situation where the induction current $(\boldsymbol{U} \times \boldsymbol{B})/\eta$ is perpendicular to the magnetic field. This phenomenon, known in the literature as α-effect, is at the core of the mean-field dynamo theory.
Let us now consider the first-order term in Eq. (2.49):

$$\mathcal{E}_i^{(1)} = \beta_{ijk} \frac{\partial B_{0j}}{\partial x_k}. \tag{2.56}$$

Assuming that velocity $\boldsymbol{u}$ is isotropic, the tensor β_{ijk} is also isotropic (see also Rincon (2019) for further information) and we can write

$$\boldsymbol{\mathcal{E}}^{(1)} = -\beta \boldsymbol{\nabla} \times \boldsymbol{B}_0 = -\beta \boldsymbol{J}_0. \tag{2.57}$$

The contribution in the induction equation for the mean magnetic field is

$$\boldsymbol{\nabla} \times \boldsymbol{\mathcal{E}}^{(1)} = \beta \nabla^2 \boldsymbol{B}_0. \tag{2.58}$$

It is evident from a comparison with Eq. (2.45) that the effect of the induced electromotive force $\boldsymbol{\mathcal{E}}^{(1)}$ is to enhance the effective value of the magnetic resistivity with $\eta \to \tilde{\eta} = \eta + \beta$. This phenomenon describes the turbulent resistivity: magnetic field lines with opposite polarities are entangled by turbulent motions, which leads to their diffusion and consequently to a decrease of the mean field. The final form of the induction equation with the inclusion of the two effects reads

$$\frac{\partial \boldsymbol{B}_0}{\partial t} = \boldsymbol{\nabla} \times (\boldsymbol{U}_0 \times \boldsymbol{B}_0) + \boldsymbol{\nabla} \times \boldsymbol{\mathcal{E}} + \eta \nabla^2 \boldsymbol{B}_0, \tag{2.59}$$

where

$$\boldsymbol{\mathcal{E}} = \alpha \boldsymbol{B}_0 - \beta \boldsymbol{\nabla} \times \boldsymbol{B}_0. \tag{2.60}$$

Eq. (2.59) can be also reformulated in terms of an effective large scale electric field $\boldsymbol{E}_0$ as

$$\frac{\partial \boldsymbol{B}_0}{\partial t} = -\boldsymbol{\nabla} \times \boldsymbol{E}_0 \tag{2.61}$$

where

$$\boldsymbol{E}_0 = -\boldsymbol{U}_0 \times \boldsymbol{B}_0 + \tilde{\eta} \boldsymbol{J}_0 - \alpha \boldsymbol{B}_0, \tag{2.62}$$

with $\boldsymbol{J}_0 = \boldsymbol{\nabla} \times \boldsymbol{B}_0$. Eq. (2.62) is a generalization of resistive Ohm's law that includes mean-field dynamo effects.

To better understand how the dynamo cycle works also in an axisymmetric configuration of an accretion disk, it can be useful to rewrite the induction equation decomposing the fields into their poloidal and toroidal components,

$$\boldsymbol{U} = \boldsymbol{U}_p + \boldsymbol{U}_T, \tag{2.63}$$

$$\boldsymbol{B} = \boldsymbol{B}_p + \boldsymbol{B}_T, \tag{2.64}$$

where for convenience the subscript 0 that characterizes the macroscopic quantities has been abolished. In a cylindrical coordinate system (R, z, ϕ) let us consider

$$\boldsymbol{U}_T = R\Omega(R, z)\boldsymbol{i}_\phi, \tag{2.65}$$

$$\boldsymbol{B}_T = B(R, z)\boldsymbol{i}_\phi, \tag{2.66}$$

$$\boldsymbol{B}_P = \boldsymbol{\nabla} \times A(R, z)\boldsymbol{i}_\phi, \tag{2.67}$$

where $\Omega(R, z)$ is the angular velocity of the plasma and $\boldsymbol{A} = A(R, z)\boldsymbol{i}_\phi$ is the vector potential. Substituting these expressions in Eq. (2.45) we obtain

$$\frac{\partial A}{\partial t} + \frac{1}{R}(\boldsymbol{U}_P \cdot \boldsymbol{\nabla})RA = \alpha B + \tilde{\eta}\left(\nabla^2 - \frac{1}{R^2}\right)A, \tag{2.68}$$

$$\frac{\partial B}{\partial t} + R(\boldsymbol{U}_P \cdot \boldsymbol{\nabla})\left(\frac{B}{R}\right) = R(\boldsymbol{B}_P \cdot \boldsymbol{\nabla})\Omega + [\boldsymbol{\nabla} \times (\alpha \boldsymbol{B}_P)] \cdot \boldsymbol{i}_\phi + \tilde{\eta}\left(\nabla^2 - \frac{1}{R^2}\right)B, \tag{2.69}$$

where we use the vectorial relations

$$\nabla^2 \boldsymbol{A} = \boldsymbol{i}_\phi\left(\nabla^2 - \frac{1}{R^2}\right)A, \tag{2.70}$$

$$\boldsymbol{U}_P \times (\boldsymbol{\nabla} \times \boldsymbol{A}) = -\frac{1}{R}(\boldsymbol{U}_P \cdot \boldsymbol{\nabla})RA. \tag{2.71}$$

The first term to the first member of the Eqs. (2.68) and (2.69) is the Euler derivative of the components of the field, while the second term represents their advection with the flow. On the right side of Eq. (2.69), the first term shows how an angular velocity shear along a line of force of $\boldsymbol{B}_P$ can produce a toroidal field. This process is known as Ω-effect and it is a fundamental phenomenon in the systems where differential rotation is present. The first term of Eq. (2.68) and the second term of Eq. (2.69), on the other hand, are source terms of toroidal and poloidal fields respectively related to the α-effect. Usually the rotation term is dominant with respect to the alpha effect term, for which Eq. (2.69) becomes

$$\frac{\partial B}{\partial t} + R(\boldsymbol{U}_P \cdot \boldsymbol{\nabla})\left(\frac{B}{R}\right) = R(\boldsymbol{B}_P \cdot \boldsymbol{\nabla})\Omega + \tilde{\eta}\left(\nabla^2 - \frac{1}{R^2}\right)B. \tag{2.72}$$

The two Eqs. (2.68) and (2.72) describe a mechanism that provides a way to close a dynamo cycle by generating poloidal magnetic fields starting from a toroidal field. In fact, such a field would

lead, according to Eq. (2.55), to a toroidal current, which consequently would generate a poloidal magnetic component. The latter then allows the amplification of the toroidal field through the Ω-effect, i.e. in presence of differential rotation. In such a system, called $\alpha - \Omega$ dynamo, it is possible to have a steady amplification of magnetic field. The individual efficiency of the Ω-effect and the α-effect in generating magnetic field against dissipation can be estimated a priori by their relative Reynolds dynamo numbers. These parameters (widely used in the literature) are defined in a disk as (Brandenburg and Subramanian, 2005)

$$C_\Omega = R\left|\frac{d\Omega}{dR}\right|\frac{H^2}{\eta} \sim \frac{\Delta\Omega H^2}{\eta}, \tag{2.73}$$

$$C_\alpha = H\left|\frac{\alpha}{\eta}\right|, \tag{2.74}$$

where H is the scale height of the disk. We can observe from Eq. (2.54) that α has the dimension of a velocity and therefore can be interpreted as a characteristic velocity of turbulent motions that we denote by v_α. On the other hand, we can identify the term η/H with the dissipation velocity of the magnetic field denoted by v_η. The meaning of the dynamo numbers is therefore clearer if we express them in terms of velocity ratios

$$C_\Omega = \frac{v_\Omega}{v_\eta}, \tag{2.75}$$

$$C_\alpha = \frac{v_\alpha}{v_\eta} \tag{2.76}$$

where $v_\Omega \sim H\Omega$ is a typical rotational velocity. We observe that by setting $\alpha = 0$ in Eq. (2.68), the laminar dynamo limit is recovered and the effects of Cowling's theorem can be seen: the term source in the equation is reduced to an exclusively dissipative contribution which leads to a decay of the poloidal field not allowing the maintenance of a stable configuration of the magnetic field.

Here we have presented a classic discussion of the mean-field dynamo theory. In the next Chapter, we show how it is possible to generalize Eq. (2.62) in GRMHD to study this phenomenon in the context of accretion disks around black holes. The main advantage of this approach is to be able to model turbulence effects by adjusting the two arbitrary free parameters η and α. We specify that in the absence of explicit dynamo terms, an amplification process is expected to naturally take place due to the MRI: both local shearing box simulations (Brandenburg et al., 1995; Ziegler and Rüdiger, 2001; Davis et al., 2010) and global models (Hawley et al., 2011, 2013) studied the saturation of the MRI in order to characterize the α coefficients; further studies have also considered the effect of the anisotropic nature of the MHD turbulence (Gressel and Pessah, 2015; Dhang et al., 2020), i.e. without the two hypotheses (2.52) and (2.57). However, the introduction of explicit dynamo terms allows for regulating the growth of selected field components in different spatial regions of the source, while MRI is more limited by the initial magnetic configuration.

Chapter 3

General relativistic magnetohydrodynamics

This chapter presents the (ideal and non ideal) General Relativistic Magnetohydrodynamics GRMHD equations that are solved by the ECHO code (Del Zanna et al., 2007). Initially, a brief description of the equations is made using the covariant approach, to then move on to the formulation in the so-called 3 + 1 formalism characterized by a separation between the spatial and temporal coordinates. This second approach, in addition to being more easily interpretable, is more advantageous from a numerical point of view because it allows to develop conservative schemes that are more robust than non-conservative ones.

3.1 Covariant approach

We begin with a brief presentation of the GRMHD equations in the covariant formalism considering an ideal fluid interacting with an electromagnetic field. The equations of relativistic hydrodynamics are:

$$\nabla_\mu(\rho u^\mu) = 0, \tag{3.1}$$

$$\nabla_\mu T^{\mu\nu} = 0, \tag{3.2}$$

where ∇_μ represents the covariant derivative. Eq. (3.1) is the well-known law of conservation of rest-mass, where ρ is the rest-mass density measured in the comoving reference with the fluid moving with the four-speed u^μ. Eq. (3.2) is the conservation law of the four-momentum, where the energy-momentum tensor $T^{\mu\nu}$ can be splitted into two contributes, one due to matter and one to the electromagnetic field:

$$T^{\mu\nu} = T^{\mu\nu}_{\rm m} + T^{\mu\nu}_{\rm em}, \tag{3.3}$$

with

$$T^{\mu\nu}_{\rm m} = \rho h u^\mu u^\nu + p g^{\mu\nu} \tag{3.4}$$

and

$$T^{\mu\nu}_{\rm em} = F^\mu_\lambda F^{\nu\lambda} - \frac{1}{4}\big(F^{\lambda\kappa}F_{\lambda\kappa}\big)g^{\mu\nu}, \tag{3.5}$$

where $h = 1 + \epsilon + p/\rho$ is the specific enthalpy, ϵ is the specific internal energy, p is the thermal pressure, $g^{\mu\nu}$ is the metric tensor and $F^{\mu\nu}$ is the antisymmetric tensor of the electromagnetic field. The metric follows the signature $(-,+,+,+)$ and Lorentz-Heaviside notation is adopted ($c = 1$ and $\sqrt{4\pi} \to 1$). Maxwell's equations can be written as

$$\nabla_\mu F^{\mu\nu} = -I^\nu, \tag{3.6}$$

$$\nabla_\mu F^{*\mu\nu} = 0, \tag{3.7}$$

where I^μ is the four-vector of the density current, $F^{*\mu\nu} = 1/2\epsilon^{\mu\nu\lambda\kappa}F_{\lambda\kappa}$ is the dual of the electromagnetic field tensor and $\epsilon^{\mu\nu\lambda\kappa} = (-g)^{-1/2}[\mu\nu\lambda\kappa]$ is the Levi-Civita space-time tensor where $g = \det g_{\mu\nu}$ and $[\mu\nu\lambda\kappa]$ is the completely antisymmetric Levi-Civita symbol with convention $[0123]=+1$.

In a perfect conductor, ideal Ohm's law is obtained by imposing the cancellation of the comoving electric field

$$F^{\mu\nu}u_\nu = 0. \tag{3.8}$$

This means that the charges in the plasma can move freely in order to effectively shield any locally electric fields. We note that this condition makes Eq. (3.6) redundant and the density current I^μ becomes a derived quantity as in classical MHD.

To close the GRMHD system of equations it is necessary to specify the equation of state $p = p(\rho, \epsilon)$. In our simulations the equation of state of perfect gas is assumed

$$p(\rho, \epsilon) = (\hat{\gamma} - 1)\rho\epsilon, \tag{3.9}$$

which, using the previous definition of specific enthalpy, can be expressed as

$$h = 1 + \frac{\hat{\gamma}}{\hat{\gamma} - 1}\frac{p}{\rho}, \tag{3.10}$$

where $\hat{\gamma}$ is the adiabatic index.

Finally, if the considered fluid is ideal (absence of shocks or other sources of dissipation), the law of conservation of total energy is equivalent to the adiabatic equation

$$\nabla_\mu(\rho s u^\mu) = 0, \tag{3.11}$$

with s proportional to the specific entropy, and for an ideal gas we have

$$s = \frac{p}{\rho^{\hat{\gamma}}}. \tag{3.12}$$

3.2 3+1 formalism

It is known that the laws of large-scale physics suggest a distinction between spatial and temporal coordinates. 3+1 formalism is an approach to the theory of general relativity and Einstein's equations based on the division of four-dimensional space-time into three-dimensional hyper-surfaces. It was born in the 1920s and has become a fundamental tool since the 1970s, a period in which numerical relativity began to spread. Today, most of the numerical codes that solve Einstein's

equations are based on the 3+1 formalism, including the ECHO code. More information can be found in Rezzolla and Zanotti (2013) and references therein.

The four-dimensional space-time is foliated in time-like, non intersecting hyper-surfaces Σ_t, defined as the iso-surfaces of a time scalar function t. We denote as

$$n_\mu = -\alpha \nabla_\mu t, \tag{3.13}$$

with α constant known as lapse function. We also impose the condition

$$n_\mu n^\mu = -1. \tag{3.14}$$

We note that the minus sign in the (3.13) is chosen so that the vector n^μ is directed towards the future. It is clear from the definition that the four-vector n^μ can be interpreted as the four-velocity of an observer known as Eulerian observer. The worldlines of the Eulerian observer are orthogonal to the hyper-surfaces. Any vector V^μ (or tensor) can be decomposed into its temporal and spatial components, applying operators $-n_\mu n^\nu$ and $g^\mu_\nu + n^\mu n_\nu$ respectively. The spatial projection operator applied to the metric tensor $g^{\mu\nu}$ allows also to obtain the spatial metric $\gamma_{\mu\nu}$ induced on Σ_t by the four-dimensional metric:

$$\gamma_{\mu\nu} = g_{\mu\nu} + n_\mu n_\nu \tag{3.15}$$

We can now introduce a coordinate system $(x^\alpha) = (t, x^i)$ which adapts to the foliation Σ_t. Then it is possible to express the line element in the so-called ADM form (Arnowitt et al., 1962):

$$g_{\mu\nu} dx^\mu dx^\nu = -\alpha^2 dt^2 + \gamma_{ij}(dx^i + \beta^i dt)(dx^j + \beta^j dt), \tag{3.16}$$

where β^μ is referred to as shift vector, which is an arbitrarily spatial vector. In this coordinate system the components of the unit vector are

$$n_\mu = (-\alpha, 0_i) \tag{3.17}$$

$$n^\mu = (1/\alpha, -\beta^i/\alpha) \tag{3.18}$$

and any purely spatial vector (or tensor) V^μ will necessary have a vanishing contravariant time component, i.e. $V^t = 0$, while the covariant time component will be given by $V_t = g_{\mu t} V^\mu = \beta_i V^i$, and will in general be different from zero. Also the gradient of the unit vector can be decomposed in time and space components

$$\nabla_\mu n_\nu = -K_{\mu\nu} - n_\mu a_\nu, \tag{3.19}$$

where $K_{\mu\nu}$ is the extrinsic curvature of the metric (a symmetric spatial tensor), and a_ν is the acceleration of the Eulerian observer (also a spatial vector). It is then possible to demonstrate that

$$a_\nu = n^\mu \nabla_\mu n_\nu. \tag{3.20}$$

We can now decompose all the quantities in the GRMHD equations into their time and space components

$$u^\mu = \Gamma n^\mu + \Gamma v^\mu, \tag{3.21}$$

$$T^{\mu\nu} = W^{\mu\nu} + S^{\mu}n^{\nu} + n^{\mu}S^{\nu} + \mathcal{E}n^{\mu}n^{\nu}, \tag{3.22}$$

$$F^{\mu\nu} = n^{\mu}E^{\nu} - E^{\mu}n^{\nu} + \epsilon^{\mu\nu\lambda\kappa}B_{\lambda}n_{\kappa}, \tag{3.23}$$

$$F^{*\mu\nu} = n^{\mu}B^{\nu} - B^{\mu}n^{\nu} - \epsilon^{\mu\nu\lambda\kappa}E_{\lambda}n_{\kappa}, \tag{3.24}$$

$$I^{\mu} = qn^{\mu} + J^{\mu}, \tag{3.25}$$

where all the newly introduced vectors and tensors are purely spatial and correspond to the usual observables measurable in the 3-dimensional space by the Eulerian obeserver. In fact v^{μ} is the fluid velocity with Lorentz factor Γ, so that

$$v^{i} = \frac{u^{i}}{\Gamma} + \frac{\beta^{i}}{\alpha}, \tag{3.26}$$

$$\Gamma = \alpha u^{t} = (1 - v^{2})^{-1/2}, \tag{3.27}$$

with $v^2 = v^i v_i$ and where we used the normalization condition $u_\mu u^\mu = -1$. The decomposition of the stress energy tensor instead provides: the momentum density,

$$S^{i} = \rho h \Gamma^{2} v^{i} + \epsilon^{ijk}E_{j}B_{k}, \tag{3.28}$$

where the 3D Levi-Civita tensorial density is given by $\epsilon^{\mu\nu\lambda} = \epsilon^{\mu\nu\lambda\kappa}n_{\kappa} \equiv \epsilon^{ijk}$, so that $\epsilon^{ijk} = \gamma^{-1/2}[ijk]$ and $\epsilon_{ijk} = \gamma^{1/2}[ijk]$ with the completely antisymmetric Levi-Civita symbol $[ijk]$ with convention $[123] = +1$; the spatial stress tensor of the plasma

$$W^{ij} = \rho h \Gamma^{2} v^{i} v^{j} + p\gamma^{ij} + \tfrac{1}{2}(E^{2} + B^{2})\gamma^{ij} - E^{i}E^{j} - B^{i}B^{i}, \tag{3.29}$$

and the energy density

$$\mathcal{E} = \rho h \Gamma^{2} - p + \tfrac{1}{2}(E^{2} + B^{2}). \tag{3.30}$$

The electric and magnetic field spatial vectors are defined as $E^{\mu} = n_{\nu}F^{\mu\nu}$ and $B^{\mu} = n_{\nu}F^{*\mu\nu}$, so their components are given by

$$E^{i} = \alpha F^{ti}, \tag{3.31}$$

$$B^{i} = \alpha F^{*ti}. \tag{3.32}$$

The electric charge density is denoted with q and the spatial conduction current with J^{μ}, both measured in the frame of the Eulerian observer. By applying the usual covariant derivation rules and splitting the time and space components of Eq. (3.1), Eq. (3.2), Eq. (3.6), Eq. (3.7) we obtain the GRMHD equations in the following form

$$(-g)^{-1/2}\partial_{\mu}[(-g)^{1/2}\rho u^{\mu}] = 0, \tag{3.33}$$

$$(-g)^{-1/2}\partial_\mu[(-g)^{1/2}T^\mu_i] = \tfrac{1}{2}T^{\mu\nu}\partial_i g_{\mu\nu}, \tag{3.34}$$

$$(-g)^{-1/2}\partial_\mu[(-g)^{1/2}T^{\mu\nu}n_\nu] = T^{\mu\nu}\nabla_\mu n_\nu, \tag{3.35}$$

$$(-g)^{-1/2}\partial_\mu[(-g)^{1/2}F^{*\mu i}] = 0, \tag{3.36}$$

$$(-g)^{-1/2}\partial_\mu[(-g)^{1/2}F^{\mu i}] = q\beta^i/\alpha - J^i, \tag{3.37}$$

$$(-g)^{-1/2}\partial_\mu[(-g)^{1/2}F^{\mu t}] = -q/\alpha, \tag{3.38}$$

$$(-g)^{-1/2}\partial_\mu[(-g)^{1/2}F^{*\mu t}] = 0. \tag{3.39}$$

We can decompose the source terms on the right-hand sides of Eq. (3.34) and Eq. (3.35) as

$$\tfrac{1}{2}T^{\mu\nu}\partial_j g_{\mu\nu} = \tfrac{1}{2}W^{ik}\partial_j\gamma_{ik} + \alpha^{-1}S_i\partial_j\beta^i - \mathcal{E}\partial_j\ln\alpha, \tag{3.40}$$

$$T^{\mu\nu}\nabla_\mu n_\nu = -K_{ij}W^{ij} + S^j\partial_j\ln\alpha. \tag{3.41}$$

The extrinsic curvature in Eq. (3.41) can be provided in terms of the covariant derivatives of the shift vector components. In the case of a stationary metric we get

$$\alpha K_{ij}W^{ij} = \tfrac{1}{2}W^{ij}\beta^k\partial_k\gamma_{ij} + W^i_j\partial_i\beta^j \tag{3.42}$$

The final form of the GRMHD equations in terms of purely 3D spatial quantities is obtained using all the previous decompositions. It reads:

$$\partial_t(\gamma^{1/2}D) + \partial_k[\gamma^{1/2}(\alpha v^k - \beta^k)D] = 0, \tag{3.43}$$

$$\partial_t(\gamma^{1/2}S_j) + \partial_i[\gamma^{1/2}(\alpha W^i_j - \beta^i S_j)] = \gamma^{1/2}[\tfrac{1}{2}\alpha W^{ik}\partial_j\gamma_{ik} + S_i\partial_j\beta^j - \mathcal{E}\partial_i\alpha], \tag{3.44}$$

$$\partial_t(\gamma^{1/2}\mathcal{E}) + \partial_i[\gamma^{1/2}(\alpha S^i - \beta^i\mathcal{E})] = \gamma^{1/2}(\tfrac{1}{2}W^{ij}\beta^k\partial_k\gamma_{ij} + W^i_j\partial_i\beta^j - S^i\partial_i\alpha), \tag{3.45}$$

$$\partial_t(\gamma^{1/2}E^i) - \gamma^{1/2}\,\epsilon^{ijk}\partial_j(\alpha B_k - \epsilon_{klm}\beta^l E^m) = -\gamma^{1/2}(\alpha J^i - q\beta^i) \tag{3.46}$$

$$\partial_t(\gamma^{1/2}B^i) + \gamma^{1/2}\,\epsilon^{ijk}\partial_j(\alpha E_k + \epsilon_{klm}\beta^l B^m) = 0, \tag{3.47}$$

$$\gamma^{-1/2}\partial_i(\gamma^{1/2}E^i) = q, \tag{3.48}$$

$$\gamma^{-1/2}\partial_i(\gamma^{1/2}B^i) = 0, \tag{3.49}$$

where $\gamma = \det\{\gamma_{ij}\}$ is the determinant of the spatial metric, related to the four dimensional one by $(-g)^{1/2} = \alpha\gamma^{1/2}$.
Eq. (3.43) describes the continuity equation for $D = \rho\Gamma$, i.e. the mass density measured by the Eulerian observer; Eq. (3.44) is the momentum equation, containing the divergence of the stress tensor W_{ij} and its last term with the lapse function gradient reduces to the usual gravitational force in the Newtonian limit; Eq. (3.45) is the energy equation (note that the total energy density is $\mathcal{E} + D$); finally, Eqs. (3.46) and (3.47) are the general relativistic extension of the induction equation and Ampere's law respectively while Eqs. (3.38) and (3.39) are the two constraints on the electromagnetic field.

3.2.1 The dynamo closure in GRMHD

Eqs. (3.43)-(3.47) are valid regardless of the particular form of Ohm's law, that is, how the conductive medium reacts to the presence of an electric field. To obtain a generalized Ohm's law it is first convenient to decompose the quantities related to the frame comoving with the fluid within the 3 + 1 Eulerian split of time and space, namely

$$e^\mu = \Gamma[E^i v_i]n^\mu + \Gamma(E^\mu + \epsilon^{\mu\nu\lambda}v_\nu B_\lambda), \tag{3.50}$$

$$b^\mu = \Gamma[B^i v_i]n^\mu + \Gamma(B^\mu - \epsilon^{\mu\nu\lambda}v_\nu E_\lambda), \tag{3.51}$$

$$j^\mu = (q - q_0\Gamma)n^\mu + J^\mu - q_0\Gamma v^\mu, \tag{3.52}$$

where $q_0 = \Gamma(q - J^i v_i)$. Bucciantini and Del Zanna (2013) describe the three possible choices for Ohm's law:

- Ideal GRMHD.
  In an ideal conductor the electric field in the moving reference system must be zero, that is $e^\mu = 0$. Taking the spatial projection, we get

  $$E^i + \epsilon^{ijk}v_j B_k = 0, \tag{3.53}$$

  which is the well-known usual ideal MHD assumption.

- Resistive GRMHD.
  If a finite conductivity is present, the comoving electric field is assumed to be proportional to the conduction current, $e^\mu = \eta j^\mu$ where η is the reistivity measured in the comoving system. Taking the spatial projection, we get

  $$\Gamma(E^i v_i) = \eta(q - q_0\Gamma), \tag{3.54}$$

which may be used to express q_0 in the spatial component. The result is

$$\Gamma[E^i + \epsilon^{ijk} v_j B_k - (E^j v_j) v^i] = \eta(J^i - q v^i) \tag{3.55}$$

- Resistive GRMHD + dynamo.
  The natural extension of the mean-field dynamo equation (2.62) with the inclusion of the alpha effect can be obtained by imposing that the electric field in the fluid reference system is given by

  $$e^\mu = \eta j^\mu + \xi b^\mu, \tag{3.56}$$

  where we put $\xi = -\alpha$ to avoid misunderstandings with the lapse function. This expression was first introduced by Bucciantini and Del Zanna (2013) and it is the first example in the literature of an attempt to include mean-field dynamo processes in the context of GRMHD. The time projection is now

  $$\Gamma(E^i v_i) = \eta(q - q_0 \Gamma) + \xi \Gamma(B^i v_i), \tag{3.57}$$

  which, again used to express q_0 in the spatial component, provides

  $$\Gamma[E^i + \epsilon^{ijk} v_j B_k - (E^j v_j) v^i] = \eta(J^i - q v^i) + \xi \Gamma[B^i - \epsilon^{ijk} v_j E_k - (B^j v_j) v^i] \tag{3.58}$$

In relativistic MHD only in the ideal case it is possible to neglect the displacement current. In the relativistic non-ideal regime, on the other hand, the electric field must be evolved using Eq. (3.46). Ohm's law provides an expression for the density current, while the constraint on the charge is given by Eq. (3.48). In the more general case of resistive GRMHD dynamo, the electric field evolution equation is given by:

$$\begin{aligned} &\gamma^{-1/2} \partial_t (\gamma^{1/2} E^i) - \epsilon^{ijk} \partial_j (\alpha B_k - \epsilon_{klm} \beta^l E^m) + (\alpha v^i - \beta^i) q = \\ &- \alpha \Gamma / \eta [E^i + \epsilon^{ijk} v_j B_k - (E^j v_j) v^i] + \alpha \xi \Gamma / \eta [B^i - \epsilon^{ijk} v_j E_k - (B^j v_j) v^i)] \end{aligned} \tag{3.59}$$

3.3 Classical and relativistic MHD limits

We illustrate first the weak gravity limit and a flat Minkowski metric can be assumed. Now $\alpha = 1$, $\beta = 0$ e γ_{ij} is the 3×3 identity tensor. Eqs. (3.43) - (3.49) become:

$$\partial_t D + \partial_i (D v^i) = 0, \tag{3.60}$$

$$\partial_t S_i + \partial_j W_i^j = 0, \tag{3.61}$$

$$\partial_t \mathcal{E} + \partial_i S^i = 0, \tag{3.62}$$

$$\partial_t E^i - \epsilon^{ijk}\partial_j B_k + v^i Q = -\Gamma/\eta[E^i + \epsilon^{ijk} v_j B_k - (E^j v_j)v^i] + \xi\Gamma/\eta[B^i - \epsilon^{ijk} v_j E_k - (B^j v_j)v^i], \tag{3.63}$$

$$\partial_t B^i + \epsilon^{ijk}\partial_j E_k = 0, \tag{3.64}$$

$$\partial_i E^i = q, \tag{3.65}$$

$$\partial_i B^i = 0, \tag{3.66}$$

It can be seen that the source terms related to the curvature of the metric have disappeared. The limit of classic MHD can instead be obtained by requiring $\Gamma \to 1$, $p \ll \rho$, $\rho \ll \rho\epsilon$, $E \ll B$ e $B^2 \ll \rho$. The equation of mass and momentum become

$$\partial_t \rho + \partial_i(\rho v^i) = 0, \tag{3.67}$$

$$\partial_t(\rho v^i) + \partial_j(\rho v^i v^j + p\gamma^{ij} + \tfrac{1}{2}B^2\gamma^{ij} - B^i B^j) = 0. \tag{3.68}$$

To obtain the energy equation it is necessary to subtract the continuity Eq. (3.60) to Eq. (3.62) and consider the approximation

$$\rho h\Gamma^2 - \rho\Gamma = \rho\Gamma(h\Gamma - 1) \simeq 1/2\rho v^2 + \hat{\gamma}/(\hat{\gamma} - 1)p, \tag{3.69}$$

con $\Gamma \simeq 1 + 1/2\, v^2$. We get

$$\partial_t(1/2\rho v^2 + p/(\hat{\gamma} - 1) + B^2/2) + \partial_i[v_i(1/2\rho v^2 + \hat{\gamma}p/(\hat{\gamma} - 1)) + \epsilon^{ijk} E^j B^k] = 0. \tag{3.70}$$

Dynamo Ohm's law is obtained by applying the limit MHD to Eq. (3.58). We get

$$E^i + \epsilon^{ijk} v_j B_k = \eta J^i + \xi B^i, \tag{3.71}$$

which replaced in Eq. (3.64) allows to obtain the induction equation

$$\partial_t B^i + \partial_j(v^j B^i - v^i B^j) = \eta\nabla^2 B^i - \xi J^i - \epsilon^{ijk}[(\partial_j \eta)J_k + (\partial_j \xi)B_k]. \tag{3.72}$$

3.4 GRMHD disks

We now present in more detail an analytical stationary solution for the GRMHD equations (3.43) - (3.49) which describe the models used in our simulations. After showing the characteristics of Kerr's space-time we describe two important analytical and axisymmetric solutions for a non-magnetized torus in such a gravitational field. Finally, we show the first numerical results of kinematic dynamo in thick disks.

3.4.1 Kerr spacetime

Let us consider a rotating black hole of mass M and angular momentum per unit of mass $a = J/M$ and adopt the Boyer-Lindquist coordinates $(t;\, r;\, \theta;\, \phi)$. The line element is expressed as

$$\mathrm{d}s^2 = g_{tt}\mathrm{d}t^2 + 2g_{t\phi}\mathrm{d}t\mathrm{d}\phi + g_{rr}\mathrm{d}r^2 + g_{\theta\theta}\mathrm{d}\theta^2 + g_{\phi\phi}\mathrm{d}\phi^2, \tag{3.73}$$

where the coefficients are given by

$$g_{tt} = -\left(1 - \frac{2Mr}{\varrho^2}\right), \tag{3.74}$$

$$g_{t\phi} = -\frac{2Mar\sin^2\theta}{\varrho^2}, \tag{3.75}$$

$$g_{rr} = \frac{\varrho^2}{\Delta}, \tag{3.76}$$

$$g_{\theta\theta} = \varrho^2, \tag{3.77}$$

$$g_{\phi\phi} = \varpi^2, \tag{3.78}$$

with the following definitions

$$\Delta = r^2 - 2Mr + a^2, \tag{3.79}$$

$$\varrho^2 = r^2 + a^2\cos^2\theta, \tag{3.80}$$

$$\Sigma^2 = (r^2 + a^2)^2 - a^2\Delta\sin^2\theta, \tag{3.81}$$

$$\varpi = \frac{\Sigma}{\varrho}\sin\theta. \tag{3.82}$$

In these equations it is important not to confuse the geometric factor ϱ with the mass density ρ. Considering the 3+1 decomposition and comparing Eq. (3.73) with Eq. (3.16) we can represent the corresponding 3D spatial metric tensor γ_{ij} as a diagonal matrix with coefficients

$$\gamma_{rr} = \frac{\varrho^2}{\Delta}, \quad \gamma_{\theta\theta} = \varrho^2, \quad \gamma_{\phi\phi} = \varpi^2 \tag{3.83}$$

while the shift vector and the lapse function are respectively given by

$$\beta = \left(0, 0, -\frac{2Mar}{\Sigma^2}\right), \quad \alpha = \frac{\varrho}{\Sigma}\Delta^{1/2}. \tag{3.84}$$

This solution of the Einstein field equations due to Kerr (1963) shows that the metric retains the stationary and axisymmetric character of the mass distribution that generates it, i.e. a rotating black hole with constant mass and spin. When $a = 0$, the limit of the stationary and spherically

symmetric Schwarzschild metric of a non-rotating black hole is obtained

$$\mathrm{d}s^2 = -\left(1 - \frac{2M}{r}\right)\mathrm{d}t^2 + \left(1 - \frac{2M}{r}\right)^{-1}\mathrm{d}r^2 + r^2\mathrm{d}\theta^2 + r^2\sin^2\theta\mathrm{d}\phi^2. \tag{3.85}$$

The Kerr metric is singular when $\varrho = 0$ and $\Delta = 0$. The first condition gives rise to the so-called naked singularity, a physically unacceptable solution because it would imply the possibility of observing an infinite density. From the second relation we obtain

$$r_\pm = M \pm (M^2 - a^2)^{1/2}. \tag{3.86}$$

It is understood that, in order for an event horizon capable of hiding the naked singularity to be present, one must necessarily have $a^2 \leq M^2$ implying the existence of an upper limit for the angular momentum per unit of mass, $a = M$; in this case the black hole is called maximally rotating. The event horizon radius ranges between M and $2M$ depending on the value of a and it is given by the greater of the two roots of Eq. (3.86),

$$r_\mathrm{h} = M + (M^2 - a^2)^{1/2} \tag{3.87}$$

Let us now consider an external stationary observer orbiting around the black hole with angular velocity

$$\Omega = \frac{u^\phi}{u^t}. \tag{3.88}$$

Developing the condition $u^\mu u_\mu = -1$ and using Eq. (3.88) we obtain

$$(u^t)^2(g_{tt} + 2\Omega g_{t\phi} + \Omega^2 g_{\phi\phi}) = -1, \tag{3.89}$$

which implies

$$g_{tt} + 2\Omega g_{t\phi} + \Omega^2 g_{t\phi} < 0, \tag{3.90}$$

i.e. the value of the observer's angular velocity is in range $[\Omega_-, \Omega_+]$ where

$$\Omega_\pm = \omega \pm \left(\omega^2 - \frac{g_{tt}}{g_{\phi\phi}}\right)^{1/2} \tag{3.91}$$

and where we defined $\omega = -g_{t\phi}/g_{\phi\phi}$. In those regions where $g_{tt} < 0$ the observer's angular velocity can be zero (since $\Omega_- < 0$), but where $g_{tt} > 0$ there will be a minimum value $\Omega_- > 0$ below which Ω cannot drop. The observer that in other circumstances would be at rest will be dragged by the rotating spacetime. Such a region is referred to as the ergosphere. It is limited by the surfaces where the coefficient g_{tt} is zero, i.e. at a distance from the black hole given by

$$r_\mathrm{erg} = M + (M^2 - a^2\cos^2\theta)^{1/2}. \tag{3.92}$$

The importance of this region (schematized in Figure (3.1)), external to the event horizon (i.e. $r_\mathrm{h} < r_\mathrm{erg}$), is related to one of the best known processes by which it is possible to extract energy from a rotating black hole, namely the Blandford-Znajek mechanism (Blandford and Znajek, 1977). In fact, although the process was initially conceived as a mechanism that extracts energy directly

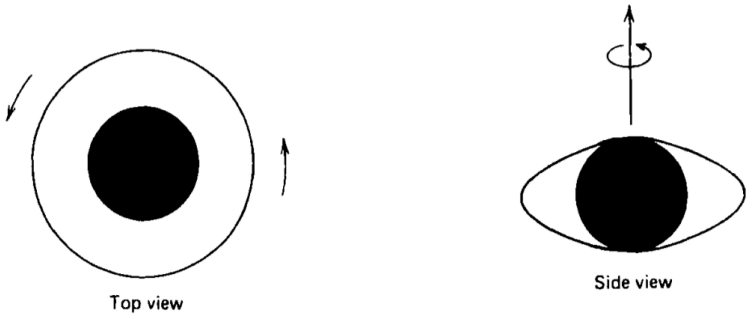

Figure 3.1: The ergosphere of a Kerr black hole is the region between the static limit (the flattened outer surface defined by Eq. (3.92)) and the event horizon defined by Eq. (3.87) (Shapiro and Teukolsky, 1986).

from the black hole, recently it has been shown that only the magnetic field lines threading the ergosphere of the black hole rotate due to the frame dragging effect, whether or not they cross the horizon (Komissarov, 2004, 2005). These twisted magnetic fields carry the energy of the relativistic jet, which seems to come from the ergosphere.

From a numerical point of view it is problematic to deal with the singularity located at the black hole event horizon due to numerical artifacts that could arise from the inner radial boundary. For this reason we adopt in our simulations the so-called Kerr-Schild coordinates (KS) that allow one to remove the unphysical singularity and place the domain's inner boundary beyond it. This formulation is described in the Appendix A.

3.4.2 Two analytical solutions

The simplest analytic model of a black hole accretion disk is the Polish doughnut, in which self-gravity, the contribution due to viscous forces, the radiative effects are neglected and the support against gravity is provided only by thermal pressure.
Let us consider a perfect non-magnetized fluid that orbits around a Kerr black hole along the positive azimuth direction with the four-velocity $u^\mu = (u^t, 0, 0, u^\phi)$. The stress-energy tensor is

$$T^{\mu\nu} = \omega u^\mu u^\nu + p g^{\mu\nu} \tag{3.93}$$

where $\omega = \rho h$ is the fluid enthalphy density. We define the specific angular momentum as

$$l = -\frac{u_\phi}{u_t}. \tag{3.94}$$

This is the most natural and reasonable choice because it satisfies the properties of being a constant of motion and besides generating a simple stability criterion (Kozlowski et al., 1978). From the definitions (3.88) and (3.94) it follows that

$$l = -\frac{g_{t\phi} + g_{\phi\phi}\Omega}{g_{tt} + g_{t\phi}\Omega}, \tag{3.95}$$

$$\Omega = -\frac{g_{t\phi} + g_{tt} l}{g_{\phi\phi} + g_{t\phi} l}. \tag{3.96}$$

Let's briefly summarize the steps that allow us to derive the fundamental equation that determines the equilibrium. First Eq. (3.2) is contracted with the projection operator $h^\mu_\nu = \delta^\mu_\nu + u^\mu u_\nu$. Using the assumptions of stationarity and symmetry we obtain

$$\omega u_\mu \nabla_\nu u^\mu + \nabla_\nu p = 0. \tag{3.97}$$

Combining Eqs. (3.95), (3.96), (3.97) and the normalization $u_\mu u^\mu = -1$ we obtain

$$\nabla_i(\ln|u_t|) - \frac{\Omega}{1-l\Omega}\nabla_i l + \frac{\nabla_i p}{\omega} = 0, \tag{3.98}$$

where

$$|u_t| = \sqrt{\frac{\mathcal{L}}{\mathcal{A}}}, \tag{3.99}$$

where

$$\mathcal{L} = g_{t\phi}^2 - g_{tt}g_{\phi\phi} \tag{3.100}$$

is the relativistic generalization of the distance from the black hole rotational axis and

$$\mathcal{A} = g_{\phi\phi} + 2lg_{t\phi} + l^2 g_{tt}. \tag{3.101}$$

The algebraic steps leading to Eq. (3.98) are described in detail for a magnetized disk in the appendix of Komissarov (2006). It is sufficient to set $b^\mu = 0$ to obtain the equations of the hydrodynamic equilibrium we have considered here.
The assumption of a barotropic equation of state now allows us to rewrite Eq. (3.98) as

$$d\left(\ln|u_t| + \int_0^p \frac{\mathrm{d}p}{\omega}\right) = \frac{\Omega}{1-\Omega l}\mathrm{d}l. \tag{3.102}$$

This equation implies that $\Omega = \Omega(l)$: the surfaces with constant l and Ω coincide and are called von Zeipel's cylinders (Kozlowski et al., 1978). By integrating Eq. (3.102) we get

$$\ln|u_t| + \int_0^p \frac{\mathrm{d}p}{\omega} - \int_0^l \frac{\Omega}{1-\Omega l}\mathrm{d}l = K. \tag{3.103}$$

The integration constant K is easily obtained by imposing the conditions $p = 0$, $u_t = u_t^{in}$, $l = l_{in}$ on the internal radius of the disk r_{in} on the equatorial plane ($\theta = \pi/2$). We get

$$K = \ln|u_t^{in}| - \int_0^{l_{in}} \frac{\Omega}{1-\Omega l}\mathrm{d}l \tag{3.104}$$

Substituting the value of the constant in the Eq. (3.103) we get

$$\ln|u_t| - \ln|u_t^{in}| - \int_{l_{in}}^l \frac{\Omega}{1-\Omega l}\mathrm{d}l + \int_0^p \frac{\mathrm{d}p}{\omega} = 0. \tag{3.105}$$

It is convenient at this point to introduce the potential W defined as

$$W = \ln|u_t| + \int_l^{l_\infty} \frac{\Omega}{1-\Omega l}\mathrm{d}l, \tag{3.106}$$

where l_∞ is the value of the angular momentum evaluated at $r \to \infty$, such that $u_t^\infty = -1$ and $W_\infty = 0$. This potential in the Newtonian limit is reduced to the sum of the centrifugal and gravitational contributions. We can now rewrite Eq. (3.105) as

$$W - W_{in} + \int_0^p \frac{\mathrm{d}p}{\omega} = 0. \tag{3.107}$$

We now give the explicit solutions satisfying two von Zeipel's relations.

- The first solution we consider is

$$l = \text{const.} \tag{3.108}$$

  This solution was introduced by introduced by Abramowicz et al. (1978) and it is important for two physical reasons: first, because such configurations are stable to axisymmetric perturbations; second, the region near the inner edge is well approximated by (3.108). The potential is given by

$$W = \frac{1}{2} \ln \left| \frac{\mathcal{L}}{\mathcal{A}} \right|, \tag{3.109}$$

- The second important solution is

$$l/(1 - \Omega l) \equiv l_* = \text{const.} \tag{3.110}$$

  On the contrary, the solution (3.110), used for the first time by Fishbone and Moncrief (1976), does not have strong physical motivations but it is widely used in recent literature. Now, the potential is given by

$$W = \ln |\mathcal{A}_*| + l_* \Omega. \tag{3.111}$$

  where

$$\mathcal{A}_* \equiv u^t = (g_{tt} + 2\Omega g_{t\phi} + g_{\phi\phi}\Omega^2)^{-1/2}, \tag{3.112}$$

  is called the redshift factor.

Assigned l or l_*, the potential W is defined in each point of space and matter fills every closed equipotential surface, i.e. the surfaces where $W < 0$ (see Figure 3.2). To understand how the values of the angular momentum of the disks are assigned, we first refer to the Figure 3.3 which shows the radial distribution of the specific angular momentum defined by

$$l_k = \frac{r^2 - 2ar^{1/2} + a^2}{r^{3/2} - 2r^{1/2} + a}. \tag{3.113}$$

and the horizontal line corresponding to a constant value of specific angular momentum, l_0. Furthermore, the values of l_k at the radii of the marginally bound and marginally stable orbits (r_{mb} and r_{ms}) are indicated with l_{mb} and l_{ms} respectively. In particular, if $l_{ms} < l_0 < l_{mb}$, it is possible to define two geometric points called cusp (located at radius r_{in}) and center (located at radius r_c) which respectively represent the innermost and outermost point where the constant angular momentum l_0 takes the Keplerian value. The disk models considered in the simulations of Chapters 5 and 6 are initialized according to the procedure illustrated in Del Zanna et al. (2007).

- We assign the black hole parameters that define the metric: the mass M and angular momen-

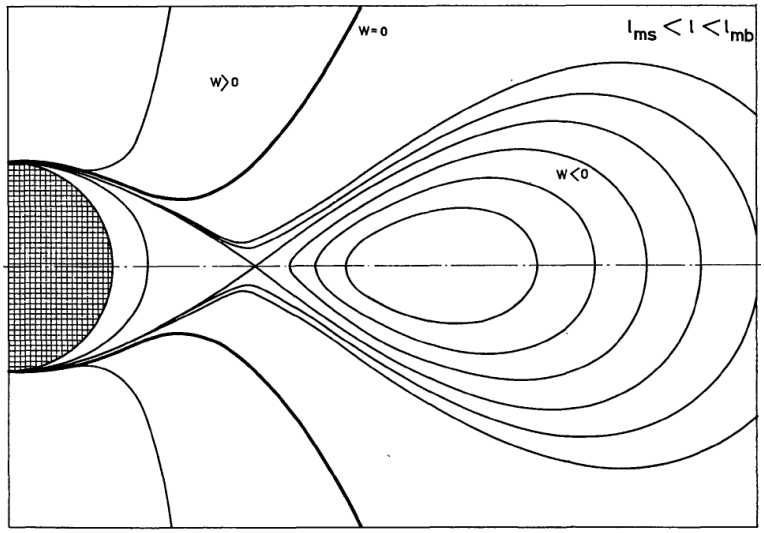

Figure 3.2: Equipotential surfaces for a disk orbiting around a Schwarzschild black hole (Abramowicz et al., 1978).

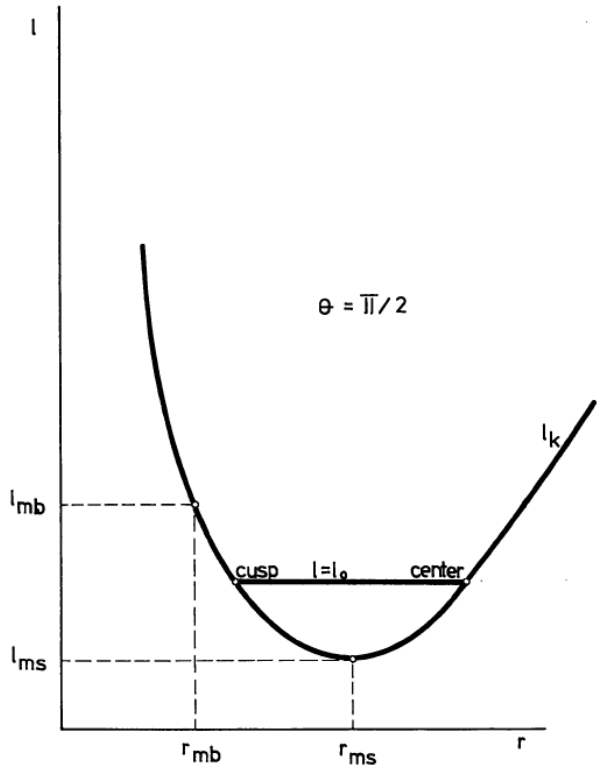

Figure 3.3: Location of disk's center and its cusp (Abramowicz et al., 1978).

tum per unit of mass a.

- We assign the cusp r_{in} and the center of the disk r_c.
- We evaluate $l_0 = l_k(r_c)$ and we put $l = l_0$ for Abramowicz's disks and $l_* = l_0/(1 - \Omega(l_0)l_0)$ for Fishbone and Moncrief's.
- The potential W can be defined in each point of space.
- By adopting a polytropic EoS, $p = K_1\omega^{\hat{\gamma}}$, the potential become

$$W - W_{in} + \frac{\hat{\gamma}}{\hat{\gamma} - 1}\frac{p}{\omega} = 0, \tag{3.114}$$

or equivalently

$$h = h_{in}\exp(W - W_{in}) \tag{3.115}$$

The constant K_1 is obtained by assigning the central enthalpy density w_c and deriving the central pressure p_c from Eq. (3.114).

- We can compute enthalpy density as

$$\omega = \omega_c\left(\frac{W_{in} - W}{W_{in} - W_c}\right)^{1/\hat{\gamma}-1}, \tag{3.116}$$

while pressure is defined immediately from the EoS. Mass density is obtained from

$$\rho = \omega - \frac{\hat{\gamma}}{\hat{\gamma} - 1}p. \tag{3.117}$$

3.5 Kinematic $\alpha - \Omega$ dynamo in axisymmetric thick disks

In this section we briefly show the results of the first application of the GRMHD equations with dynamo closure to thick disks. The simulations, described in detail in Bugli et al. (2014), are restricted to the kinematic regime in which the fluid quantities are kept fixed, i.e. the back-reaction of the evolution of the e.m. fields on them is neglected.
The initial model is an axisymmetric magnetized thick torus, similar to the first solution described in paragraph 3.4.2 but also including magnetic pressure as a contribution to equilibrium (see Komissarov (2006) for more details). The disk orbits around a Kerr black hole of mass M and spin $a = 0.99$ and its inner edge and center are located at $r_{in} = 3M$ and $r_c = 5M$ respectively. Configurations with both toroidal and poloidal initial magnetic fields are studied, while the resistivity and dynamo profiles are initialized as

$$\eta(r,\theta) = \eta_{\max}S_\eta(r,\theta), \qquad \xi(r,\theta) = \xi_{\max}S_\xi(r,\theta) \tag{3.118}$$

where

$$S_\eta(r,\theta) = \frac{\sqrt{\rho} - \sqrt{\rho_{\min}}}{\sqrt{\rho_{\max}} - \sqrt{\rho_{\min}}}, \qquad S_\xi(r,\theta) = \frac{\rho\cos\theta}{(\rho\cos\theta)_{\max}}, \tag{3.119}$$

with $\rho_{\min}$ is the density minimum reached in the atmosphere and $\eta_{\max}$ and $\xi_{\max}$ are free parameters that allow us to adjust the intensity of the alpha effect and the dissipation of the magnetic field. The

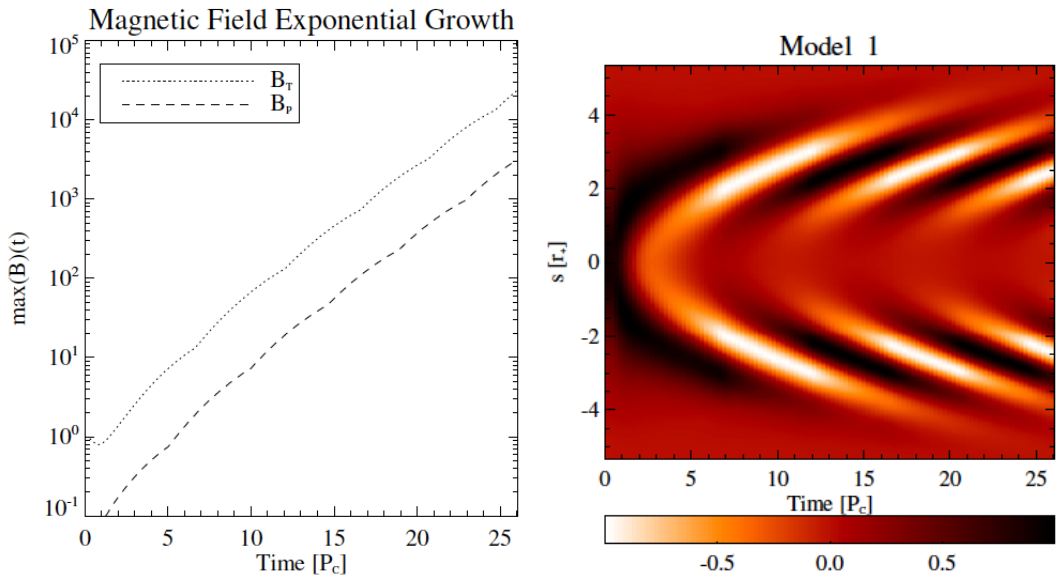

Figure 3.4: Exponential growth of the maximum values of B_T and B_P (Left) and butterfly diagrams (Right) of Model 1 in Bugli et al. (2014).

authors have built several models that differ by the values of η and ξ. In all cases, the magnetic field evolves rapidly towards an eigenstate of the system characterized by a dynamo wave propagating away from the equatorial plane ($\xi > 0$) or towards the equatorial plane ($\xi < 0$). This migration was characterized for each run by a butterfly diagram considering the value of the toroidal field along the trajectories of its maxima at different times. Besides this drifting, the amplitude of both the toroidal and poloidal components, defined as

$$B_T = \sqrt{B_\phi B^\phi}, \qquad B_P = \sqrt{B_r B^r + B_\theta B^\theta}, \tag{3.120}$$

grows exponentially over time.

Here we report the results that refer to the Model 1 which presents an initial toroidal field and the resistivity and dynamo parameters are $\eta_{\max} = 10^{-3}$ and $\xi_{\max} = 10^{-3}$. Figure 3.4 (Left) shows the time evolution with exponential growth of the maximum values of the toroidal an poloidal components of the magnetic field. The dynamo mode patterns are shown in Figure 3.5: after an initial transient, all three components present an oscillatory pattern that drifts from the equatorial plane towards higher latitudes. The periodicity and length-scale of the eigenmodes selected by the system are quantified by the butterfly diagram (Figure 3.4 Right) obtained by plotting the value of B_T as a function of a parameter s with respect to which two almost vertical half-lines starting from a point on the equatorial plane are parameterized. The migration of the toroidal field from the equatorial plane towards higher latitudes is evident.

The work of this paper which characterized the GRMHD mean-dynamo in thick disks represents the starting point for a generalization to the dynamic regime in which the effects of Lorentz force on the charged particles that constitute the plasma can no longer be neglected. In Chapter 6 we show some advances in the study of $\alpha - \Omega$ dynamo in disks, also focusing on the main diagnostics of accretion.

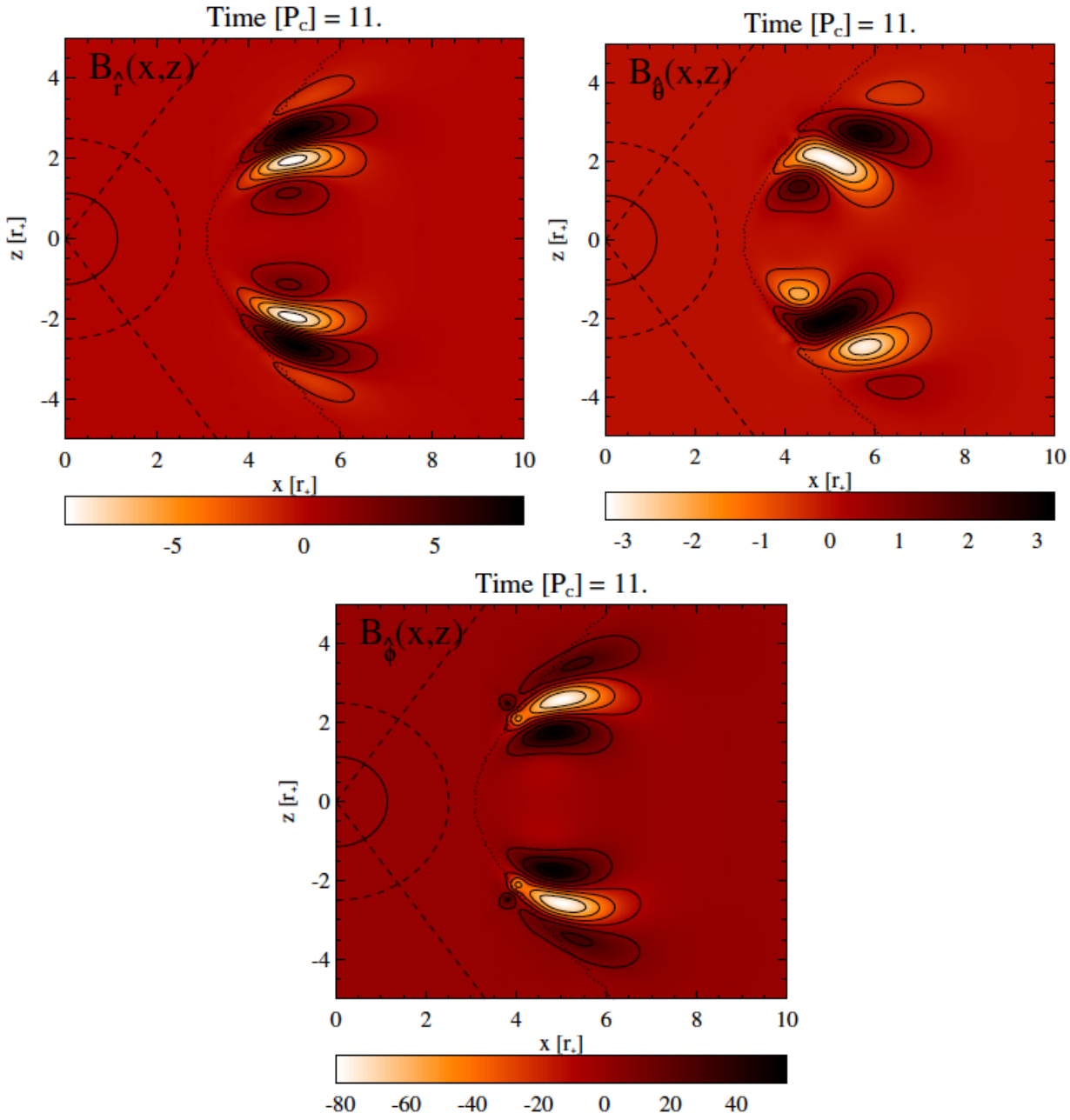

Figure 3.5: Cartesian maps of the magnetic field components after 11 central disk periods of Model 1 in Bugli et al. (2014).

Chapter 4

The ECHO code

In this chapter we describe the numerical methods and algorithms used to perform our disk accretion simulations. We used the ECHO code (Eulerian Conservative High Order scheme) (Del Zanna and Bucciantini, 2002; Del Zanna et al., 2003, 2007) specifically developed to treat magnetohydrodynamics problems in a generic metric even in the presence of discontinuities. After a brief introduction to the original scheme used to solve the ideal GRMHD equations, we describe the changes made to adapt the code to include non-ideal effects such as resistivity and mean-field dynamo (Bucciantini and Del Zanna, 2013) and also chiral anomaly (Del Zanna and Bucciantini, 2018).

4.1 ECHO's original version

The first version of the code allowed the integration of ideal GRMHD equations. Consider first Eqs. (3.43) - (3.47), postponing the discussion of the constraints on the electric and magnetic fields (3.48) and (3.49). Assuming a stationary metric and expanding the covariant derivation operators, it is possible to rewrite them as (Del Zanna et al., 2007):

$$\frac{\partial}{\partial t}\boldsymbol{\mathcal{U}} + \frac{\partial}{\partial x^i}\boldsymbol{\mathcal{F}}^i = \boldsymbol{\mathcal{S}} \tag{4.1}$$

, where $\boldsymbol{\mathcal{U}}$, $\boldsymbol{\mathcal{F}}^i$ and $\boldsymbol{\mathcal{S}}$ are defined as

$$\boldsymbol{\mathcal{U}} = \gamma^{1/2} \begin{bmatrix} D \\ S_j \\ \mathcal{E} \\ E^j \\ B^j \end{bmatrix} \quad i = 1, ..., d, \tag{4.2}$$

$$\boldsymbol{\mathcal{F}}^i = \gamma^{1/2} \begin{bmatrix} D(\alpha v^i - \beta^i) \\ \alpha W_i^j - \beta^j S_i \\ \alpha S^i - \mathcal{E}\beta^i \\ [jik](-\gamma^{-1/2}\alpha B_k + [klm]\beta^l E^m) \\ [jik](\gamma^{-1/2}\alpha E_k + [klm]\beta^l B^m) \end{bmatrix}, \tag{4.3}$$

$$\boldsymbol{\mathcal{S}} = \gamma^{1/2} \begin{bmatrix} 0 \\ \frac{1}{2}\alpha W^{ik}\partial_j \gamma_{ik} + S_i \partial_j \beta^i - \mathcal{E}\partial_j \alpha \\ \frac{1}{2} W^{ik}\beta^j \partial_j \gamma_{ik} + W_i{}^j \partial_j \beta^i - S^j \partial_j \alpha \\ q\beta^j - \alpha J^j \\ 0 \end{bmatrix}. \tag{4.4}$$

Eq. (4.1) is a set of hyperbolic partial differential equations where the elements of the vector $\boldsymbol{\mathcal{U}}$ are referred to as the conservative variables, since their time evolution is controlled by a conservation law with fluxes $\boldsymbol{\mathcal{F}}$ and source terms $\boldsymbol{\mathcal{S}}$. We note that for convenience in the relativistic numerical simulations of the most recent version of ECHO, instead of energy $\mathcal{E}$, the quantity τ, defined as $\tau = \mathcal{E} - D$, is evolved.

The starting point is to discretize Eq. (4.1). Let us consider, for the sake of simplicity, the unidimensional case, $d = 1$ and divide the domain defined by the interval $[a, b]$ in N cells $I_i = [x_{i-1/2}, x_{i+1/2}]$. Let us assume that the intervals have equal length $\Delta x = (b - a)/N$ and are each centered at the grid point

$$x_i = a + (i - 1/2)\Delta x; \quad i = 1, ..., N. \tag{4.5}$$

Calling r the spatial accuracy order, the point value of a generic quantity $g(x)$ at a given time t is $g_i = g(x_i) + O((\Delta x)^r)$ and its interface values are $g_{i\pm1/2} = g(x_{i\pm1/2}) + O((\Delta x)^r)$. We are now looking for a spatial discretization of Eq. (4.1) on this grid. For the moment we neglect the source terms, since they will not need to be discretized but they are computed at the cell centers x_i. The discretization scheme implemented in ECHO is a so-called finite difference one. To calculate spatial derivatives of a flux we expand it into a Taylor series

$$\frac{\partial \mathcal{F}}{\partial t}(x_i) = \frac{\hat{\mathcal{F}}_{i+1/2} - \hat{\mathcal{F}}_{i-1/2}}{\Delta x} + O((\Delta x)^2), \tag{4.6}$$

and express Eq. (4.1) as

$$\frac{\partial \boldsymbol{\mathcal{U}_i}}{\partial t} = -\frac{\hat{\boldsymbol{\mathcal{F}}}_{i+1/2} - \hat{\boldsymbol{\mathcal{F}}}_{i-1/2}}{\Delta x}, \tag{4.7}$$

where $\hat{\boldsymbol{\mathcal{F}}}_{i\pm1/2}$ represents an approximation of the primitive of physical flux function $\boldsymbol{\mathcal{F}}(x)$ at the right (left) interface of the i-th cell. This means that the cell averages of $\boldsymbol{\mathcal{F}}$ must coincide with the point value $\boldsymbol{\mathcal{F}}_i$ of the flux $\boldsymbol{\mathcal{F}}(x)$, to the given accuracy. This simple discretization provides a scheme of 2^{nd} order accuracy. To achieve higher orders it is necessary to consider further terms in the expansion in Eq. (4.6). Once the quantities are known, it is possible to perform the time integration as described in Eq. (4.7), but it is clear from Eq. (4.3) that to compute the fluxes it is necessary to calculate the so-called primitive variables

$$\boldsymbol{\mathcal{P}} = \{\rho, v^j, p, E^j, B^j\}, \tag{4.8}$$

where ρ, $\boldsymbol{v}$ and p are respectively the rest mass density, the velocity, and the pressure of the fluid, while $\boldsymbol{E}$ and $\boldsymbol{B}$ are the usual electric and magnetic fields. Since the code evolves the conservative variables $\boldsymbol{\mathcal{U}}$, one has first to invert the relation between $\boldsymbol{\mathcal{U}}$ and $\boldsymbol{\mathcal{P}}$ by using Eqs.(3.28) - (3.30). The interface value of the primitive variables can be retrieved by means of polynomial interpolation during the reconstruction phase of the algorithm. As a consequence there will be in general two

different states at both sides of each cell interface (as the fluid equations allow for discontinuous solutions) and at the lowest order we can identify them with $\boldsymbol{\mathcal{P}}^L_{i+1/2} = \boldsymbol{\mathcal{P}}_i$ and $\boldsymbol{\mathcal{P}}^R_{i+1/2} = \boldsymbol{\mathcal{P}}_{i+1}$. To achieve a higher accuracy it is necessary to compute the left and right states using stencils of grid points centered respectively at x_i and x_{i+1}. In this way the interface values are computed with high order accuracy in the sufficiently smooth regions of the computational domain, while in the presence of strong gradients the algorithm has to limit the interpolation to 1$^{\text{st}}$ order to ensure stability and avoid spurious oscillations. The ECHO code, in the original implementation, allows for a large number of different reconstruction schemes to be used, such as

- 2$^{\text{nd}}$ order like-TVD reconstructions (Total Variation Diminishing);
- 3$^{\text{nd}}$ order CENO (Convex Essentially Non-Oscillatory, Liu and Osher (1998));
- 3$^{\text{nd}}$ order PPM (Piece-wise Parabolic Method, Colella and Woodward (1984));
- 5$^{\text{nd}}$ order MP5 (Monotonicity Preserving, Suresh and Huynh (1997).

The discontinuities at the cell interfaces define a set of local Riemann problems. To better describe the structure of this problem, let us consider Eq. (4.1) rewritten as

$$\frac{\partial \boldsymbol{\mathcal{U}}}{\partial t} + \frac{\partial \boldsymbol{\mathcal{F}}}{\partial \boldsymbol{\mathcal{U}}} \frac{\partial \boldsymbol{\mathcal{U}}}{\partial x} = 0 \tag{4.9}$$

which is a hyperbolic system of n PDEs (where n coincides with the number of conservative variables) whose solution requires the computation of n real and distinct eigenvalues of the Jacobian $\partial \boldsymbol{\mathcal{F}}/\partial \boldsymbol{\mathcal{U}}$ (which in general depends on both the primitive and conservative variables). The eigenvalues are referred to as the characteristic velocities of the system, as they represent the speeds at which the information is transported by the fluid fluxes through the characteristic waves of the system, i.e. the eigenvectors. Although there are algorithms that provide a numerically exact solution to this problem, their computational cost makes them unsuitable for the GRMHD context. A far more appropriate and affordable choice is the approximate Riemann solver HLL (Harten et al., 1983) implemented in ECHO, since it only calculates the fastest and slowest characteristic velocity (respectively a^+ and a^-). It is still necessary though to ensure that the information propagates in the correct direction, a property that makes a scheme to be called upwind. The application of the HLL solver finally provides with the value of the flux at the cell interface (Londrillo and Del Zanna, 2004)

$$\boldsymbol{\mathcal{F}}^{\text{HLL}} = \frac{a^+ \boldsymbol{\mathcal{F}}^{\text{L}} + a^- \boldsymbol{\mathcal{F}}^{\text{R}} - a^+ a^- (\boldsymbol{\mathcal{U}}^{\text{R}} - \boldsymbol{\mathcal{U}}^{\text{L}})}{a^+ + a^-} \tag{4.10}$$

Finally we are ready to perform the time-integration of the conservative quantities, for instance with a 3$^{\text{rd}}$ order explicit Runge-Kutta scheme

$$\boldsymbol{\mathcal{U}}^{(1)} = \boldsymbol{\mathcal{U}}^n + \Delta t \mathcal{L}[\boldsymbol{\mathcal{U}}^n], \tag{4.11}$$

$$\boldsymbol{\mathcal{U}}^{(2)} = \tfrac{3}{4}\boldsymbol{\mathcal{U}}^n + \tfrac{1}{4}\boldsymbol{\mathcal{U}}^{(1)} + \tfrac{1}{4}\Delta t \mathcal{L}[\boldsymbol{\mathcal{U}}^{(1)}], \tag{4.12}$$

$$\boldsymbol{\mathcal{U}}^{n+1} = \tfrac{1}{3}\boldsymbol{\mathcal{U}}^n + \tfrac{2}{3}\boldsymbol{\mathcal{U}}^{(2)} + \tfrac{2}{3}\Delta t \mathcal{L}[\boldsymbol{\mathcal{U}}^{(2)}], \tag{4.13}$$

where the n index denotes the time step iteration, $\boldsymbol{\mathcal{U}}^{(1)}$ and $\boldsymbol{\mathcal{U}}^{(2)}$ are intermediate states, and $\mathcal{L}[\boldsymbol{\mathcal{U}}]$ is the member on the right-hand side of Eq. (4.7) plus the source term $\boldsymbol{\mathcal{S}}$.

4.2 Upwind Constrained Transport

Contrary to the other variables evolved in time, the magnetic field $\boldsymbol{B}$ has also to fulfill at all times the constraint given by Eq. (3.49), which formally could be regarded as an initial condition: the structure of the induction equation guarantees the analytical null divergence of $\boldsymbol{B}$. From a numerical perspective this is in general not true, since for upwind schemes the derivations in different directions are no longer commutable, so that spurious magnetic monopoles can appear during the computation. To properly deal with this problem the Upwind Constrained Transport scheme (UCT, presented by Londrillo and Del Zanna (2004)) was implemented in ECHO. For this method it is convenient to introduce the quantities

$$\mathcal{B}^i = \gamma^{1/2} B^i, \tag{4.14}$$

$$\mathcal{E}_i = \alpha E_i + \epsilon_{ijk} \beta^j B^k, \tag{4.15}$$

to rewrite Eq. (3.47) and Eq. (3.49) as

$$\partial_t \mathcal{B}^i + [ijk] \partial_j \mathcal{E}_k = 0, \tag{4.16}$$

$$\partial_i \mathcal{B}^i = 0. \tag{4.17}$$

We now integrate over the cell $I_{i,j,k}$ with center at the point $P_{i,j,k} = (x_i, y_j, z_k)$, apply Stoke's theorem and assume for simplicity a 2nd order accuracy, obtaining for the component $\mathcal{B}_x$

$$\frac{\mathrm{d}\mathcal{B}_x}{\mathrm{d}t} = -\frac{\Delta_y \mathcal{E}_z}{\Delta y} + \frac{\Delta_z \mathcal{E}_y}{\Delta z}, \tag{4.18}$$

where $\mathcal{B}_x$ is evaluated at the middle of the interface between cell $I_{i,j,k}$ and $I_{i+1,j,k}$ (i.e. point $P_{i+1/2,j,k}$), while $\mathcal{E}_z$ and $\mathcal{E}_y$ are evaluated respectively at $P_{i+1/2,j+1/2,k}$ and $P_{i+1/2,j,k+1/2}$. The operator Δ_x centered at $P_{i,j,k}$ is defined by

$$[\Delta_x f]_{i,j,k} = f_{i+1/2,j,k} - f_{i-1/2,j,k}. \tag{4.19}$$

Extending this calculation to the remaining two components of the magnetic field defined by Eq. (4.14) and considering the time derivative of the spatially discretized solenoidal constraint, we obtain

$$\frac{\mathrm{d}}{\mathrm{d}t}\left(\frac{\Delta_x \mathcal{B}_x}{\Delta x} + \frac{\Delta_y \mathcal{B}_y}{\Delta y} + \frac{\Delta_z \mathcal{B}_z}{\Delta z}\right) = 0, \tag{4.20}$$

which guarantees Eq. (4.17) to be algebraically satisfied for all times, assuming that the magnetic field at the initial time is divergence free. For this reason the quantities evolved in time with the CT method (Constrained Transport) are the staggered components

$$[\mathcal{B}_x]_{i+1/2,j,k}, [\mathcal{B}_y]_{i,j+1/2,k}, [\mathcal{B}_z]_{i,j,k+1/2}, \tag{4.21}$$

which represent the point values of the components of the magnetic field evaluated respectively at $P_{i+1/2,j,k}$, $P_{i,j+1/2,k}$, $P_{i,j,k+1/2}$, i.e. the centers of the interfaces orthogonal to the corresponding magnetic field component.

It can be shown (Londrillo and Del Zanna, 2004) that the staggered components have the important property of being continuous along the normal to the interface on which they are defined. Hence, the left and right states coincide and need not to be reconstructed as the other variables for the fluxes calculation. The obvious drawback is that when the values of the magnetic field components are required at the cell center $P_{i,j,k}$ (for instance, when the data are written into an output file) they can be retrieved only by an interpolation step.

4.3 IMEX schemes for the treatment of the non-ideal terms

The introduction of resistive and dynamo terms in the GRMHD equations entails the need to modify the original algorithm. In fact, if we consider the evolution time scale of the terms of Eq. (3.59) we observe that non-ideal contributions evolve inversely to resistivity η. For this reason it is possible that in areas of high (low) conductivity the evolution times of these so called stiff terms are considerably large (small) compared to the advection times and the evolutionary times of the sources. This fact can represent a problem for the stability of the code: it is known that a necessary condition for stability is the so-called Courant-Friedrichs-Lewy (CFL) which is based on the idea that the propagation velocity of any perturbation must always be smaller than the numerical velocity defined as $\lambda_{\rm N} = \Delta x/\Delta t$, where Δx and Δt are the spatial and temporal discretizations. Basically, satisfying the CFL condition does not allow a physical signal to propagate for more than a fraction of the numerical grid during a single time step. However, the presence of stiff terms results in a significant reduction in the maximum time interval necessary to ensure stability, significantly increasing the calculation times.

In order to integrate a system of stiff differential equations using time steps that guarantee both stability and reasonable computation times, the explicit third-order Runge-Kutta algorithm has been replaced with an IMplicit-Explicit (IMEX) Runge-Kutta (Palenzuela et al., 2009; Pareschi and Russo, 2005). We now illustrate the main features of the algorithm introduced in ECHO for the first time in the works of Bucciantini and Del Zanna (2013); Bugli et al. (2014). Let us consider the system (4.1) and separate the variables $\mathcal{U}$ into two subsets $\{\boldsymbol{\mathcal{X}}, \boldsymbol{\mathcal{Y}}\} = \boldsymbol{\mathcal{U}}$, where $\boldsymbol{\mathcal{X}}$ represents variables whose evolution is governed by a stiff differential equation and $\boldsymbol{\mathcal{Y}}$ stands for all other variables. We get

$$\partial_t \boldsymbol{\mathcal{Y}} = \boldsymbol{Q}_{\boldsymbol{\mathcal{Y}}}(\boldsymbol{\mathcal{X}}, \boldsymbol{\mathcal{Y}}), \tag{4.22}$$

$$\partial_t \boldsymbol{\mathcal{X}} = \boldsymbol{Q}_{\boldsymbol{\mathcal{X}}}(\boldsymbol{\mathcal{X}}, \boldsymbol{\mathcal{Y}}) + \boldsymbol{R}_{\boldsymbol{\mathcal{X}}}(\boldsymbol{\mathcal{X}}, \boldsymbol{\mathcal{Y}}), \tag{4.23}$$

where the operators $\boldsymbol{Q}_{\boldsymbol{\mathcal{Y}}}$ e $\boldsymbol{Q}_{\boldsymbol{\mathcal{X}}}$ include both the spatial derivatives with respect to $\boldsymbol{\mathcal{Y}}$ and $\boldsymbol{\mathcal{X}}$ and the non stiff source terms; the operator $\boldsymbol{R}_{\boldsymbol{\mathcal{X}}}$ contains the stiff source terms which regulate $\boldsymbol{\mathcal{X}}$. In the most general case of a resistive plasma with mean-field dynamo action, a comparison with Eq. (3.59) provides the following form for the latter operator

$$R^i_{\boldsymbol{\mathcal{X}}} = -\gamma^{1/2}\alpha\Gamma\{E^i + \epsilon^{ijk} v_j B_k - (E^j v_j) v^i - \xi[B^i - \epsilon^{ijk} v_j E_k - (B^j v_j) v^i)]\}/\eta. \tag{4.24}$$

Each intermediate step of the IMEX Runge-Kutta method can now be divided in two parts:

1 First the explicit intermediate values are obtained at each sub-step. They are

$$\boldsymbol{\mathcal{Y}}_{\star}^{(i)} = \boldsymbol{\mathcal{Y}}^{n} + \Delta t \sum_{j=1}^{i-1} \tilde{a}_{ij} \boldsymbol{\mathcal{Q}}_{\boldsymbol{\mathcal{Y}}}[\boldsymbol{\mathcal{U}}^{(j)}], \tag{4.25}$$

$$\boldsymbol{\mathcal{X}}_{\star}^{(i)} = \boldsymbol{\mathcal{X}}^{n} + \Delta t \sum_{j=1}^{i-1} \tilde{a}_{ij} \boldsymbol{\mathcal{Q}}_{\boldsymbol{\mathcal{X}}}[\boldsymbol{\mathcal{U}}^{(j)}] + \Delta t \sum_{j=1}^{i-1} a_{ij} \boldsymbol{\mathcal{R}}_{\boldsymbol{\mathcal{X}}}[\boldsymbol{\mathcal{U}}^{(j)}], \tag{4.26}$$

where the index (i) is referred to the substep of the scheme, while the index n indicates the step of the time discretization. It is essential that the summation extends up to the index $i-1$ so as to avoid the appearance of implicit terms in this passage. The matrices with coefficients $\tilde{a}_{ij}$ e a_{ij} have dimensions $N_{IMEX} \times N_{IMEX}$ where N_{IMEX} is a number that refers to the specific accuracy of the scheme and the number of intermediate steps.

2 Then we perform the implicit integration. The non-stiff variables can be regarded as completely evolved (as far as the intermediate step is concerned)

$$\boldsymbol{\mathcal{Y}}^{(i)} = \boldsymbol{\mathcal{Y}}_{\star}^{(i)}, \tag{4.27}$$

while the stiff variables have to be integrated further

$$\boldsymbol{\mathcal{X}}^{(i)} = \boldsymbol{\mathcal{X}}_{\star}^{(i)} + a_{ii} \Delta t \boldsymbol{\mathcal{R}}_{\boldsymbol{\mathcal{X}}}(\boldsymbol{\mathcal{X}}^{(i)}, \boldsymbol{\mathcal{Y}}_{\star}^{(i)}) \tag{4.28}$$

After computing in each intermediate step i the two vectors $\{\boldsymbol{\mathcal{X}}^{(i)}, \boldsymbol{\mathcal{Y}}^{(i)}\}$ the final value of the conservative variable $\boldsymbol{\mathcal{U}}$ at the time $t + \Delta t$ is given by

$$\boldsymbol{\mathcal{U}}^{n+1} = \boldsymbol{\mathcal{U}}^{n} + \Delta t \sum_{i=1}^{N_{IMEX}} \tilde{w}_i \boldsymbol{\mathcal{Q}}(\boldsymbol{\mathcal{U}}^{(i)}) + \Delta t \sum_{i=1}^{N_{IMEX}} w_i \boldsymbol{\mathcal{R}}_{\boldsymbol{\mathcal{X}}}(\boldsymbol{\mathcal{U}}^{(i)}), \tag{4.29}$$

where $\tilde{w}_i$ e w_i constant coefficients that along with the matrices a_{ij} and $\tilde{a}_{ij}$ completely define the specific numerical scheme.

There are a large number of possible IMEX schemes in the literature, which differ in the number of intermediate steps, and their spatial and temporal order of accuracy. In the case of ECHO we implemented three different IMEX schemes of SSP type (Strong Stability Preserving), classified with the notation SSPk(s, σ, p), where k indicates the order of the scheme SSP, s is the number of number of implicit steps, σ is the number of explicit steps and p is the order of the IMEX scheme. Usually the so-called Butcher tables (Butcher, 2016) are used to describe these schemes. They are defined as

$$\begin{array}{c|c} c_i & a_{ij} \\ \hline & (w_i)^T \end{array}, \qquad \begin{array}{c|c} \tilde{c}_i & \tilde{a}_{ij} \\ \hline & (\tilde{w}_i)^T \end{array}, \tag{4.30}$$

where the apex T indicate the transposed matrix and the coefficients c_i and $\tilde{c}_i$ are given by

$$c_i = \sum_{j=1}^{i} a_{ij}, \qquad \tilde{c}_i = \sum_{j=1}^{i-1} \tilde{a}_{ij}. \tag{4.31}$$

It can be demonstrated that these assumptions for the coefficients c_i and $\tilde{c}_i$ are necessary to ensure consistency of the scheme. Here are the schemes used in ECHO (Pareschi and Russo, 2005)

SSP2(2,2,2)

- implicit part

$$\begin{array}{c|cc} \mu & \mu & 0 \\ 1-\mu & 1-2\mu & \mu \\ \hline & 1/2 & 1/2 \end{array} \tag{4.32}$$

- explicit part

$$\begin{array}{c|cc} 0 & 0 & 0 \\ 1 & 1 & 0 \\ \hline & 1/2 & 1/2 \end{array} \tag{4.33}$$

SSP3(3,3,2)

- implicit part

$$\begin{array}{c|ccc} \mu & \mu & 0 & 0 \\ 1-\mu & 1-2\mu & \mu & 0 \\ 1/2 & 1/2-\mu & 0 & \mu \\ \hline & 1/6 & 1/6 & 2/3 \end{array} \tag{4.34}$$

- explicit part

$$\begin{array}{c|ccc} 0 & 0 & 0 & 0 \\ 1 & 1 & 0 & 0 \\ 1/2 & 1/4 & 1/4 & 0 \\ \hline & 1/6 & 1/6 & 2/3 \end{array} \tag{4.35}$$

SSP3(4,3,3)

- implicit part

$$\begin{array}{c|cccc} \alpha & \alpha & 0 & 0 & 0 \\ 0 & -\alpha & \alpha & 0 & 0 \\ 1 & 0 & 1-\alpha & \alpha & 0 \\ 1/2 & \delta & \zeta & 1/2-\delta-\zeta-\alpha & \alpha \\ \hline & 0 & 1/6 & 1/6 & 2/3 \end{array} \tag{4.36}$$

- explicit part

$$\begin{array}{c|cccc} 0 & 0 & 0 & 0 & 0 \\ 0 & 0 & 0 & 0 & 0 \\ 1 & 0 & 1 & 0 & 0 \\ 1/2 & 0 & 1/4 & 1/4 & 0 \\ \hline & 0 & 1/6 & 1/6 & 2/3 \end{array} \tag{4.37}$$

with

$$\begin{aligned}\mu &= 1 - 1/\sqrt{2}\\ \alpha &= 0.24169426078821\\ \delta &= 0.06042356519705\\ \zeta &= 0.12915286960590\end{aligned} \tag{4.38}$$

4.4 Evolution of the electric field in the IMEX schemes

In this section we show how IMEX schemes are implemented in ECHO and how the inversion of the relation (4.28) takes place, that is the most delicate aspect of the implicit step. From the inversion, an explicit expression for the electric field as a function of the velocity and known quantities can be derived as shown in Bucciantini and Del Zanna (2013)[1]. Here we choose to write it in the form

$$\begin{aligned}A_0 E^i = \tilde{\eta} E^i_\star + A_1 (E_{\star k}\tilde{u}^k)\tilde{u}^i + A_2 \epsilon^{ilm}\tilde{u}_l E_{\star m}\\ + A_3 B^i + A_4 (B_k \tilde{u}^k)\tilde{u}^i + A_5 \epsilon^{ilm}\tilde{u}_l B_m,\end{aligned} \tag{4.39}$$

where all coefficients are function of the Lorentz factor Γ (hence of the velocity) alone. See the Appendix B for a derivation of the above equation and for the expressions of the coefficients. It is convenient to work with the new spatial vector $\tilde{u}^i = \Gamma v^i$ (not coincident with the spatial component of the 4-velocity, unless $\beta^i \neq 0$ as in the Minkowski or Schwarzschild metrics), and $\tilde{u}_i = \Gamma v_i$, so that $\Gamma^2 = 1 + \tilde{u}^i \tilde{u}_i$. Above we have also defined $E^k_\star = \mathcal{X}^k_\star/\sqrt{\gamma}$, where $\mathcal{X}^k_\star$ are the electric field components, multiplied by $\sqrt{\gamma}$, computed thanks to the previous explicit substeps $j < i$ of the IMEX scheme, or at the previous timestep when $i = 1$. Moreover

$$\tilde{\eta} = \frac{\eta/\alpha}{a_{ii}\Delta t}, \tag{4.40}$$

with $j = i$ referring to the last, implicit substep. Notice that when $\eta = 0$ and $\xi = 0$ we recover the ideal GRMHD case.

The relation (4.39) allows one to calculate the electric field as a function of the velocity and of the magnetic field at the end of each substep. However, since the numerical scheme evolves in time the conserved variables $\boldsymbol{\mathcal{U}}$, primitives variables such as the velocity are not readily available and the implicit step must be nested in the non-linear iterative procedure which recovers primitive variables from the above set of conservative ones. We describe in the following paragraphs the two inversion algorithms used in ECHO in the non-ideal and ideal cases.

4.4.1 Recovery of primitive variables in non-ideal GRMHD

Starting with a straightforward guess for $\tilde{u}^{j\,(0)}$, that is the value corresponding to the set of conserved variables at the previous timestep, we proceed by adopting the following Newton-Raphson scheme:

- at any iteration (k), with a value $\tilde{u}^{j\,(k)}$ for the velocity, work out the electric field given by solving Eq. (4.39);

[1] Equation (35) in Bucciantini and Del Zanna (2013) contains an error in the purely resistive term, fortunately not in the corresponding part of the code. The correct version can also be found in Del Zanna et al. (2016)

- evaluate the function

$$f_i(\tilde{u}^j) = \tilde{w}\gamma_{ij}\tilde{u}^j + \epsilon_{ilm}E^l B^m - S_i, \tag{4.41}$$

where the modified enthalpy

$$\tilde{w} = w\Gamma = \frac{\Gamma[\mathcal{E} - \frac{1}{2}(B^2 + E^2)] - D/\hat{\gamma}_1}{\Gamma^2 - 1/\hat{\gamma}_1}, \tag{4.42}$$

obtained using $\omega = \rho h$ and placing $\hat{\gamma}_1 = \hat{\gamma}/(\hat{\gamma} - 1)$, is also given in terms of conservative variables and velocity components alone;

- evaluate the Jacobian

$$J_{ij} = \frac{\partial f_i}{\partial \tilde{u}^j} = \tilde{w}\gamma_{ij} + \tilde{u}_i\frac{\partial \tilde{w}}{\partial \tilde{u}^j} + \epsilon_{ilm}\frac{\partial E^l}{\partial \tilde{u}^j}B^m, \tag{4.43}$$

where

$$\frac{\partial \tilde{w}}{\partial \tilde{u}^j} = \frac{[\mathcal{E} - \frac{1}{2}(B^2 + E^2)]\tilde{u}_j/\Gamma - 2\tilde{w}\tilde{u}_j - \Gamma E_i(\partial E^i/\partial \tilde{u}^j)}{\Gamma^2 - 1/\hat{\gamma}_1}, \tag{4.44}$$

and where we have used $\partial\Gamma/\partial\tilde{u}^j = \tilde{u}_j/\Gamma$. The expression for the Jacobian of the electric field is more involved. Recalling that for any function $f(\Gamma)$ we have $\partial f/\partial u^j = \dot{f}\, u_j/\Gamma$, one can write

$$\begin{aligned} A_0\Gamma(\partial E^i/\partial \tilde{u}^j) = \\ -\dot{A}_0 E^i u_j + A_1\Gamma u^i E_{\star j} + \dot{A}_3 B^i u_j + A_4\Gamma u^i B_j \\ +(A_1\Gamma\gamma^i_j + \dot{A}_1 u^i u_j)(E_{\star k}u^k) + \epsilon^{ilm}(A_2\Gamma\gamma_{lj} + \dot{A}_2 u_l u_j)E_{\star m} \\ +(A_4\Gamma\gamma^i_j + \dot{A}_4 u^i u_j)(B_k u^k) + \epsilon^{ilm}(A_5\Gamma\gamma_{lj} + \dot{A}_5 u_l u_j)B_m \end{aligned} \tag{4.45}$$

and the expressions for the derivative of the coefficients are reported in the Appendix. Once the full Jacobian is known, we can finally update the velocity as

$$\tilde{u}^{j\,(k+1)} = \tilde{u}^{j\,(k)} - [J^{(k)}_{ij}]^{-1} f^{(k)}_i. \tag{4.46}$$

The iterations are repeated until the desired accuracy is reached, so that the primitive variables at every substep j can be computed for the IMEX scheme.

The above 3-D Newton-Raphson scheme based on the vanishing of momentum equations and using the $\tilde{u}_m$ variables, first introduced by Bucciantini and Del Zanna (2013), has proved to be the most robust one and has been recently adopted in other resistive relativistic MHD codes (Mignone et al., 2019; Ripperda et al., 2019). The novel feature introduced here is the analytical calculation of the Jacobian in Eq. (4.43), that appears to be more robust in critical situations and to require $10 - 20\%$ less iterations compared to the approach in Bucciantini and Del Zanna (2013), where the Jacobian was computed numerically, by evaluating the momenta twice for nearby values of $\tilde{u}^j$.

4.4.2 Recovery of primitive variables in ideal GRMHD

A significant improvement in the procedure for recovering primitive variables in ideal GRMHD was achieved by the adoption of the scheme proposed by Kastaun et al. (2021). The strengths of

this work concern the mathematically demonstrated ability to always find a unique solution with rigorously derived accuracy bounds. We show here the essential elements of the algorithm. Given the conserved variables $D, \mathcal{E}, S_i$, we define:

$$\overline{q} = \frac{\tau - \frac{1}{2}(B^2 + E^2)}{D}, \quad \overline{r}_i = \frac{S_i - \epsilon_{ijk} E^j B^k}{\sqrt{D}} \tag{4.47}$$

$$q = \frac{\tau}{D}, \quad r_i = \frac{S_i}{\sqrt{D}}, \quad b_i = \frac{B_i}{\sqrt{D}} \tag{4.48}$$

We also need to decompose the momentum r in parts parallel and normal to the magnetic field:

$$r^i_{\parallel} = \frac{(b^l r_l) b^i}{b^2}, \quad r^i_{\perp} = r^i - r^i_{\parallel} \tag{4.49}$$

We note that the decomposition is undefined for the case of zero magnetic field, so we put $r^i_{\parallel} = 0$ when $B^i = 0$. We now collect some definitions and fundamental relations in the construction of the master function. First, we define two quantities that play a key role:

$$\mu = \frac{1}{\Gamma h}, \quad x = \frac{1}{1 + \mu b^2} \tag{4.50}$$

with their ranges are limited to

$$0 < \mu \leq 1/h_0, \quad 0 < x \leq 1 \tag{4.51}$$

where h_0 is a positive lower bound for the enthalpy.
Then we remove the electromagnetic part of the conserved variables. From the ideal condition (3.53) we get:

$$E^2 = x^2 \mu^2 B^2 x^2_{\perp}, \tag{4.52}$$

$$\overline{r}^i = x r^i_{\perp} + r^i_{\parallel}. \tag{4.53}$$

This allows to compute the pure fluid part of the conserved variables. The corresponding quantities relevant for our purpose can be written as

$$\overline{r}^2 = x^2 r^2_{\perp} + r^2_{\parallel}. \tag{4.54}$$

$$\overline{q} = q - \frac{1}{2} b^2 - \frac{1}{2} x^2 \mu^2 b^2 r^2_{\perp}. \tag{4.55}$$

We can now express the velocity as

$$v = \mu \overline{r}. \tag{4.56}$$

This expression does however not guarantee that $v < 1$. To avoid excessive speed values, the velocity is required to be less than a threshold velocity v_0 which depends on $z_0 = \overline{r}/h_0$,

$$v_0 = \frac{z_0}{\sqrt{1 + z_0^2}} \tag{4.57}$$

After obtaining velocity and Lorentz factor, we compute rest mass density and specific internal energy using the expressions

$$\rho = D/\Gamma, \tag{4.58}$$

$$\epsilon = \Gamma(\overline{q} - \mu\overline{r}^2) + v^2\frac{\Gamma^2}{1+\Gamma}. \tag{4.59}$$

Pressure and enthalpy are evaluated from the EOS.
We can now define the master function $f(\mu)$ as

$$f(\mu) = \mu - \hat{\mu}(\mu), \tag{4.60}$$

where

$$\hat{\mu}(\mu) = \frac{1}{\nu(\mu) + \overline{r}^2(\mu)\mu}, \tag{4.61}$$

with

$$\nu(\mu) = \max(\nu_A(\mu), \nu_B(\mu)), \tag{4.62}$$

$$\nu_A(\mu) = \left[1 + \frac{p(\mu)}{\rho(\mu)(1+\epsilon(\mu))}\right]\frac{1+\epsilon(\mu)}{\Gamma(\mu)}, \tag{4.63}$$

$$\nu_B(\mu) = \left[1 + \frac{p(\mu)}{\rho(\mu)(1+\epsilon(\mu))}\right](1 + \overline{q}(\mu) - \mu\overline{r}^2(\mu)). \tag{4.64}$$

Kastaun et al. (2021) showed that the master function has always a unique root in the interval $(0, \mu_+]$, where μ_+ is the root of a smooth auxiliary function,

$$f_a(\mu) = \mu\sqrt{h_0^2 + \overline{r}^2(\mu)} - 1, \tag{4.65}$$

obtained by using a Newton-Raphson method. Instead, in order to find the root of the master function our implementation uses a Newton/bisection hybrid method. We can now retrieve the primitive variables.
The algorithm proved to be extremely efficient in MAD simulations where there is high magnetization in low-density regions and did not produce any errors during iterations in the primitive recovery phase.

Chapter 5

Numerical simulations: GRMHD Code Comparison Project

In the previous Chapters, we have seen that it is possible to write GRMHD equations in a conservative form that allows us to evolve them using techniques commonly adopted for the treatment of non-relativistic magnetized fluids. Over the last decades, several GRMHD codes have been developed, most using conservation form, and applied to a large variety of astrophysical scenarios.

The non-linear properties of the equations allow the formation of fundamental phenomena such as turbulence and shocks but necessarily complicate their treatment. In the scenario of accretion around black holes, there are two crucial phenomena in modeling. First, the turbulence seeded by the magnetorotational instability provides a mechanism to transport the angular momentum of the orbiting plasma and although the nature of the problem is inherently chaotic, it can be demonstrated that certain global properties of the solutions exhibit signs of convergence. A second challenge is the region of the funnel near the polar axis where low angular momentum material falls into the black hole. A magnetized near-vacuum region forms in this area, traditionally difficult to model.

An interesting question undoubtedly concerns the validity and robustness of the results obtained by the community of GRMHD codes, each of which is specialized with different numerical techniques in dealing with an increasing application of simulations. The GRMHD Code Comparison Project aims to compare GRMHD solutions and quantify the magnitude of systematic differences for the evolution of a thick accretion disk from a set of GRMHD codes. The work is divided into two parts: the first part is described in Porth and EHT-Collaboration (2019) and deals with the modeling of a SANE disk and involves nine codes (Athena++, BHAC, Cosmos++, ECHO, H-AMR, iharm3D, HARM-Noble, IllinoisGRMHD, and KORAL); the second, concerning the more interesting MAD regime, is currently in preparation (Olivares et al. in prep) and involves thirteen codes.

5.1 First part: SANE

The recent observations by EHT have confirmed the idea that M87* and SgrA* sources accrete as MAD disks. However, it was considered appropriate that the first part of the project concerned the study of the SANE regime which is well known in the literature, in order to standardize the results and prepare the codes to deal with the modeling of the MAD regime. We present here the results shown in Porth and EHT-Collaboration (2019) focusing in particular on ECHO simulations.

5.1.1 Setup

As the initial condition for our 3D GRMHD simulations, a Fishbone and Moncrief torus in hydrodynamic equilibrium threaded by a single weak ($\beta \gg 1$) poloidal magnetic field loop is considered. The spacetime is a Kerr black hole with dimensionless spin parameter $a = 0.9375$. The inner radius of the torus is set to $r_{\rm in} = 6M$ and the density maximum is located at $r_{\rm max} = 12M$. An ideal gas equation of state is adopted with an adiabatic index of $\hat{\gamma} = 4/3$ and a weak single magnetic field loop defined by the vector potential

$$A_\phi \propto \max(\rho/\rho_{\rm max} - 0.2, 0), \tag{5.1}$$

is added to the stationary solution. The field strength is set such that $2p_{\rm max}/B^2_{\rm max} = 100$, where the global maxima of pressure $p_{\rm max}$ and magnetic field strength $B^2_{\rm max}$ do not necessarily coincide. With this choice of initial magnetic field geometry and strength, the simulations are anticipated to progress according to the SANE regime, although this can only be verified a posteriori.

In order to excite the MRI inside the torus, the thermal pressure is perturbed by white noise of amplitude 4%. More precisely,

$$p^* = p(1 + X_p), \tag{5.2}$$

and X_p is a uniformly distributed random variable between -0.02 and 0.02.

To avoid density and pressures dropping to zero in the funnel region, floor models are customarily employed in fluid codes. Each code had the freedom to adopt the strategies it deemed most appropriate. In ECHO we adopted the following floor model:

$$\rho_{\rm fl} = 10^{-5} r^{-3/2}, \quad p_{\rm fl} = 1/3 \cdot 10^{-7} r^{-5/2}. \tag{5.3}$$

Thus, for all cells that satisfy $\rho \leq \rho_{\rm fl}$ and/or $p \leq p_{\rm fl}$ we set $\rho = \rho_{\rm fl}$ and/or $p = p_{\rm fl}$. The floor defined by the relations (5.3) also defines the initial static and non-magnetized atmosphere. In addition, to avoid high Lorentz factor in the funnel, we enforce that it stay within reasonable bounds, that is, $\Gamma_{\rm fl} = 50$. This delimits the momentum and energy of faulty cells and thus aids in keeping the error localized.

In terms of coordinates and grids, ample freedom is left to the various codes for two reasons: first, in this way, the results inform us about the setups used with a particular code and can allow us to make comparisons between the various methods; the second reason is purely utilitarian, as settling for a common grid setup would incur extra work and likely introduce unnecessary bugs. The domain of interest is:

$$r \in [r_{\rm h}, 50], \quad \theta \in [0, \pi], \quad \phi \in [0, 2\pi], \tag{5.4}$$

where $r_{\rm h}$ is the radius at the event horizon defined by (3.87), and three rounds of resolutions are suggested in order to judge the convergence between codes. These are low-res: 96^3, mid-res: 128^3, and high-res: 192^3, where the resolution corresponds to the domain of interest mentioned above.

Our simulations carried out with ECHO in Kerr–Schild coordinates adopt a numerical grid logarithmically stretched in radius and uniform in both θ and ϕ, excluding from the polar angle domain the regions close to the rotation axis to avoid excessively small time steps. At the radial and

polar boundaries, we impose outflow boundary conditions, i.e., we copy the value of the primitive variables and set the velocity normal to the boundary to zero whenever it has a positive (negative) value at the inner (outer) boundary.

The time integration performed in ECHO uses the third-order accurate IMEX strong-stability-preserving scheme, which in the case of ideal GRMHD reduces effectively to a third-order Runge–Kutta. The upwind fluxes are computed with the HLL Riemann solver with PPM reconstruction, using the UCT scheme for the treatment of the magnetic field. For the primitive variable recovery we first use the three dimensional scheme described in paragraph 4.4.1, and in the case of failure we attempt to retrieve the primitives using the advected entropy instead of the total energy. In case of persisting failures, we finally reset the value of density and pressure to the atmospheric floor values and set the Eulerian velocity to zero, without modifying the magnetic field.

5.1.2 Results

A consistent set of diagnostics focusing both on horizon scale quantities and on the global evolution of the accretion flow is performed with all codes. We describe the quantifications and show the results.

Horizon-penetrating fluxes

The relevant quantities: mass, magnetic, angular momentum, and (reduced) energy fluxes are defined as follows:

$$\dot{M} = \int_0^{2\pi} \int_0^{\pi} \rho u^r (-g)^{1/2} d\theta d\phi, \tag{5.5}$$

$$\phi_{\rm BH} = \frac{1}{2} \int_0^{2\pi} \int_0^{\pi} |F^{*rt}| (-g)^{1/2} d\theta d\phi, \tag{5.6}$$

$$\dot{L} = \int_0^{2\pi} \int_0^{\pi} T^r_{\phi} (-g)^{1/2} d\theta d\phi, \tag{5.7}$$

$$\dot{E} = \int_0^{2\pi} \int_0^{\pi} (-T^r_t) (-g)^{1/2} d\theta d\phi, \tag{5.8}$$

where all quantities are evaluated at the outer horizon $r_{\rm h}$ with a cadence of $1M$. In practice, these quantities are nondimensionalized with the accretion rate, yielding, for example, the normalized magnetic flux that we have defined in paragraph 2.2.2, $\phi = \phi_{\rm BH}/\sqrt{\dot{M}}$, also known as the "MAD parameter". As we have already said, there is a critical value $\phi_{\rm max}$ for the amount of magnetic field that the black hole can absorb depending on the scale height and spin of the black hole. For $a = 0.9375$ and torus scale height $H/R \sim 0.3$ the parameter has the critical value $\phi_{\rm max} \sim 15$.

Time series data of horizon-penetrating fluxes is presented in Figures 5.1-5.3 for low, medium, and high resolutions respectively in which the results of our simulations performed with ECHO are represented by light blue lines. Because the mass accretion governs the behavior of these fluxes, the data have been appropriately normalized by the accretion rate. All codes capture accurately the linear phase of the MRI leading to an onset of accretion to the black hole at $t \simeq 300M$. While there is still a good correspondence of $\dot{M}$ for early times $< 1000M$, the chaotic nature of the problem fully asserts itself after $2000M$. At low resolution, there exist order of magnitude variations in the

data, most notably for the normalized horizon-penetrating magnetic fluxes and the energy fluxes. Concerning our results, we can see how the magnetic flux and the angular momentum flux are respectively lower and higher at the lower resolution compared to the high-resolution run. As indicated by $\phi \sim 0.5 - 6 < \phi_{\rm max}$, all simulations are in the SANE regime of radiatively inefficient black hole accretion.

As a measure for the convergence and variance between the codes, the peak fluxes as well as the average values far in the nonlinear regime are quantified in the table of Figure 5.4. Both average and peak values show a tendency to converge to values common to all codes as resolution increases; the agreement with very high resolution runs is also good. It is worthwhile to point out the good agreement in angular momentum and energy fluxes at high resolution for the codes employing spherical grids (Figure 5.3), where the highest average values differ from the lowest ones by 12% and 40%. Because meshes with various amounts of compression in the midplane were employed by the different groups, a comparison purely based on the number of grid cells is, however, hardly fair even in the spherical cases. Hence, Figure 5.5 shows the data of Table in Figure 5.4 against the proper grid spacing at the location of the initial density maximum, $\Delta\theta_p$: upon increased resolution, the spread in the quantities decreases and one can make out a critical resolution $\Delta\theta_p = 0.0125-0.25$, below which accretion rates and horizon-penetrating fluxes tend to converge to the same answer. The accreted angular momentum flux $\dot{L}/\dot{M}$ is very well captured at all resolutions with minimal spread.

Disk-averaged quantities

We compare averages of the basic flow variables $q \in \{\rho, p, u^\phi, \sqrt{b_\mu b^\mu}, \beta^{-1}\}$. Hence, for a quantity $q(r, \theta, \phi, t)$, the shell average is defined as

$$\langle q \rangle (r,t) = \frac{\int_0^{2\pi} \int_{\theta_{\rm min}}^{\theta_{\rm max}} q(r,\theta,\phi,t)(-g)^{1/2} {\rm d}\theta {\rm d}\phi}{\int_{\theta_{\rm min}}^{\theta_{\rm max}} (-g)^{1/2} {\rm d}\theta {\rm d}\phi}, \tag{5.9}$$

which is then further averaged over the time interval $t_{\rm KS} \in [5000, 10000]M$ to yield $\langle q \rangle$(r). The limits $\theta_{\rm min} = \pi/3$ and $\theta_{\rm max} = 2\pi/3$ ensure that only material from the disk is taken into account in the averaging.

The disk-averaged profiles of the relevant quantities q are presented in Figures 5.6-5.8. At the late times under consideration, viscous spreading and accretion have significantly transformed the initial distributions; for example, the peak densities are now an order of magnitude below the initial state. There is a fair spread in some quantities between codes, most notably in the profiles of density and (inverse) plasma beta, while all codes capture very well the rotation law of the disk, which can be approximated by a power law with slope $r^{-1.75}$, somewhat steeper than the Keplerian case. Interestingly, the profiles of the magnetic field are also captured quite accurately and tend to agree very well with a very high-resolution reference case computed with the H-AMR code (dashed red curves). The approximate scaling of the disk magnetic field as r^{-1} indicates a dominance of the toroidal field component (e.g., Hirose et al. (2004)). Taking the inverse plasma β (bottom-right panel) as a proxy for the Maxwell stresses, the decrease in torus density is consistent with an increase in the turbulent transport of angular momentum, due to the increase in magnetization. Turning to the high-resolution data, the spread in all quantities becomes dramatically reduced. Starting at a

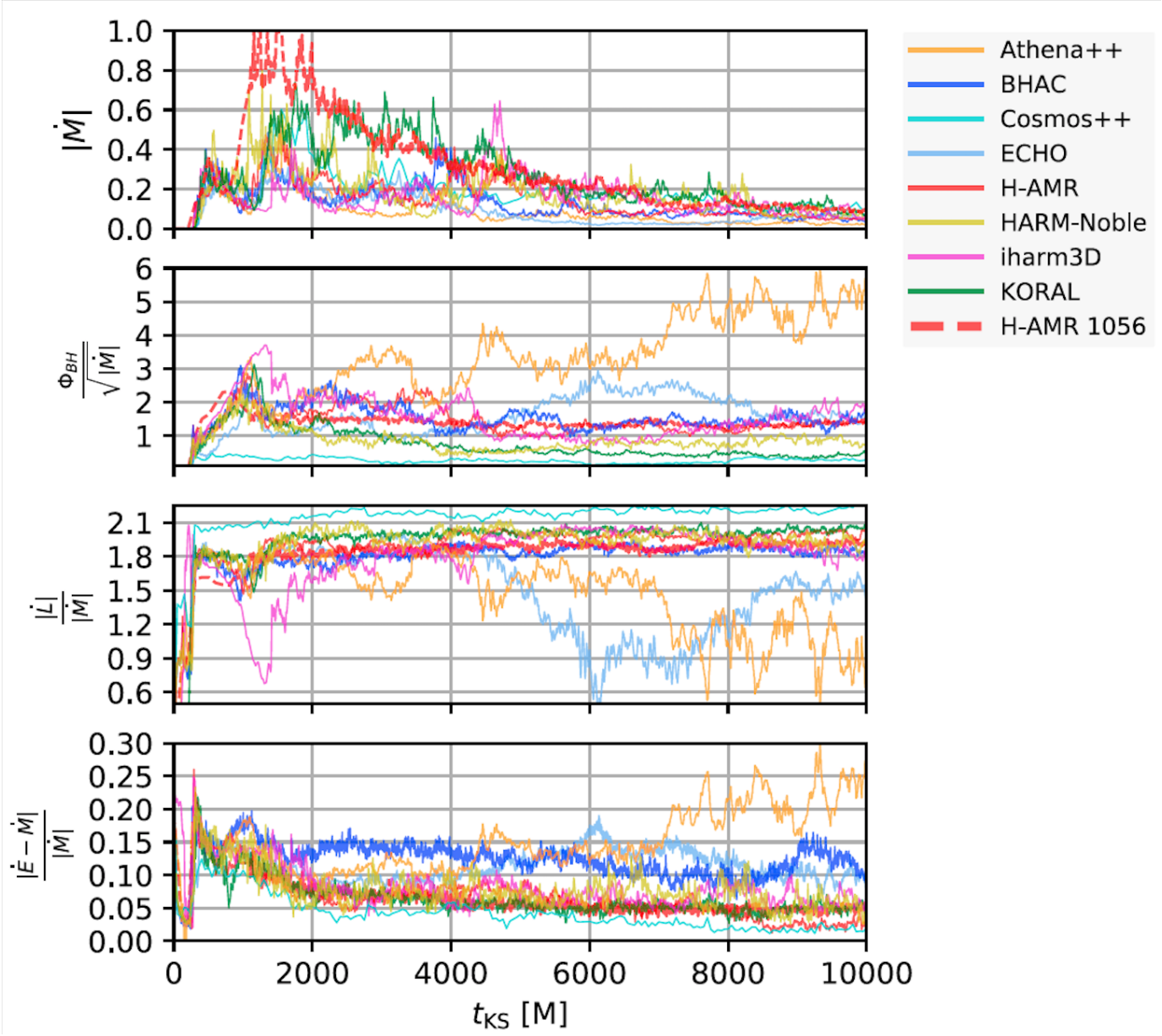

Figure 5.1: Time series at the resolution of 96^3 in the domain of interest for all codes. From top to bottom, the panels show the mass accretion rate, horizon-penetrating magnetic flux, accretion of angular momentum and energy. The data in panels 2–4 have been nondimensionalized with the accretion rate M (Figure adapted from Porth and EHT-Collaboration (2019)).

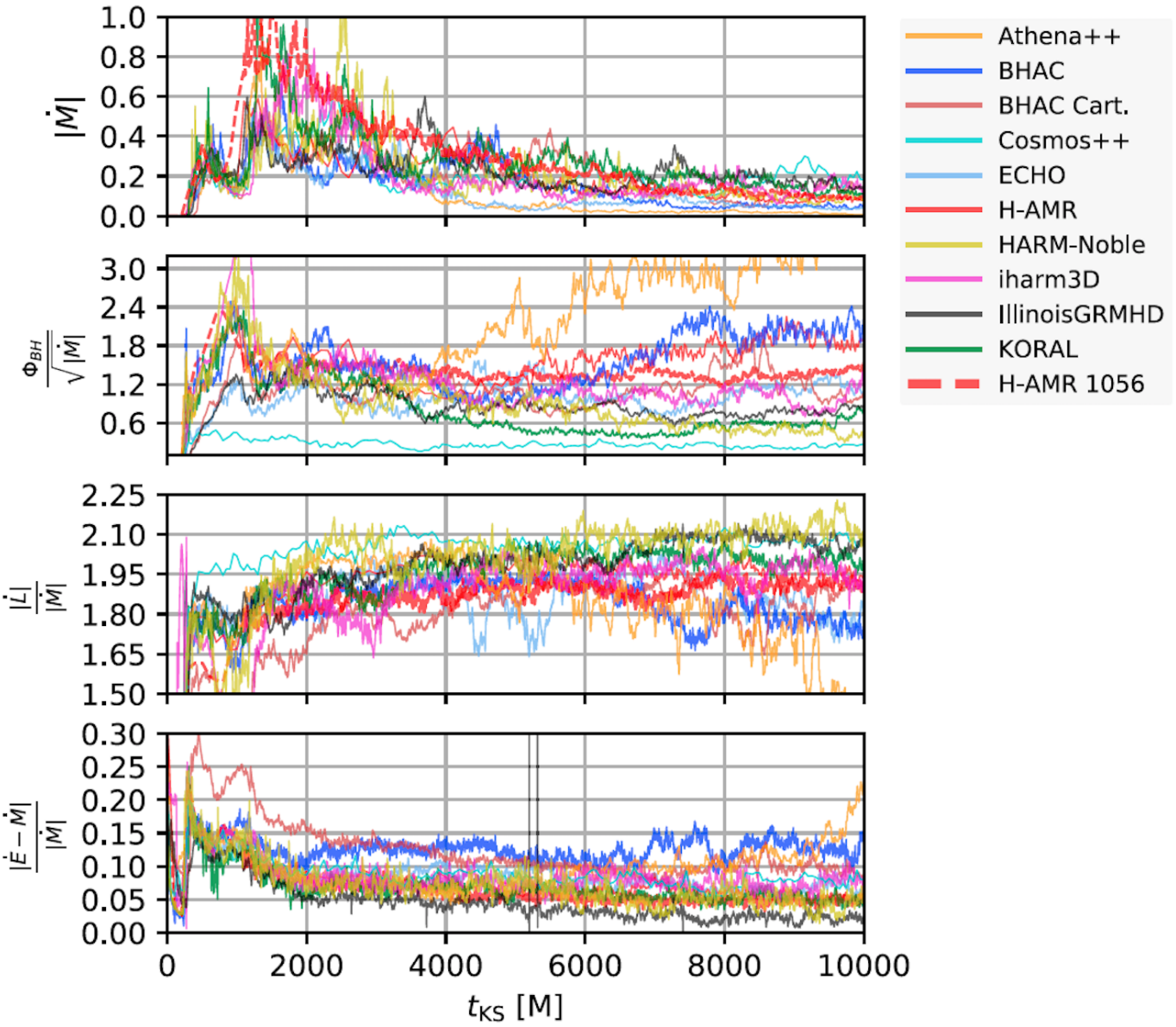

Figure 5.2: As Figure 5.1 for the 128^3 data. Cartesian realizations next to the medium-resolution cases are added here. It should be kept in mind though that the resolution in the Cartesian cases is typically much worse near the horizon but better at larger radii, which makes it hard to directly compare the simulations. Qualitatively, there is very good agreement of the Cartesian runs with the spherical data in all quantities except for the energy fluxes where BHAC Cart. is systematically higher and IllinoisGRMHD is slightly lower than all spherical codes (Figure adapted from Porth and EHT-Collaboration (2019)).

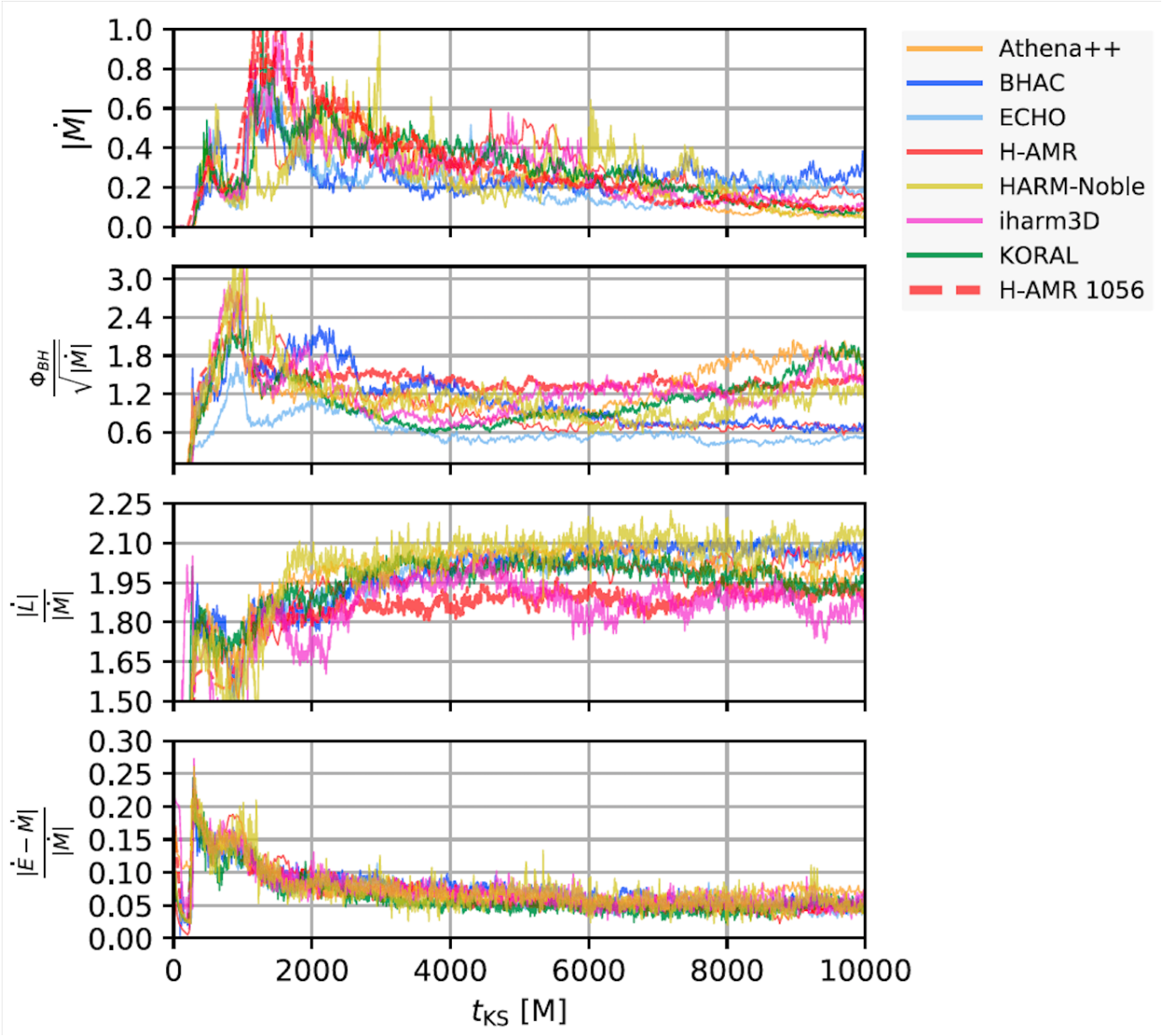

Figure 5.3: As Figure 5.1 for the 192^3 data.

Quantifications—Time Series Data

N_θ	Code	$\dot{M}_{\rm Peak}$	$\langle \dot{M} \rangle$	$\frac{\Phi_{\rm BH}}{\sqrt{\dot{M}}}\Big\vert_{\rm Peak}$	$\langle \Phi_{\rm BH}/\sqrt{\dot{M}} \rangle$	$\dot{L}/\dot{M}\vert_{\rm Peak}$	$\langle \dot{L}/\dot{M} \rangle$	$\frac{\dot{E}-\dot{M}}{\dot{M}}\Big\vert_{\rm Peak}$	$\langle \frac{\dot{E}-\dot{M}}{\dot{M}} \rangle$
96	Athena++	0.461	0.041 ± 0.019	5.951	4.164 ± 0.869	1.95	1.276 ± 0.326	0.332	0.18 ± 0.044
	BHAC	0.507	0.074 ± 0.021	3.099	1.426 ± 0.16	1.964	1.865 ± 0.033	0.33	0.112 ± 0.017
	Cosmos++	0.602	0.142 ± 0.036	0.481	0.239 ± 0.065	2.268	2.207 ± 0.025	0.232	0.025 ± 0.009
	ECHO	0.331	0.04 ± 0.018	2.949	2.021 ± 0.377	2.005	1.211 ± 0.289	0.33	0.124 ± 0.022
	H-AMR	0.536	0.091 ± 0.048	2.908	1.249 ± 0.131	2.066	1.985 ± 0.028	0.336	0.046 ± 0.018
	HARM-Noble	0.797	0.125 ± 0.05	2.236	0.786 ± 0.119	2.206	1.964 ± 0.051	0.327	0.067 ± 0.017
	iharm3D	0.645	0.136 ± 0.06	3.705	1.239 ± 0.346	2.083	1.958 ± 0.087	0.331	0.067 ± 0.011
	KORAL	0.738	0.157 ± 0.051	3.13	0.458 ± 0.072	2.1	2.027 ± 0.026	0.328	0.05 ± 0.007
	max/min	2.406	3.903	12.374	17.408	1.163	1.823	1.448	7.096
128	Athena++	0.847	0.023 ± 0.012	5.385	2.995 ± 0.694	2.082	1.743 ± 0.208	0.332	0.108 ± 0.029
	BHAC	0.66	0.078 ± 0.046	2.492	1.74 ± 0.407	1.974	1.829 ± 0.074	0.331	0.123 ± 0.015
	BHAC Cart.	0.57	0.163 ± 0.091	2.137	1.123 ± 0.277	1.947	1.864 ± 0.061	0.331	0.097 ± 0.009
	Cosmos++	0.642	0.177 ± 0.045	0.484	0.245 ± 0.032	2.133	2.073 ± 0.019	0.232	0.078 ± 0.01
	ECHO	0.507	0.059 ± 0.021	1.575	1.056 ± 0.182	2.028	1.876 ± 0.083	0.331	0.073 ± 0.012
	H-AMR	0.588	0.117 ± 0.039	2.378	1.729 ± 0.204	2.04	1.961 ± 0.031	0.336	0.061 ± 0.008
	HARM-Noble	1.28	0.128 ± 0.051	3.23	0.61 ± 0.179	2.259	2.093 ± 0.054	0.328	0.052 ± 0.017
	iharm3D	0.841	0.132 ± 0.035	3.464	1.019 ± 0.135	2.089	1.964 ± 0.037	0.325	0.076 ± 0.01
	IllinoisGRMHD	0.6	0.177 ± 0.041	1.477	0.779 ± 0.08	2.141	2.053 ± 0.044	0.361	0.026 ± 0.009
	KORAL	1.221	0.199 ± 0.062	2.351	0.517 ± 0.097	2.084	2.017 ± 0.025	0.332	0.056 ± 0.008
	max/min	2.525	8.604	11.126	12.24	1.16	1.201	1.552	4.631
192	Athena++	0.875	0.134 ± 0.071	2.739	1.405 ± 0.39	2.109	2.025 ± 0.047	0.332	0.065 ± 0.008
	BHAC	0.825	0.238 ± 0.042	2.754	0.773 ± 0.107	2.121	2.072 ± 0.021	0.331	0.059 ± 0.009
	ECHO	0.843	0.167 ± 0.047	1.698	0.506 ± 0.057	2.139	2.047 ± 0.033	0.332	0.05 ± 0.008
	H-AMR	0.671	0.237 ± 0.104	2.798	0.691 ± 0.049	2.086	2.019 ± 0.026	0.265	0.048 ± 0.009
	HARM-Noble	0.994	0.201 ± 0.116	3.593	0.972 ± 0.216	2.224	2.097 ± 0.044	0.33	0.057 ± 0.013
	iharm3D	1.106	0.18 ± 0.091	3.161	1.292 ± 0.19	2.066	1.871 ± 0.046	0.32	0.057 ± 0.01
	KORAL	1.01	0.183 ± 0.081	2.256	1.217 ± 0.338	2.082	1.987 ± 0.041	0.331	0.046 ± 0.007
	max/min	1.649	1.772	2.116	2.777	1.077	1.121	1.25	1.405
256*	BHAC	0.697	0.203 ± 0.065	2.552	1.021 ± 0.091	2.097	2.034 ± 0.019	0.332	0.064 ± 0.007
384	BHAC	0.91	0.221 ± 0.067	3.424	0.946 ± 0.128	2.12	2.043 ± 0.021	0.331	0.049 ± 0.006
1056	H-AMR	1.143	0.152 ± 0.056	2.324	1.341 ± 0.068	1.975	1.901 ± 0.028	0.336	0.05 ± 0.006

Figure 5.4: Quantities in angular brackets $\langle \cdot \rangle$ denote time averages in the interval $t \in [5000, 10000]M$ with error given by the standard deviation. For further convergence testing, another two BHAC runs (256* using $256 \times 256 \times 128$ cells and $384 \times 384 \times 384$ cells) and an H-AMR run with $1608 \times 1056 \times 1024$ cells are listed here (Figure adapted from Porth and EHT-Collaboration (2019)).

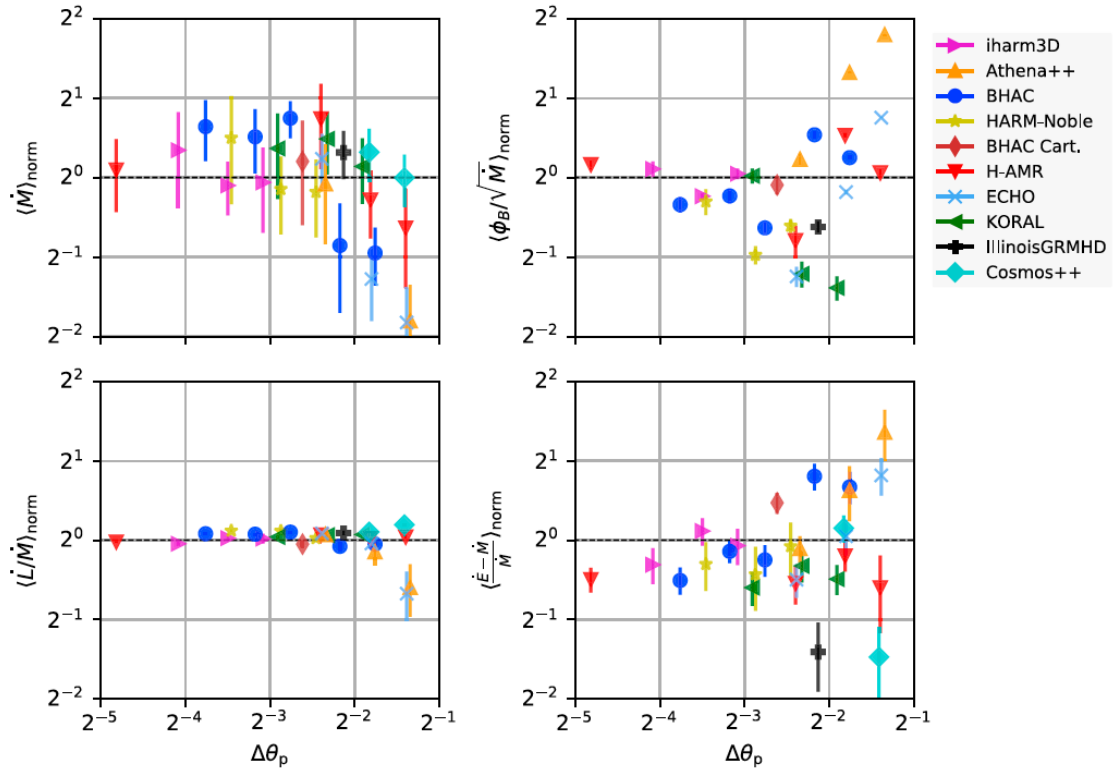

Figure 5.5: Resolution dependence of the averaged quantities for all runs of Table of Figure 5.4. The figure has been normalized to the mean of the distribution, allowing the overall spread to be judged, and errors mark the standard deviation over the averaging interval.

few gravitational radii, the magnetization of the disk is nearly constant, with values in the range $0.04 - 0.1$. Here, the Cartesian runs are the exception (BHAC Cart. and IllinoisGRMHD in Figure 5.7); their magnetization decreases within $r \sim 10M$ and reaches a minimum of ~ 0.01. We suppose that this stems from increased numerical dissipation, due to the comparatively low resolution in the inner regions of the Cartesian grids.

We compute also the density scale height averaged over time:

$$\langle H/R \rangle(r,t) = \frac{\int_0^{2\pi} \int_{\theta_{\rm min}}^{\theta_{\rm max}} |\pi/2 - \theta_{\rm KS}| \rho(t,r,\theta,\phi)(-g)^{1/2} {\rm d}\theta {\rm d}\phi}{\int_{\theta_{\rm min}}^{\theta_{\rm max}} \rho(t,r,\theta,\phi)(-g)^{1/2} {\rm d}\theta {\rm d}\phi}. \tag{5.10}$$

A scale height of $\langle H/R \rangle = 0.25 - 0.3$ between $r_{\rm KS} \in [10, 50]M$ is consistently recovered with all codes. As shown in Figure 5.9 The largest departures from the general trend are seen in the inner regions for the Cartesian runs.

Emission proxy

We also integrate the pseudo-emissivity for thermal synchrotron radiation following an appropriate nonlinear combination of flow variables:

$$\mathcal{L}(t) = \int_0^{2\pi} \int_{\theta_{\rm min}}^{\theta_{\rm max}} \int_{r_{\rm h}}^{r_{\rm max}} j(B,p,\rho)(-g)^{1/2} {\rm d}\phi {\rm d}\theta {\rm d}r, \tag{5.11}$$

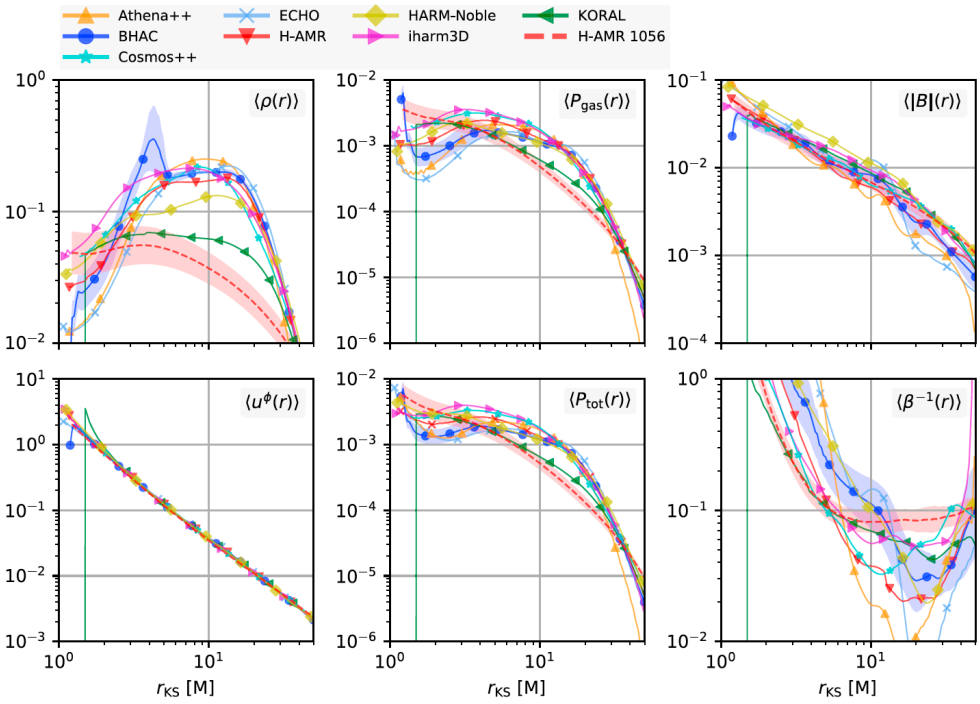

Figure 5.6: Disk-averaged quantities at the resolution of 96^3 in the domain of interest for all codes. Data have been averaged over the θ and ϕ angles as well as over the time interval $t \in [5000, 10000]M$. For reference, the H-AMR $N_\theta = 1056$ solution was added.

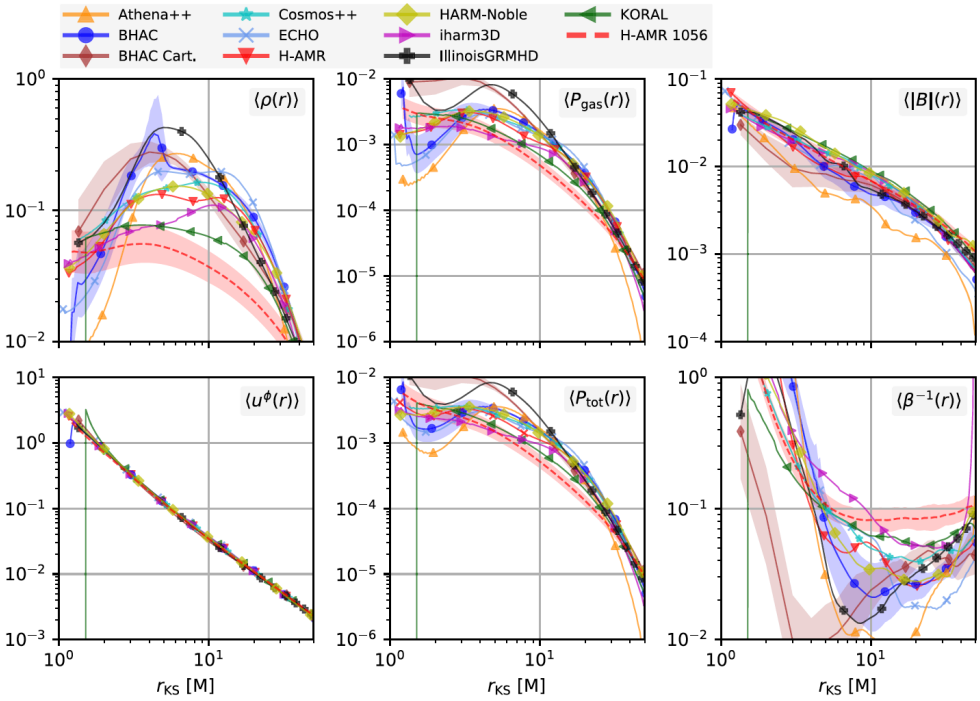

Figure 5.7: As Figure 5.6 for the 128^3 data.

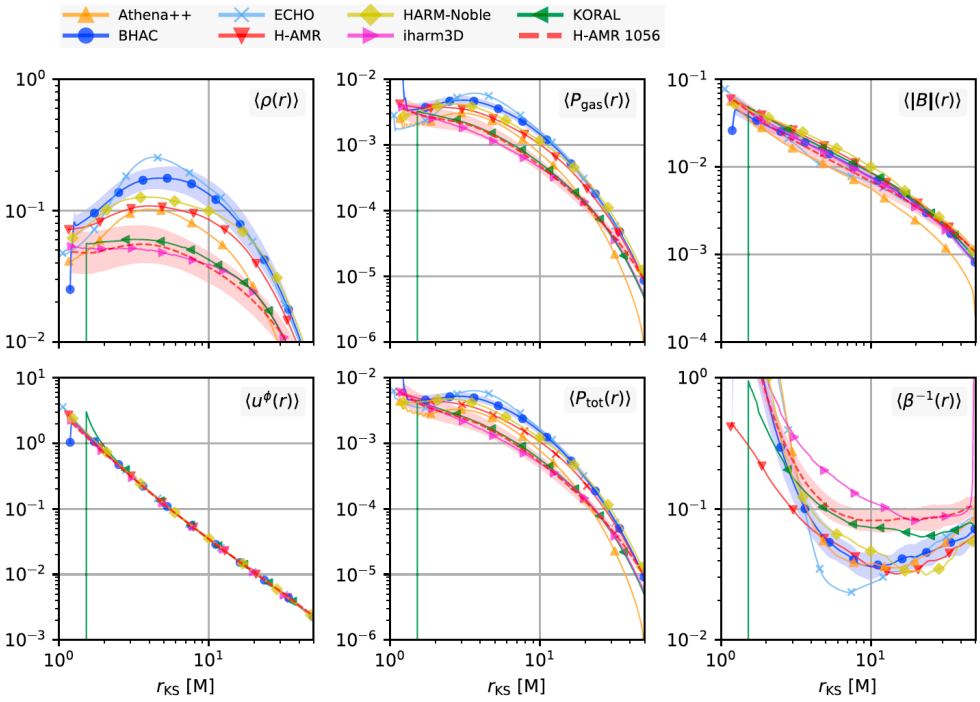

Figure 5.8: As Figure 5.6 for the 192^3 data.

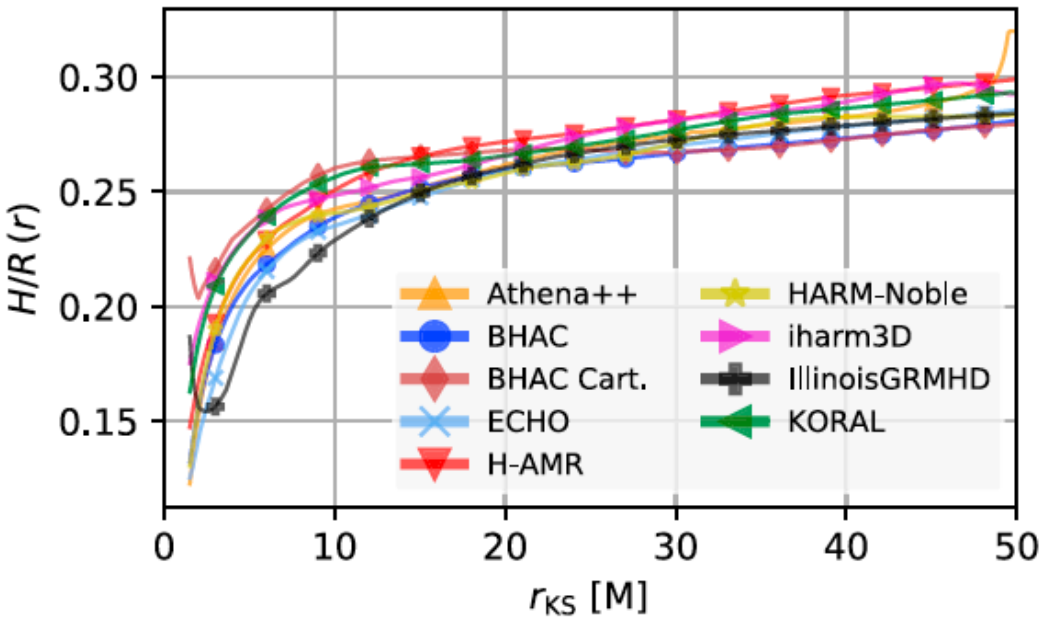

Figure 5.9: Scale height profiles of the high-resolution models ($N_\theta = 192$) according to Eq. (5.10).

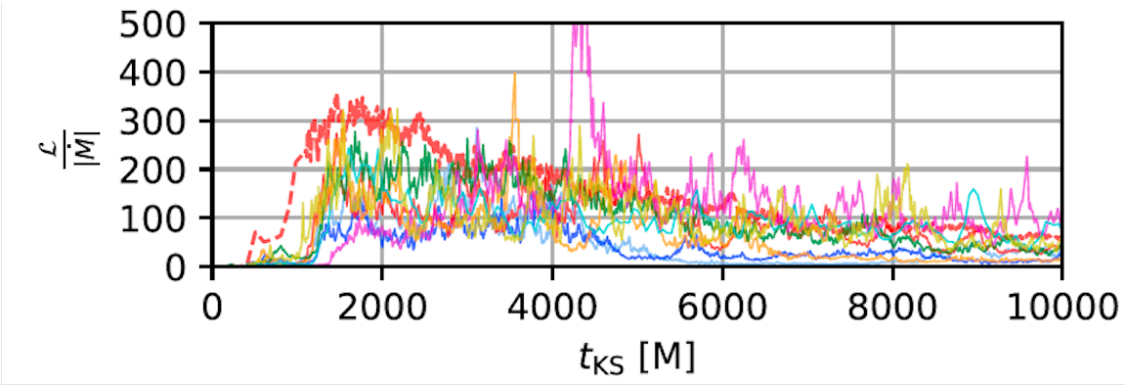

Figure 5.10: Time series at the resolution of 96^3 of the pseudo-luminosity for all codes (Figure adapted from Porth and EHT-Collaboration (2019)).

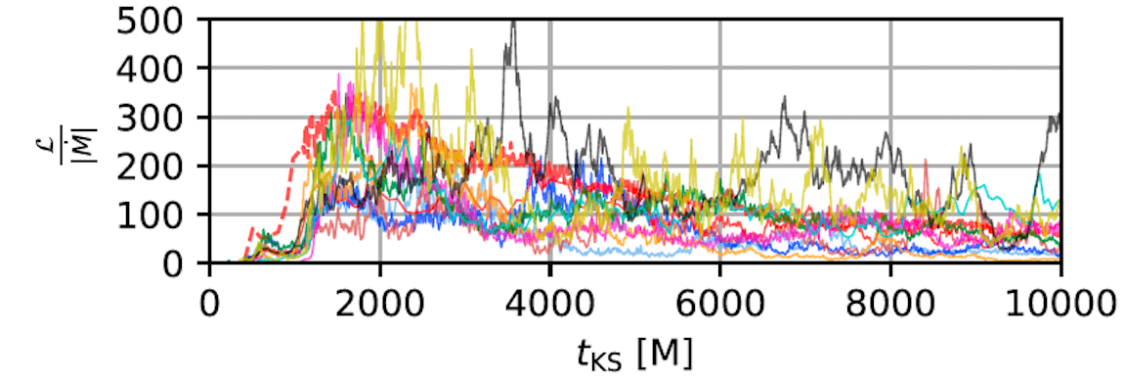

Figure 5.11: As Figure 5.10 for the 128^3 data (Figure adapted from Porth and EHT-Collaboration (2019)).

where again $\theta_{\rm min} = \pi/3$, $\theta_{\rm max} = 2\pi/3$ and $r_{\rm max} = 50M$. The emissivity j_ν is defined following the description of the paragraph 2.1.2. In the dimensionless units adopted here, Eq. (2.31) integrated in the frequencies can be written as

$$j = \rho^3 p^{-2} \exp\left[-C\left(\frac{\rho^2}{Bp^2}\right)^{1/3}\right]. \tag{5.12}$$

The constant C is chosen such that the radiation is cut off after a few gravitational radii, resembling the expected millimeter emission from the Galactic Center, that is, $C = 0.2$ in geometrized units. This emission proxy is optimized for the science case of the EHT where near optically thin synchrotron emission is expected. Figures 5.10-5.12 show the time series: also in this case the spread is smaller at high resolution.

t, ϕ averages

Finally, we compare temporally and azimuthally averaged data for a more global impression of the disk and jet system:

$$\langle q \rangle(r,\theta) = \frac{\int_{t_{\rm beg}}^{t_{\rm end}} \int_0^{2\pi} q(r,\theta,\phi,t)(-g)^{1/2} {\rm d}\phi {\rm d}t}{2\pi(t_{\rm end} - t_{\rm end})} \tag{5.13}$$

for density, inverse beta-plasma and magnetization, $q \in \{\rho, \beta^{-1}, \sigma\}$, in the time range delimited by $t_{\rm min} = 5000M$ and $t_{\rm max} = 10000M$.

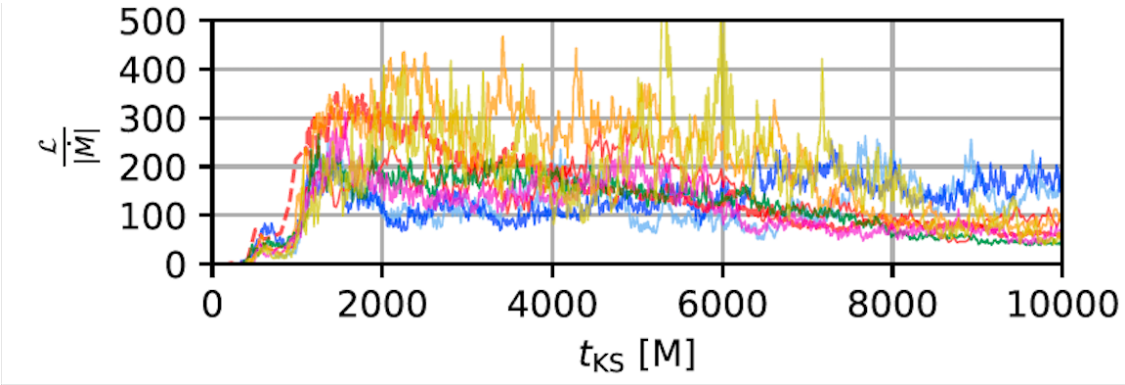

Figure 5.12: As Figure 5.10 for the 192^3 data (Figure adapted from Porth and EHT-Collaboration (2019)).

To gain an overall impression of the solutions in the quasi stationary state, we compute averages over the $t-$ and $\phi-$coordinates in Figure 5.13. The different panels depict the rest-frame density, inverse plasma β, and the magnetization obtained for ECHO at the highest resolution available. Though qualitatively very similar between codes, the maps (in particular the maps of β^{-1}) exhibit spreads in the funnel region: depending on the pole treatment, the inverse plasma β decreases toward the axis for some codes including ECHO, while others see an increase of β^{-1} or a near-constant behavior.

It is interesting to examine the jet–disk boundary defined as $\sigma = 1$ in more detail. Figure 5.14 illustrates that as the resolution is increased, the contour is more faithfully recovered across codes: whereas some low-resolution runs do not capture the highly magnetized funnel, at high resolution, all runs show a clearly defined jet–disk boundary. Despite the large variances in floor treatment, at $N_\theta = 192$ cells, the difference is reduced to five degrees and the polar angle of the disk–jet boundary ranges between 10° and 15° at $r = 50M$. For illustrative purposes, we also overplot flux-functions of the approximate force-free solutions discussed in Tchekhovskoy et al. (2008) and Nakamura et al. (2018):

$$\Psi(r, \theta) = \left(\frac{r}{r_h}\right)^{\kappa} (1 - \cos\theta). \tag{5.14}$$

In the recent 2D simulations of Nakamura et al. (2018), the jet boundary given by $\sigma = 1$ was accurately described by the choice $\kappa = 0.75$ for a wide range of initial conditions, black hole spins, and horizon-penetrating flux: $\phi \in [5, 10]$. This results in a field line shape $z \propto R^{1.6}$, which matches well the shape derived from VLBI observations on the scale of $10 - 10^5 M$ (Asada and Nakamura, 2012; Hada et al., 2013). In our ECHO models, the line $\kappa = 0.75$ is recovered at low resolution, and the more collimated genuinely paraboloid shape $\kappa = 1$ ($z \propto R^2$) resembling the solution of Blandford and Znajek (1977) seems to be a better match for the funnel-wall shape at higher resolutions for all codes. We suspect that the narrower jet profile compared to Nakamura et al. (2018) is due to the lower $\phi \simeq 2 - 3$ of our benchmark configuration (at high resolution). We believe that in ECHO the polar cutout coupled with low resolution can negatively affect a correct modeling of the funnel magnetization.

Comparing the torus density in more detail, in Figure 5.15 we illustrate contours of $\langle\rho\rangle/\langle\rho\rangle_{\max}$ for the runs with $N_\theta = 192$ cells. Normalized in this way, the agreement in torus extent generally improves as it compensates for the spread in peak densities (see Figure 5.8). Nonetheless, there remains a large variance in the given contours.

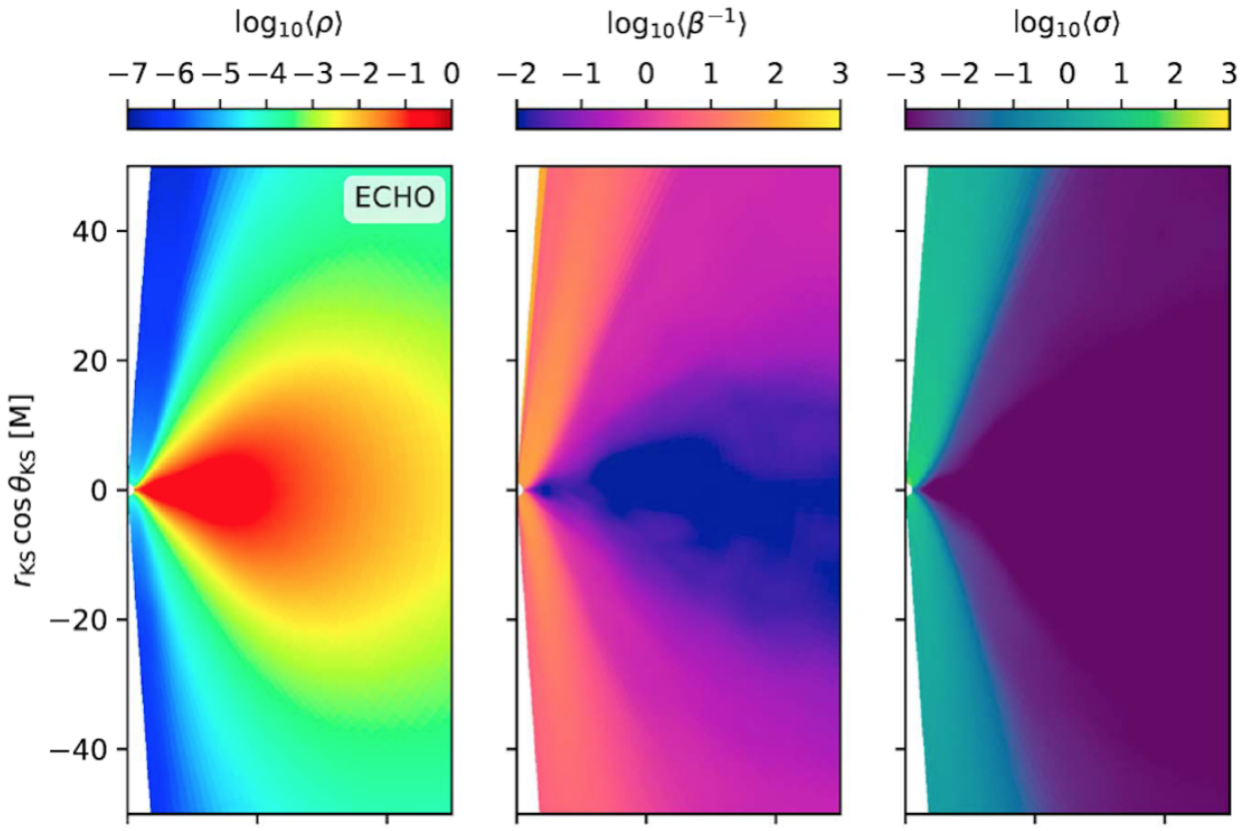

Figure 5.13: $t-$ and $\phi-$averaged data. We show averages of the rest-frame density, inverse plasma β, and the magnetization σ (Figure adapted from Porth and EHT-Collaboration (2019)).

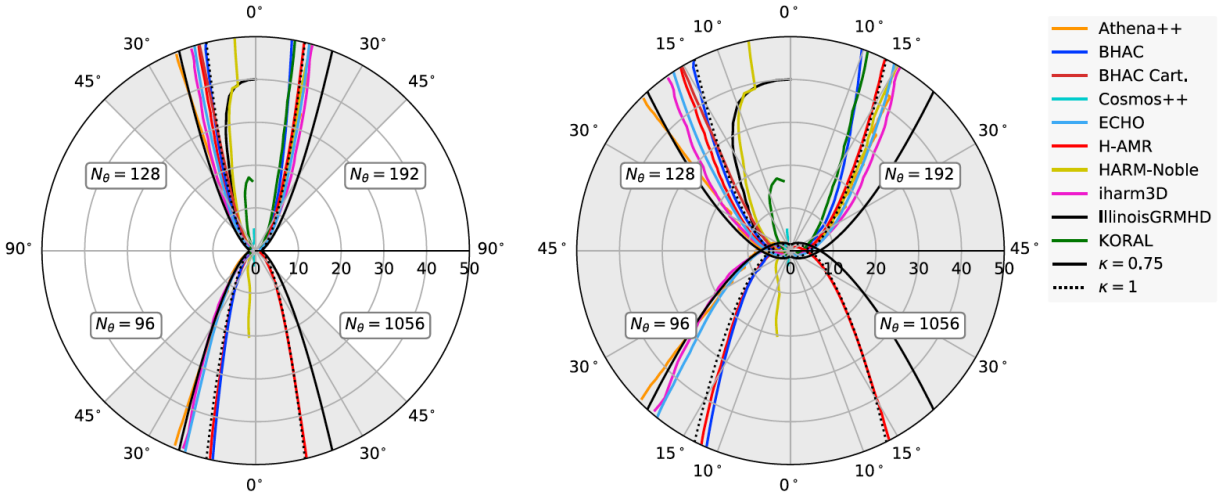

Figure 5.14: Contours of the jet–disk boundary $\sigma = 1$ for increasing resolution (left) and a zoom into the region $\theta \in [0°, 45°]$ (right). Only in the high-resolution case is the jet recovered with all codes. The paraboloid curves according to Eq. (5.14), corresponding to $z \propto R^2$ ($\kappa = 1$, thin dotted black) and $z \propto R^{1.6}$ ($\kappa = 0.75$, thin solid black) are also showed.

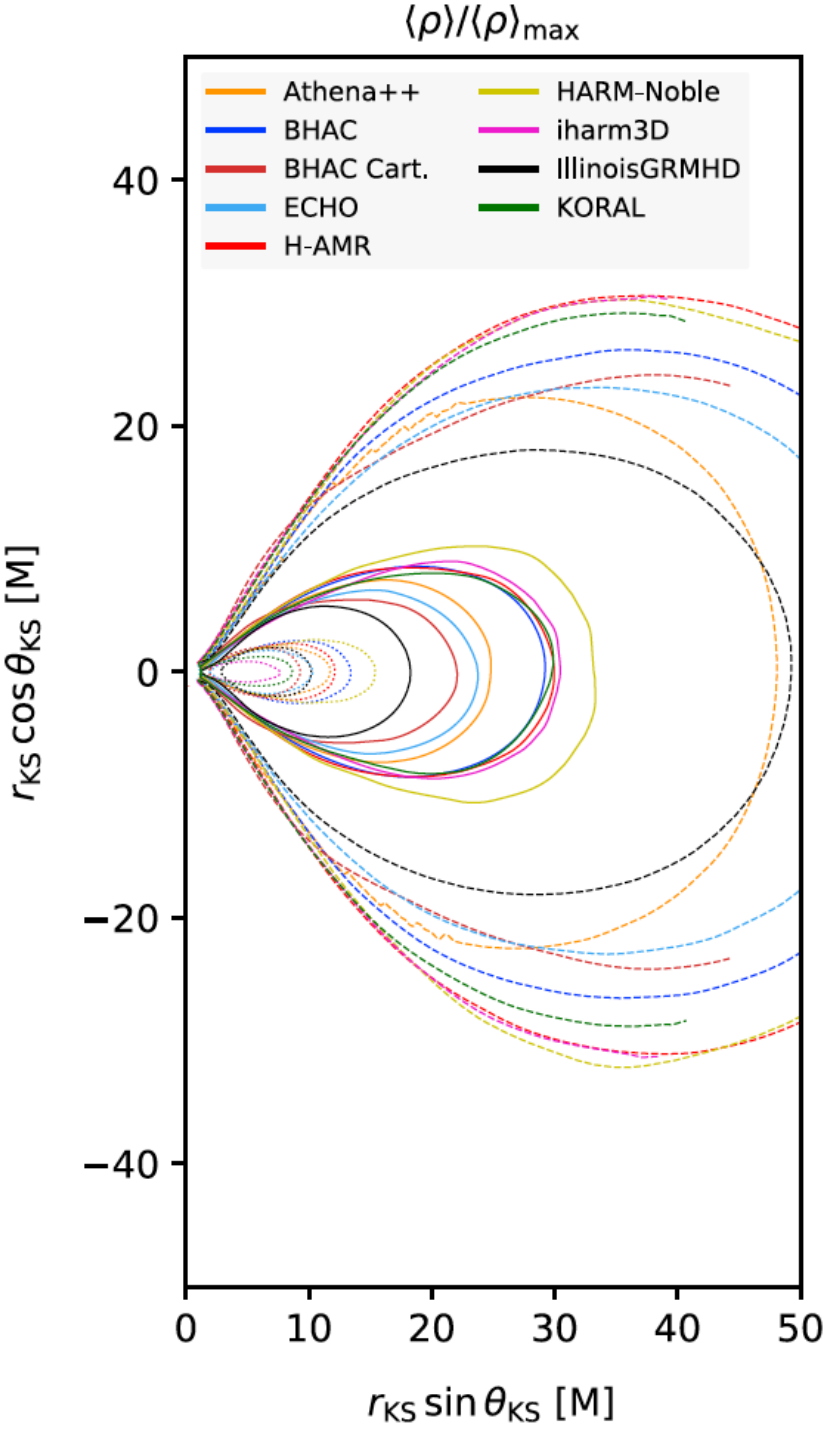

Figure 5.15: Comparison of the density contours at fixed ratios of the peak value for the high-resolution models. Contours are placed at $\langle\rho\rangle/\langle\rho\rangle_{\max} \in [0.0078125, 0.125, 0.5]$.

Variability

In order to get a feeling for the predictive power of variability from GRMHD simulations in a turbulent regime, we now compute the power-spectrum densities (PSDs) of the emission proxy $\mathcal{L}$. The data is presented in Figure 5.16 for all available resolutions. At low and mid resolution, all light curves are compatible with a red-noise spectrum with $\beta = 2$, and we obtain a steepening near $f = 0.1M^{-1}$ while for high resolution this break is less apparent. The same analysis is performed also with the time series of $\dot{M}$. The right panels of Figure 5.16 indicates that the low-frequency power law seen in $\mathcal{L}$ is not recovered in $\dot{M}$. For frequencies $f = 0.01M^{-1}$, the power in all codes is definitely shallower than f^{-2}, approaching a flicker-type noise, f^{-1}, and indications for a spectral break in the vicinity of the ISCO frequency are found.

Finally, the root mean square (RMS) of the accretion rate is computed after zeroing out all Fourier amplitudes with frequency below $1/1000M$. This serves as an effective detrending of the low-frequency secular evolution. In order to avoid edge effects, the rms is computed in the region $t \in [2500, 7500]M$. Exemplary data of the remaining high-frequency variability is shown for the high-resolution runs in the left panel of Figure 5.17. The (normalized) rms values shown against midplane resolution (right panel) quantify this further and indicate quite a universal behavior with values in the range $1.2 - 1.6$ across all codes and resolutions. With increased resolution, all codes tend to be attracted to the point $k = \mathrm{rms}(\dot{M})/\langle\dot{M}\rangle \simeq 1.3$. Repeating the same analysis with the emission proxy yielded essentially the same outcome. This quite striking result (after all, there is a scatter in mean accretion rates itself by a factor of $\sim$8 in the sample) is a restatement of the rms–flux relationship, which is a ubiquitous feature of black hole accretion across all mass ranges (Uttley and McHardy, 2001; Heil et al., 2012). The quotient $k \sim 1.3$ is consistent with the recent simulations of Hogg and Reynolds (2016) who find an rms–flux relationship of the accretion rate with $k = 1.4 \pm 0.4$.

5.2 Second part: MAD

The first part of the EHT GRMHD Code Comparison Project (Porth and EHT-Collaboration, 2019) showed that different simulations of a SANE accretion flow starting from the same initial conditions produce outcomes that are consistent against the diversity of numerical methods and implementations employed by codes in the community. However, while SANEs are relatively simple to simulate and have been widely discussed in the literature, the transition to a MAD state introduces significant changes in the dynamics that can easily bring GRMHD codes to their limits. Given the importance of MADs as viable models for the plasma surrounding M87*, it is essential to assess the consistency of GRMHD codes also in this more challenging regime. As the work is in progress, we show here only some results obtained with ECHO without making comparisons with other codes.

5.2.1 Setup

The initial condition consists of a Fishbone-Moncrief torus around a Kerr black hole with dimensionless spin parameter $a = 0.9375$. The inner radius of the torus is located at $r_{\mathrm{in}} = 20M$, and its pressure maximum at $r_{\mathrm{max}} = 41M$. An ideal gas equation of state is adopted with an adiabatic

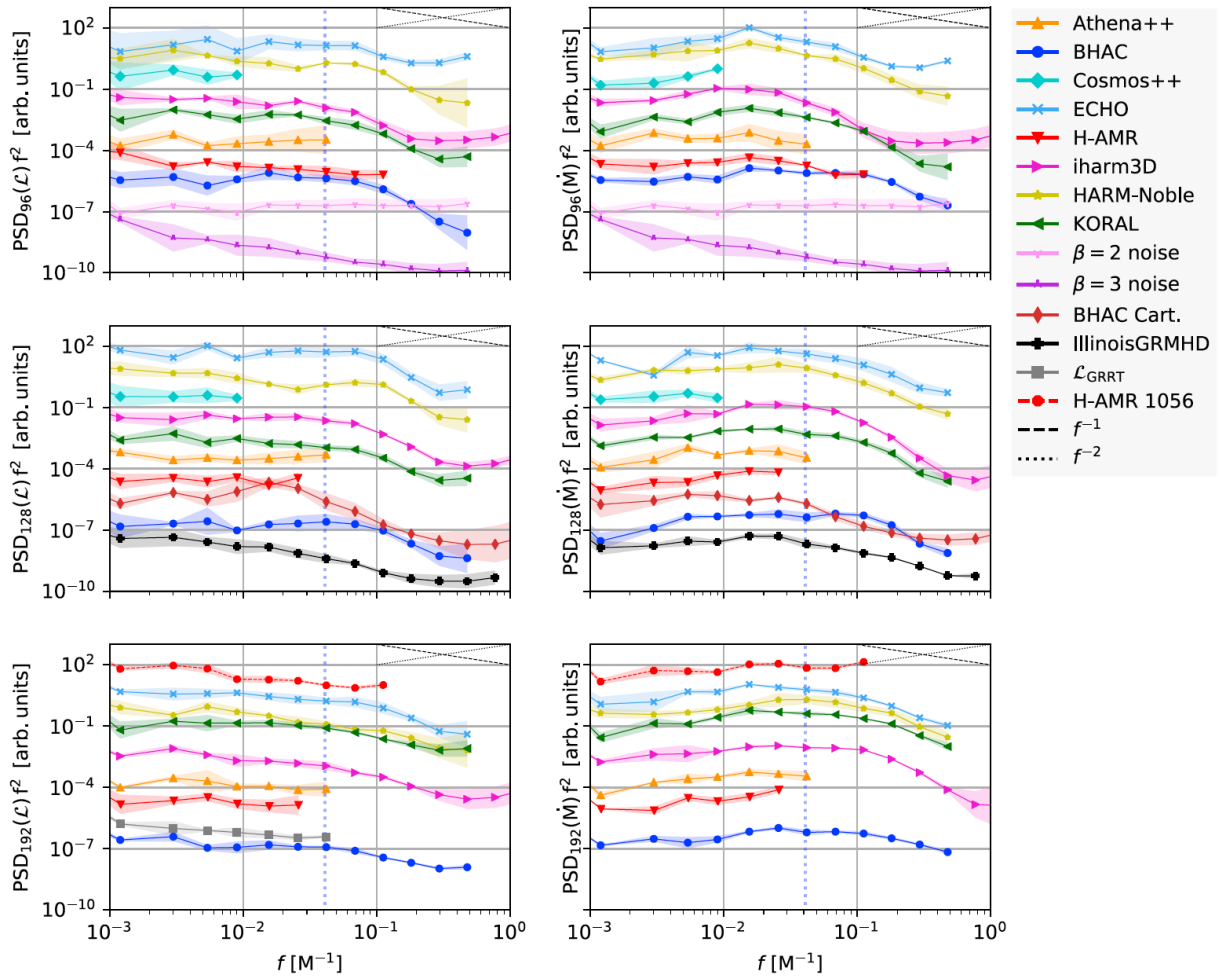

Figure 5.16: Periodograms, compensated with f^{-2}, of the emission proxy $\mathcal{L}$ (left) and for the accretion rate $\dot{M}$ (right) for increasing resolutions (top to bottom). Also, the PSD of a synthetic light curve at 230 GHz and inclination $i = 0$ is shown in the lower panel (light gray curve). To better visually separate the curves, they have been progressively shifted by factors of 10. The blue dotted vertical line denotes the orbital frequency of the ISCO.

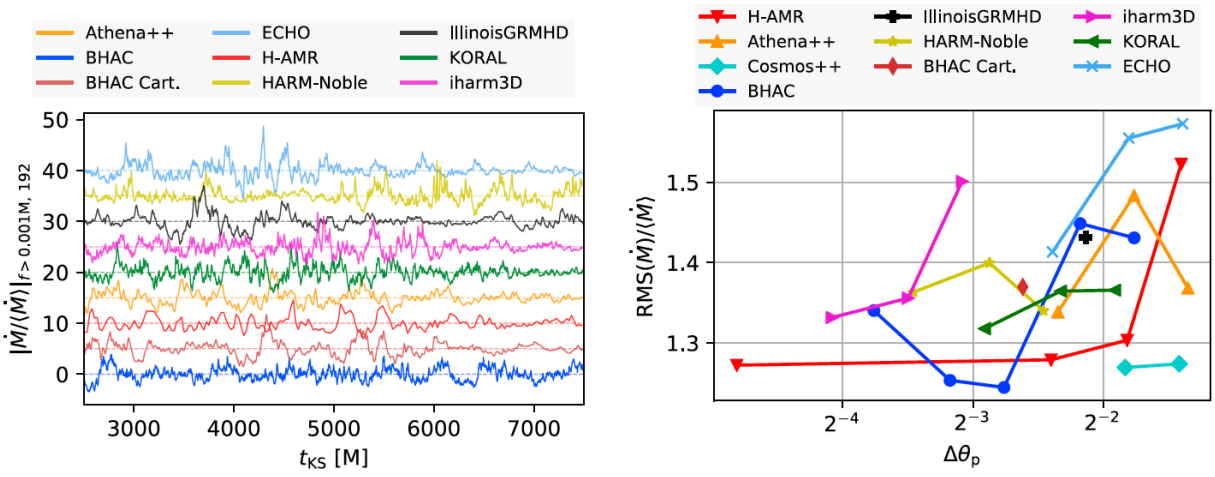

Figure 5.17: Variability of the detrended accretion rates. The long time secular evolution has been removed by zeroing out all Fourier amplitudes below $1/1000M$. An example of the high-resolution data is shown in the left panel. In the right, we compare the resolution dependence in the rms accretion rate normalized by its mean value. We obtain a clear "rms–flux" relation in all codes with quotient converging to $k \simeq 1.3$.

index of $\hat{\gamma} = 13/9$ and the magnetic field is given by the vector potential $A_\phi \propto \max(q, 0)$, where

$$q = \frac{\rho}{\rho_{\max}} \left(\frac{r}{r_{\rm in}} \right)^3 \sin^3\theta \exp\left(-\frac{r}{400} \right) - 0.2, \tag{5.15}$$

and it is normalized in such a way that the ratio of the maximum gas pressure to that of the maximum magnetic pressure in the disk (at different locations) is $(p_{\rm g})_{\max}/(p_{\rm mag})_{\max} = 100$. To trigger the MRI, the equilibrium configuration is perturbed by adding white noise to the fluid pressure according again to the Eq. (5.2).

The initial atmosphere profile adopted in our simulation is given again by relations (5.3). During evolution, ceilings are applied to the Lorentz factor Γ the plasma magnetization σ, and the ratio between magnetic and fluid pressure $\beta_{\rm p}^{-1}$. Velocity is limited in such a way that the Lorentz factor is at most $\Gamma_{\rm fl} = 20$ and matter or fluid pressure are added so that $\sigma < \sigma_{\rm fl}$ and $\beta_{\rm p}^{-1} < (\beta_{\rm p}^{-1})_{\rm fl} = (10\sigma_{\rm fl})^{\hat{\gamma}-1}$, with $\sigma_{\rm fl} = 100$. The floors on density and pressure are therefore

$$\rho_{\rm fl} = \frac{b^2}{\sigma_{\rm fl}}, \qquad p_{\rm fl} = \frac{b^2}{2}(10\sigma_{\rm fl})^{1-\hat{\gamma}}. \tag{5.16}$$

For the present simulations at the two suggested resolutions, low (192x96x96) and high (384x192x192), we have adopted the main numerical strategies adopted for the first part with the addition of the scheme described in the paragraph 4.4.2 which turned out to be able to easily handle low-density regions.

Like the first part, the grid is stretched logarithmically in the radial direction with $r \in [r_{\rm h} - \Delta r, 3000]M$ where Δr is chosen to have five radial grid points for $r < r_{\rm h}$ and uniform in the angular directions. A small aperture cone is removed along the polar axis to avoid numerical problems. Outflow boundary conditions are adopted in the radial direction, for both the inner and outer radii, reflection conditions are applied at the polar axis whereas periodicity is assumed in the azimuthal direction.

5.2.2 Results

We now briefly present some results obtained with ECHO: the main diagnostics are the same as in the first part with the addition of a quantification used to estimate the power of the jets.

Horizon-penetrating fluxes

Figure 5.18 show time series of the radial fluxes defined in Section measured at the event horizon (the blue line refers to low resolution and the red line to high resolution). Because the simulations are scale free until the accretion rate is fixed, each of them has been been appropriately normalised by the mass accretion rate $\dot{M}$, similarly as in Porth and EHT-Collaboration (2019); however, due to the larger variations in $\dot{M}$ that characterise the MAD state, here we have used the average value of this quantity instead of pointwise values. Mass, magnetic and angular momentum flux rise during a transient phase from roughly one orbital period of the original density maximum (≈ 1649.5) to $5500M$, after which they reach a quasi-stationary state that lasts until the end of the simulations, at $\sim 10000M$. For both runs the normalised magnetic flux saturates at a value close to $\phi_{\max} \sim 15$ which confirms that they are in the MAD regime. Note that both a and H/R are the same as in

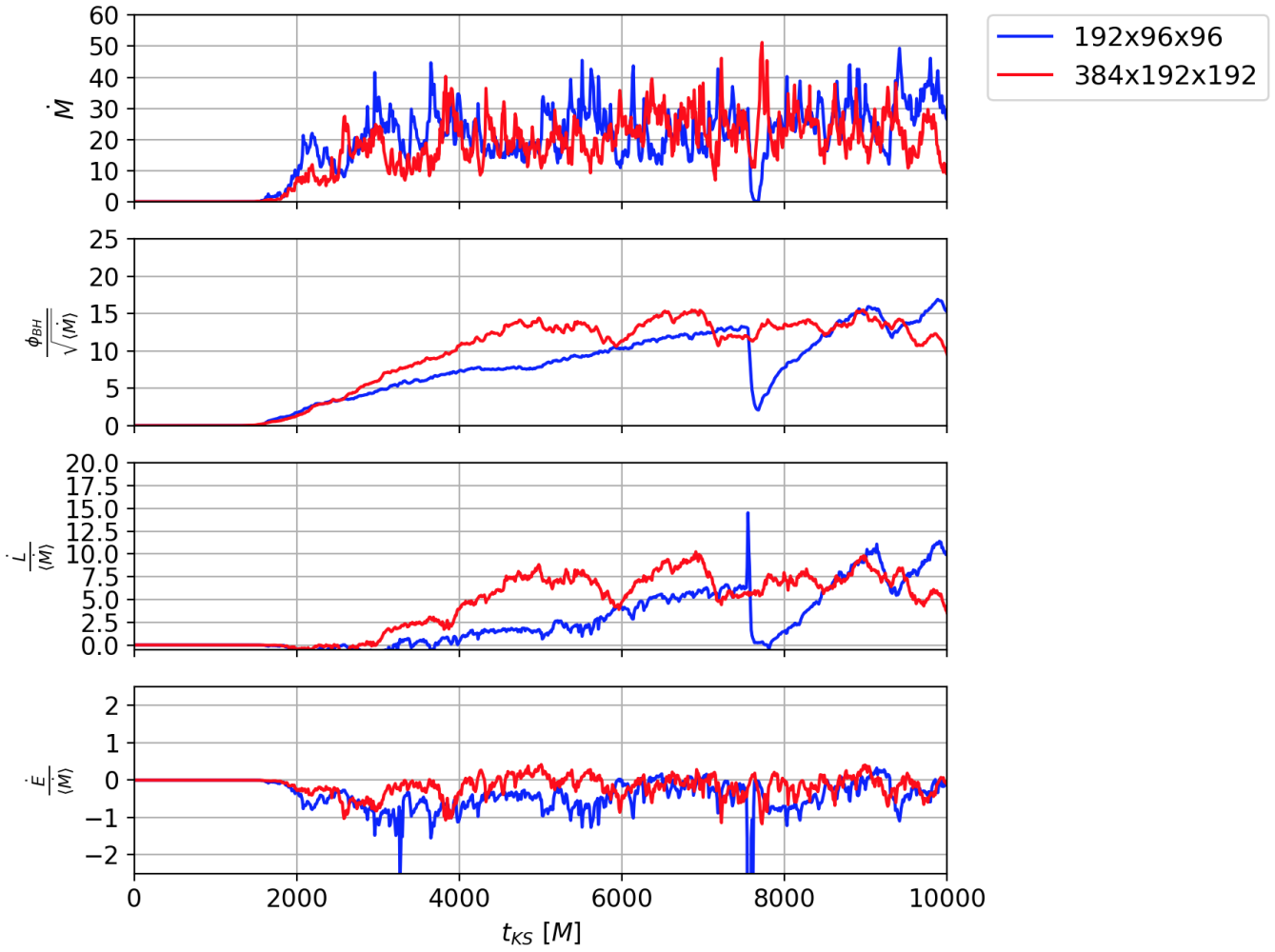

Figure 5.18: Horizon-penetrating fluxes as defined in Eqs. (5.5)-(5.8) for the low (blue line) and high (red line) resolution simulations, after normalization by the average of $\dot{M}$ over $t \in [6000, 10000]M$.

SANE project (see Figure 5.20 for scale height profile), so the critical value $\phi_{\rm max}$ is again ~ 15. In the low-resolution run we observe an episode of interruption of the accretion at $t \sim 7500M$. It could be due to a sudden accumulation of magnetic field that managed to inhibit all the accretion channels at the same time. We note, however, that the accretion immediately restarts and the magnetic flux manages to reach the critical value. The energy flux through the event horizon is fairly constant and higher in the high-resolution run.

Disk-averaged profiles

Disk- and time-averaged profiles of several quantities of interest are shown in Figure 5.19 for the simulations performed at low and high resolutions. The averages are also computed during the interval $t \in [6000, 10000]M$, when angular momentum has redistributed and the profiles of the initial state is have been completely transformed into those of a new quasi-stationary state. A first comparison of the codes (not reported here) shows a good agreement at high resolutions and overall less spreads than SANE simulations. Figure 5.20 shows that the scale height profile of the high-resolution model is $\simeq 0.25$ like the previous disk model adopted for SANE.

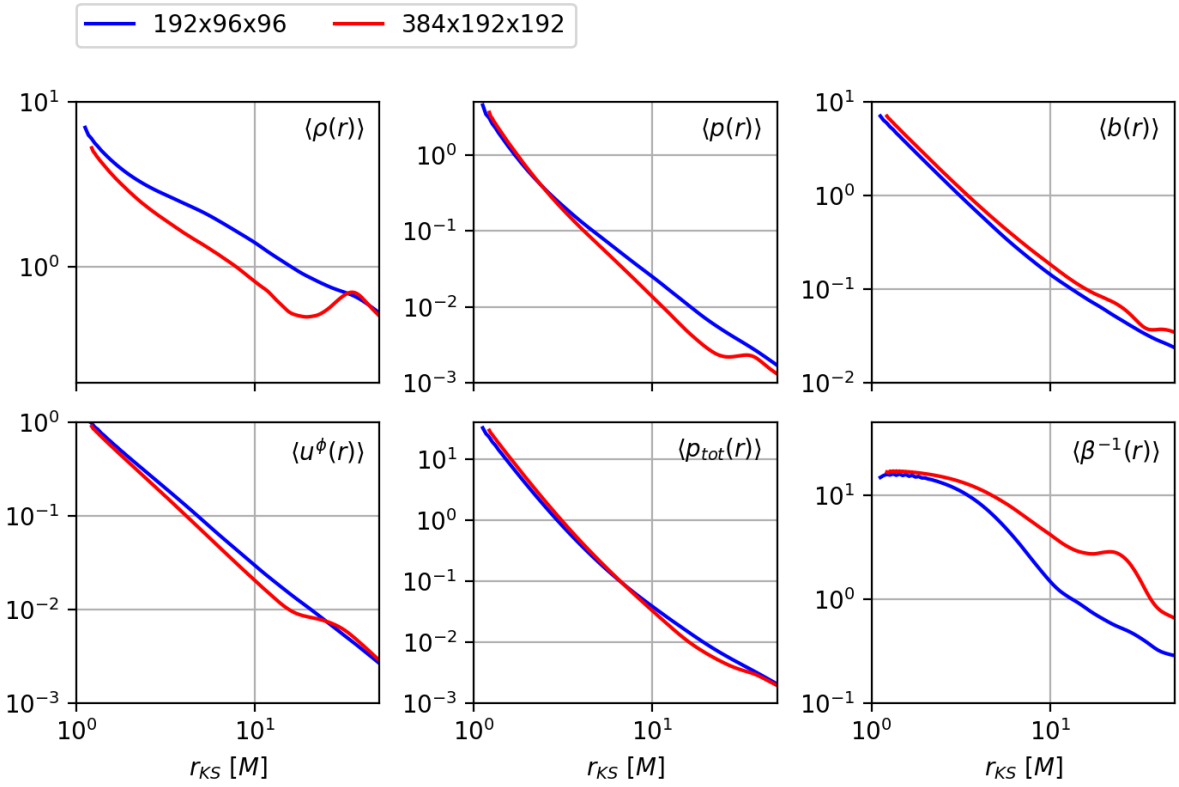

Figure 5.19: Disk-averaged profiles for the low (blue line) and high (red line) resolution simulations. The quantities as been averaged over θ and ϕ coordinates using the integral given in the Eq. (5.9) at every snapshot, as well as over the time evolution over the interval $t \in [6000, 10000]M$.

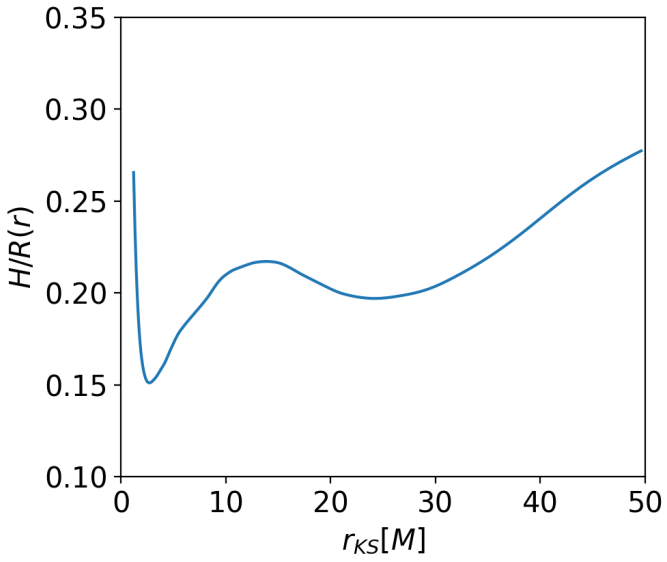

Figure 5.20: Scale height profile of the high-resolution model according to Eq. (5.10) and averaged in the interval $t \in [6000, 10000]M$.

t, ϕ averages

In order to study the flow configuration in the quasi-stationary state, we studied time- and ϕ-averaged quantities in the interval $t \in [6000, 10000]M$. Figure 5.21 show these averages for rest-frame density, inverse plasma β and magnetisation σ for the run performed at highest resolution. It is possible to see density rising and magnetization decreasing towards the pole probably due to the effect of the reflecting boundary conditions.

Jet luminosity

Given its importance in identifying viable models for the EHT observations of M87*, we would like to repeat one of the quantifications used in EHT-Collaboration (2019e) to estimate jet power. However, to gain more information on the mechanisms of energy conversion in the jet and how they are affected by floors, we split the energy momentum tensor into electromagnetic, particle kinetic energy and thermal contributions, as done in McKinney et al. (2012). These are defined, respectively, as:

$$(T^{\rm EM})^{\mu}_{\nu} = \left(u^{\mu}u_{\nu} + \frac{1}{2}\delta^{\mu}_{\nu}\right)b^2 - b^{\mu}b_{\nu}, \tag{5.17}$$

$$(T^{\rm PAKE})^{\mu}_{\nu} = (u_{\nu} + \delta^0_{\nu})\rho u^{\mu}, \tag{5.18}$$

$$(T^{\rm EN})^{\mu}_{\nu} = (\rho\epsilon + p)u^{\mu}u_{\nu} + p\delta^{\mu}_{\nu}, \tag{5.19}$$

so that the total energy-momentum tensor is

$$T^{\mu}_{\nu} = (T^{\rm EM})^{\mu}_{\nu} + (T^{\rm PAKE})^{\mu}_{\nu} + (T^{\rm EN})^{\mu}_{\nu} - \delta^0_{\nu}\rho u^{\mu}. \tag{5.20}$$

The diagnostics that we measure are the outgoing radial energy fluxes integrated over a mask used to define the jet, at several times and radii:

$$P_{\rm EM}(r,t) = -\int\int_{\rm jet}(T^{\rm EM})^{\mu}_{\nu}(-g)^{1/2}{\rm d}\theta{\rm d}\phi, \tag{5.21}$$

$$P_{\rm PAKE}(r,t) = -\int\int_{\rm jet}(T^{\rm PAKE})^{\mu}_{\nu}(-g)^{1/2}{\rm d}\theta{\rm d}\phi, \tag{5.22}$$

$$P_{\rm EN}(r,t) = -\int\int_{\rm jet}(T^{\rm EN})^{\mu}_{\nu}(-g)^{1/2}{\rm d}\theta{\rm d}\phi, \tag{5.23}$$

together with the outgoing mass flux integrated over the same mask:

$$\dot{M}_{\rm jet}(r,t) = \int\int \rho u^{r}(-g)^{1/2}{\rm d}\theta{\rm d}\phi. \tag{5.24}$$

The total radial energy flux is given by $P_{\rm total}(r,t) = P_{\rm EM}(r,t) + P_{\rm PAKE}(r,t) + P_{\rm EN}(r,t) + \dot{M}_{\rm jet}(r,t)$ while the jet power is defined, consistently with EHT-Collaboration (2019e) as $P_{\rm jet}(r,t) = P_{\rm total}(r,t) -$

$\dot{M}_{\rm jet}(r,t)$. Finally, the jet mask is defined as the region where $v\Gamma > (v\Gamma)_{\rm th}$, where

$$(v\Gamma)^2 = \left(\frac{-T^r_t}{\rho u^r}\right)^2 - 1, \tag{5.25}$$

and $(v\Gamma)_{\rm th} = 1$. Figure 5.22 show the radial dependence of time-averaged fluxes of mass and energy, subdivided in thermal, kinetic and electromagnetic contributions, as well as the total jet power, for the high resolution simulation. Consistently with what has been observed by other codes, the magnetic energy decreases at large radii favoring an increase in the thermal and kinetic contributions. However, we observe a bump of $P_{\rm EN}$ close to $r = 1000M$ which could be due to the non-optimal treatment of the area near the edge in theta in which we have removed a slice probably too large for correct modeling of the jet region; the role of the numerical resets in the atmosphere could also be decisive.

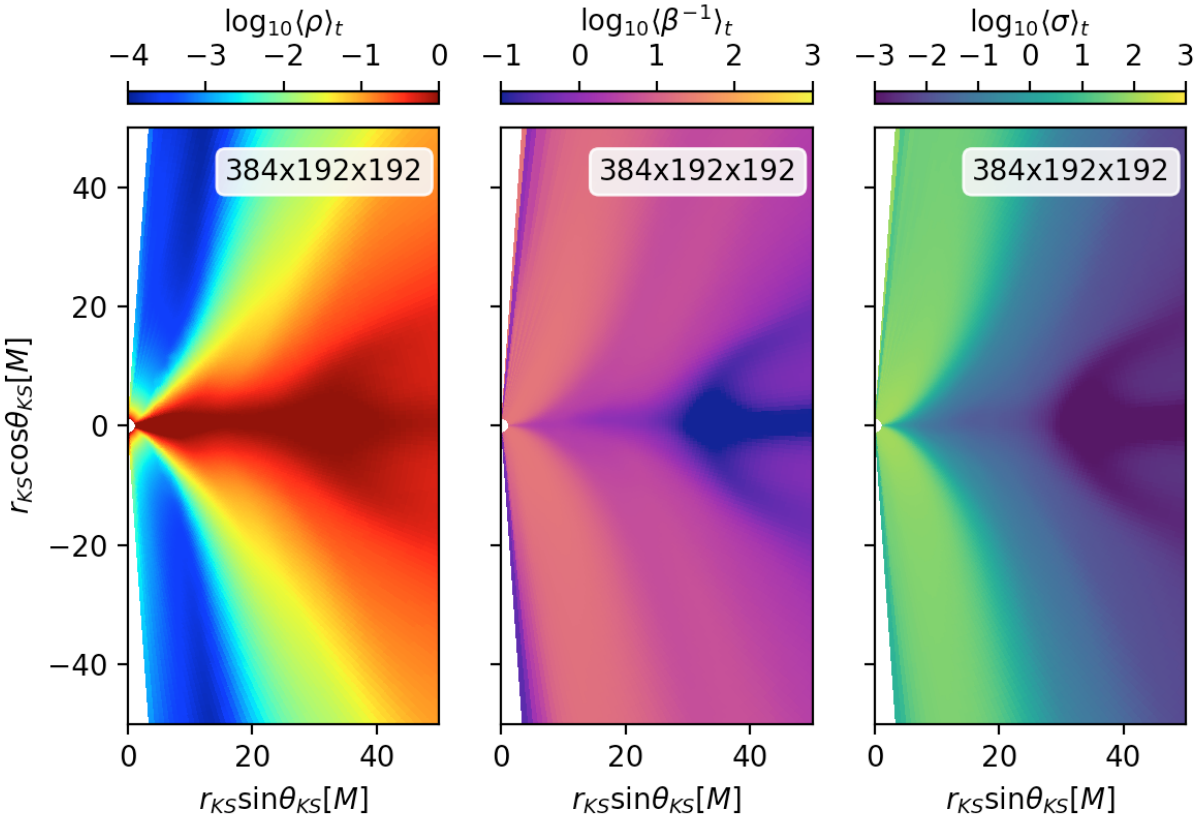

Figure 5.21: Axisymmetrized and time-averaged spatial distributions of ρ, β^{-1} and σ over the interval $t \in [6000, 10000]M$ for the high resolution simulation.

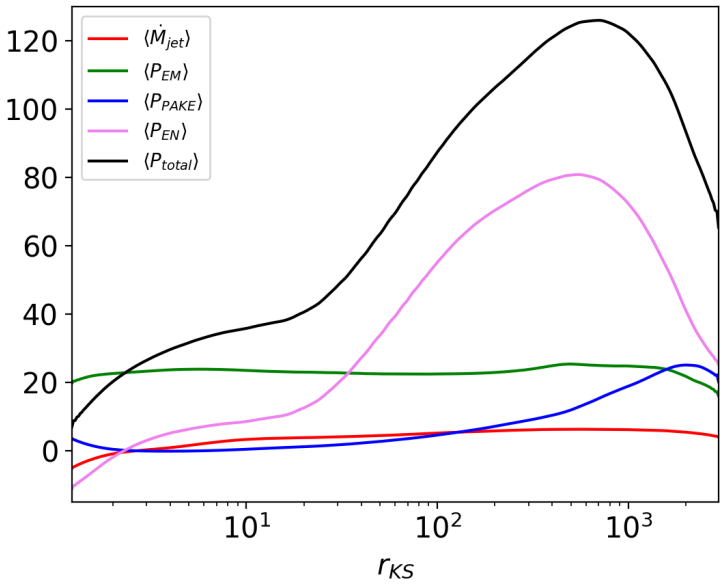

Figure 5.22: Contributions to the jet power versus radius, averaged over the interval $t \in [6000, 10000]M$ for the high resolution simulation.

Chapter 6

Numerical simulations: GRMHD mean-field dynamo in accretion disks

In the previous Chapter we showed the ideal GRMHD accretion simulations taken as a reference to model EHT observations. However, it must be noticed that the simulations employed by the EHT community and for the code comparison tests all rely on initial magnetic fields with pressure which is one hundredth of the kinetic pressure. This value corresponds to a subdominant field, but it is not far from the value needed to reproduce both the dynamics needed to launch the polar jets and the non-thermal synchrotron emission (once a model for the distribution for the emitting electrons has been established). A more natural scenario would be the one in which a very low initial field is evolved and amplified by some kind of dynamo process, so to reach self-consistently the correct threshold for MRI to induce accretion and to reproduce the correct dynamical and emission properties. A promising mechanism is $\alpha - \Omega$ dynamo described in the Paragraph 2.4. Synthetically, α-effect is supposed to be given by the coupling between unresolved velocity and field fluctuations while the Ω-effect is due to the differential rotation of the disk.

The first mean-field simulations in resistive GRMHD applied to the accretion disks are found in the work of Bugli et al. (2014) that we summarized in the Paragraph 3.5. As we have seen, it characterizes the kinematic regime in which only the magnetic field evolves, growing exponentially. However, to study consistently the accretion it is necessary to consider the feedback on the disk due to the action of the dynamo. The new results obtained in the dynamic regime are published in two works: Tomei et al. (2020, 2021). While the first work focuses on the characterization of the saturation of the exponential growth of the magnetic field, the second reconnects to the diagnostics analyzed in the Code Comparison Project with the idea of proposing a valid alternative to ideal 3D GRMHD modeling.

6.1 First fully non-linear simulations

In the first paper (Tomei et al., 2020) we generalize our previous work on the mean-field dynamo in accreting discs (Bugli et al., 2014) by investigating the completely self-consistent and non-linear regime (dynamic regime) during the accretion phase. The linear growth of the fields cannot reasonably continue for an arbitrarily long time, and it is expected to be quenched naturally by the feedback on the disc. Our goal is to see how the transition to the non-linear phase occurs, to inves-

a_{BH}	r_{in}	r_c	w_c	A_0	ρ_{min}	p_{min}
0.9375	6	12	1	10^{-8}	10^{-4}	10^{-6}

Table 6.1: Parameters of the initial equilibrium model.

tigate the interplay with MRI, and the effect of accretion on the dynamo process itself, for a given disc model and a variety of dynamo parameters. Finally, on top of our GRMHD model based on the dynamo action, we compute the local emissivity and integrated flux in the radio band (in the approximation of an optically thin plasma), and we propose a comparison with observational data for Sgr A*.

6.1.1 Disk model and numerical setup

The simulations are initialized with the hydrodynamical equilibrium solution for a differentially rotating thick disk with $l = \mathrm{const}$ described in the paragraph 3.4.2. A small magnetic field is then introduced in such a way that the initial equilibrium is not affected by its presence ($B^2 \ll w$). In particular, a large poloidal loop has been superimposed over the hydrodynamical torus, described by the vector potential (Liska et al., 2018)

$$A = A_0 \rho^2 r^3, \tag{6.1}$$

where A_0 is a constant. In Table 6.1 the parameters used to characterize the disk configuration are shown. Lengths and times are expressed in units of $r_g = GM_{\mathrm{BH}}/c^2$ (the gravitational radius) and r_g/c, respectively. The mass density is normalized against $\rho_0 = n_0 m_p$, where n_0 is a reference peak number density in the disk, whereas enthalpy, energy density and fluid and magnetic pressure are normalized against $\rho_0 c^2$. The spin parameter a_{BH} must also be provided in order to characterize the Kerr-type metric, and here we choose the same value used in Porth and EHT-Collaboration (2019).

Outside the disk we introduce a static, unmagnetized and tenuous atmosphere, with density and pressure radial profiles given by

$$\rho_{\mathrm{atm}} = \rho_{\mathrm{min}} r^{-3/2}, \quad p_{\mathrm{atm}} = p_{\mathrm{min}} r^{-5/2}. \tag{6.2}$$

In order to quantify the dynamo action, we can introduce the two characteristic numbers defined by Eqs. (2.73)-(2.74) that describe the importance of α dynamo and rotation with respect to the dissipation of magnetic fields. The η and ξ profiles are chosen so that the diffusion and dynamo processes occur only within the disk. Starting from the maximum values ξ_{max} and η_{max}, those actually entering the definition of the dynamo numbers, at each point of the domain we impose

$$\eta(r, \theta) = \eta_{\mathrm{max}} S_\eta(r, \theta), \tag{6.3}$$

with

$$S_\eta(r, \theta) = \frac{\rho - \rho_{\mathrm{atm}}}{\rho_{\mathrm{max}}}, \tag{6.4}$$

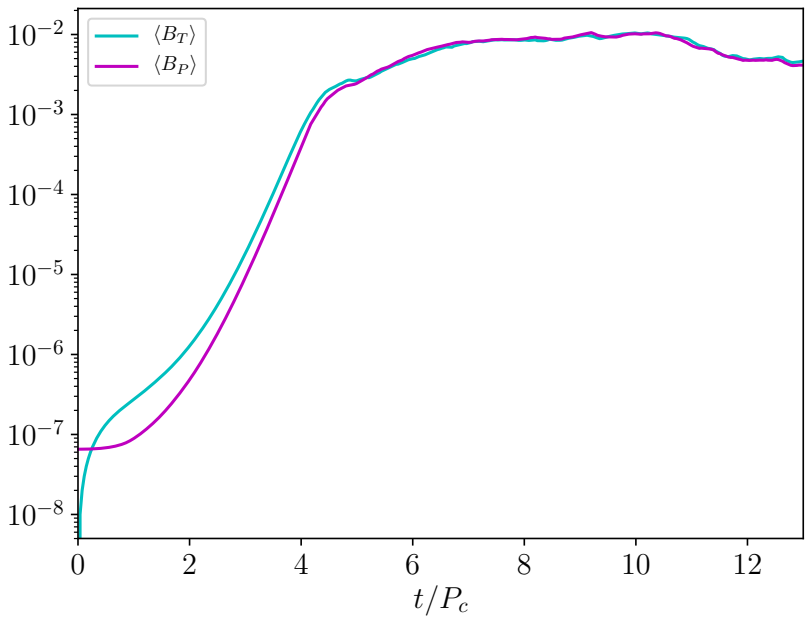

Figure 6.1: The time evolution of the average values of the toroidal $B_T = \sqrt{B^\phi B_\phi}$ and poloidal $B_P = \sqrt{B^2 - B_T^2}$ components of the magnetic field. Here, time is normalized with the initial central period, $P_c = 268$.

and

$$\xi(r,\theta) = \begin{cases} \xi_{\max} S_\xi(r,\theta), & \text{inside the disk,} \\ 0 & \text{in the atmosphere,} \end{cases} \tag{6.5}$$

with

$$S_\xi(r,\theta) = \frac{\rho \cos\theta}{[\rho \cos\theta]_{\max}}, \tag{6.6}$$

where the presence of an odd function with respect to the equator will lead to a symmetric dynamo action. In Table 6.2 we show the models we have considered for our simulations. We have explored different dynamo numbers C_ξ, starting from a reference value (Run1), in order to cover a significant range in the parameter space. In the present analysis, we have chosen to leave the hydrodynamical equilibrium, hence the $\Omega(r)$ profile, unchanged as well as a fixed $\eta_{\max}$, so that C_η has also been kept constant.

We adopt here the horizon-penetrating Kerr-Schild metric (see section 3.4) and 2-D axisymmetric spherical coordinates. The two-dimensional numerical domain extends in the regions delimited by $r_{\min} = r_h - 0.3$, inside the horizon r_h, and $r_{\max} = 100$ in the radial direction, and by 0.06 and $\pi - 0.06$ in the θ direction. The grid (512×256) employed is uniform in θ but not along the radial direction, where points are defined by the nonlinear function

$$r_i = r_{\min} + \frac{r_{\max} - r_{\min}}{\Psi} \tan(m_i \arctan \Psi), \tag{6.7}$$

with m_i covering uniformly the range $[0,1]$ and Ψ a stretching factor fixed to 10 as in Bugli et al. (2014). This choice allows to have a higher resolution in the inner region where larger gradients are expected.

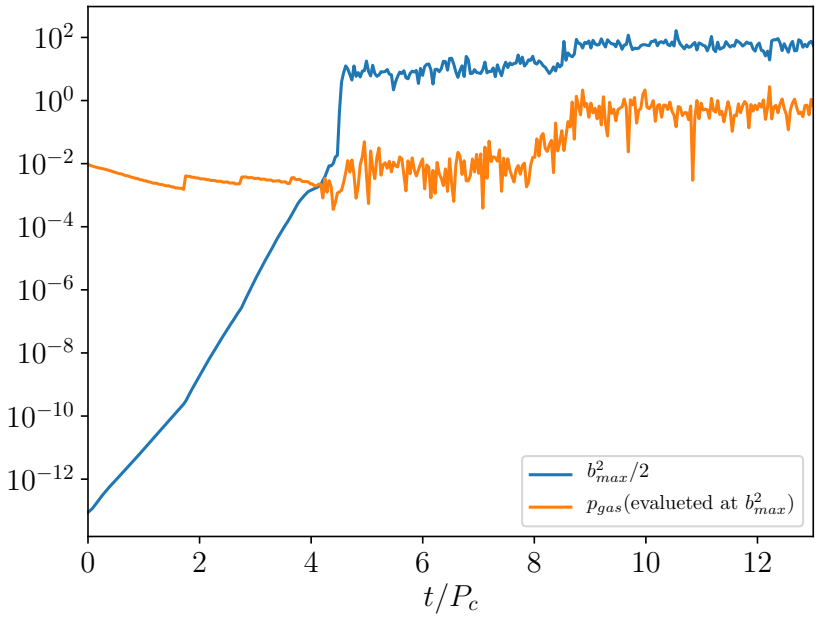

Figure 6.2: Time evolution of $p_{\rm mag} = \frac{1}{2}b^2$ and $p_{\rm gas} \equiv p$, both evaluated where $p_{\rm mag}$ takes its maximum value.

6.1.2 Results

In this section we show the results of $\alpha - \Omega$ dynamo simulations. We start by defining the average on the disk of any quantity $f = f(r, \theta)$ as

$$\langle f \rangle = \frac{\int_{r_1}^{r_2} \mathrm{d}r \int_{\theta_1}^{\theta_2} \mathrm{d}\theta \, \alpha\sqrt{\gamma}\, f}{\int_{r_1}^{r_2} \mathrm{d}r \int_{\theta_1}^{\theta_2} \mathrm{d}\theta \, \alpha\sqrt{\gamma}}, \tag{6.8}$$

where $r_1 = 4$, $r_2 = 30$, $\theta_1 = \pi/3$, and $\theta_2 = 2\pi/3$. The assumption of limiting the average in this range is arbitrary, the reason behind this choice is to define a region of the disk in which the quantities of interest are significantly appreciable. Note that because of the presence of the lapse function α this is not a proper $3+1$ spatial averaging, though the above formula is the one most commonly adopted within the GRMHD community (Porth and EHT-Collaboration, 2019). The time range of the simulations goes from 0 to $13P_c$, where $P_c = 268$ is the initial central period.

Figure 6.1 shows the time evolution of the average poloidal and toroidal components of the magnetic field in the Run1. We can see that a toroidal field immediately arises due to the Ω effect and, after a transient, the mean-field $\alpha-$dynamo starts as well and supports the exponential amplification of the two components up to $\sim 4.5\ t/P_c$. This phase coincides with the kinematic regime studied by Bugli et al. (2014), as there is there is no noticeable feedback on the disk and the field grows following the normal modes of the dynamo, propagating towards the outer edge of the disk. During this linear phase the toroidal fields remain always stronger than the poloidal component. The new interesting aspect is represented by the situation around $t \simeq 4.5P_c$, where the linear dynamo action saturates. As shown in the Figure 6.2, the transition occurs when there are

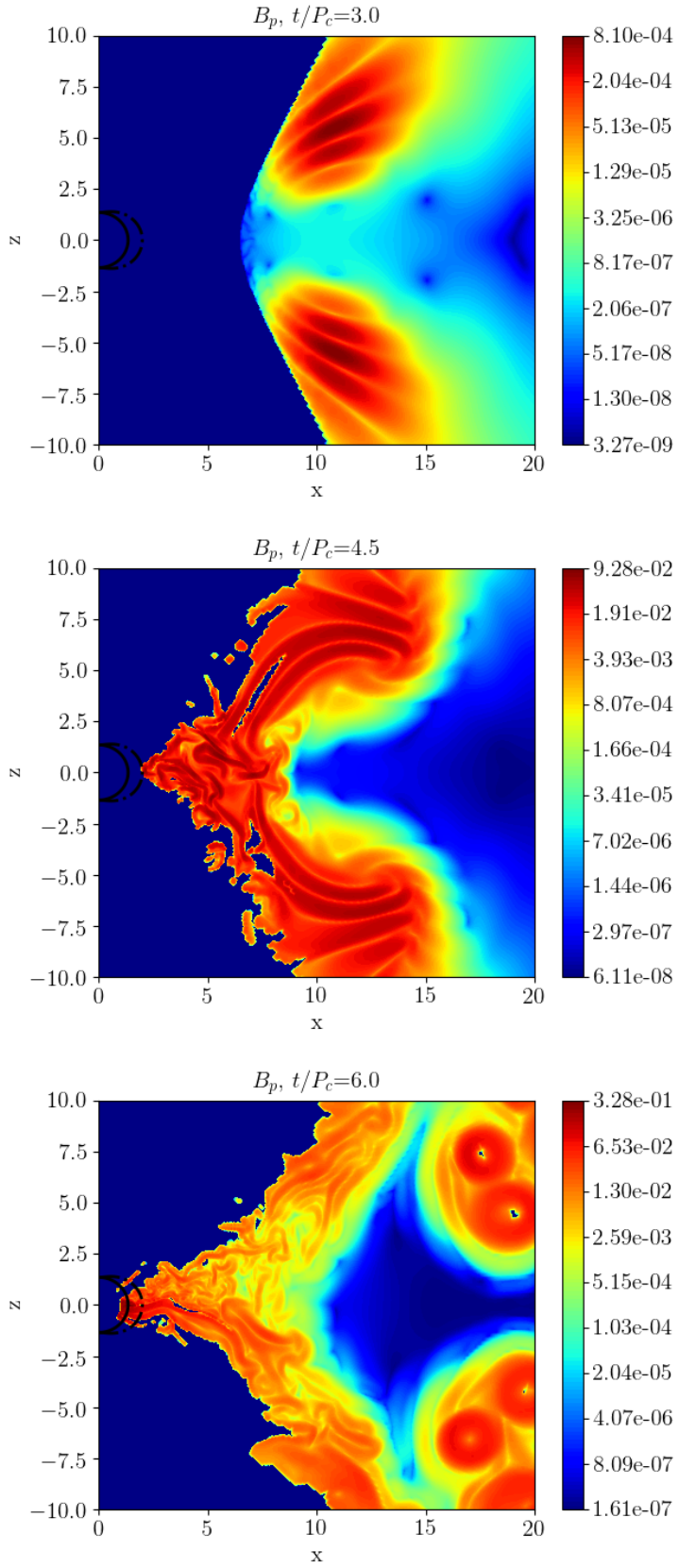

Figure 6.3: Color maps of the poloidal magnetic field B_P in logarithmic scale, for three different times t/P_c Black lines near the origin are the contours of the black hole's ergosphere (dashed line) and horizon r_h (solid line).

	$\eta_{\max}$	$\xi_{\max}$	C_ξ	C_Ω	$\gamma_1(B_P)$	$\gamma_1(B_T)$	$\gamma_2(B_P)$	$\gamma_2(B_T)$
Run1	$1.0 \cdot 10^{-3}$	$3.0 \cdot 10^{-2}$	$3.6 \cdot 10^2$	$8.3 \cdot 10^2$	3.76 ± 0.010	3.57 ± 0.01	0.720 ± 0.010	0.634 ± 0.008
Run2	$1.0 \cdot 10^{-3}$	$3.5 \cdot 10^{-2}$	$4.2 \cdot 10^2$	$8.3 \cdot 10^2$	4.190 ± 0.030	3.960 ± 0.030	0.220 ± 0.009	0.225 ± 0.008
Run3	$1.0 \cdot 10^{-3}$	$4.0 \cdot 10^{-2}$	$4.8 \cdot 10^2$	$8.3 \cdot 10^2$	4.930 ± 0.030	4.660 ± 0.040	0.460 ± 0.010	0.490 ± 0.020
Run4	$1.0 \cdot 10^{-3}$	$2.5 \cdot 10^{-2}$	$3.0 \cdot 10^2$	$8.3 \cdot 10^2$	2.980 ± 0.010	2.800 ± 0.002	0.597 ± 0.008	0.476 ± 0.004
Run5	$1.0 \cdot 10^{-3}$	$2.0 \cdot 10^{-2}$	$2.4 \cdot 10^2$	$8.3 \cdot 10^2$	2.460 ± 0.010	2.267 ± 0.009	0.436 ± 0.002	0.412 ± 0.005
Run1q	$1.0 \cdot 10^{-3}$	$3.0 \cdot 10^{-2}$	$3.6 \cdot 10^2$	$8.3 \cdot 10^2$	3.450 ± 0.010	3.200 ± 0.020	0.486 ± 0.005	0.396 ± 0.003
Run2q	$1.0 \cdot 10^{-3}$	$3.5 \cdot 10^{-2}$	$4.2 \cdot 10^2$	$8.3 \cdot 10^2$	3.990 ± 0.020	3.820 ± 0.030	0.513 ± 0.006	0.449 ± 0.004
Run3q	$1.0 \cdot 10^{-3}$	$4.0 \cdot 10^{-2}$	$4.8 \cdot 10^2$	$8.3 \cdot 10^2$	4.760 ± 0.020	4.540 ± 0.040	0.570 ± 0.003	0.526 ± 0.003
Run4q	$1.0 \cdot 10^{-3}$	$2.5 \cdot 10^{-2}$	$3.0 \cdot 10^2$	$8.3 \cdot 10^2$	2.850 ± 0.010	2.760 ± 0.010	0.408 ± 0.006	0.352 ± 0.004
Run5q	$1.0 \cdot 10^{-3}$	$2.0 \cdot 10^{-2}$	$2.4 \cdot 10^2$	$8.3 \cdot 10^2$	2.336 ± 0.007	2.220 ± 0.010	0.354 ± 0.005	0.318 ± 0.003

Table 6.2: Initialization parameters for the various runs and growth rates in the two phases. The reported dynamo numbers refer to their maximum value. The initial plasma beta is $\beta = 10^9$ for all runs.

regions where the gas pressure locally equals the magnetic one

$$p_{mag} = \frac{1}{2}b^2 = \frac{1}{2}(B^2 - E^2), \tag{6.9}$$

and the sharp jump means that the most magnetized regions are no longer within the disk but start to form in the low-density atmosphere, where accretion is taking place. This corresponds to a change of slope in the growth of the magnetic field displayed in Figure 6.1: the dynamo action is less strong, though a secondary linear phase can still be recognized, and the values for the two magnetic field components are basically the same. After $t \simeq 8P_c$ a second and definitive saturation stage has been reached, the dynamo amplification slowly begins to decrease, and the magnetic field approaches more or less to a constant value.

The three phases are more clearly apparent in Figure 6.3, where spatial maps of the (poloidal) magnetic field are presented (in logarithmic scale) at three different times. In the upper panel we are clearly still in the kinematic, linear phase of the dynamo. The magnetic field does not affect the disk shape, magnetic islands corresponding to the linear dynamo modes migrate towards the outer edge of the disk while growing in amplitude. In the middle panel the disk starts to be affected by the presence of the growing field and dynamo waves are dragged towards the black hole by the accretion. The accretion process is most probably triggered by MRI (see the discussion below), that also drives turbulent motions. In this dynamic regime, magnetic structures tend to form low-pressure vortices that drag matter away (bottom panel), that for high values of the magnetic field can even evacuate the plasma locally (and safety floor density values can be required numerically, in order to limit this effect). The dynamo modes are barely visible during the phase of the secondary growth (third panel), and they seem to be localized only at the external boundary of the disk, where density and the dynamo term ξ are lower (this point will be addressed in the next section).

6.1.3 Dependence on the $\alpha-$dynamo number and on the quenching effect

We now investigate the dependence of the results on the $\alpha-$dynamo number C_ξ and on the employment of an explicit quenching effect (see below). The list of runs with the corresponding parameters is reported in Table 6.2. In particular, Run2 and Run3 are characterized by increasing values of ξ and C_ξ with respect to our reference Run1 values, whereas Run4 and Run5 by decreasing values of the same parameters. Figure 6.4 shows the dependence of the exponential growth rates of the kinematic (γ_1) and dynamic (γ_2) phases, respectively, with the dynamo number C_ξ. Growth rates are measured for both the poloidal field component (blue triangles) and for the toroidal one (blue circles), values also reported in Table 6.2. The red symbols indicate the corresponding quantities

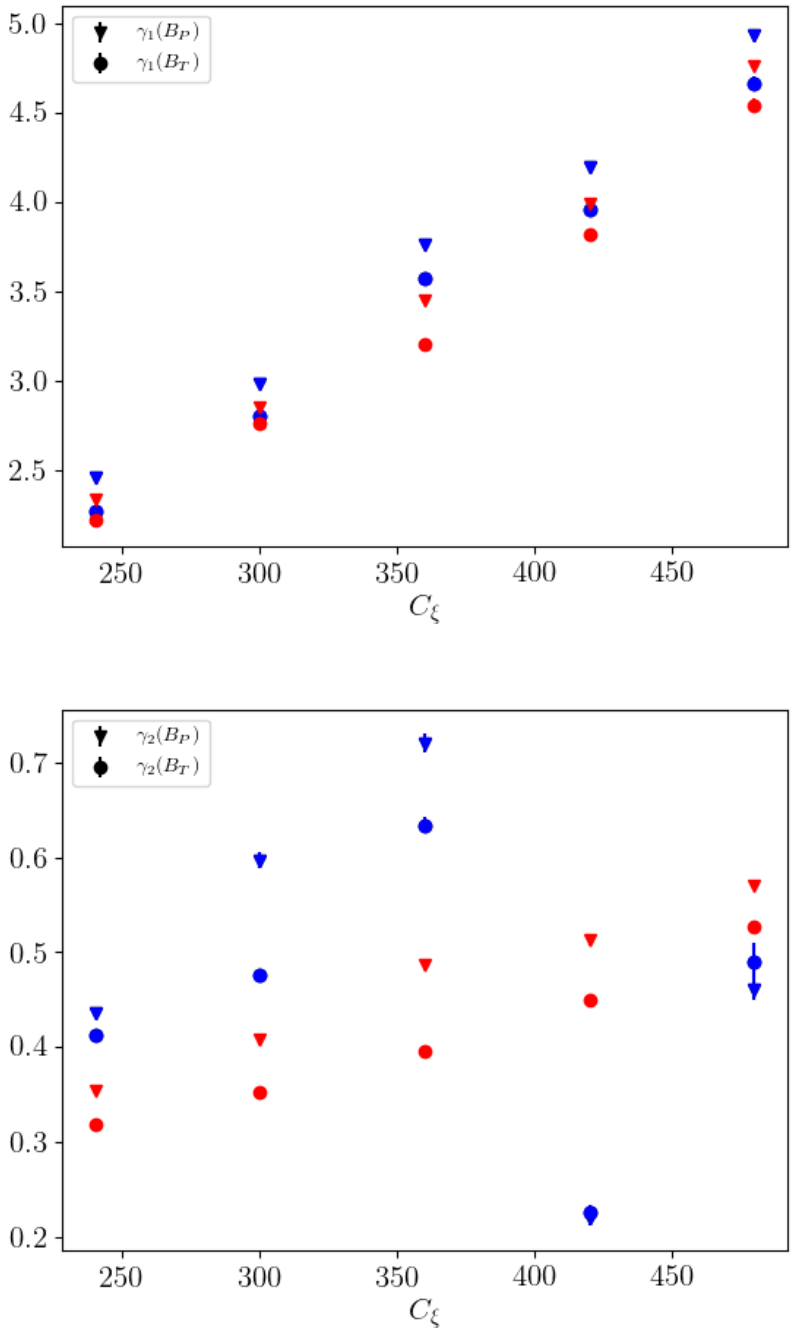

Figure 6.4: Dependence of growth rates γ_1 and γ_2 on the dynamo number C_ξ. Triangles (circles) for the poloidal (toroidal) field components, blue (red) color for runs without (with) quenching.

for simulations where quenching is active (labeled with a 'q' in the table of runs).

We observe that the rates γ_1 corresponding to the kinematic phase follow a linear trend, as expected, whereas the rates γ_2, corresponding to the phase where accretion affects the dynamo modes, show an unexpected drop at high values of ξ (blue symbols). This may be due to the rapid growth of the magnetic field, leading to values able to modify the fluid equilibrium itself. This seems to prevent, or at least to lower, a subsequent amplification, as if a saturated state has been reached.

In order to limit the dynamo action and to obtain a more regular growth it is possible to adopt a technique, used in purely kinematic dynamo models to simulate dynamic effects, that is to impose an explicit quenching in the dynamo term in situations when the field becomes comparable to the equipartition value (Brandenburg and Subramanian, 2005, e.g.). This is obtained by introducing, locally at any point, the replacement

$$\xi \to \frac{\xi}{1 + B^2/B_{\rm eq}^2}, \tag{6.10}$$

where we have considered an equipartition turbulent field defined as a given fraction of the thermal pressure (Shakura and Sunyaev, 1973), $B_{\rm eq}^2 = \bar{\alpha}_{\rm disk} p$, with $\bar{\alpha} = 0.1$. This value is the one most commonly used to model the turbulent magnetic stresses in disks (King et al., 2007).

Here we want to check whether our GRMHD simulations without quenching lead to a turbulent state with fluctuations of the required intensity. We thus compare this value with the coefficient $\alpha_{\rm disk}$ defined by the averages

$$\alpha_{\rm disk} = \frac{\langle W \rangle}{\langle p + p_{\rm mag} \rangle}, \tag{6.11}$$

where, for rotating disks in GRMHD (e.g. Bugli et al., 2018)

$$W = [(w + p + b^2)\delta u^r \delta u^\phi - b^r b^\phi]\sqrt{\gamma_{\phi\phi}}\sqrt{\gamma_{rr}} \tag{6.12}$$

is the r, ϕ component of the stress tensor of fluctuations, based on the variations of the relevant 4-velocity components (compared to the equilibrium state at $t = 0$) and on the growing fluctuations of the magnetic 4-vector components (negligible at $t = 0$). As shown in Figure 6.5, the choice of the value $\bar{\alpha} = 0.1$ for the quenching is reasonable, since all runs saturate towards average values of $\alpha_{\rm disk}$ with this value, or slightly lower. This means that the introduction of the quenching effect is not expected to affect the overall dynamics, but just to limit the growth of the field in localized, critical zones.

The five runs have been repeated with identical parameters and the addition of the quenching effect, labelled as Run1q-Run5q in Table 6.2. As expected, the dynamo growth rates are basically unchanged in the quasi-kinematic phase. However, now the rates γ_2 appear to grow linearly with C_ξ, exactly as rates γ_1, even in the phase where turbulence and accretion are present (see the red symbols in Figure 6.4, for both γ_1 and γ_2). Notice that below $C_\xi = 400$ the γ_2 values are lower than the corresponding cases without quenching, as expected, but higher above that value, where however the blue data looked pathological since no regular trend was followed. Four additional runs with C_ξ increasing from $\simeq 750$ up to $\simeq 1800$ have also been performed, again in presence of the quenching term. The linear trend for γ_2 is less evident than what shown in Figure 6.4, though we find a final value $\gamma_2 \simeq 1.5$, that is more or less what one would expect from a linear extrapolation.

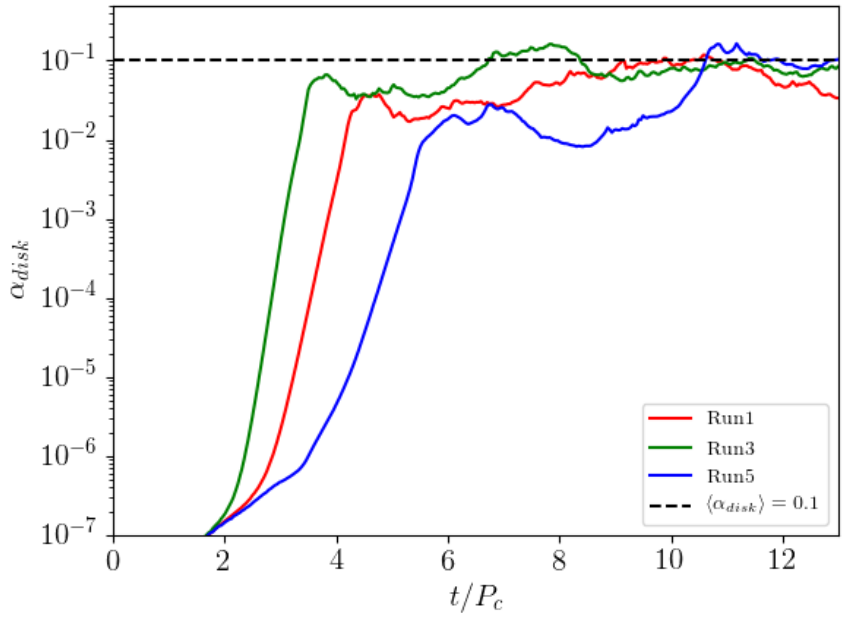

Figure 6.5: The quantity $\alpha_{\rm disk}$ defined in Eq. (6.11) as a function of time, for three runs with different dynamo number C_ξ.

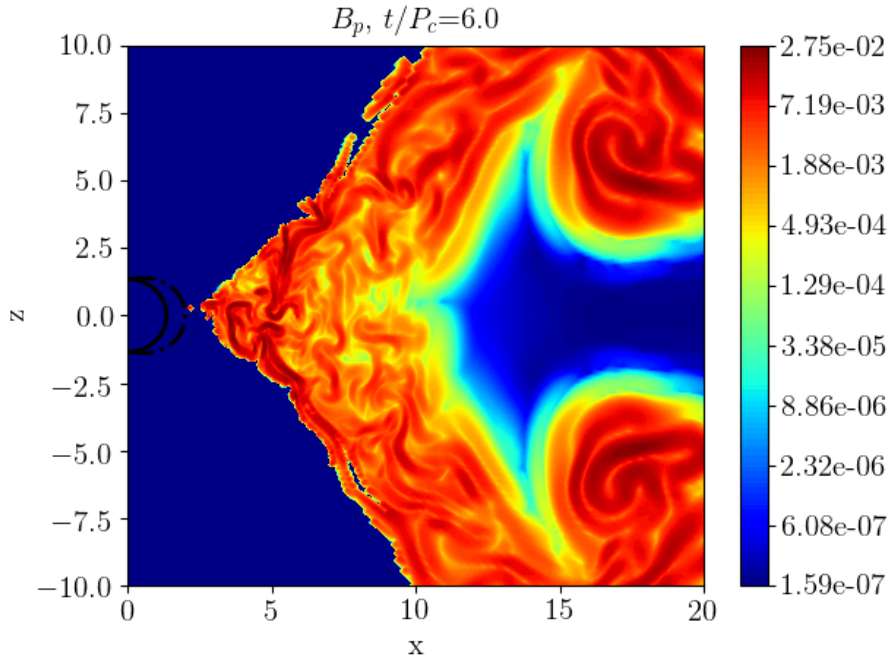

Figure 6.6: Map of the poloidal field (in logarithmic scale) for $t = 6P_c$ (Run1q, with quenching), to be compared with the third panel of Figure 6.3 (Run1, without quenching).

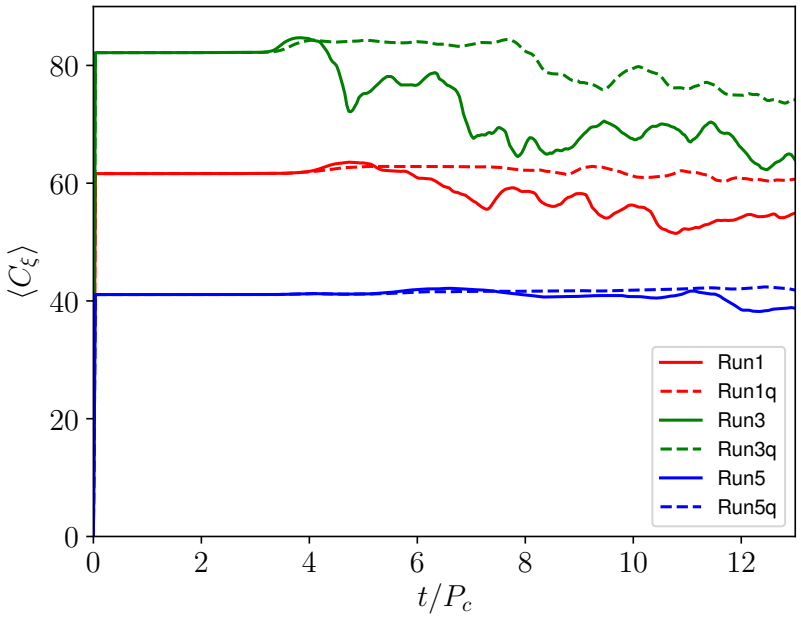

Figure 6.7: Time series of the dynamo number C_ξ averaged over the whole disk.

These results show that the dynamo appears to be the main mechanism for amplifying magnetic fields even during the phase in which the disk starts to lose mass, which is accreting onto the black hole. Furthermore, when quenching is activated, since a lower magnetic field is present, the formation of vortices evacuating the plasma is inhibited and the dynamo structures evolve more smoothly even in a turbulent environment, as clearly shown in Figure 6.6.

In order to better clarify why the secondary growth rate γ_2 is lower than the corresponding γ_1, we plot in Figure 6.7 the time series of the spatial averages of the C_ξ dynamo number. We clearly see that, when the accretion begins and the first saturation phase starts, the quantity decreases for all runs without the quenching term and for Run3q as well. This is due to the fact that during accretion the density can be modified substantially, and $\langle C_\xi \rangle$ as well, and this effect is stronger for higher magnetization levels. When the quenching term is present both magnetization and turbulence are generally lower, the presence of the low-density vortices is avoided, and the overall dynamics is certainly more regular. In any case, especially for runs with quenching, the lower values of γ_2 cannot be attributed to correspondingly smaller values of $\langle C_\xi \rangle$, while migration of the plasma near the border of the disk, where C_ξ is reduced, appears to be more important. In addition, when the density is low, the other dynamo term, C_Ω, gets larger values, and for a constant C_ξ the overall growth rates are expected to be reduced (see Table 1 in Bugli et al., 2014).

A very interesting result is that the value of C_ξ and the presence of quenching do not affect too much the value of the quantities in the final saturation stage, as can be seen in Figure 6.8, where the growth of the average strength of the magnetic field is plotted for our six reference runs. The initial kinematic growth and also the first saturation phase clearly depend on C_ξ, as the fastest growing mode occurs at a wavenumber $\sim \xi/\eta$ (Brandenburg and Subramanian, 2005), with smaller scales triggered by MRI leading to a turbulent cascade towards the dissipative scales. However, the second and final saturation phase looks approximately independent on the C_ξ value and on the

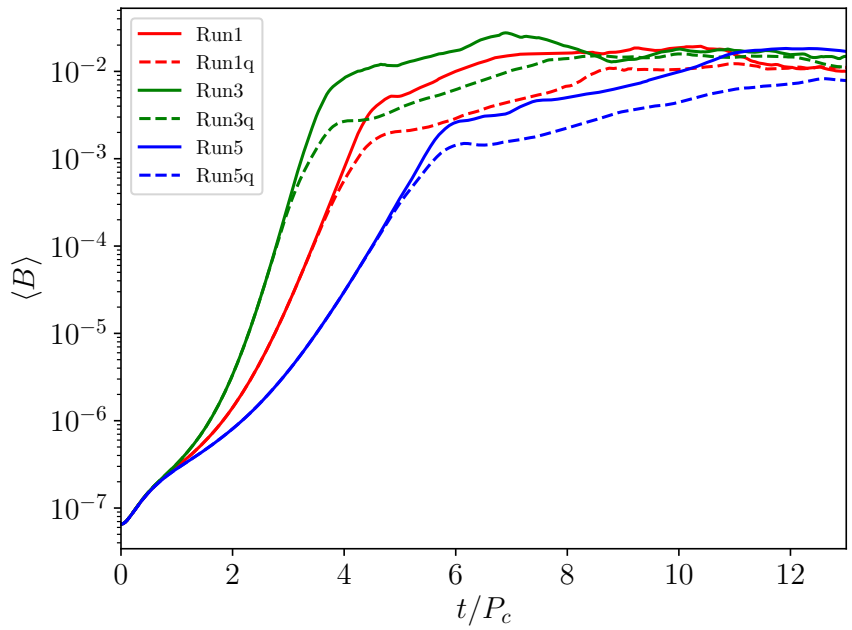

Figure 6.8: Time evolution of the averaged intensity of the magnetic field, for three runs without and with quenching.

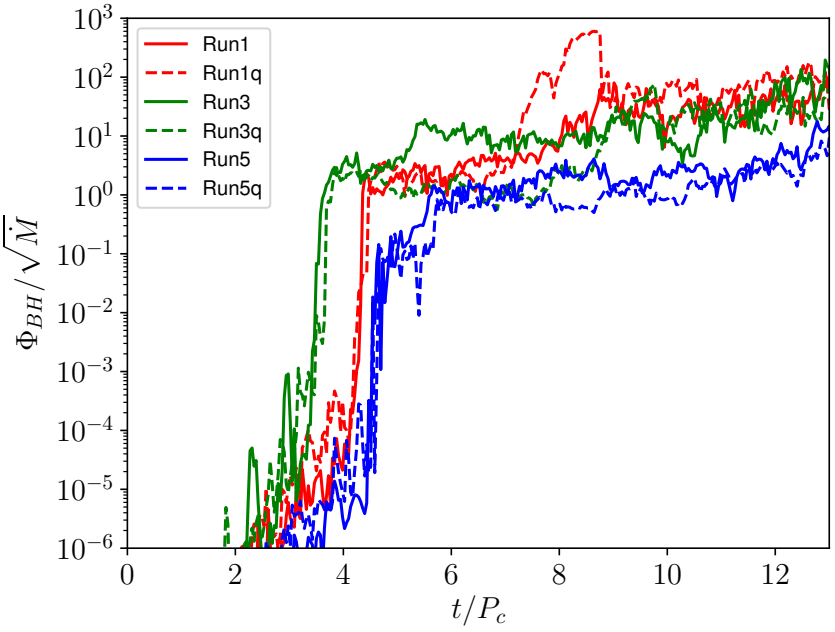

Figure 6.9: Time evolution of the magnetic flux $\Phi_{\rm BH}$ penetrating the horizon, divided by the accretion rate, for the same six runs as in Figure 6.8.

presence of quenching (all curves tend to the same value of $< B >$ within a factor of $\simeq 3$), hence we deem that the accretion dynamics and the reached equipartition with the fluid component play a major role at this final stage (see the similar behavior of $\alpha_{\rm disk}$).

For completeness, the magnetic flux threading one hemisphere of the black hole horizon, $\Phi_{\rm BH}$, has been evaluated, a quantity which is very important because the rotational energy extracted, the Blandford-Znajek power, is proportional to its square (Blandford and Znajek, 1977; Tchekhovskoy et al., 2011). This is defined as

$$\Phi_{\rm BH} = \frac{1}{2}\, 2\pi \int_0^{\pi} |B^r| \sqrt{\gamma}\, {\rm d}\theta, \tag{6.13}$$

to be evaluated at the outer event horizon r_h. Note that throughout the literature there are two different definitions of the magnetic field components in terms of the dual of the Faraday tensor: one as $B^i = F^{\star i0}$ (e.g. McKinney and Gammie, 2004), the other as $B^i = -n_\mu F^{\star \mu i} = \alpha F^{\star 0 i}$ (e.g. Del Zanna et al., 2007), where n^μ is the Eulerian observer unit vector (only this second one is a proper spatial projection according to the $3+1$ splitting). Figure 6.9 describes, for our six reference runs, the time evolution of the MAD parameter $\phi = \Phi_{\rm BH}/\sqrt{\dot{M}}$. This quantity, as we said, is commonly used to discriminate SANE evolution models from MAD ones (e.g. Porth and EHT-Collaboration, 2019), depending whether its maximum value is below or above a certain threshold. In our runs, in order to reach the typical SANE values we have of course to wait for the saturation of the first magnetic field growth. However the comparison with the values obtained in the Code Comparison Project is not possible here due to the different disk model adopted.

6.1.4 On the magnetorotational instability

In the non-linear regime it is interesting to investigate whether MRI is capable of affecting the dynamo action or, more generally, of changing substantially the structure of the magnetic field.

It is custom to define the so-called MRI quality factor, a parameter that allows to establish if a given simulation is able to resolve the characteristic MRI wavelength $\lambda_{\rm MRI}$, precisely by measuring the number of cells contained in $\lambda_{\rm MRI}$, for a given direction. In our axisymmetric case the important quality factor is the one along the direction θ, hence here we define

$$Q_\theta = \frac{\lambda_{{\rm MRI},\theta}}{\sqrt{\gamma_{\theta\theta}}\Delta\theta} = \frac{2\pi |v_A^\theta|}{\Omega \sqrt{\gamma_{\theta\theta}}\Delta\theta}, \tag{6.14}$$

where $v_A^\theta = B^\theta/\sqrt{w + B^2}$ is the θ-component of the relativistic Alfvén velocity (here neglecting the contribution by the electric fields). Values of $Q_\theta > 6 - 8$ have been shown to be necessary to capture locally the linear growth of MRI, while a threshold of $Q_\theta > 10$ can capture its nonlinear growth (Noble et al., 2010; McKinney et al., 2012; Hogg and Reynolds, 2018).

Figure 6.10 shows the time evolution of the factor Q_θ, averaged over the whole disk, in the case of Run1. Apparently the MRI instability could be resolved during the dynamical phase and therefore, if present, it would be expected to play a role in the growth of the magnetic field, competing with the ongoing dynamo process.

To investigate this aspect we have re-executed Run1 twice, the first time by setting $\xi = 0$ for $t/P_c > 4.5$, at the end of the first linear stage, and the second one for $t/P_c > 8.0$, just before the final saturation after the second linear phase. As we can see in Figure 6.11, the magnetic field

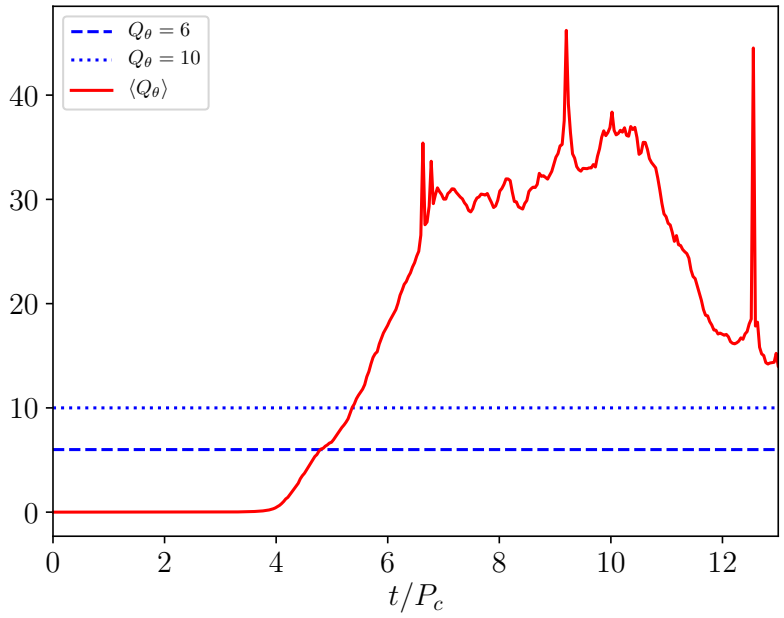

Figure 6.10: Time dependence of the averaged MRI quality factor Q_θ, for Run1 parameters. The two horizontal lines are the thresholds for resolving the linear (dashed line) and nonlinear (dotted line) phases.

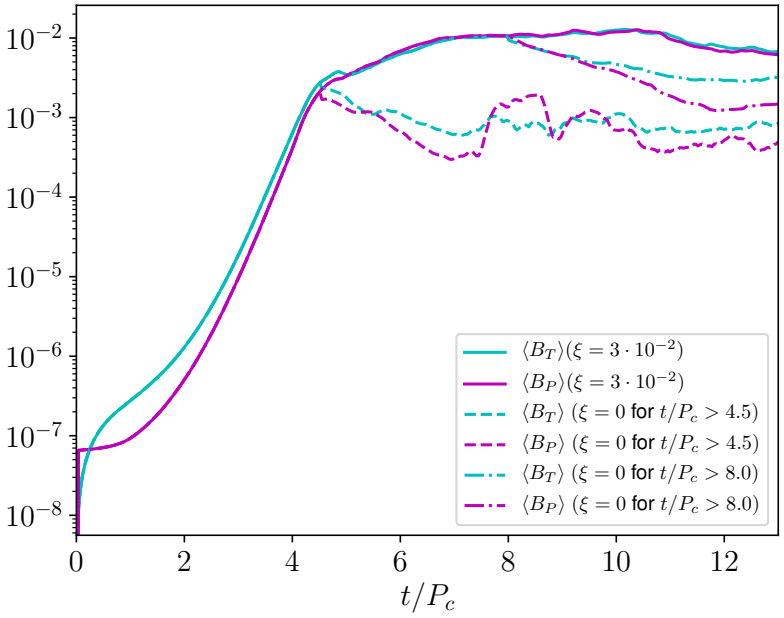

Figure 6.11: Growth of the magnetic field components for Run1 and for two additional runs with the same parameters but switching off the dynamo ($\xi = 0$) for $t/P_c > 4.5$ (dashed lines) and for $t/P_c > 8.0$ (dot-dashed lines).

components immediately start to decrease after the dynamo has been switched off, in both cases. Notice that the poloidal component is the one suffering the fastest decrease, the toroidal one is probably still supported by a residual amplification due to rotation (a purely Ω effect).

This result means that the dynamo action is the main driver for magnetic field enhancement in all phases, whereas MRI, which is surely present and resolved numerically in our simulations, seems to be responsible mainly for triggering turbulence and driving the accretion. Amplification of magnetic fields by MRI is instead less strong than the one due to the mean-field dynamo (we recall that our simulations are 2D axisymmetric), and its effect is only visible in the final saturation stage, where a faster decrease due to dissipation is inhibited. We conclude by saying that the adopted resistivity value of $\eta = 10^{-3}$ is still above the level of numerical dissipation, which is estimated to be $\eta \sim 10^{-4}$ for the resolution employed.

6.1.5 Comparison with Sgr A* radio emission

Our GRMHD models based on the dynamo action will be used here to infer the synthetic emission by the magnetized plasma of the accreting matter and to compare it with observational data. The most straightforward targets are obviously the two sources observed by EHT, Sgr A* and M87*, i.e. the cores containing the super-massive black holes of our Galactic center and of the elliptical galaxy M87. In the latter case the very first image of the emission from the regions around a black hole's event horizon has been recently taken (EHT-Collaboration, 2019a), whereas at the moment work is in progress to reduce data in the case of Sgr A*.

Since our simulations are more focused on the plasma dynamics occurring inside the disk, with the magnetic field growing from initial seed values, we choose here to compare our model with Sgr A* data, as in the case of M87* a substantial fraction of the emission is known to come from the polar jet. The structure of Sgr A* is rather uncertain because the source is hidden by optically thick interstellar medium that surrounds it. For this reason models with or without a jet have been built over the years to infer its emission properties (Mościbrodzka et al., 2009; Mościbrodzka and Falcke, 2013; Mościbrodzka et al., 2014).

The radio emission in the mm band of the Sgr A* spectrum can be modelled by the radiation produced by thermal synchrotron-emitting relativistic electrons in a ADAF model. As described in chapter 2, most of the energy is stored in the thick pressure-supported disk and advected inwards with high speed and efficiency. The large scale-height and accretion velocity makes the density low, the gas cooling time long compared to advection times (the temperature of proton remains high, $T_p \sim 10^{11} - 10^{12}$ K), and the plasma is optically thin.

The total emissivity per unit frequency j_ν is given by Eq. (2.31). For an optically thin source, like Sgr A*, the spectral luminosity is simply defined by

$$L_\nu = 2\pi \int_{r_h}^{r_2} \mathrm{d}r \int_{\theta_1}^{\theta_2} \mathrm{d}\theta \sqrt{\gamma}\, j_\nu, \tag{6.15}$$

and the observed flux would be $F_\nu = L_\nu / 4\pi d^2$, where $d = 7.86$ kpc is the estimated distance of the Galactic Center (Boehle et al., 2016).

In ADAF systems, as we said, electrons are cooled by synchrotron, inverse-Compton, and magneto-bremsstrahlung emission losses, but ions maintain their high temperatures due to inef-

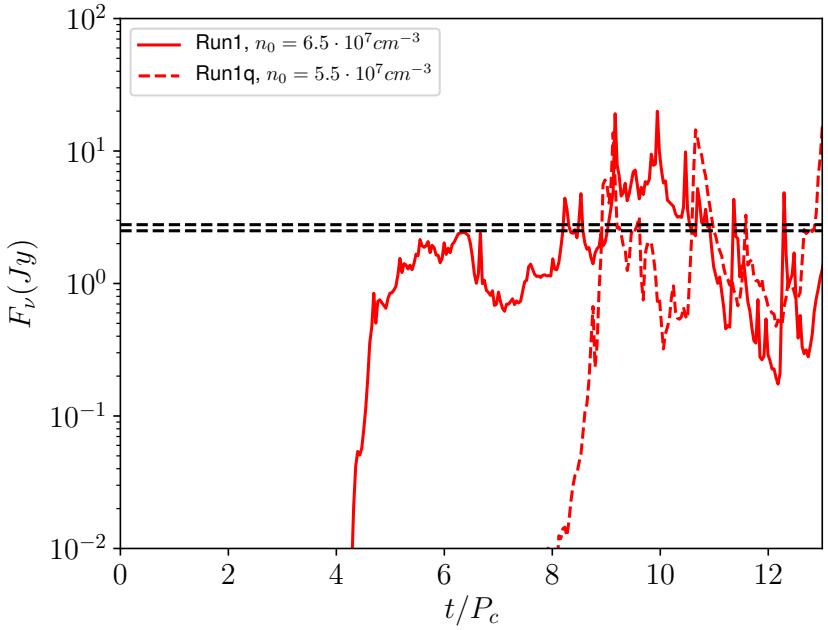

Figure 6.12: Time evolution of the synthetic flux F_ν computed on top of Run1 (solid line), and of Run1q (dashed line). The horizontal dashed lines represent the observed value at for the reference frequency $\nu = 230$ GHz.

ficient thermalization, thus a two-temperature plasma where the electron temperature is much lower than that of protons, $T_e \ll T_p$, is usually assumed. The ratio between proton and electron temperatures is assumed to be given by Eq. (2.32).

In order compute the above emission quantities it is necessary to appropriately convert all quantities from code units to the CGS system, hence

$$n_e = n_p = (\rho/\rho_0)n_0, \tag{6.16}$$

where we recall that n_0 is a free parameter providing the number density at the disk center, the magnetic field in expressed in units $B_0 = \sqrt{4\pi\rho_0 c^2}$, the normalized proton temperature is defined as

$$\Theta_p = \frac{kT_p}{m_p c^2} = \frac{p/p_0}{\rho/\rho_0}, \tag{6.17}$$

whereas Θ_e can be inferred from Eq. (2.32). Reference units for length and time are determined once the mass of the black hole has been assigned, for Sgr A* we assume $M_{\rm BH} = 4.02 \times 10^6 M_\odot$ (Boehle et al., 2016).

In the following, we show that our model (we choose Run1 and Run1q parameters) can predict that the initial magnetic field ($\sim 10^{-4}$ G) is amplified by the mean-field dynamo up to a level able to explain the observed flux in the millimeter wavelengths. The three free parameters left, namely ν, R_{high} and n_0, are chosen as follows: ν is set to 230 GHz, the same used for M87*, $R_{\rm high}$ is fixed to 20, a reasonable value in the disk and n_0 is chosen as the value that best reproduces the observed flux of 2.64 ± 0.14 Jy at 230 GHz (Mościbrodzka and Falcke, 2013; Mościbrodzka et al., 2014; EHT-Collaboration, 2019b). Let us look at Figure 6.12. The predicted synthetic flux follows

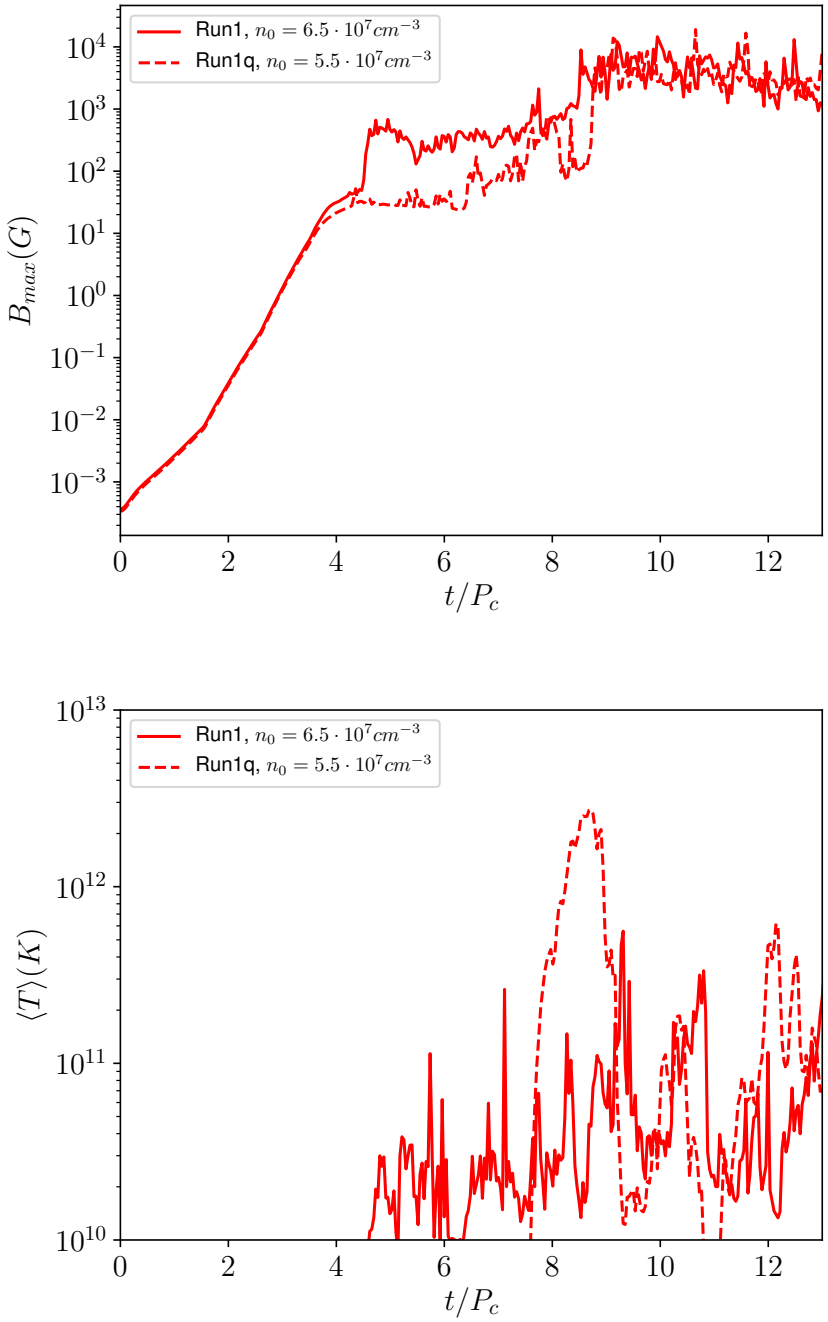

Figure 6.13: Time evolution of the maximum value of the magnetic field strength (upper panel) and of the average electron temperature (lower panel) for Run1 (solid line), and of Run1q (dashed line).

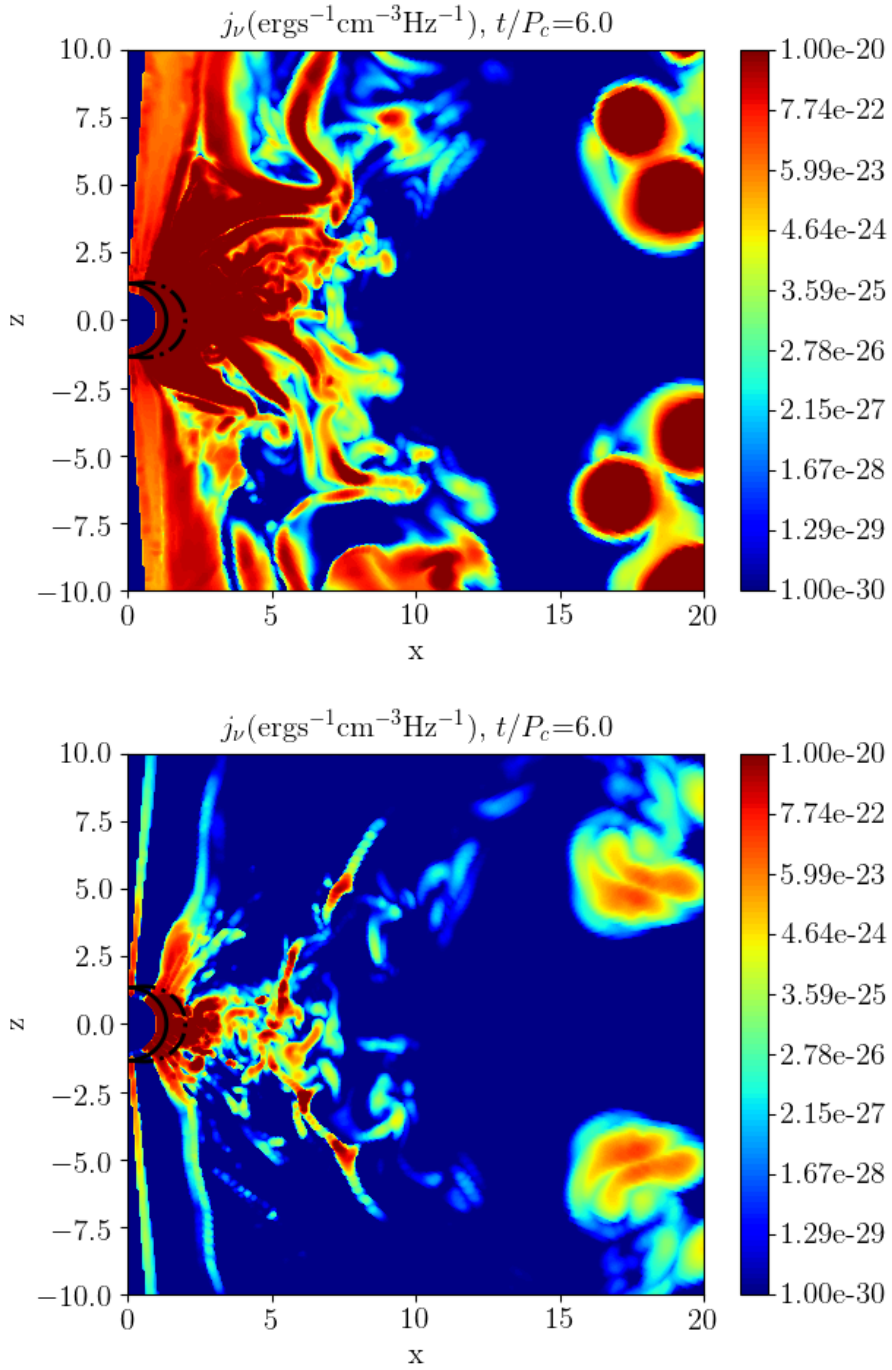

Figure 6.14: Local emissivity map for Run1 parameters in CGS units and logarithmic scale for $t/P_c = 6.0$. In the upper panel we show the situation without quenching and in the bottom panel with quenching. Values on the color bar are chosen to be the same for ease of comparison, hence the highest values of j_ν in the upper panel are actually saturated. (Figure not present in TO20)

the average magnetic field trend, increasing until it reaches a quasi-stationary value. We perform a time average in the range $t/P_c = [7-13]$, obtaining a flux of 2.59 Jy consistent with the observations when assuming $n_0 = 6.5 \cdot 10^7$ cm^{-3} for Run1 and $n_0 = 5.5 \cdot 10^7$ cm^{-3} for Run1q.

In Figure 6.13 (upper panel) we show the time evolution of the maximum value of the magnetic field in the disk, reaching $B_{\max} \simeq 3 - 4$ kG at the saturation of the dynamo process. At the same time, the average electron temperature reaches $\langle T_e \rangle$ just below 10^{11} K (lower panel). Overall these quantities result in agreement with the values obtained in the simulations of Mościbrodzka et al. (2009); Mościbrodzka and Falcke (2013).

Finally, emissivity maps (Figure 6.14) show that in this model most of the emission comes from the disk, as anticipated. In particular, significant emission comes from the very central accreting region, and from the outer regions of the disk where the dynamo process is still at work, with the same vortical structures observed for the magnetic field (much reduced in the case with quenching, as well as part of the emission from the polar jets).

6.2 Are GRMHD Mean-Field Dynamo Models of Thick Accretion Disks SANE?

The goal of the second paper (Tomei et al., 2021) is to extend the analysis of Tomei et al. (2020) (TO20 from here on), recently confirmed by Vourellis and Fendt (2021) including the case of a thin accretion disk, to a wider range of parameters and to much longer dynamical times and, above all, to reproduce the relevant standard diagnostics of the Code Comparison Project, and hence also the EHT observations, by using axisymmetric GRMHD simulations of accretion disks with mean-field dynamo action. The main purpose is to show how we can correctly model the SANE accretion scenario that, although SANE models now seem to be less favored compared to MAD models for M87* (EHT-Collaboration, 2021b), can still be considered an interesting case for other sources and a perfect benchmark for GRMHD theoretical models. In particular we show how it is possible to model this regime even adopting much cheaper 2D simulations, rather than 3D, and this can be achieved by starting from a more agnostic, though very unfavorable, initial configuration of a very weak (toroidal) magnetic field ($\sigma_{\max} \sim 10^{-6}$), which is to be naturally amplified in both the toroidal and poloidal components by the action of the dynamo.

6.2.1 Disk Model and Numerical Setup

We consider the hydrodynamic torus described by the Fishbone–Moncrief's solution (Fishbone and Moncrief, 1976) commonly adopted in the literature, as well as in Porth and EHT-Collaboration (2019). The space-time is determined by a Kerr black hole with dimensionless spin $a = 0.9375$. The inner edge of the disk is localized at $r_{in} = 6M$, and the density has a maximum of $\rho = \rho_c$ at $r_c = 12M$. We assumed an ideal gas equation of state with adiabatic index $\hat{\gamma} = 4/3$. Unlike TO20, here, we chose to superimpose on the hydrodynamic torus an initial toroidal magnetic field with negligible amplitude, so that the equilibrium is essentially preserved. Such a configuration is the most unfavorable to reproduce the conditions observed in ideal GRMHD models, as they generally assume large-scale poloidal magnetic fields. We take an initial magnetic field intensity $B_\phi \propto \rho$ as in Vourellis and Fendt (2021), with a maximum magnetization at the center of the torus

of $\sigma_{\rm max} = 10^{-6}$. The resistivity and dynamo profiles are similar to those in TO20, that is:

$$\eta = \begin{cases} \eta_0 \sqrt{\rho/\rho_c} & \rho \geq \rho_{\rm disk} \\ 0 & \rho < \rho_{\rm disk}, \end{cases} \tag{6.18}$$

$$\xi = \begin{cases} \xi_0 (\rho/\rho_c) \cos\theta & \rho \geq \rho_{\rm disk} \\ 0 & \rho < \rho_{\rm disk}, \end{cases} \tag{6.19}$$

where η_0 and ξ_0 are the maximum values of the resistivity and dynamo coefficients at $t = 0$ (note that the density varies both in space and time), and $\rho_{\rm disk} = 10^{-3}\rho_c$ is the density threshold that defines the boundary between disk and atmosphere. We also define the dynamo numbers as in Vourellis and Fendt (2021):

$$C_\Omega = r \left| \frac{\partial \Omega}{\partial r} \right| \frac{H^2}{\eta}, \tag{6.20}$$

$$C_\xi = H \frac{\xi}{\eta}, \tag{6.21}$$

where $\Omega = u^\phi / u^t$, and $H \simeq 0.25r$ is the scale height of the disk.

Using the horizon-penetrating Kerr–Schild coordinates, we carried out a series of axisymmetric simulations, expanding the range of parameters with respect to TO20 (see Table 6.3). In order to assess the validity of our results with respect to the diagnostics in the Code Comparison Project, we adopted the same resolutions as the simulations of Porth and EHT-Collaboration (2019) (see Table 6.4 for details). Unlike in TO20, here, we did not adopt any explicit dynamo quenching.

Table 6.3: Maximum initial values of η, ξ, C_Ω, and C_ξ for each model.

Run	$\boldsymbol{\eta_0}$	$\boldsymbol{\xi_0}$	$\boldsymbol{C^{max}_{\Omega,0}}$	$\boldsymbol{C^{max}_{\xi,0}}$
Eta-3Xi-3	10^{-3}	10^{-3}	8.2×10^4	0.75
Eta-3Xi-2	10^{-3}	10^{-2}	8.2×10^4	7.5
Eta-3Xi-1	10^{-3}	10^{-1}	8.2×10^4	75
Eta-4Xi-3	10^{-4}	10^{-3}	8.2×10^5	7.5
Eta-4Xi-2	10^{-4}	10^{-2}	8.2×10^5	75
Eta-4Xi-1	10^{-4}	10^{-1}	8.2×10^5	750

Table 6.4: Details on the numerical grid adopted. Here $r_h \simeq M$ is the event horizon radius.

Axis	**Grid Points**	**Domain**	**Stretching**
r	192	$(r_h - 0.25M, 3000M)$	Logarithmic
θ	192	$(0.06, \pi - 0.06)$	Uniform

6.2.2 Results

We first describe the time evolution of the radial magnetic field in the torus driven by the mean-field dynamo. The creation of a poloidal component within the disk begins from the earliest times, as shown in Figure 6.15, where the temporal evolution of the disk-averaged $\langle |b^r| \rangle$, with $|b^r| =$

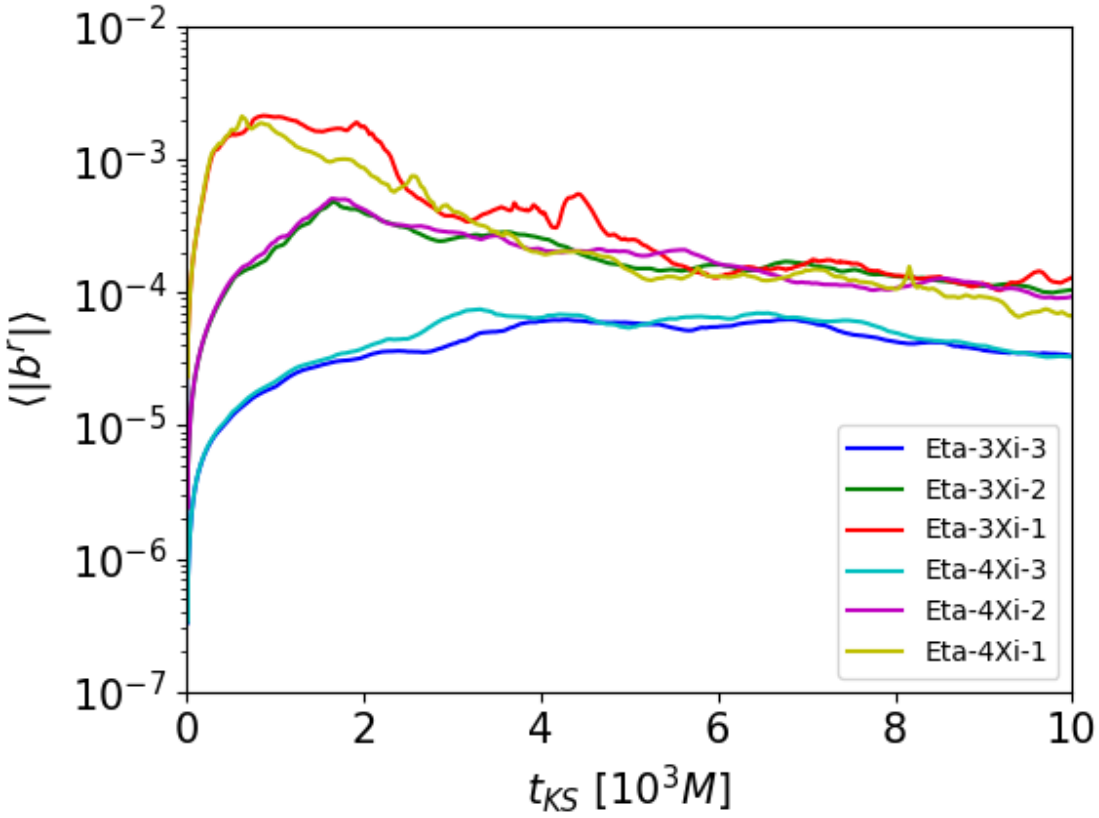

Figure 6.15: Time evolution of $|b^r|$ averaged on the disk for each model.

$\sqrt{b^r b^r g_{rr}}$, is plotted (we consider the comoving field). Here, the averaging operation of any quantity q is defined as Eq. (6.8) in TO20, with $r_1 = r_h$, $r_2 = 50M$, $\theta_1 = \pi/3$, $\theta_2 = 2\pi/3$.

The dependence on ξ_0 (i.e., the dynamo α effect) is evident in the duration of the initial kinematic phase, in the steepness of the curve, and in the maximum value that is reached: the higher the ξ_0, the faster the evolution towards a higher radial magnetic field value. After a transient, there is a saturation phase followed by a decrease in $|b^r|$ inside the torus. In particular, in the runs of strong and intermediate dynamo, the saturation value is similar, while it is lower in models with weak dynamo. As shown later, the low intensity of the initial dynamo in runs Eta-3Xi-3 and Eta-4Xi-3 seems not to be able to produce the turbulence needed to resolve the fastest growing mode of the MRI, and thus, the accretion is entirely driven by the action of the weak dynamo.

The decrease of the amplification of the poloidal magnetic field in all simulations does not seem to depend on an intrinsic decrease in dynamo action. Figure 6.16 shows that dynamo numbers remain fairly constant over time. The most likely explanation is that the fragmentation of the magnetic structures leads to a global loss of efficiency in the dynamo coupling mechanism, hence leading naturally to a self-regulated quenching, as first observed by TO20 and later confirmed in Vourellis and Fendt (2021).

In order to understand whether the accretion regime that is established in our dynamo runs is consistent with 3D ideal GRMHD simulations of SANE disks, in the remainder of the paper, we attempt to reproduce the main standard diagnostics as studied in Porth and EHT-Collaboration

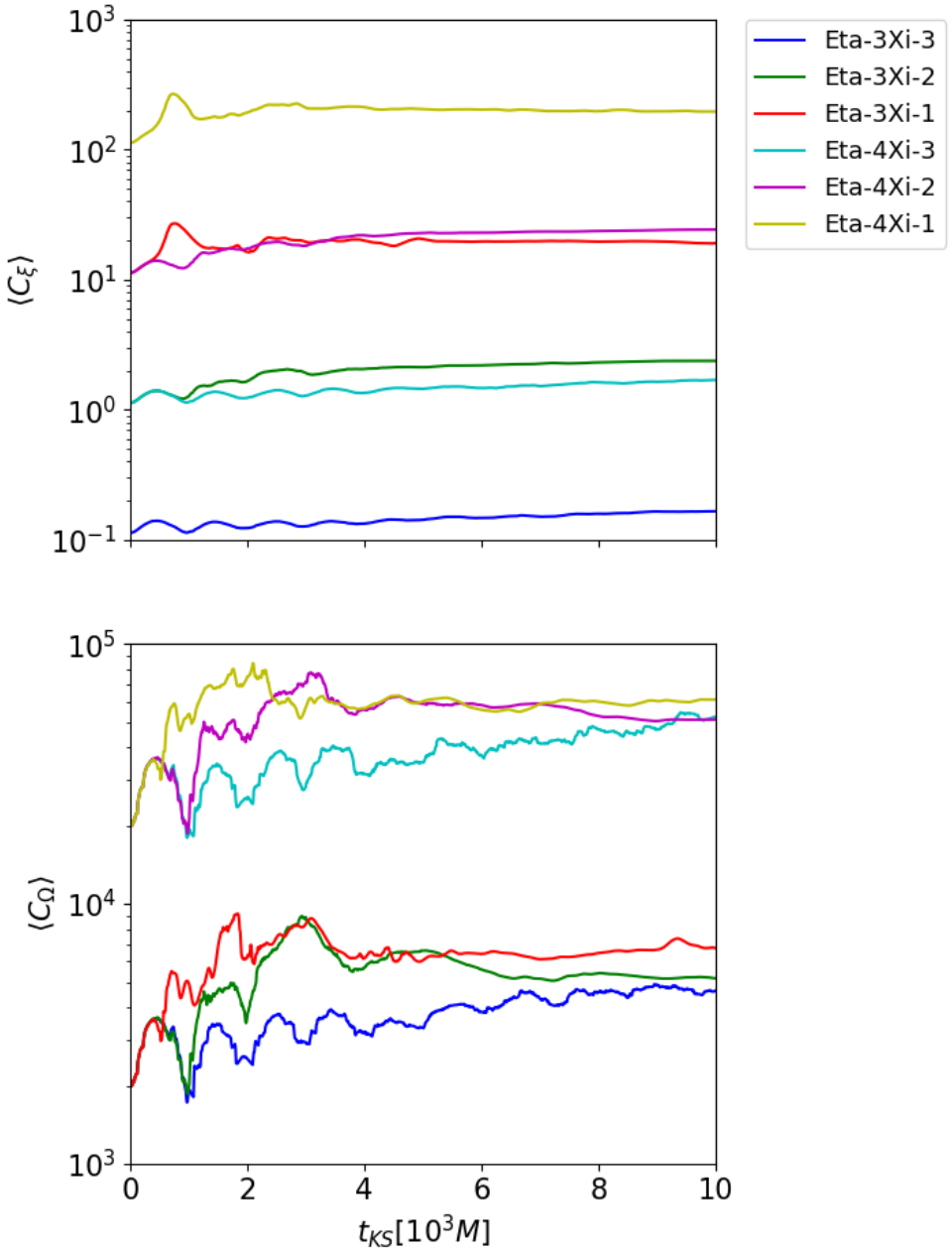

Figure 6.16: Time evolution of the dynamo numbers averaged on the disk for each model.

(2019).

Horizon Penetrating Fluxes

We briefly recall that the definitions of the mass, magnetic, angular momentum and energy fluxes evaluated at the horizon (see Section 5.1.2) in the axisymmetric case are

$$\dot{M} = 2\pi \int_0^\pi \rho u^r \sqrt{-g}\, d\theta, \tag{6.22}$$

$$\Phi_{BH} = \pi \int_0^\pi |{}^*F^{rt}| \sqrt{-g}\, d\theta, \tag{6.23}$$

$$\dot{L} = 2\pi \int_0^\pi T^r_\phi \sqrt{-g}\, d\theta, \tag{6.24}$$

$$\dot{E} = 2\pi \int_0^\pi (-T^r_t) \sqrt{-g}\, d\theta, \tag{6.25}$$

where ${}^*F^{\mu\nu}$ is the Maxwell tensor, and $T^{\mu\nu}$ is the stress-energy tensor. Usually, the fluxes defined by (6.22)–(6.25) are normalized with the accretion rate $\dot{M}$. We also remember that the critical value of the normalized magnetic flux is $\phi_{\max} = 15$ in the case of a black hole with spin $a = 0.9375$ and a disk with scale ratio $H/R \sim 0.25$

In the ideal simulations of Porth and EHT-Collaboration (2019), the accretion starts at $t \simeq 300$M when the linear MRI, triggered by pressure perturbations, is captured. After the transient, ϕ reaches the value $\phi \sim 1$, typical of the SANE regime. Accretion rate, angular momentum flow, and net energy flow efficiency also become stationary, with average values of $\dot{M} \sim 0.1$, $\dot{L}/\dot{M} \sim 2$, and $|\dot{E} - \dot{M}|/\dot{M} \sim 0.05$.

Figure 6.17 shows the time series of the normalized fluxes obtained in our dynamo runs. The evolution clearly depends on the value of ξ_0, while there is no substantial dependence on η_0. The two runs with weak dynamo (Eta-3Xi-3, Eta-4Xi-3) produce low accretion rates and cannot be considered good SANE models. Instead, the two runs with intermediate dynamo (Eta-3Xi-2, Eta-4Xi-2) show a very good agreement with the results shown in Figure 4 of Porth and EHT-Collaboration (2019): the accretion starts at $t \sim 1000$M, and after an initial transient, the accretion rate saturates to the value of $\dot{M} \sim 0.1$.

The magnetic flux and the angular momentum flux remain almost constant during the simulation, $\phi \sim 1$ and $\dot{L}/\dot{M} \sim 2$. The trend in net energy flow efficiency, $(\dot{E} - \dot{M})/\dot{M}$, differs slightly from that of Porth and EHT-Collaboration (2019): in our dynamo models it can assume negative values, although the final value is consistent with the one presented in the code comparison project, $(\dot{E} - \dot{M})/\dot{M} \lesssim 0.1$. Finally, the two models with strong dynamo (Eta-3Xi-1, Eta-4Xi-1) show a good agreement with Porth and EHT-Collaboration (2019), although with some differences compared to the case of intermediate dynamo. The initial transient is characterized by a higher and more impulsive accretion rate.

The magnetic flux in our models with $\xi_0 = 0.1$ is on average higher, with run Eta-3Xi-1 even showing two intensity spikes approaching the critical threshold of $\phi = 15$. The action of the stronger dynamo seems to affect the evolution of the angular momentum flux, which is less smooth and has

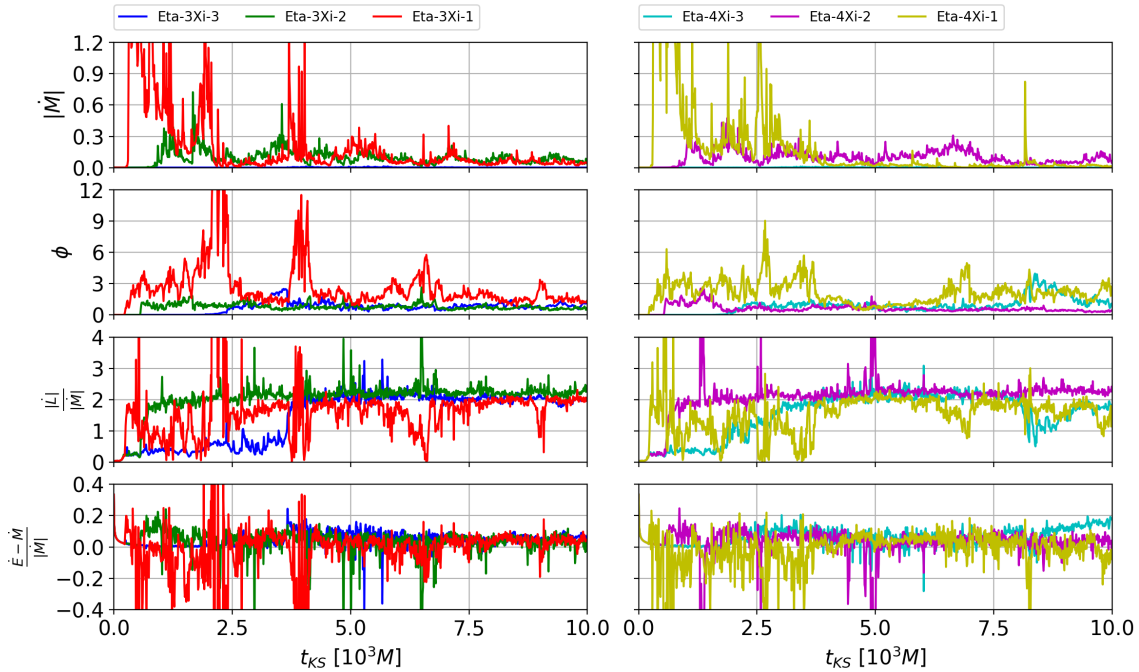

Figure 6.17: Time series of the horizon penetrating fluxes for each model (on the left panels, runs with $\eta_0 = 10^{-3}$; on the right panels, runs with $\eta_0 = 10^{-4}$).

values $\dot{L}/\dot{M} \lesssim 2$ in the stationary phase. As for net energy flow efficiency, an initial phase dominated by negative values is observed, except for the two positive bursts in run Eta-3Xi-1. The negative contribution to the energy efficiency is given by the enthalpy term (McKinney et al., 2012). In our simulations, we note that the contribution of enthalpy grows with ξ_0, meaning that the black hole is accreting more and more thermo-kinetically unbound matter.

MRI Quality Factors

The role of the MRI can be studied from the values assumed by the so-called quality factor. Along the θ direction, Q_θ is defined by Eq. (6.14). As in TO20, we considered $\langle Q_\theta \rangle = 6$ to be the threshold for resolving the MRI. Figure 6.18 shows that there is an initial time interval in which $\langle Q_\theta \rangle > 6$ for runs Eta-3Xi-2, Eta-3Xi-1, Eta-4Xi-2, and Eta-4Xi-1. Then the dissipation stops the MRI and the accretion is driven by the mean-field dynamo. Run Eta-3Xi-1 has a higher value of $\langle Q_\theta \rangle$ and is kept above the threshold for a longer time than the other runs, which is consistent with the higher observed magnetic flux. Overall, according to what has been observed by TO20, it seems that MRI cannot develop for a long time with an axisymmetric mean-field dynamo mechanism: while in the initial transient, MRI and dynamo can coexist, the subsequent stationary phase seems to be regulated exclusively by the self-quenched dynamo.

Time-Averaged Maps

To better appreciate the spatial structure of various quantities, a picture of the quasi-stationary state can be obtained from the time averaged rest-frame density, inverse plasma β, and the magnetization σ (Figures 6.20 and 6.21). We identify the disk with the regions occupied by bound denser and

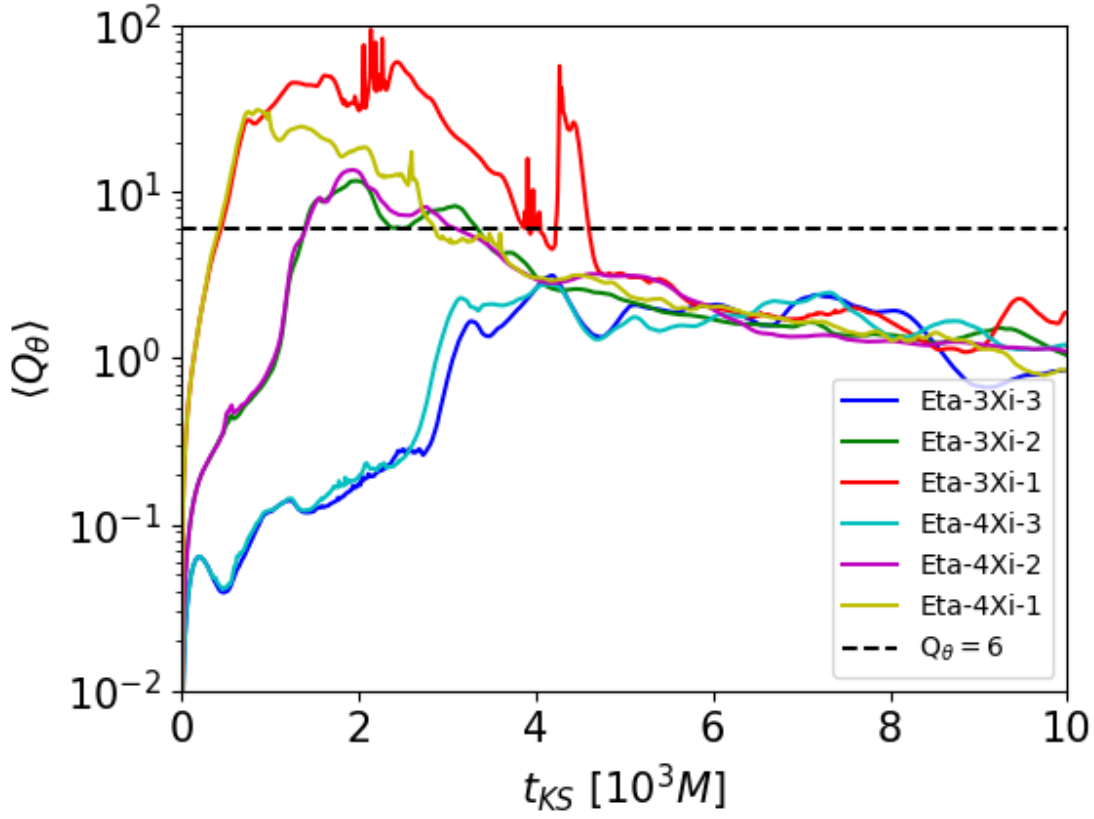

Figure 6.18: Time evolution of the Q_θ quality factor averaged on the disk for each model. The dashed black line indicates the minimum threshold for solving the linear MRI.

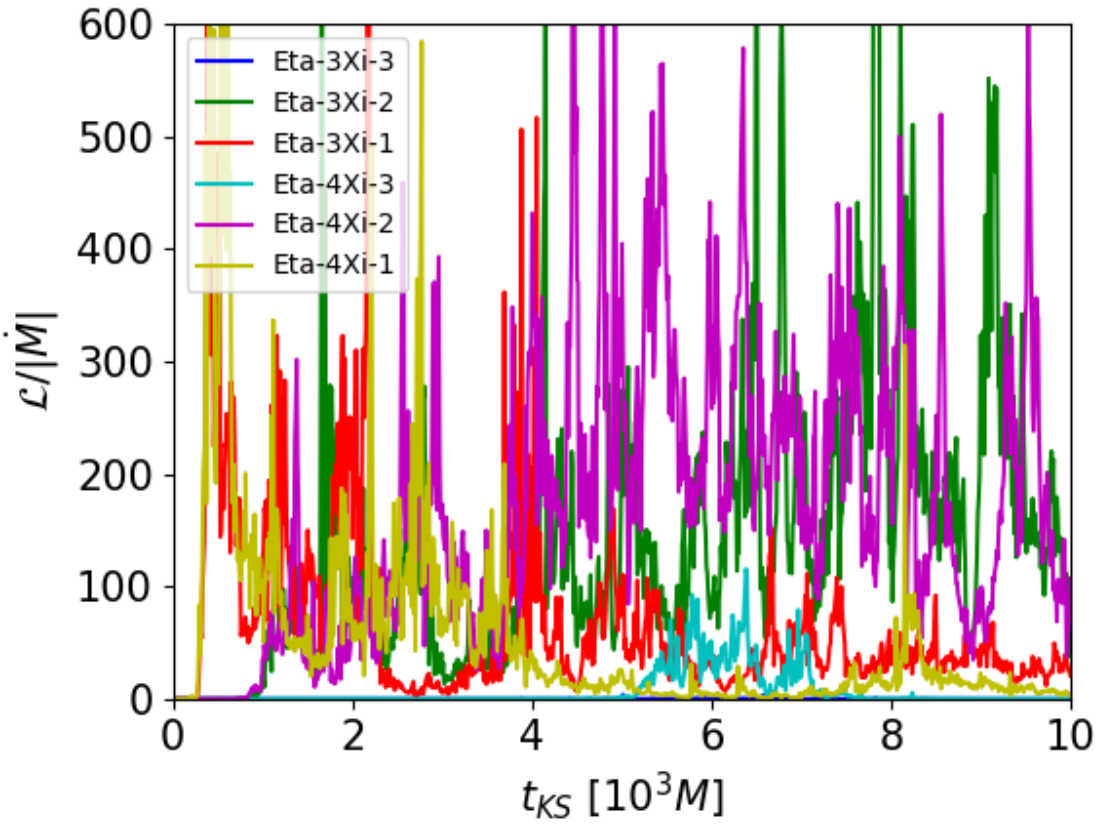

Figure 6.19: Time evolution of the pseudo-luminosity for each model. In runs with strong and intermediate dynamo, we see more noise than simulations of Porth and EHT-Collaboration (2019).

weakly magnetized plasma, the funnel by low-density and highly magnetized (Poynting-dominated) plasma, and the jet sheath separating them and containing the larger part of the material outflows. The time window $[5000M, 10{,}000M]$ is chosen so as to cover the stationary state for all simulations, and by adopting the same color scale used in Porth and EHT-Collaboration (2019), we will more easily compare our results.

The dynamo action of the dynamo significantly changes the structure of the torus. By increasing the parameter ξ_0, the disk evolves to a stationary state with lower density and pressure and has a more flattened shape on the equatorial plane. The funnel and the jet sheath are progressively wider as ξ_0 increases, as the central and right panels in Figures 6.20 and 6.21 show. By increasing C_Ω by a factor of 10 (i.e., reducing the resistivity), the contribution of the α effect of the dynamo during the initial transient is probably less dominant, leading the torus to lose less matter and tend more to the ideal case of Porth and EHT-Collaboration (2019) (Figure 6.21).

6.2.3 Synchrotron Pseudo-Luminosity

A further diagnostic is a proxy for the luminosity due to (thermal) synchrotron radiation defined as in Section 5.1.2 by Eq (5.11). Again, the time series of the luminosity in Figure 6.19 shows the best agreement with Porth and EHT-Collaboration (2019) in the two runs with intermediate dynamo, where $\mathcal{L}/\dot{M} \sim 200$ in the stationary phase. The strong dynamo produces lower luminosity because

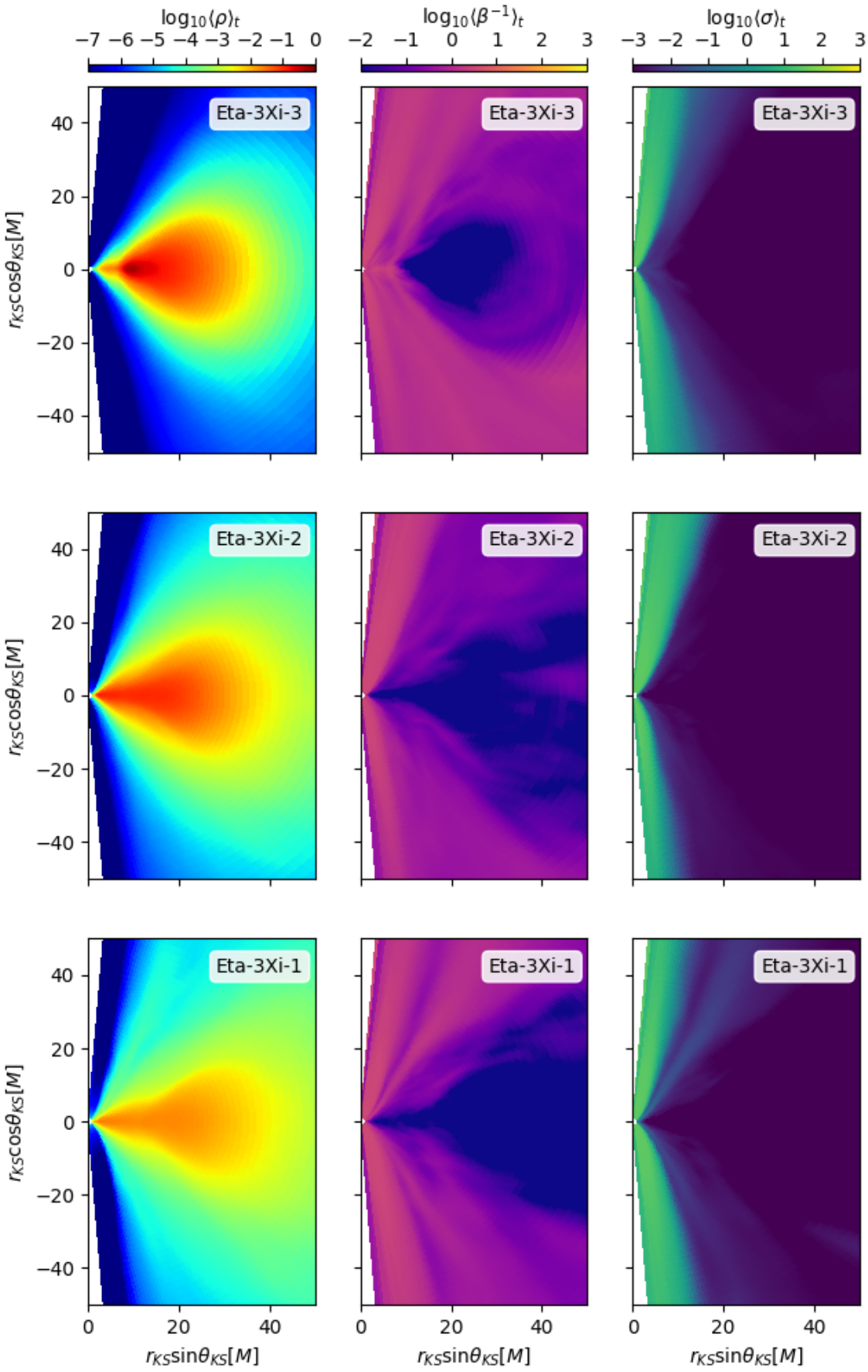

Figure 6.20: Time-averaged data for rest-mass density, inverse plasma β, and magnetization for runs with $\eta_0 = 10^{-3}$. We indicate with $\langle\cdot\rangle_t$ the time average in the range $[5000M, 10,000M]$.

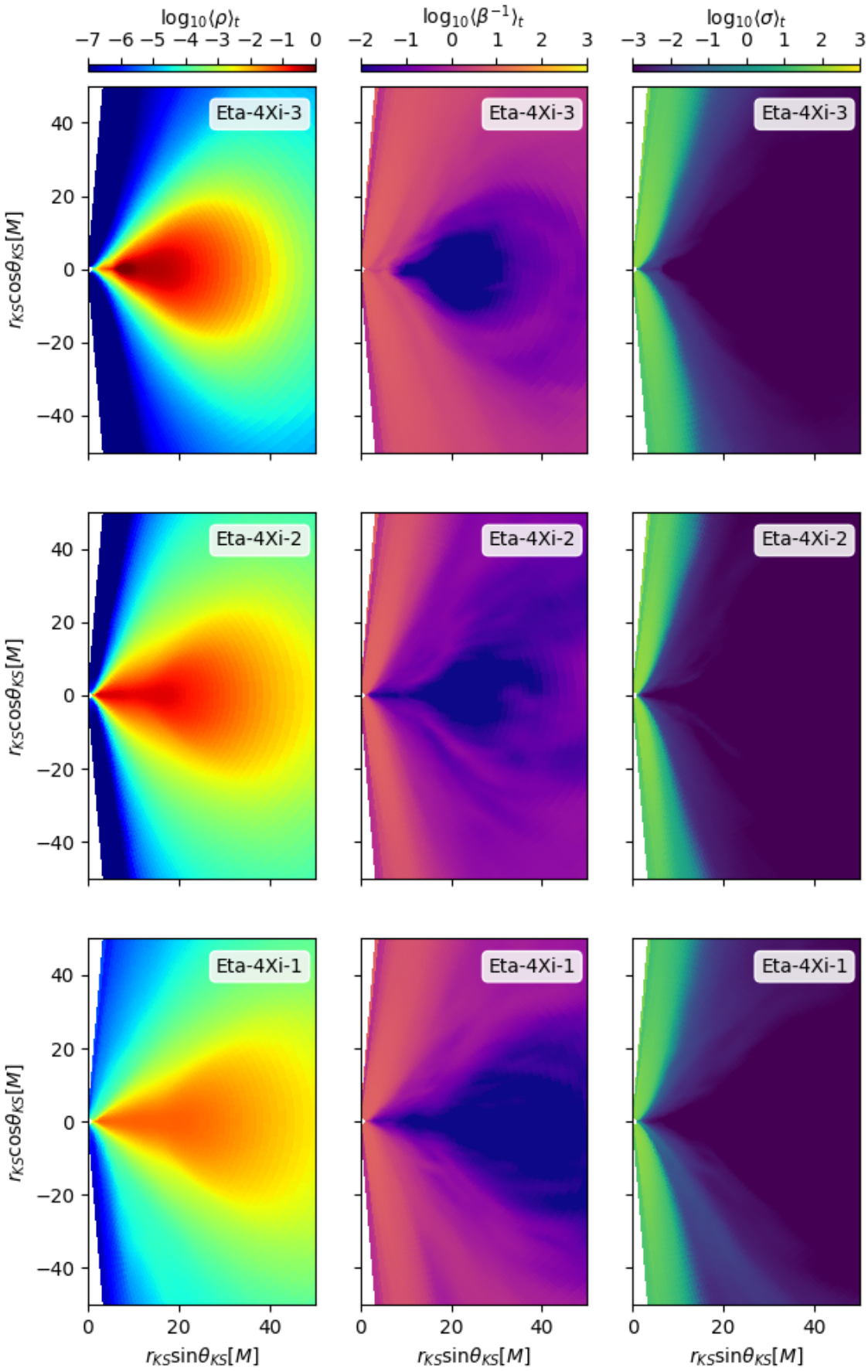

Figure 6.21: Time-averaged data for rest-mass density, inverse plasma β, and magnetization for runs with $\eta_0 = 10^{-4}$.

the disk has lost more matter, while the weak dynamo fails to produce a magnetic field intense enough to support this emission. This diagnostic shows greater variability than the ideal case due to the presence of extra fluctuations in both the magnetic field and the mass accretion rate.

Chapter 7

Conclusions

In this thesis work, we describe the non-ideal axisymmetric simulations, including both the resistive effects and, above all, the mean-field dynamo action due to sub-scale, unresolved turbulence, applied for the first time to black hole accretion disks in the fully non-linear regime. The work contained in the paper Tomei et al. (2020) can be seen as a first follow-up of our previous analysis in the purely kinematical regime (Bugli et al., 2014). Similar GRMHD simulations have been recently employed to model the dynamics and emission of the central core of the galaxy M87 (EHT-Collaboration, 2019e), comparing with observational data including the very first image of the shadow of a black hole's event horizon (EHT-Collaboration, 2019c). Contrary to the standard numerical initial set-up, where subdominant but non-negligible magnetic field ($p_{\rm mag}/p \sim 10^{-2}$) is present in the disc right from the start (e.g. Porth and EHT-Collaboration (2019)), here we initialize the simulation with an extremely small magnetic field ($p_{\rm mag}/p \sim 10^{-9}$), which is later self-consistently amplified during the evolution by the $\alpha-\Omega$ dynamo process. A linear kinematic exponential growth, followed by another one with a reduced rate when accretion becomes important, is observed for a variety of dynamo parameters. Both rates increase linearly with the dynamo parameter at least for the limited range explored here. The dynamo is clearly the main driver, with the second, reduced stage due to the fact that due to accretion the density in the disc is modified and the non-dimensional dynamo number C_ξ reduces in time, especially for runs with a stronger dynamo. At later times the accretion process and the stronger field are capable of affecting the overall structure of the disc itself and the growth of the magnetic field ceases, reaching a saturation phase where the magnetic field is approximately constant in time. The presence of an explicit quenching term in the α-dynamo shortens the linear phase but seems not to affect the final saturation stage, occurring roughly for similar values of the magnetic field strength (within a factor of three). The quenching also helps in avoiding the formation of a few pathological structures with highly magnetized vortices evacuating the plasma in the outer disc regions, and the overall dynamics is more regular. In spite of the widely recognized importance of MRI for global simulation of discs around black holes (e.g. Bugli et al. (2018), and references therein), and in spite of our simulations having the sufficient spatial accuracy to resolve such instability (the MRI quality factor exceeds 10 after a few rotational periods), this does not seem to play a major role here, if not as an initial trigger for the turbulent cascade and accretion on to the black hole. We have tested this hypothesis by switching off the dynamo term at the end of each growth phase (in different runs with otherwise the same parameters): the field starts to decrease immediately, and MRI seems to be just capable of balancing dissipation at small

scales, reaching a steady (turbulent) state at late times. By assuming the approximation of an optically thin plasma, as expected for Sgr A*, the accreting supermassive black hole of our Galaxy, we have computed on top of our simulations the expected emission, at millimetre wavelengths, for such source. A two-temperature plasma and all the recipes commonly employed for ADAF systems have been used, obtaining very reasonable results, compared to previous works (Mościbrodzka et al., 2009, 2014). This confirms that the dynamo action, believed to occur in these systems due to small-scale turbulence, is capable of amplifying the magnetic fields, in a self-consistent way, up to the values required to reproduce the observations.

Recently our results have been confirmed by the $\alpha-\Omega$ dynamo GRMHD simulations of Vourellis and Fendt (2021) although the configuration of the torus and the initial magnetic field are different from ours and this does not allow quantitative comparisons. The authors observe an initial exponential amplification of the magnetic field and a mechanism of self-quenching that leads to interrupting the growth. In accordance with our work, they also argue that the induced magnetic field dynamo is strong enough to remove angular momentum from the disk, triggering accretion. In agreement with Tomei et al. (2020), the authors also argue that that MRI, although detectable in simulations, does not play a crucial role in determining the steady-state of accretion.

The second paper Tomei et al. (2021) was born with the idea of linking dynamo simulations in a more quantitative way with the literature and can be considered an extension of our previous work. We have reproduced some of the SANE disk diagnostics of the Code Comparison Project of Porth and EHT-Collaboration (2019) by expanding the range of resistivity and dynamo parameters compared to our previous paper. We have also extended the duration of simulations to investigate the stationary regime in more detail. Our main purpose is to show that the approach of mean-field dynamo in axisymmetric simulations is able to reproduce the amplification of the magnetic field due to MRI-driven turbulence. Even when starting from initial conditions not particularly favorable, such as a seed (toroidal) magnetic field with very low magnetization, our models can reproduce the same results of expensive 3D GRMHD simulations after saturation and dynamical quenching of the dynamo process, similarly to the simulated disks of Sądowski et al. (2015) exhibiting sustained turbulence, with the poloidal and toroidal magnetic field components driven towards a state not different to that seen in 3D studies. We observe that the action of a mean-field dynamo is able to generate equipartition-like poloidal fields as already seen in Tomei et al. (2020) and later confirmed by Vourellis and Fendt (2021). Then in our simulations, we find a considerable dependence on the initialization value of the α effect. In particular, there is a minimum initial ξ_0 ($\equiv \xi_{\rm max}$ in Tomei et al. (2020)) under which the dynamo is too weak to grow out the poloidal magnetic field significantly within the duration of our runs. On the other hand, an excessively high value causes a rapid and violent initial evolution, bringing a discrepancy of the diagnostics with the ideal three-dimensional case. However, we find an intermediate range that has a good agreement in all the diagnostics analyzed. The dependence from η_0 ($\equiv \eta_{\rm max}$ in Tomei et al. (2020)) is less evident in the horizon fluxes. However, the time averages in the stationary phase show that as η_0 increases, the average disk density decreases and the magnetization in the funnel increases. This is probably due to the fact that the action of $\alpha-\Omega$ dynamo is stronger, and it more effectively influences the accretion dynamics. Finally, we evaluated the time evolution of the θ-quality factor to test the ability to solve MRI in our simulations. In runs with intermediate and strong dynamo, the action of the dynamo combined with the adopted resolution allows for resolving the characteristic MRI wavelength during

the initial phase. If the dynamo is too low, the instability can never develop. This behavior is confirmed by the fact that as ξ_0 increases, the accretion during the transient is progressively more intense. On the other hand, the stationary regime seems to be regulated exclusively by the action of the mean-field dynamo, as also stated by Vourellis and Fendt (2021). In conclusion, we believe that the much more computationally convenient approach of mean-field dynamo in axisymmetric simulations can reproduce SANE accretion disks whose properties are in accordance with the fully three-dimensional ideal simulations present in the literature. This result opens up the possibility of performing large parameter studies of axisymmetric thick disks to fit observational data and better constrain the physical properties of the accretion flows.

Part of the thesis work included our participation with ECHO in the Code Comparison project that aims to compare the results obtained by the various participating groups in some well-defined black hole accretion tests. In the first part of the project, we studied the SANE configuration in the paper Porth and EHT-Collaboration (2019). Each code was given ample freedom on the algorithm, implementation and grid choice: the main similarities of ECHO with the other codes concern the use of the PPM for spatial reconstruction and the Riemann solver HLL. The suggested resolution is the one commonly adopted in the literature to study the black hole accretion. In general, the level of concordance between the various codes improves as the resolution increases: for example, the spread between the lowest and the highest value of the mean horizon fluxes decreases from ~ 3.9 to ~ 1.7 for the mass accretion rate. ECHO results follow the general trend: in particular, we can see how the high spread of the magnetic flux and the flux of the angular momentum in the low-resolution run is significantly reduced in the high-resolution runs. We observe that the magnetic flux is the lowest among all the other high-resolution values. Similar considerations about convergence apply to disk-averaged quantities and the contour of the jet-disk boundary. As for the latter, the low-resolution run shows good agreement with the profile observed in the 2D simulations of Nakamura et al. (2018), although the high-resolution simulations converge on a narrower jet profile. The non-consistency with the other codes at low resolution is probably due to the polar cutout adopted in our grids that generally leads to a decrease in magnetization in the funnel. By increasing the resolution this effect becomes less important and the agreement with the other codes is recovered. The comparison with light curves and their spectra shows good agreement between all codes (including ECHO) at all resolutions. The Power Sectral Density of the light curves is compatible with a red-noise spectrum up to $0.1M^{-1}$ where a steepening is observed indicating the presence of an inner emission ring at or within the ISCO. Finally, the results of the convergence test carried out are interesting, showing that there is a midplane resolution threshold $\Delta\theta_p \sim 0.25-0.0125$ beyond which the differences between the algorithms become less important and the scatter between the results obtained decreases significantly.

The second part of the project concerning the MAD configuration is currently in progress and although our results are ready, the comparison with the other codes involved has not yet been completed. The initial difficulties in dealing with the modeling of the highly magnetized funnel led us to modify the algorithm for the recovery of primitive variables. We currently believe that the code has improved in terms of robustness. The preliminary results obtained in the MAD test show a good agreement with the other codes except for the jets diagnostics probably due to the polar cutout again.

As we have said, the polarized image of M87* seems to exclude that the accretion evolves in the

SANE configuration, favoring the MAD models instead (EHT-Collaboration, 2021b). The future development of this thesis work therefore naturally moves towards the search for efficient modeling of this regime: on the one hand, through the completion of the ideal simulations and analyzes of the second part of the code comparison project; on the other hand, through further advances in the characterization of the dynamo mean-field mechanism, which can be even more crucial in MAD disks than SANE disks due to the need to deal with more magnetized and turbulent environments. First, it will be necessary to perform 3D GRMHD simulations since in axisymmetric MAD configurations the intense magnetic field, not being absorbed by the black hole, completely inhibits the accretion at almost regular intervals. In 3D configuration the situation is different because the magnetic field is unable to inhibit all the accretion channels; matter falls into the black hole through irregular bursts but never stops. The 3D simulations also allow studying possible interactions of the dynamo with non-axisymmetric instabilities (Bugli et al., 2018). Furthermore, a more accurate prescription of the spatial profile of resistivity could be crucial. In our study the regions of high magnetization coincide with those of high density, hence the magnetic field dissipation was particularly effective. However, there are shearing box studies that seem to indicate that the most dissipative regions are rather the edges of the disk (Gressel and Pessah, 2015). For this reason, more accurate and consistent implementation of resistivity and dynamo profiles could lead to increased dynamo amplification action and reduced MRI damping.

Bibliography

M. Abramowicz, M. Jaroszynski, and M. Sikora. Relativistic, accreting disks. *Astronomy and Astrophysics, Vol. 63, p. 221-224 (1978)*, 63:221, Feb. 1978. ISSN 0004-6361. URL https://ui.adsabs.harvard.edu/abs/1978A%26A....63..221A/abstract.

M. A. Abramowicz and P. C. Fragile. Foundations of Black Hole Accretion Disk Theory. *Living Rev. Relativ.*, 16(1):1, Dec. 2013. ISSN 2367-3613, 1433-8351. doi: 10.12942/lrr-2013-1. URL http://link.springer.com/10.12942/lrr-2013-1.

M. A. Abramowicz, X. Chen, S. Kato, J.-P. Lasota, and O. Regev. Thermal Equilibria of Accretion Disks. *The Astrophysical Journal*, 438:L37, Jan. 1995. ISSN 0004-637X. doi: 10.1086/187709. URL https://ui.adsabs.harvard.edu/abs/1995ApJ...438L..37A.

M. A. Abramowicz, X. M. Chen, M. Granath, and J. P. Lasota. Advection-dominated Accretion Flows around Kerr Black Holes. *The Astrophysical Journal*, 471:762, Nov. 1996. ISSN 0004-637X. doi: 10.1086/178004. URL https://ui.adsabs.harvard.edu/abs/1996ApJ...471..762A.

M. A. Abramowicz, A. Lanza, and M. J. Percival. Accretion Disks around Kerr Black Holes: Vertical Equilibrium Revisited. *The Astrophysical Journal*, 479:179–183, Apr. 1997. ISSN 0004-637X. doi: 10.1086/303869. URL https://ui.adsabs.harvard.edu/abs/1997ApJ...479..179A.

S. W. Allen, G. B. Taylor, P. E. J. Nulsen, R. M. Johnstone, L. P. David, S. Ettori, A. C. Fabian, W. Forman, C. Jones, and B. McNamara. Chandra X-ray observations of the 3C 295 cluster core. *Monthly Notices of the Royal Astronomical Society*, 324:842–858, July 2001. ISSN 0035-8711. doi: 10.1046/j.1365-8711.2001.04315.x. URL https://ui.adsabs.harvard.edu/abs/2001MNRAS.324..842A. ADS Bibcode: 2001MNRAS.324..842A.

S. K. Antiochos, C. R. DeVore, and J. A. Klimchuk. A Model for Solar Coronal Mass Ejections. *The Astrophysical Journal*, 510:485–493, Jan. 1999. ISSN 0004-637X. doi: 10.1086/306563. URL https://ui.adsabs.harvard.edu/abs/1999ApJ...510..485A. ADS Bibcode: 1999ApJ...510..485A.

R. L. Arnowitt, S. Deser, and C. W. Misner. *Canonical analysis of general relativity.* Jan. 1962. URL https://ui.adsabs.harvard.edu/abs/1962rdgr.book..127A. Pages: 127 Publication Title: Recent Developments in General Relativity ADS Bibcode: 1962rdgr.book..127A.

K. Asada and M. Nakamura. The Structure of the M87 Jet: A Transition from Parabolic to Conical Streamlines. *The Astrophysical Journal*, 745:L28, Feb. 2012. ISSN 0004-637X. doi: 10.1088/2041-8205/745/2/L28. URL https://ui.adsabs.harvard.edu/abs/2012ApJ...745L..28A. ADS Bibcode: 2012ApJ...745L..28A.

S. Balbus and J. Hawley. Instability, Turbulence, and Enhanced Transport in Accretion Disks. *Reviews of Modern Physics*, 121:90, Jan. 1998. doi: 10.1103/RevModPhys.70.1.

S. A. Balbus and J. F. Hawley. A powerful local shear instability in weakly magnetized disks. I - Linear analysis. II - Nonlinear evolution. *The Astrophysical Journal*, 376:214–233, July 1991. ISSN 0004-637X. doi: 10.1086/170270. URL http://adsabs.harvard.edu/abs/1991ApJ...376..214B.

S. L. Baliunas, R. A. Donahue, W. H. Soon, J. H. Horne, J. Frazer, L. Woodard-Eklund, M. Bradford, L. M. Rao, O. C. Wilson, Q. Zhang, W. Bennett, J. Briggs, S. M. Carroll, D. K. Duncan, D. Figueroa, H. H. Lanning, T. Misch, J. Mueller, R. W. Noyes, D. Poppe, A. C. Porter, C. R. Robinson, J. Russell, J. C. Shelton, T. Soyumer, A. H. Vaughan, and J. H. Whitney. Chromospheric Variations in Main-Sequence Stars. II. *The Astrophysical Journal*, 438:269, Jan. 1995. ISSN 0004-637X. doi: 10.1086/175072. URL `https://ui.adsabs.harvard.edu/abs/1995ApJ...438..269B`. ADS Bibcode: 1995ApJ...438..269B.

R. Beck. The Role of Magnetic Fields in Spiral Galaxies. *Astrophysics and Space Science, v. 289, Issue 3, p. 293-302 (2004).*, 289(3):293, Feb. 2004. ISSN 0004-640X. doi: 10.1023/B:ASTR.0000014957.31590.50. URL `https://ui.adsabs.harvard.edu/abs/2004Ap%26SS.289..293B/abstract`.

A. M. Beloborodov, M. A. Abramowicz, and I. D. Novikov. Inertia of Heat in Advective Accretion Disks around Kerr Black Holes. *ApJ*, 491(1):267–269, Dec. 1997. ISSN 0004-637X, 1538-4357. doi: 10.1086/304956. URL `http://arxiv.org/abs/astro-ph/9705084`. arXiv: astro-ph/9705084.

P. Bhat, F. Ebrahimi, E. G. Blackman, and K. Subramanian. Evolution of the magnetorotational instability on initially tangled magnetic fields. *Monthly Notices of the Royal Astronomical Society*, 472:2569–2574, Dec. 2017. ISSN 0035-8711. doi: 10.1093/mnras/stx1989. URL `https://ui.adsabs.harvard.edu/abs/2017MNRAS.472.2569B`. ADS Bibcode: 2017MNRAS.472.2569B.

L. Biermann. Kometenschweife und solare Korpuskularstrahlung. *Zeitschrift fur Astrophysik*, 29:274, Jan. 1951. ISSN 0372-8331. URL `https://ui.adsabs.harvard.edu/abs/1951ZA.....29..274B`. ADS Bibcode: 1951ZA.....29..274B.

G. S. Bisnovatyi-Kogan and A. A. Ruzmaikin. The Accretion of Matter by a Collapsing Star in the Presence of a Magnetic Field. II: Self-consistent Stationary Picture. *Astrophysics and Space Science, Volume 42, Issue 2, pp.401-424*, 42(2):401, July 1976. ISSN 0004-640X. doi: 10.1007/BF01225967. URL `https://ui.adsabs.harvard.edu/abs/1976Ap%26SS..42..401B/abstract`.

R. D. Blandford and M. C. Begelman. On the fate of gas accreting at a low rate on to a black hole. *Monthly Notices of the Royal Astronomical Society*, 303:L1–L5, Feb. 1999. ISSN 0035-8711. doi: 10.1046/j.1365-8711.1999.02358.x. URL `https://ui.adsabs.harvard.edu/abs/1999MNRAS.303L...1B`.

R. D. Blandford and D. G. Payne. Hydromagnetic flows from accretion disks and the production of radio jets. *Monthly Notices of the Royal Astronomical Society*, 199:883–903, June 1982. ISSN 0035-8711. doi: 10.1093/mnras/199.4.883. URL `https://ui.adsabs.harvard.edu/abs/1982MNRAS.199..883B`. ADS Bibcode: 1982MNRAS.199..883B.

R. D. Blandford and R. L. Znajek. Electromagnetic extraction of energy from Kerr black holes. *Monthly Notices of the Royal Astronomical Society*, 179:433–456, May 1977. ISSN 0035-8711. doi: 10.1093/mnras/179.3.433. URL `https://ui.adsabs.harvard.edu/abs/1977MNRAS.179..433B`. ADS Bibcode: 1977MNRAS.179..433B.

A. Boehle, A. M. Ghez, R. Schödel, L. Meyer, S. Yelda, S. Albers, G. D. Martinez, E. E. Becklin, T. Do, J. R. Lu, K. Matthews, M. R. Morris, B. Sitarski, and G. Witzel. An Improved Distance

and Mass Estimate for Sgr A* from a Multistar Orbit Analysis. *The Astrophysical Journal*, 830: 17, Oct. 2016. ISSN 0004-637X. doi: 10.3847/0004-637X/830/1/17. URL https://ui.adsabs.harvard.edu/abs/2016ApJ...830...17B. ADS Bibcode: 2016ApJ...830...17B.

A. Bonanno, L. Rezzolla, and V. Urpin. Mean-field dynamo action in protoneutron stars. *Astronomy and Astrophysics, v.410, p.L33-L36 (2003)*, 410:L33, Oct. 2003. ISSN 0004-6361. doi: 10.1051/0004-6361:20031459. URL https://ui.adsabs.harvard.edu/abs/2003A%26A...410L..33B/abstract.

C. Bonnerot, D. J. Price, G. Lodato, and E. M. Rossi. Magnetic field evolution in tidal disruption events. *Monthly Notices of the Royal Astronomical Society*, 469:4879–4888, Aug. 2017. ISSN 0035-8711. doi: 10.1093/mnras/stx1210. URL https://ui.adsabs.harvard.edu/abs/2017MNRAS.469.4879B. ADS Bibcode: 2017MNRAS.469.4879B.

T. J. M. Boyd and J. J. Sanderson. *The Physics of Plasmas*. Jan. 2003. URL https://ui.adsabs.harvard.edu/abs/2003phpl.book.....B. Publication Title: The Physics of Plasmas ADS Bibcode: 2003phpl.book.....B.

A. Brandenburg. Testing Cowling's Antidynamo Theorem near a Rotating Black Hole. *The Astrophysical Journal*, 465:L115, July 1996. ISSN 0004-637X. doi: 10.1086/310142. URL https://ui.adsabs.harvard.edu/abs/1996ApJ...465L.115B. ADS Bibcode: 1996ApJ...465L.115B.

A. Brandenburg and K. Subramanian. Astrophysical magnetic fields and nonlinear dynamo theory. *Physics Reports*, 417(1-4):1–209, Oct. 2005. ISSN 03701573. doi: 10.1016/j.physrep.2005.06.005. URL http://arxiv.org/abs/astro-ph/0405052. arXiv: astro-ph/0405052.

A. Brandenburg, A. Nordlund, R. F. Stein, and U. Torkelsson. Dynamo-generated Turbulence and Large-Scale Magnetic Fields in a Keplerian Shear Flow. *The Astrophysical Journal*, 446:741, June 1995. ISSN 0004-637X. doi: 10.1086/175831. URL http://adsabs.harvard.edu/abs/1995ApJ...446..741B.

N. Bucciantini and L. Del Zanna. Local Kelvin-Helmholtz instability and synchrotron modulation in Pulsar Wind Nebulae. *Astronomy and Astrophysics, Volume 454, Issue 2, August I 2006, pp.393-400*, 454(2):393, Aug. 2006. ISSN 0004-6361. doi: 10.1051/0004-6361:20054491. URL https://ui.adsabs.harvard.edu/abs/2006A%26A...454..393B/abstract.

N. Bucciantini and L. Del Zanna. A fully covariant mean-field dynamo closure for numerical 3 + 1 resistive GRMHD. *Monthly Notices of the Royal Astronomical Society*, 428(1):71, Jan. 2013. doi: 10.1093/mnras/sts005. URL https://ui.adsabs.harvard.edu/abs/2013MNRAS.428..71B/abstract.

N. Bucciantini, E. Amato, R. Bandiera, J. M. Blondin, and L. Del Zanna. Magnetic Rayleigh-Taylor instability for Pulsar Wind Nebulae in expanding Supernova Remnants. *Astronomy and Astrophysics, v.423, p.253-265 (2004)*, 423:253, Aug. 2004. ISSN 0004-6361. doi: 10.1051/0004-6361:20040360. URL https://ui.adsabs.harvard.edu/abs/2004A%26A...423..253B/abstract.

N. Bucciantini, E. Quataert, B. D. Metzger, T. A. Thompson, J. Arons, and L. Del Zanna. Magnetized relativistic jets and long-duration GRBs from magnetar spin-down during core-collapse

supernovae. *Monthly Notices of the Royal Astronomical Society*, 396:2038–2050, July 2009. ISSN 0035-8711. doi: 10.1111/j.1365-2966.2009.14940.x. URL https://ui.adsabs.harvard.edu/abs/2009MNRAS.396.2038B. ADS Bibcode: 2009MNRAS.396.2038B.

N. Bucciantini, B. D. Metzger, T. A. Thompson, and E. Quataert. Short gamma-ray bursts with extended emission from magnetar birth: jet formation and collimation. *Monthly Notices of the Royal Astronomical Society*, 419:1537–1545, Jan. 2012. ISSN 0035-8711. doi: 10.1111/j.1365-2966.2011.19810.x. URL https://ui.adsabs.harvard.edu/abs/2012MNRAS.419.1537B. ADS Bibcode: 2012MNRAS.419.1537B.

M. Bugli, L. Del Zanna, and N. Bucciantini. Dynamo action in thick discs around Kerr black holes: high-order resistive GRMHD simulations. *Monthly Notices of the Royal Astronomical Society*, 440:L41–L45, May 2014. ISSN 0035-8711. doi: 10.1093/mnrasl/slu017. URL https://ui.adsabs.harvard.edu/abs/2014MNRAS.440L..41B. ADS Bibcode: 2014MNRAS.440L..41B.

M. Bugli, J. Guilet, E. Müller, L. Del Zanna, N. Bucciantini, and P. J. Montero. Papaloizou-Pringle instability suppression by the magnetorotational instability in relativistic accretion discs. *Monthly Notices of the Royal Astronomical Society*, 475(1):108, Mar. 2018. doi: 10.1093/mnras/stx3158. URL https://ui.adsabs.harvard.edu/abs/2018MNRAS.475..108B/abstract.

A. Burrows, L. Dessart, E. Livne, C. D. Ott, and J. Murphy. Simulations of Magnetically Driven Supernova and Hypernova Explosions in the Context of Rapid Rotation. *The Astrophysical Journal*, 664:416–434, July 2007. ISSN 0004-637X. doi: 10.1086/519161. URL https://ui.adsabs.harvard.edu/abs/2007ApJ...664..416B. ADS Bibcode: 2007ApJ...664..416B.

J. C. Butcher. *Numerical Methods for Ordinary Differential Equations*. John Wiley & Sons, Hoboken, New Jersey, third edition, 2016. ISBN 978-1-119-12150-3. doi: 10.1002/9781119121534. URL https://onlinelibrary.wiley.com/doi/book/10.1002/9781119121534.

A. Chael, R. Narayan, and M. D. Johnson. Two-temperature, Magnetically Arrested Disc simulations of the jet from the supermassive black hole in M87. *Monthly Notices of the Royal Astronomical Society*, 486:2873–2895, June 2019. ISSN 0035-8711. doi: 10.1093/mnras/stz988. URL https://ui.adsabs.harvard.edu/abs/2019MNRAS.486.2873C. ADS Bibcode: 2019MNRAS.486.2873C.

S. Chandrasekhar. The Stability of Non-Dissipative Couette Flow in Hydromagnetics. *Proceedings of the National Academy of Science*, 46:253–257, Feb. 1960. ISSN 0027-8424. doi: 10.1073/pnas.46.2.253. URL https://ui.adsabs.harvard.edu/abs/1960PNAS...46..253C.

X. Chen, M. A. Abramowicz, J.-P. Lasota, R. Narayan, and I. Yi. Unified Description of Accretion Flows Around Black Holes. *ApJ*, 443:L61, Apr. 1995. ISSN 0004-637X, 1538-4357. doi: 10.1086/187836. URL http://arxiv.org/abs/astro-ph/9502015. arXiv: astro-ph/9502015.

X. Chen, M. A. Abramowicz, and J.-P. Lasota. Advection-dominated Accretion: Global Transonic Solutions. *The Astrophysical Journal*, 476:61–69, Feb. 1997. ISSN 0004-637X. doi: 10.1086/303592. URL https://ui.adsabs.harvard.edu/abs/1997ApJ...476...61C.

P. Colella and P. R. Woodward. The Piecewise Parabolic Method (PPM) for Gas-Dynamical Simulations. *Journal of Computational Physics*, 54:174–201, Sept. 1984. ISSN 0021-9991. doi: 10.1016/0021-9991(84)90143-8. URL https://ui.adsabs.harvard.edu/abs/1984JCoPh..54..174C. ADS Bibcode: 1984JCoPh..54..174C.

T. G. Cowling. *Magnetohydrodynamics*. Jan. 1976. URL https://ui.adsabs.harvard.edu/abs/1976magn.book.....C. Publication Title: Monographs on Astronomical Subjects ADS Bibcode: 1976magn.book.....C.

T. G. Cowling. The present status of dynamo theory. *In: Annual review of astronomy and astrophysics. Volume 19. (A82-11551 02-90) Palo Alto, CA, Annual Reviews, Inc., 1981, p. 115-135.*, 19:115, 1981. ISSN 0066-4146. doi: 10.1146/annurev.aa.19.090181.000555. URL https://ui.adsabs.harvard.edu/abs/1981ARA%26A..19..115C/abstract.

S. Dall'Osso, S. N. Shore, and L. Stella. Early evolution of newly born magnetars with a strong toroidal field. *Monthly Notices of the Royal Astronomical Society*, 398:1869–1885, Oct. 2009. ISSN 0035-8711. doi: 10.1111/j.1365-2966.2008.14054.x. URL https://ui.adsabs.harvard.edu/abs/2009MNRAS.398.1869D. ADS Bibcode: 2009MNRAS.398.1869D.

S. W. Davis, J. M. Stone, and M. E. Pessah. Sustained Magnetorotational Turbulence in Local Simulations of Stratified Disks with Zero Net Magnetic Flux. *The Astrophysical Journal*, 713: 52–65, Apr. 2010. ISSN 0004-637X. doi: 10.1088/0004-637X/713/1/52. URL http://adsabs.harvard.edu/abs/2010ApJ...713...52D.

L. Del Zanna and N. Bucciantini. An efficient shock-capturing central-type scheme for multidimensional relativistic flows. I. Hydrodynamics. *A&A*, 390(3):1177–1186, Aug. 2002. ISSN 0004-6361, 1432-0746. doi: 10.1051/0004-6361:20020776. URL http://arxiv.org/abs/astro-ph/0205290. arXiv: astro-ph/0205290.

L. Del Zanna and N. Bucciantini. Covariant and 3 + 1 equations for dynamo-chiral general relativistic magnetohydrodynamics. *Monthly Notices of the Royal Astronomical Society*, 479(1): 657, Sept. 2018. doi: 10.1093/mnras/sty1633. URL https://ui.adsabs.harvard.edu/abs/2018MNRAS.479..657D/abstract.

L. Del Zanna, O. Zanotti, N. Bucciantini, and P. Londrillo. An efficient shock-capturing central-type scheme for multidimensional relativistic flows. II. Magnetohydrodynamics. *Astronomy and Astrophysics*, 400(1):397–413, Mar. 2003. ISSN 0004-6361. doi: 10.1051/0004-6361:20021641. URL https://ui.adsabs.harvard.edu/abs/2003A&A...400..397D/abstract.

L. Del Zanna, O. Zanotti, N. Bucciantini, and P. Londrillo. ECHO: a Eulerian conservative high-order scheme for general relativistic magnetohydrodynamics and magnetodynamics. *Astronomy and Astrophysics*, 473(1):11, Oct. 2007. doi: 10.1051/0004-6361:20077093. URL https://ui.adsabs.harvard.edu/abs/2007A%26A...473...11D/abstract.

L. Del Zanna, E. Papini, S. Landi, M. Bugli, and N. Bucciantini. Fast reconnection in relativistic plasmas: the magnetohydrodynamics tearing instability revisited. *Monthly Notices of the Royal Astronomical Society*, 460:3753–3765, Aug. 2016. ISSN 0035-8711. doi: 10.1093/mnras/stw1242. URL http://adsabs.harvard.edu/abs/2016MNRAS.460.3753D.

P. Dhang, A. Bendre, P. Sharma, and K. Subramanian. Characterizing the dynamo in a radiatively inefficient accretion flow. *Monthly Notices of the Royal Astronomical Society*, 494(4):4854–4866, June 2020. ISSN 0035-8711. doi: 10.1093/mnras/staa996. URL https://doi.org/10.1093/mnras/staa996.

S. Dibi, S. Drappeau, P. C. Fragile, S. Markoff, and J. Dexter. General relativistic magnetohydrodynamic simulations of accretion on to Sgr A*: how important are radiative losses? *Monthly Notices of the Royal Astronomical Society*, 426:1928–1939, Nov. 2012. ISSN 0035-8711. doi: 10.1111/j.1365-2966.2012.21857.x. URL https://ui.adsabs.harvard.edu/abs/2012MNRAS.426.1928D. ADS Bibcode: 2012MNRAS.426.1928D.

G. Dubus, J.-M. Hameury, and J.-P. Lasota. The disc instability model for X-ray transients: evidence for truncation and irradiation. *A&A*, 373(1):251–271, July 2001. ISSN 0004-6361, 1432-0746. doi: 10.1051/0004-6361:20010632. URL http://arxiv.org/abs/astro-ph/0102237. arXiv: astro-ph/0102237.

R. C. Duncan and C. Thompson. Formation of Very Strongly Magnetized Neutron Stars: Implications for Gamma-Ray Bursts. *The Astrophysical Journal*, 392:L9, June 1992. ISSN 0004-637X. doi: 10.1086/186413. URL https://ui.adsabs.harvard.edu/abs/1992ApJ...392L...9D. ADS Bibcode: 1992ApJ...392L...9D.

EHT-Collaboration. First M87 Event Horizon Telescope Results. III. Data Processing and Calibration. *The Astrophysical Journal*, 875(1):L3, Apr. 2019a. doi: 10.3847/2041-8213/ab0c57. URL https://ui.adsabs.harvard.edu/abs/2019ApJ...875L...3E/abstract.

EHT-Collaboration. First M87 Event Horizon Telescope Results. II. Array and Instrumentation. *The Astrophysical Journal*, 875(1):L2, Apr. 2019b. doi: 10.3847/2041-8213/ab0c96. URL https://ui.adsabs.harvard.edu/abs/2019ApJ...875L...2E/abstract.

EHT-Collaboration. First M87 Event Horizon Telescope Results. I. The Shadow of the Supermassive Black Hole. *The Astrophysical Journal*, 875(1):L1, Apr. 2019c. doi: 10.3847/2041-8213/ab0ec7. URL https://ui.adsabs.harvard.edu/abs/2019ApJ...875L...1E/abstract.

EHT-Collaboration. First M87 Event Horizon Telescope Results. VI. The Shadow and Mass of the Central Black Hole. *The Astrophysical Journal*, 875(1):L6, Apr. 2019d. doi: 10.3847/2041-8213/ab1141. URL https://ui.adsabs.harvard.edu/abs/2019ApJ...875L...6E/abstract.

EHT-Collaboration. First M87 Event Horizon Telescope Results. V. Physical Origin of the Asymmetric Ring. *The Astrophysical Journal*, 875(1):L5, Apr. 2019e. doi: 10.3847/2041-8213/ab0f43. URL https://ui.adsabs.harvard.edu/abs/2019ApJ...875L...5E/abstract.

EHT-Collaboration. First M87 Event Horizon Telescope Results. IV. Imaging the Central Supermassive Black Hole. *The Astrophysical Journal*, 875(1):L4, Apr. 2019f. doi: 10.3847/2041-8213/ab0e85. URL https://ui.adsabs.harvard.edu/abs/2019ApJ...875L...4E/abstract.

EHT-Collaboration. First M87 Event Horizon Telescope Results. VIII. Magnetic Field Structure near The Event Horizon. *The Astrophysical Journal Letters*, page 43, 2021a.

EHT-Collaboration. First M87 Event Horizon Telescope Results. VII. Polarization of the Ring. *The Astrophysical Journal Letters*, page 48, 2021b.

T. A. Enßlin and C. Vogt. The magnetic power spectrum in Faraday rotation screens. *Astronomy and Astrophysics, v.401, p.835-848 (2003)*, 401:835, Apr. 2003. ISSN 0004-6361. doi: 10.1051/0004-6361:20030172. URL https://ui.adsabs.harvard.edu/abs/2003A%26A...401..835E/abstract.

A. A. Esin, J. E. McClintock, and R. Narayan. Advection-Dominated Accretion and the Spectral States of Black Hole X-Ray Binaries: Application to Nova Muscae 1991. *The Astrophysical Journal*, 489:865–889, Nov. 1997. ISSN 0004-637X. doi: 10.1086/304829. URL https://ui.adsabs.harvard.edu/abs/1997ApJ...489..865E.

H. Falcke, K. Mannheim, and P. L. Biermann. The Galactic Center radio jet. *Astronomy and Astrophysics, Vol. 278, p. L1-L4 (1993)*, 278:L1, Oct. 1993. ISSN 0004-6361. URL https://ui.adsabs.harvard.edu/abs/1993A%26A...278L...1F/abstract.

L. Feretti. Observational Properties of Diffuse Halos in Clusters. 199:133, Jan. 2002. URL https://ui.adsabs.harvard.edu/abs/2002IAUS..199..133F. Conference Name: The Universe at Low Radio Frequencies ADS Bibcode: 2002IAUS..199..133F.

L. G. Fishbone and V. Moncrief. Relativistic fluid disks in orbit around Kerr black holes. *The Astrophysical Journal*, 207:962–976, Aug. 1976. ISSN 0004-637X. doi: 10.1086/154565. URL http://adsabs.harvard.edu/abs/1976ApJ...207..962F.

B. D. Fried. Mechanism for Instability of Transverse Plasma Waves. *Physics of Fluids*, 2:337–337, May 1959. ISSN 0899-82131070-6631. doi: 10.1063/1.1705933. URL https://ui.adsabs.harvard.edu/abs/1959PhFl....2..337F. ADS Bibcode: 1959PhFl....2..337F.

D. J. Galloway and N. O. Weiss. Convection and magnetic fields in stars. *The Astrophysical Journal*, 243:945–953, Feb. 1981. ISSN 0004-637X. doi: 10.1086/158659. URL https://ui.adsabs.harvard.edu/abs/1981ApJ...243..945G. ADS Bibcode: 1981ApJ...243..945G.

C. F. Gammie and R. Popham. Advection-dominated Accretion Flows in the Kerr Metric. I. Basic Equations. *The Astrophysical Journal*, 498:313–326, May 1998. ISSN 0004-637X. doi: 10.1086/305521. URL https://ui.adsabs.harvard.edu/abs/1998ApJ...498..313G.

B. Giacomazzo, J. Zrake, P. C. Duffell, A. I. MacFadyen, and R. Perna. Producing Magnetar Magnetic Fields in the Merger of Binary Neutron Stars. *The Astrophysical Journal*, 809:39, Aug. 2015. ISSN 0004-637X. doi: 10.1088/0004-637X/809/1/39. URL https://ui.adsabs.harvard.edu/abs/2015ApJ...809...39G. ADS Bibcode: 2015ApJ...809...39G.

O. Gressel and M. E. Pessah. Characterizing the mean-field dynamo in turbulent accretion disks. *ApJ*, 810(1):59, Aug. 2015. ISSN 1538-4357. doi: 10.1088/0004-637X/810/1/59. URL http://arxiv.org/abs/1507.08634. arXiv: 1507.08634.

X. Guan and C. F. Gammie. Radially Extended, Stratified, Local Models of Isothermal Disks. *The Astrophysical Journal*, 728:130, Feb. 2011. ISSN 0004-637X. doi: 10.1088/0004-637X/728/2/130. URL https://ui.adsabs.harvard.edu/abs/2011ApJ...728..130G.

J. Guilet and E. Müller. Numerical simulations of the magnetorotational instability in protoneutron stars - I. Influence of buoyancy. *Monthly Notices of the Royal Astronomical Society*, 450:2153–2171, June 2015. ISSN 0035-8711. doi: 10.1093/mnras/stv727. URL https://ui.adsabs.harvard.edu/abs/2015MNRAS.450.2153G. ADS Bibcode: 2015MNRAS.450.2153G.

K. Hada, M. Kino, A. Doi, H. Nagai, M. Honma, Y. Hagiwara, M. Giroletti, G. Giovannini, and N. Kawaguchi. The Innermost Collimation Structure of the M87 Jet Down to ˜10 Schwarzschild Radii. *The Astrophysical Journal*, 775:70, Sept. 2013. ISSN 0004-637X. doi: 10.1088/0004-637X/775/1/70. URL https://ui.adsabs.harvard.edu/abs/2013ApJ...775...70H. ADS Bibcode: 2013ApJ...775...70H.

A. Harten, P. D. Lax, and B. v. Leer. On Upstream Differencing and Godunov-Type Schemes for Hyperbolic Conservation Laws. *SIAM Rev.*, 25(1):35–61, Jan. 1983. ISSN 0036-1445. doi: 10.1137/1025002. URL https://epubs.siam.org/doi/10.1137/1025002. Publisher: Society for Industrial and Applied Mathematics.

J. F. Hawley, X. Guan, and J. H. Krolik. Assessing Quantitative Results in Accretion Simulations: From Local to Global. *The Astrophysical Journal*, 738:84, Sept. 2011. ISSN 0004-637X. doi: 10.1088/0004-637X/738/1/84. URL https://ui.adsabs.harvard.edu/abs/2011ApJ...738...84H.

J. F. Hawley, S. A. Richers, X. Guan, and J. H. Krolik. Testing Convergence for Global Accretion Disks. *The Astrophysical Journal*, 772:102, Aug. 2013. ISSN 0004-637X. doi: 10.1088/0004-637X/772/2/102. URL https://ui.adsabs.harvard.edu/abs/2013ApJ...772..102H.

L. M. Heil, S. Vaughan, and P. Uttley. The ubiquity of the rms-flux relation in black hole X-ray binaries. *Monthly Notices of the Royal Astronomical Society*, 422:2620–2631, May 2012. ISSN 0035-8711. doi: 10.1111/j.1365-2966.2012.20824.x. URL https://ui.adsabs.harvard.edu/abs/2012MNRAS.422.2620H. ADS Bibcode: 2012MNRAS.422.2620H.

L. E. Held and H. N. Latter. Hydrodynamic convection in accretion discs. *Monthly Notices of the Royal Astronomical Society*, Aug. 2018. ISSN 0035-8711, 1365-2966. doi: 10.1093/mnras/sty2097. URL http://arxiv.org/abs/1808.00267. arXiv: 1808.00267.

L. E. Held and H. N. Latter. Magnetohydrodynamic convection in accretion discs. *Monthly Notices of the Royal Astronomical Society*, 504(2):2940–2960, May 2021. ISSN 0035-8711, 1365-2966. doi: 10.1093/mnras/stab974. URL http://arxiv.org/abs/2104.02473. arXiv: 2104.02473.

J. Heyvaerts and E. R. Priest. Coronal heating by reconnection in DC current systems - A theory based on Taylor's hypothesis. *Astronomy and Astrophysics (ISSN 0004-6361), vol. 137, no. 1, Aug. 1984, p. 63-78.*, 137(1):63, Aug. 1984. ISSN 0004-6361. URL https://ui.adsabs.harvard.edu/abs/1984A%26A...137...63H/abstract.

S. Hirose, J. H. Krolik, J.-P. De Villiers, and J. F. Hawley. Magnetically Driven Accretion Flows in the Kerr Metric. II. Structure of the Magnetic Field. *The Astrophysical Journal*, 606:1083–1097, May 2004. ISSN 0004-637X. doi: 10.1086/383184. URL https://ui.adsabs.harvard.edu/abs/2004ApJ...606.1083H. ADS Bibcode: 2004ApJ...606.1083H.

J. D. Hogg and C. S. Reynolds. Testing the Propagating Fluctuations Model with a Long, Global Accretion Disk Simulation. *The Astrophysical Journal*, 826:40, July 2016. ISSN 0004-637X. doi: 10.3847/0004-637X/826/1/40. URL `https://ui.adsabs.harvard.edu/abs/2016ApJ...826...40H`. ADS Bibcode: 2016ApJ...826...40H.

J. D. Hogg and C. S. Reynolds. The Influence of Accretion Disk Thickness on the Large-scale Magnetic Dynamo. *The Astrophysical Journal*, 861:24, July 2018. doi: 10.3847/1538-4357/aac439. URL `http://adsabs.harvard.edu/abs/2018ApJ...861...24H`.

C. M. Johns-Krull, J. A. Valenti, and C. Koresko. Measuring the Magnetic Field on the Classical T Tauri Star BP Tauri. *The Astrophysical Journal*, 516:900–915, May 1999. ISSN 0004-637X. doi: 10.1086/307128. URL `https://ui.adsabs.harvard.edu/abs/1999ApJ...516..900J`. ADS Bibcode: 1999ApJ...516..900J.

W. Kastaun, J. V. Kalinani, and R. Ciolfi. Robust recovery of primitive variables in relativistic ideal magnetohydrodynamics. *Physical Review D*, 103:023018, Jan. 2021. ISSN 1550-79980556-2821. doi: 10.1103/PhysRevD.103.023018. URL `https://ui.adsabs.harvard.edu/abs/2021PhRvD.103b3018K`. ADS Bibcode: 2021PhRvD.103b3018K.

R. P. Kerr. Gravitational Field of a Spinning Mass as an Example of Algebraically Special Metrics. *Physical Review Letters*, 11:237–238, Sept. 1963. ISSN 0031-9007. doi: 10.1103/PhysRevLett.11.237. URL `https://ui.adsabs.harvard.edu/abs/1963PhRvL..11..237K`. ADS Bibcode: 1963PhRvL..11..237K.

R. Khanna and M. Camenzind. The {omega}{Omega} dynamo in accretion disks of rotating black holes. *Astronomy and Astrophysics*, 307:665, Mar. 1996. URL `https://ui.adsabs.harvard.edu/abs/1996A%26A...307..665K/abstract`.

A. R. King, J. E. Pringle, and M. Livio. Accretion disc viscosity: how big is alpha? *Monthly Notices of the Royal Astronomical Society*, 376:1740–1746, Apr. 2007. ISSN 0035-8711. doi: 10.1111/j.1365-2966.2007.11556.x. URL `https://ui.adsabs.harvard.edu/abs/2007MNRAS.376.1740K`.

S. S. Komissarov. Electrodynamics of black hole magnetospheres. *Monthly Notices of the Royal Astronomical Society*, 350:427–448, May 2004. ISSN 0035-8711. doi: 10.1111/j.1365-2966.2004.07598.x. URL `https://ui.adsabs.harvard.edu/abs/2004MNRAS.350..427K`. ADS Bibcode: 2004MNRAS.350..427K.

S. S. Komissarov. Observations of the Blandford-Znajek process and the magnetohydrodynamic Penrose process in computer simulations of black hole magnetospheres. *Monthly Notices of the Royal Astronomical Society*, 359:801–808, May 2005. ISSN 0035-8711. doi: 10.1111/j.1365-2966.2005.08974.x. URL `https://ui.adsabs.harvard.edu/abs/2005MNRAS.359..801K`. ADS Bibcode: 2005MNRAS.359..801K.

S. S. Komissarov. Magnetized tori around Kerr black holes: analytic solutions with a toroidal magnetic field. *Monthly Notices of the Royal Astronomical Society*, 368(3):993, May 2006. doi: 10.1111/j.1365-2966.2006.10183.x. URL `https://ui.adsabs.harvard.edu/abs/2006MNRAS.368..993K/abstract`.

M. Kozlowski, M. Jaroszynski, and M. A. Abramowicz. The analytic theory of fluid disks orbiting the Kerr black hole. *Astronomy and Astrophysics, vol. 63, no. 1-2, Feb. 1978, p. 209-220. Research supported by the Universita di Padova.*, 63(1-2):209, Feb. 1978. ISSN 0004-6361. URL https://ui.adsabs.harvard.edu/abs/1978A%26A....63..209K/abstract.

F. Krause and K.-H. Raedler. Mean-field magnetohydrodynamics and dynamo theory. *Organic Photonics and Photovoltaics*, 1980. URL http://adsabs.harvard.edu/abs/1980opp..bookR....K.

P. P. Kronberg. Extragalactic magnetic fields. *Reports on Progress in Physics*, 57:325–382, Apr. 1994. ISSN 0034-4885. doi: 10.1088/0034-4885/57/4/001. URL https://ui.adsabs.harvard.edu/abs/1994RPPh...57..325K. ADS Bibcode: 1994RPPh...57..325K.

R. M. Kulsrud, R. Cen, J. P. Ostriker, and D. Ryu. The Protogalactic Origin for Cosmic Magnetic Fields. *The Astrophysical Journal*, 480:481–491, May 1997. ISSN 0004-637X. doi: 10.1086/303987. URL https://ui.adsabs.harvard.edu/abs/1997ApJ...480..481K. ADS Bibcode: 1997ApJ...480..481K.

P. Kumar and B. Zhang. The physics of gamma-ray bursts & relativistic jets. *Physics Reports*, 561:1–109, Feb. 2015. ISSN 0370-1573. doi: 10.1016/j.physrep.2014.09.008. URL https://ui.adsabs.harvard.edu/abs/2015PhR...561....1K. ADS Bibcode: 2015PhR...561....1K.

C. Y. Kuo, K. Asada, R. Rao, M. Nakamura, J. C. Algaba, H. B. Liu, M. Inoue, P. M. Koch, P. T. P. Ho, S. Matsushita, H. Y. Pu, K. Akiyama, H. Nishioka, and N. Pradel. Measuring Mass Accretion Rate onto the Supermassive Black Hole in M87 Using Faraday Rotation Measure with the Submillimeter Array. *The Astrophysical Journal*, 783:L33, Mar. 2014. ISSN 0004-637X. doi: 10.1088/2041-8205/783/2/L33. URL https://ui.adsabs.harvard.edu/abs/2014ApJ...783L..33K. ADS Bibcode: 2014ApJ...783L..33K.

R. A. Laing. Magnetic fields in extragalactic radio sources. *The Astrophysical Journal*, 248:87–104, Aug. 1981. ISSN 0004-637X. doi: 10.1086/159132. URL https://ui.adsabs.harvard.edu/abs/1981ApJ...248...87L. ADS Bibcode: 1981ApJ...248...87L.

P. K. Leung, C. F. Gammie, and S. C. Noble. Numerical Calculation of Magnetobremsstrahlung Emission and Absorption Coefficients. *The Astrophysical Journal*, 737:21, Aug. 2011. ISSN 0004-637X. doi: 10.1088/0004-637X/737/1/21. URL https://ui.adsabs.harvard.edu/abs/2011ApJ...737...21L. ADS Bibcode: 2011ApJ...737...21L.

M. Liska, C. Hesp, A. Tchekhovskoy, A. Ingram, M. van der Klis, and S. Markoff. Formation of Precessing Jets by Tilted Black-hole Discs in 3D General Relativistic MHD Simulations. *Monthly Notices of the Royal Astronomical Society: Letters*, 474(1):L81–L85, Feb. 2018. ISSN 1745-3925, 1745-3933. doi: 10.1093/mnrasl/slx174. URL http://arxiv.org/abs/1707.06619. arXiv: 1707.06619.

M. L. Lister, M. F. Aller, H. D. Aller, D. C. Homan, K. I. Kellermann, Y. Y. Kovalev, A. B. Pushkarev, J. L. Richards, E. Ros, and T. Savolainen. MOJAVE: XIII. Parsec-scale AGN Jet Kinematics Analysis Based on 19 years of VLBA Observations at 15 GHz. *The Astronomical*

Journal, 152:12, July 2016. ISSN 0004-6256. doi: 10.3847/0004-6256/152/1/12. URL https://ui.adsabs.harvard.edu/abs/2016AJ....152...12L. ADS Bibcode: 2016AJ....152...12L.

X.-D. Liu and S. Osher. Convex ENO High Order Multi-dimensional Schemes without Field by Field Decomposition or Staggered Grids. *Journal of Computational Physics*, 142:304–330, May 1998. ISSN 0021-9991. doi: 10.1006/jcph.1998.5937. URL https://ui.adsabs.harvard.edu/abs/1998JCoPh.142..304L. ADS Bibcode: 1998JCoPh.142..304L.

P. Londrillo and L. Del Zanna. On the Divergence-Free Condition in Godunov-Type Schemes for Ideal Magnetohydrodynamics: the Upwind Constrained Transport Method. *Journal of Computational Physics*, 195(1):17–48, Mar. 2004. ISSN 00219991. doi: 10.1016/j.jcp.2003.09.016. URL http://arxiv.org/abs/astro-ph/0310183. arXiv: astro-ph/0310183.

D. W. Longcope and L. A. Tarr. Relating magnetic reconnection to coronal heating. *Philosophical Transactions of the Royal Society of London Series A*, 373:20140263–20140263, Apr. 2015. ISSN 1364-503X0080-46140962-8436. doi: 10.1098/rsta.2014.0263. URL https://ui.adsabs.harvard.edu/abs/2015RSPTA.37340263L. ADS Bibcode: 2015RSPTA.37340263L.

MAGIC-Collaboration. Teraelectronvolt emission from the γ-ray burst GRB 190114C. *Nature*, 575(7783):455–458, Nov. 2019. ISSN 1476-4687. doi: 10.1038/s41586-019-1750-x. URL https://www.nature.com/articles/s41586-019-1750-x. Bandiera_abtest: a Cg_type: Nature Research Journals Number: 7783 Primary_atype: Research Publisher: Nature Publishing Group Subject_term: Astronomy and astrophysics;Astronomy and planetary science;High-energy astrophysics;Transient astrophysical phenomena Subject_term_id: astronomy-and-astrophysics;astronomy-and-planetary-science;high-energy-astrophysics;transient-astrophysical-phenomena.

R. Mahadevan and E. Quataert. Are Particles in Advection-dominated Accretion Flows Thermal? *The Astrophysical Journal*, 490:605–618, Dec. 1997. ISSN 0004-637X. doi: 10.1086/304908. URL https://ui.adsabs.harvard.edu/abs/1997ApJ...490..605M.

D. P. Marrone, J. M. Moran, J.-H. Zhao, and R. Rao. An Unambiguous Detection of Faraday Rotation in Sagittarius A*. *The Astrophysical Journal*, 654:L57–L60, Jan. 2007. ISSN 0004-637X. doi: 10.1086/510850. URL https://ui.adsabs.harvard.edu/abs/2007ApJ...654L..57M. ADS Bibcode: 2007ApJ...654L..57M.

J. C. McKinney and C. F. Gammie. A Measurement of the Electromagnetic Luminosity of a Kerr Black Hole. *ApJ*, 611(2):977–995, Aug. 2004. ISSN 0004-637X, 1538-4357. doi: 10.1086/422244. URL http://arxiv.org/abs/astro-ph/0404512. arXiv: astro-ph/0404512.

J. C. McKinney, A. Tchekhovskoy, and R. D. Blandford. General Relativistic Magnetohydrodynamic Simulations of Magnetically Choked Accretion Flows around Black Holes. *Monthly Notices of the Royal Astronomical Society*, 423(4):3083–3117, July 2012. ISSN 00358711. doi: 10.1111/j.1365-2966.2012.21074.x. URL http://arxiv.org/abs/1201.4163. arXiv: 1201.4163.

L. Mestel. *Stellar magnetism*. Jan. 1999. URL https://ui.adsabs.harvard.edu/abs/1999stma.book.....M. Publication Title: Stellar magnetism / Leon Mestel. Oxford : Clarendon ADS Bibcode: 1999stma.book.....M.

B. D. Metzger, D. Giannios, T. A. Thompson, N. Bucciantini, and E. Quataert. The protomagnetar model for gamma-ray bursts. *Monthly Notices of the Royal Astronomical Society*, 413:2031–2056, May 2011. ISSN 0035-8711. doi: 10.1111/j.1365-2966.2011.18280.x. URL https://ui.adsabs.harvard.edu/abs/2011MNRAS.413.2031M. ADS Bibcode: 2011MNRAS.413.2031M.

A. Mignone, G. Mattia, G. Bodo, and L. Del Zanna. A constrained transport method for the solution of the resistive relativistic MHD equations. *Monthly Notices of the Royal Astronomical Society*, 486(3):4252–4274, July 2019. ISSN 0035-8711. doi: 10.1093/mnras/stz1015. URL https://doi.org/10.1093/mnras/stz1015.

H. K. Moffatt. Magnetic field generation in electrically conducting fluids. *Cambridge, England, Cambridge University Press, 1978. 353 p.*, 1978. URL http://adsabs.harvard.edu/abs/1978mfge.book.....M.

R. L. Moore, A. C. Sterling, H. S. Hudson, and J. R. Lemen. Onset of the Magnetic Explosion in Solar Flares and Coronal Mass Ejections. *The Astrophysical Journal*, 552:833–848, May 2001. ISSN 0004-637X. doi: 10.1086/320559. URL https://ui.adsabs.harvard.edu/abs/2001ApJ...552..833M. ADS Bibcode: 2001ApJ...552..833M.

M. Mościbrodzka and H. Falcke. Coupled jet-disk model for Sagittarius A*: explaining the flat-spectrum radio core with GRMHD simulations of jets. *Astronomy and Astrophysics*, 559:L3, Nov. 2013. doi: 10.1051/0004-6361/201322692. URL https://ui.adsabs.harvard.edu/abs/2013A%26A...559L...3M/abstract.

M. Mościbrodzka, C. F. Gammie, J. C. Dolence, H. Shiokawa, and P. K. Leung. Radiative Models of SGR A* from GRMHD Simulations. *The Astrophysical Journal*, 706(1):497, Nov. 2009. doi: 10.1088/0004-637X/706/1/497. URL https://ui.adsabs.harvard.edu/abs/2009ApJ...706..497M/abstract.

M. Mościbrodzka, H. Falcke, H. Shiokawa, and C. F. Gammie. Observational appearance of inefficient accretion flows and jets in 3D GRMHD simulations: Application to Sagittarius A*. *Astronomy and Astrophysics*, 570:A7, Oct. 2014. doi: 10.1051/0004-6361/201424358. URL https://ui.adsabs.harvard.edu/abs/2014A%26A...570A...7M/abstract.

M. Mościbrodzka, H. Falcke, and H. Shiokawa. General relativistic magnetohydrodynamical simulations of the jet in M 87. *Astronomy and Astrophysics*, 586:A38, Feb. 2016. doi: 10.1051/0004-6361/201526630. URL https://ui.adsabs.harvard.edu/abs/2016A%26A...586A..38M/abstract.

P. Mösta, C. D. Ott, D. Radice, L. F. Roberts, E. Schnetter, and R. Haas. A large-scale dynamo and magnetoturbulence in rapidly rotating core-collapse supernovae. *Nature*, 528:376–379, Dec. 2015. ISSN 0028-0836. doi: 10.1038/nature15755. URL https://ui.adsabs.harvard.edu/abs/2015Natur.528..376M. ADS Bibcode: 2015Natur.528..376M.

M. Nakamura, K. Asada, K. Hada, H.-Y. Pu, S. Noble, C. Tseng, K. Toma, M. Kino, H. Nagai, K. Takahashi, J.-C. Algaba, M. Orienti, K. Akiyama, A. Doi, G. Giovannini, M. Giroletti, M. Honma, S. Koyama, R. Lico, K. Niinuma, and F. Tazaki. Parabolic Jets from the Spinning Black Hole in M87. *The Astrophysical Journal*, 868:146, Dec. 2018. ISSN 0004-637X.

doi: 10.3847/1538-4357/aaeb2d. URL https://ui.adsabs.harvard.edu/abs/2018ApJ...868..146N. ADS Bibcode: 2018ApJ...868..146N.

R. Narayan. Advection-dominated Models of Luminous Accreting Black Holes. *The Astrophysical Journal*, 462:136, May 1996. ISSN 0004-637X. doi: 10.1086/177136. URL https://ui.adsabs.harvard.edu/abs/1996ApJ...462..136N.

R. Narayan and J. E. McClintock. Advection-Dominated Accretion and the Black Hole Event Horizon. *New Astronomy Reviews*, 51(10-12):733–751, May 2008. ISSN 13876473. doi: 10.1016/j.newar.2008.03.002. URL http://arxiv.org/abs/0803.0322. arXiv: 0803.0322.

R. Narayan and I. Yi. Advection-dominated accretion: A self-similar solution. *The Astrophysical Journal Letters*, 428:L13–L16, June 1994. ISSN 0004-637X. doi: 10.1086/187381. URL http://adsabs.harvard.edu/abs/1994ApJ...428L..13N.

R. Narayan and I. Yi. Advection-dominated Accretion: Underfed Black Holes and Neutron Stars. *The Astrophysical Journal*, 452:710, Oct. 1995a. doi: 10.1086/176343. URL http://adsabs.harvard.edu/abs/1995ApJ...452..710N.

R. Narayan and I. Yi. Advection-dominated Accretion: Self-Similarity and Bipolar Outflows. *The Astrophysical Journal*, 444:231, May 1995b. ISSN 0004-637X. doi: 10.1086/175599. URL https://ui.adsabs.harvard.edu/abs/1995ApJ...444..231N.

R. Narayan, I. Yi, and R. Mahadevan. Explaining the spectrum of Sagittarius A* with a model of an accreting black hole. *Nature*, 374:623–625, Apr. 1995. ISSN 0028-0836. doi: 10.1038/374623a0. URL https://ui.adsabs.harvard.edu/abs/1995Natur.374..623N. ADS Bibcode: 1995Natur.374..623N.

R. Narayan, S. Kato, and F. Honma. Global Structure and Dynamics of Advection-dominated Accretion Flows around Black Holes. *The Astrophysical Journal*, 476:49–60, Feb. 1997. ISSN 0004-637X. doi: 10.1086/303591. URL https://ui.adsabs.harvard.edu/abs/1997ApJ...476..49N.

R. Narayan, I. V. Igumenshchev, and M. A. Abramowicz. Magnetically Arrested Disk: an Energetically Efficient Accretion Flow. *Publications of the Astronomical Society of Japan*, 55:L69–L72, Dec. 2003. ISSN 0004-6264. doi: 10.1093/pasj/55.6.L69. URL http://adsabs.harvard.edu/abs/2003PASJ...55L..69N.

R. Narayan, A. SÄ dowski, R. F. Penna, and A. K. Kulkarni. GRMHD simulations of magnetized advection-dominated accretion on a non-spinning black hole: role of outflows. *Monthly Notices of the Royal Astronomical Society*, 426:3241–3259, Nov. 2012. ISSN 0035-8711. doi: 10.1111/j.1365-2966.2012.22002.x. URL https://ui.adsabs.harvard.edu/abs/2012MNRAS.426.3241N.

S. C. Noble, J. H. Krolik, and J. F. Hawley. Dependence of Inner Accretion Disk Stress on Parameters: The Schwarzschild Case. *The Astrophysical Journal*, 711:959–973, Mar. 2010. doi: 10.1088/0004-637X/711/2/959. URL http://adsabs.harvard.edu/abs/2010ApJ...711..959N.

I. D. Novikov and K. S. Thorne. *Astrophysics of black holes.* Jan. 1973. URL https://ui.adsabs.harvard.edu/abs/1973blho.conf..343N. Conference Name: Black Holes (Les Astres Occlus) Pages: 343-450.

M. Obergaulinger, H. T. Janka, and M. A. Aloy. Magnetic field amplification and magnetically supported explosions of collapsing, non-rotating stellar cores. *Monthly Notices of the Royal Astronomical Society*, 445:3169–3199, Dec. 2014. ISSN 0035-8711. doi: 10.1093/mnras/stu1969. URL https://ui.adsabs.harvard.edu/abs/2014MNRAS.445.3169O. ADS Bibcode: 2014MNRAS.445.3169O.

F. Pacini. Energy Emission from a Neutron Star. *Nature*, 216:567–568, Nov. 1967. ISSN 0028-0836. doi: 10.1038/216567a0. URL https://ui.adsabs.harvard.edu/abs/1967Natur.216..567P. ADS Bibcode: 1967Natur.216..567P.

C. Palenzuela, L. Lehner, O. Reula, and L. Rezzolla. Beyond ideal MHD: towards a more realistic modelling of relativistic astrophysical plasmas. *Monthly Notices of the Royal Astronomical Society*, 394:1727–1740, Apr. 2009. ISSN 0035-8711. doi: 10.1111/j.1365-2966.2009.14454.x. URL https://ui.adsabs.harvard.edu/abs/2009MNRAS.394.1727P. ADS Bibcode: 2009MNRAS.394.1727P.

D. M. Palmer, S. Barthelmy, N. Gehrels, R. M. Kippen, T. Cayton, C. Kouveliotou, D. Eichler, R. a. M. J. Wijers, P. M. Woods, J. Granot, Y. E. Lyubarsky, E. Ramirez-Ruiz, L. Barbier, M. Chester, J. Cummings, E. E. Fenimore, M. H. Finger, B. M. Gaensler, D. Hullinger, H. Krimm, C. B. Markwardt, J. A. Nousek, A. Parsons, S. Patel, T. Sakamoto, G. Sato, M. Suzuki, and J. Tueller. A giant gamma-ray flare from the magnetar SGR 1806-20. *Nature*, 434(7037):1107–1109, Apr. 2005. ISSN 1476-4687. doi: 10.1038/nature03525.

J. C. B. Papaloizou and J. E. Pringle. The dynamical stability of differentially rotating discs with constant specific angular momentum. *Monthly Notices of the Royal Astronomical Society*, 208:721–750, June 1984. ISSN 0035-8711. doi: 10.1093/mnras/208.4.721. URL https://ui.adsabs.harvard.edu/abs/1984MNRAS.208..721P. ADS Bibcode: 1984MNRAS.208..721P.

L. Pareschi and G. Russo. Implicit–Explicit Runge–Kutta Schemes and Applications to Hyperbolic Systems with Relaxation. *J Sci Comput*, 25(1):129–155, Oct. 2005. ISSN 1573-7691. doi: 10.1007/s10915-004-4636-4. URL https://doi.org/10.1007/s10915-004-4636-4.

E. N. Parker. Hydromagnetic Dynamo Models. *The Astrophysical Journal*, 122:293, Sept. 1955. ISSN 0004-637X. doi: 10.1086/146087. URL https://ui.adsabs.harvard.edu/abs/1955ApJ...122..293P. ADS Bibcode: 1955ApJ...122..293P.

A. G. Pili, N. Bucciantini, A. Drago, G. Pagliara, and L. Del Zanna. Quark deconfinement in the proto-magnetar model of long gamma-ray bursts. *Monthly Notices of the Royal Astronomical Society*, 462:L26–L30, Oct. 2016. ISSN 0035-8711. doi: 10.1093/mnrasl/slw115. URL https://ui.adsabs.harvard.edu/abs/2016MNRAS.462L..26P. ADS Bibcode: 2016MNRAS.462L..26P.

A. G. Pili, N. Bucciantini, and L. Del Zanna. General relativistic models for rotating magnetized neutron stars in conformally flat space-time. *Monthly Notices of the Royal Astronomical Society*, 470:2469–2493, Sept. 2017. ISSN 0035-8711. doi: 10.1093/mnras/stx1176. URL https://ui.adsabs.harvard.edu/abs/2017MNRAS.470.2469P. ADS Bibcode: 2017MNRAS.470.2469P.

O. Porth and EHT-Collaboration. The Event Horizon General Relativistic Magnetohydrodynamic Code Comparison Project. *The Astrophysical Journal Supplement Series*, 243(2):26, Aug. 2019. doi: 10.3847/1538-4365/ab29fd. URL https://ui.adsabs.harvard.edu/abs/2019ApJS..243...26P/abstract.

O. Porth, H. Olivares, Y. Mizuno, Z. Younsi, L. Rezzolla, M. Moscibrodzka, H. Falcke, and M. Kramer. The black hole accretion code. *Computational Astrophysics and Cosmology*, 4: 1, May 2017. doi: 10.1186/s40668-017-0020-2. URL https://ui.adsabs.harvard.edu/abs/2017ComAC...4....1P. ADS Bibcode: 2017ComAC...4....1P.

J. E. Pringle. Accretion discs in astrophysics. *Annual Review of Astronomy and Astrophysics*, 19:137–162, 1981. ISSN 0066-4146. doi: 10.1146/annurev.aa.19.090181.001033. URL https://ui.adsabs.harvard.edu/abs/1981ARA&A..19..137P/abstract.

Q. Qian, C. Fendt, and C. Vourellis. Jet Launching in Resistive GR-MHD Black Hole-Accretion Disk Systems. *The Astrophysical Journal*, 859:28, May 2018. ISSN 0004-637X. doi: 10.3847/1538-4357/aabd36. URL https://ui.adsabs.harvard.edu/abs/2018ApJ...859...28Q. ADS Bibcode: 2018ApJ...859...28Q.

R. Raynaud, J. Guilet, H.-T. Janka, and T. Gastine. Magnetar formation through a convective dynamo in protoneutron stars. *Science Advances*, 6:eaay2732, Mar. 2020. doi: 10.1126/sciadv.aay2732. URL https://ui.adsabs.harvard.edu/abs/2020SciA....6.2732R. ADS Bibcode: 2020SciA....6.2732R.

A. Reboul-Salze, J. Guilet, R. Raynaud, and M. Bugli. A global model of the magnetorotational instability in protoneutron stars. *arXiv:2005.03567 [astro-ph, physics:physics]*, May 2020. URL http://arxiv.org/abs/2005.03567. arXiv: 2005.03567.

S. M. Ressler, A. Tchekhovskoy, E. Quataert, M. Chandra, and C. F. Gammie. Electron thermodynamics in GRMHD simulations of low-luminosity black hole accretion. *Monthly Notices of the Royal Astronomical Society*, 454:1848–1870, Dec. 2015. ISSN 0035-8711. doi: 10.1093/mnras/stv2084. URL https://ui.adsabs.harvard.edu/abs/2015MNRAS.454.1848R. ADS Bibcode: 2015MNRAS.454.1848R.

L. Rezzolla and O. Zanotti. *Relativistic Hydrodynamics*. Sept. 2013. URL https://ui.adsabs.harvard.edu/abs/2013rehy.book.....R. Publication Title: Relativistic Hydrodynamics ADS Bibcode: 2013rehy.book.....R.

L. Rezzolla, B. Giacomazzo, L. Baiotti, J. Granot, C. Kouveliotou, and M. A. Aloy. The Missing Link: Merging Neutron Stars Naturally Produce Jet-like Structures and Can Power Short Gamma-ray Bursts. *The Astrophysical Journal*, 732:L6, May 2011. ISSN 0004-637X. doi: 10.1088/2041-8205/732/1/L6. URL https://ui.adsabs.harvard.edu/abs/2011ApJ...732L...6R. ADS Bibcode: 2011ApJ...732L...6R.

F. Rincon. Dynamo theories. *Journal of Plasma Physics*, 85:205850401, Aug. 2019. ISSN 0022-3778. doi: 10.1017/S0022377819000539. URL https://ui.adsabs.harvard.edu/abs/2019JPlPh..85d2001R. ADS Bibcode: 2019JPlPh..85d2001R.

B. Ripperda, F. Bacchini, O. Porth, E. R. Most, H. Olivares, A. Nathanail, L. Rezzolla, J. Teunissen, and R. Keppens. General-relativistic Resistive Magnetohydrodynamics with Robust Primitive-variable Recovery for Accretion Disk Simulations. *ApJS*, 244(1):10, Sept. 2019. ISSN 0067-0049. doi: 10.3847/1538-4365/ab3922. URL https://doi.org/10.3847%2F1538-4365%2Fab3922. Publisher: American Astronomical Society.

P. H. Roberts and A. M. Soward. Dynamo theory. *Annual Review of Fluid Mechanics*, 24:459–512, Jan. 1992. ISSN 0066-4189. doi: 10.1146/annurev.fl.24.010192.002331. URL https://ui.adsabs.harvard.edu/abs/1992AnRFM..24..459R. ADS Bibcode: 1992AnRFM..24..459R.

A. A. Ruzmaikin, D. D. Sokolov, and A. M. Shukurov. Magnetic Fields of Galaxies. *Astrophysics and Space Science Library*, 133, Jan. 1988. doi: 10.1007/978-94-009-2835-0. URL https://ui.adsabs.harvard.edu/abs/1988ASSL..133.....R. Num Pages: 328 ADS Bibcode: 1988ASSL..133.....R.

M. R. Schreiber, J.-M. Hameury, and J.-P. Lasota. Delays in dwarf novae I: The case of SS Cygni. *A&A*, 410(1):239–252, Oct. 2003. ISSN 0004-6361, 1432-0746. doi: 10.1051/0004-6361:20031221. URL http://arxiv.org/abs/astro-ph/0308089. arXiv: astro-ph/0308089.

M. R. Schreiber, J.-M. Hameury, and J.-P. Lasota. Delays in dwarf novae: VW Hyi, the tidal instability and enhanced mass transfer models. *A&A*, 427(2):621–635, Nov. 2004. ISSN 0004-6361, 1432-0746. doi: 10.1051/0004-6361:20041148. URL http://arxiv.org/abs/astro-ph/0408179. arXiv: astro-ph/0408179.

N. I. Shakura and R. A. Sunyaev. Reprint of 1973A&A....24..337S. Black holes in binary systems. Observational appearance. *Astronomy and Astrophysics*, 500:33, June 1973. URL https://ui.adsabs.harvard.edu/abs/1973A%26A....24..337S/abstract.

S. L. Shapiro and S. A. Teukolsky. *Black Holes, White Dwarfs and Neutron Stars: The Physics of Compact Objects*. June 1986. URL https://ui.adsabs.harvard.edu/abs/1986bhwd.book.....S. Publication Title: Black Holes ADS Bibcode: 1986bhwd.book.....S.

P. Sharma, E. Quataert, G. W. Hammett, and J. M. Stone. Electron Heating in Hot Accretion Flows. *The Astrophysical Journal*, 667:714–723, Oct. 2007. ISSN 0004-637X. doi: 10.1086/520800. URL https://ui.adsabs.harvard.edu/abs/2007ApJ...667..714S.

J. B. Simon, K. Beckwith, and P. J. Armitage. Emergent mesoscale phenomena in magnetized accretion disc turbulence. *Monthly Notices of the Royal Astronomical Society*, 422:2685–2700, May 2012. ISSN 0035-8711. doi: 10.1111/j.1365-2966.2012.20835.x. URL https://ui.adsabs.harvard.edu/abs/2012MNRAS.422.2685S.

H. C. Spruit and A. A. van Ballegooijen. Stability of toroidal flux tubes in stars. *Astronomy and Astrophysics, vol. 106, no. 1, Feb. 1982, p. 58-66. Research supported by the Nederlandse Organisatie voor Zuiver-Wetenschappelijk Onderzoek.*, 106(1):58, Feb. 1982. ISSN 0004-6361. URL https://ui.adsabs.harvard.edu/abs/1982A%26A...106...58S/abstract.

J. O. Stenflo. Global Wave Patterns in the Sun's Magnetic Field. *Astrophysics and Space Science, Volume 144, Issue 1-2, pp. 321-336*, 144(1-2):321, May 1988. ISSN 0004-640X. doi: 10.1007/BF00793189. URL https://ui.adsabs.harvard.edu/abs/1988Ap%26SS.144..321S/abstract.

J. O. Stenflo. Cycle patterns of the axisymmetric magnetic field. 433:365, Jan. 1994. URL https://ui.adsabs.harvard.edu/abs/1994ASIC..433..365S. Conference Name: Solar Surface Magnetism ADS Bibcode: 1994ASIC..433..365S.

A. Suresh and H. T. Huynh. Accurate Monotonicity-Preserving Schemes with Runge Kutta Time Stepping. *Journal of Computational Physics*, 136:83–99, Sept. 1997. ISSN 0021-9991. doi: 10.1006/jcph.1997.5745. URL https://ui.adsabs.harvard.edu/abs/1997JCoPh.136...83S. ADS Bibcode: 1997JCoPh.136...83S.

A. Sądowski, R. Narayan, R. Penna, and Y. Zhu. Energy, momentum and mass outflows and feedback from thick accretion discs around rotating black holes. *Monthly Notices of the Royal Astronomical Society*, 436:3856–3874, Dec. 2013. ISSN 0035-8711. doi: 10.1093/mnras/stt1881. URL https://ui.adsabs.harvard.edu/abs/2013MNRAS.436.3856S.

A. Sądowski, R. Narayan, A. Tchekhovskoy, D. Abarca, Y. Zhu, and J. C. McKinney. Global simulations of axisymmetric radiative black hole accretion discs in general relativity with a mean-field magnetic dynamo. *Monthly Notices of the Royal Astronomical Society*, 447(1):49, Feb. 2015. doi: 10.1093/mnras/stu2387. URL https://ui.adsabs.harvard.edu/abs/2015MNRAS.447...49S/abstract.

A. Sądowski, E. Tejeda, E. Gafton, S. Rosswog, and D. Abarca. Magnetohydrodynamical simulations of a deep tidal disruption in general relativity. *Monthly Notices of the Royal Astronomical Society*, 458:4250–4268, June 2016. ISSN 0035-8711. doi: 10.1093/mnras/stw589. URL https://ui.adsabs.harvard.edu/abs/2016MNRAS.458.4250S. ADS Bibcode: 2016MNRAS.458.4250S.

A. Sądowski, M. Wielgus, R. Narayan, D. Abarca, J. C. McKinney, and A. Chael. Radiative, two-temperature simulations of low-luminosity black hole accretion flows in general relativity. *Monthly Notices of the Royal Astronomical Society*, 466:705–725, Apr. 2017. ISSN 0035-8711. doi: 10.1093/mnras/stw3116. URL https://ui.adsabs.harvard.edu/abs/2017MNRAS.466..705S. ADS Bibcode: 2017MNRAS.466..705S.

G. B. Taylor and R. A. Perley. Magnetic Fields in the Hydra A Cluster. *The Astrophysical Journal*, 416:554, Oct. 1993. ISSN 0004-637X. doi: 10.1086/173257. URL https://ui.adsabs.harvard.edu/abs/1993ApJ...416..554T. ADS Bibcode: 1993ApJ...416..554T.

G. B. Taylor, F. Govoni, S. W. Allen, and A. C. Fabian. Magnetic fields in the 3C 129 cluster. *Monthly Notices of the Royal Astronomical Society*, 326:2–10, Sept. 2001. ISSN 0035-8711. doi: 10.1046/j.1365-8711.2001.04587.x. URL https://ui.adsabs.harvard.edu/abs/2001MNRAS.326....2T. ADS Bibcode: 2001MNRAS.326....2T.

A. Tchekhovskoy, J. C. McKinney, and R. Narayan. Simulations of ultrarelativistic magnetodynamic jets from gamma-ray burst engines. *Monthly Notices of the Royal Astronomical Society*, 388:551–572, Aug. 2008. ISSN 0035-8711. doi: 10.1111/j.1365-2966.2008.13425.x. URL https://ui.adsabs.harvard.edu/abs/2008MNRAS.388..551T. ADS Bibcode: 2008MNRAS.388..551T.

A. Tchekhovskoy, R. Narayan, and J. C. McKinney. Efficient generation of jets from magnetically arrested accretion on a rapidly spinning black hole. *Monthly Notices of the Royal Astronomical Society*, 418:L79–L83, Nov. 2011. ISSN 0035-8711. doi: 10.1111/j.1745-3933.2011.01147.x. URL https://ui.adsabs.harvard.edu/abs/2011MNRAS.418L..79T. ADS Bibcode: 2011MNRAS.418L..79T.

A. Tchekhovskoy, J. C. McKinney, and R. Narayan. General Relativistic Modeling of Magnetized Jets from Accreting Black Holes. *J. Phys.: Conf. Ser.*, 372:012040, July 2012. ISSN 1742-6596. doi: 10.1088/1742-6596/372/1/012040. URL https://doi.org/10.1088/1742-6596/372/1/012040. Publisher: IOP Publishing.

C. Thompson and R. C. Duncan. The soft gamma repeaters as very strongly magnetized neutron stars - I. Radiative mechanism for outbursts. *Monthly Notices of the Royal Astronomical Society*, 275:255–300, July 1995. ISSN 0035-8711. doi: 10.1093/mnras/275.2.255. URL https://ui.adsabs.harvard.edu/abs/1995MNRAS.275..255T. ADS Bibcode: 1995MNRAS.275..255T.

N. Tomei, L. Del Zanna, M. Bugli, and N. Bucciantini. General relativistic magnetohydrodynamic dynamo in thick accretion discs: fully non-linear simulations. *Monthly Notices of the Royal Astronomical Society*, 491:2346–2359, Jan. 2020. ISSN 0035-8711. doi: 10.1093/mnras/stz3146. URL http://adsabs.harvard.edu/abs/2020MNRAS.491.2346T.

N. Tomei, L. Del Zanna, M. Bugli, and N. Bucciantini. Are GRMHD Mean-Field Dynamo Models of Thick Accretion Disks SANE? *arXiv e-prints*, page arXiv:2107.10630, July 2021. URL https://ui.adsabs.harvard.edu/abs/2021arXiv210710630T.

V. V. Usov. Millisecond pulsars with extremely strong magnetic fields as a cosmological source of γ-ray bursts. *Nature*, 357:472–474, June 1992. ISSN 0028-0836. doi: 10.1038/357472a0. URL https://ui.adsabs.harvard.edu/abs/1992Natur.357..472U. ADS Bibcode: 1992Natur.357..472U.

P. Uttley and I. M. McHardy. The flux-dependent amplitude of broadband noise variability in X-ray binaries and active galaxies. *Monthly Notices of the Royal Astronomical Society*, 323:L26–L30, May 2001. ISSN 0035-8711. doi: 10.1046/j.1365-8711.2001.04496.x. URL https://ui.adsabs.harvard.edu/abs/2001MNRAS.323L..26U. ADS Bibcode: 2001MNRAS.323L..26U.

C. Vogt and T. A. Enßlin. Measuring the cluster magnetic field power spectra from Faraday rotation maps of Abell 400, Abell 2634 and Hydra A. *Astronomy and Astrophysics, v.412, p.373-385 (2003)*, 412:373, Dec. 2003. ISSN 0004-6361. doi: 10.1051/0004-6361:20031434. URL https://ui.adsabs.harvard.edu/abs/2003A%26A...412..373V/abstract.

C. Vourellis and C. Fendt. Relativistic outflows from a GRMHD mean-field disk dynamo. *arXiv:2102.12482 [astro-ph]*, Feb. 2021. URL http://arxiv.org/abs/2102.12482. arXiv: 2102.12482.

R. C. Walker, P. E. Hardee, F. B. Davies, C. Ly, and W. Junor. The Structure and Dynamics of the Subparsec Jet in M87 Based on 50 VLBA Observations over 17 Years at 43 GHz. *The Astrophysical Journal*, 855:128, Mar. 2018. ISSN 0004-637X. doi: 10.3847/1538-4357/aaafcc. URL https://ui.adsabs.harvard.edu/abs/2018ApJ...855..128W. ADS Bibcode: 2018ApJ...855..128W.

E. S. Weibel. Spontaneously Growing Transverse Waves in a Plasma Due to an Anisotropic Velocity Distribution. *Physical Review Letters*, 2:83–84, Feb. 1959. ISSN 0031-9007. doi: 10.1103/PhysRevLett.2.83. URL https://ui.adsabs.harvard.edu/abs/1959PhRvL...2...83W. ADS Bibcode: 1959PhRvL...2...83W.

F. Yuan and R. Narayan. Hot Accretion Flows Around Black Holes. *Annual Review of Astronomy and Astrophysics, vol. 52, p.529-588*, 52:529, Aug. 2014. ISSN 0066-4146. doi: 10.1146/annurev-astro-082812-141003. URL https://ui.adsabs.harvard.edu/abs/2014ARA%26A..52..529Y/abstract.

F. Yuan, S. Markoff, H. Falcke, and P. L. Biermann. NGC 4258: A jet-dominated low-luminosity AGN? *Astronomy and Astrophysics, v.391, p.139-148 (2002)*, 391:139, Aug. 2002. ISSN 0004-6361. doi: 10.1051/0004-6361:20020817. URL https://ui.adsabs.harvard.edu/abs/2002A%26A...391..139Y/abstract.

F. Yuan, E. Quataert, and R. Narayan. Nonthermal Electrons in Radiatively Inefficient Accretion Flow Models of Sagittarius A*. *The Astrophysical Journal*, 598:301–312, Nov. 2003. ISSN 0004-637X. doi: 10.1086/378716. URL https://ui.adsabs.harvard.edu/abs/2003ApJ...598..301Y.

F. Yuan, M. Wu, and D. Bu. Numerical Simulation of Hot Accretion Flows. I. A Large Radial Dynamical Range and the Density Profile of Accretion Flow. *The Astrophysical Journal*, 761:129, Dec. 2012. ISSN 0004-637X. doi: 10.1088/0004-637X/761/2/129. URL https://ui.adsabs.harvard.edu/abs/2012ApJ...761..129Y.

R. T. Zavala and G. B. Taylor. Faraday rotation as a probe of the physical conditions near relativistic jets. *New Astronomy Reviews*, 47:589–592, Oct. 2003. ISSN 1387-6473. doi: 10.1016/S1387-6473(03)00100-3. URL https://ui.adsabs.harvard.edu/abs/2003NewAR..47..589Z. ADS Bibcode: 2003NewAR..47..589Z.

U. Ziegler and G. Rüdiger. Shear rate dependence and the effect of resistivity in magneto-rotationally unstable, stratified disks. *Astronomy and Astrophysics*, 378:668–678, Nov. 2001. ISSN 0004-6361. doi: 10.1051/0004-6361:20011245. URL http://adsabs.harvard.edu/abs/2001A%26A...378..668Z.

Appendix A

Kerr-Schild coordinates

The coordinate singularity at the event horizon in the Boyer-Lindquist coordinates can be removed via the following integrable coordinate transformation (Komissarov, 2004), also singular at the event horizon

$$\mathrm{d}t \to \mathrm{d}t + G(r)\mathrm{d}r, \tag{A.1}$$

$$\mathrm{d}\phi \to \mathrm{d}\phi + H(r)\mathrm{d}r, \tag{A.2}$$

where

$$G(r) = -\frac{2r}{\Delta}, \qquad H(r) = -\frac{a}{\Delta}. \tag{A.3}$$

The corresponding transformation matrix is

$$\mathcal{A}^{\mu}_{\mu'} = \begin{pmatrix} 1 & G & 0 & 0 \\ 0 & 1 & 0 & 0 \\ 0 & 0 & 1 & 0 \\ 0 & H & 0 & 1 \end{pmatrix}, \tag{A.4}$$

where the primed indices refer to the Boyer-Lindquist coordinates. This transformation relates vector and tensor respectively

$$x^{\mu} = \mathcal{A}^{\mu}_{\mu'} x^{\mu'}, \tag{A.5}$$

$$T^{\mu\nu} = \mathcal{A}^{\mu}_{\mu'} \mathcal{A}^{\nu}_{\nu'} T^{\mu'\nu'}. \tag{A.6}$$

The line element is expressed as

$$\mathrm{d}s^2 = g_{tt}\mathrm{d}t^2 + 2g_{t\phi}\mathrm{d}t\mathrm{d}\phi + g_{rr}\mathrm{d}r^2 + g_{\theta\theta}\mathrm{d}\theta^2 + g_{\phi\phi}\mathrm{d}\phi^2 + g_{r\phi}\mathrm{d}r\mathrm{d}\phi, \tag{A.7}$$

where the coefficients are given by

$$g_{tt} = z - 1, \tag{A.8}$$

$$g_{tr} = z, \tag{A.9}$$

$$g_{t\phi} = -za\sin^2\theta, \tag{A.10}$$

$$g_{rr} = z + 1, \tag{A.11}$$

$$g_{r\phi} = -a(1+z)\sin^2\theta, \tag{A.12}$$

$$g_{\theta\theta} = \varrho^2, \tag{A.13}$$

$$g_{\phi\phi} = \overline{\omega}^2, \tag{A.14}$$

where

$$z = 2r/\varrho^2 \tag{A.15}$$

and the Kerr-Schild shift vector and the lapse function are

$$\beta = \left(\frac{z}{1+z}, 0, 0\right), \qquad \alpha = \frac{1}{(1+z)^{1/2}}. \tag{A.16}$$

We have to consider that Eulerian observers in the two coordinate systems are not identical in general: if we want to derive the quantities measured by a Kerr-Schild Eulerian observer we cannot apply the transformations (A.4) to the quantities measured by a Boyer-Lindquist Eulerian observer. We follow the procedure described in Bugli et al. (2018):

- first consider the quantities measured by an Eulerian Kerr-Schild observer

$$v^i_{\rm KS} = \frac{1}{\alpha_{\rm KS}}\left(\frac{u^i_{\rm KS}}{u^t_{\rm KS}} + \beta^i_{\rm KS}\right), \tag{A.17}$$

$$B^i_{\rm KS} = \alpha_{\rm KS} F^{*ti}_{\rm KS}, \tag{A.18}$$

$$E^i_{\rm KS} = \alpha_{\rm KS} F^{ti}_{\rm KS}; \tag{A.19}$$

- we use Eq. (A.4) to transform the components of $u^i_{\rm KS}$, $F^{*ti}_{\rm KS}$, $F^{ti}_{\rm KS}$ in BL coordinates;
- then, using Eqs. (3.21), (3.23), (3.24), we write them in terms of $v^{i'}_{\rm BL}$, $B^{i'}_{\rm BL}$, $E^{i'}_{\rm BL}$

The result gives the correct transformation rules:

$$v^i_{\rm KS} = \frac{1}{\alpha_{\rm KS}}\left[\frac{\mathcal{A}^i_{j'}(\alpha_{\rm BL} v^{j'}_{\rm BL} - \beta^{j'}_{\rm BL})}{1 - \mathcal{A}^0_{r'}\alpha_{\rm BL} v^{r'}_{\rm BL}} + \beta^i_{\rm KS}\right], \tag{A.20}$$

$$B^i_{\rm KS} = \frac{\alpha_{\rm KS}}{\alpha_{\rm BL}}\left\{B^i_{\rm BL} - \mathcal{A}^0_{r'}\left[B^{r'}_{\rm BL}\beta^i_{\rm BL} + \frac{\alpha_{\rm BL}}{\gamma^{1/2}_{\rm BL}}(\delta^i_{\phi'}E^{\rm BL}_{\theta'} - \delta^i_{\theta'}E^{\rm BL}_{\phi'})\right]\right\}, \tag{A.21}$$

$$E^i_{\rm KS} = \frac{\alpha_{\rm KS}}{\alpha_{\rm BL}} \left\{ E^i_{\rm BL} - \mathcal{A}^0_{r'} \left[E^{r'}_{\rm BL} \beta^i_{\rm BL} - \frac{\alpha_{\rm BL}}{\gamma^{1/2}_{\rm BL}} (\delta^i_{\phi'} B^{\rm BL}_{\theta'} - \delta^i_{\theta'} B^{\rm BL}_{\phi'}) \right] \right\}, \tag{A.22}$$

Appendix B

The coefficients for the electric field and for its Jacobian

In the present Appendix we show how Eq. (4.39) has been derived and we provide the expressions for the required coefficients of Γ and of their derivatives, to be used in Eq. (4.45). Since we are working with spatial vectors alone, involving the 3-D metric tensor γ_{ij} (not diagonal in Kerr-Schild coordinates), we use here for simplicity the standard vector notation, for which $\boldsymbol{v}$ is employed rather than v^i.

The implicit step of the IMEX scheme for the electric field can be written as

$$\begin{aligned}\boldsymbol{E} = \boldsymbol{E}_\star - \tilde{\eta}^{-1}\Gamma\{&\boldsymbol{E} + \boldsymbol{v}\times\boldsymbol{B} - (\boldsymbol{E}\cdot\boldsymbol{v})\boldsymbol{v} \\ &- \xi[\boldsymbol{B} - \boldsymbol{v}\times\boldsymbol{E} - (\boldsymbol{B}\cdot\boldsymbol{v})\boldsymbol{v}]\}\end{aligned} \tag{B.1}$$

and after the introduction of $\tilde{\boldsymbol{u}} = \Gamma\boldsymbol{v}$, for which $\Gamma^2 = 1 + \tilde{u}^2$, we can rewrite the above expression as

$$\begin{aligned}(\Gamma + \tilde{\eta})\boldsymbol{E} = \tilde{\eta}\boldsymbol{E}_\star - \tilde{\boldsymbol{u}}\times\boldsymbol{B} + (\boldsymbol{E}\cdot\tilde{\boldsymbol{u}})\tilde{\boldsymbol{u}}/\Gamma \\ + \xi\Gamma\boldsymbol{B} - \xi(\tilde{\boldsymbol{u}}\times\boldsymbol{E}) - \xi(\boldsymbol{B}\cdot\tilde{\boldsymbol{u}})\tilde{\boldsymbol{u}}/\Gamma.\end{aligned} \tag{B.2}$$

The dot product with $\tilde{\boldsymbol{u}}$ allows one to write

$$(1 + \tilde{\eta}\Gamma)(\boldsymbol{E}\cdot\tilde{\boldsymbol{u}}) = \tilde{\eta}\Gamma(\boldsymbol{E}_\star\cdot\tilde{\boldsymbol{u}}) + \xi(\boldsymbol{B}\cdot\tilde{\boldsymbol{u}}), \tag{B.3}$$

whereas the curl with $\tilde{\boldsymbol{u}}$ (necessary when $\xi \neq 0$) leads to

$$\begin{aligned}(\Gamma + \tilde{\eta})(\tilde{\boldsymbol{u}}\times\boldsymbol{E}) = \tilde{\eta}(\tilde{\boldsymbol{u}}\times\boldsymbol{E}_\star) + (\Gamma^2 - 1)\boldsymbol{B} \\ - (\boldsymbol{B}\cdot\tilde{\boldsymbol{u}})\tilde{\boldsymbol{u}} + \xi\Gamma(\tilde{\boldsymbol{u}}\times\boldsymbol{B}) + \xi[(\Gamma^2 - 1)\boldsymbol{E} - (\boldsymbol{E}\cdot\tilde{\boldsymbol{u}})\tilde{\boldsymbol{u}}].\end{aligned} \tag{B.4}$$

Eqs. (B.3 - B.4) can be plugged into Eq. (B.2) to derive an explicit expression for $\boldsymbol{E}$. In a compact form the required expression is

$$\begin{aligned}A_0\,\boldsymbol{E} = \tilde{\eta}\boldsymbol{E}_\star + A_1\,(\boldsymbol{E}_\star\cdot\tilde{\boldsymbol{u}})\tilde{\boldsymbol{u}} + A_2\,\tilde{\boldsymbol{u}}\times\boldsymbol{E}_\star \\ + A_3\,\boldsymbol{B} + A_4\,(\boldsymbol{B}\cdot\tilde{\boldsymbol{u}})\tilde{\boldsymbol{u}} + A_5\,\tilde{\boldsymbol{u}}\times\boldsymbol{B},\end{aligned} \tag{B.5}$$

that is precisely Eq. (4.39), where we have defined six new coefficients, functions of Γ alone, namely

$$A_0(\Gamma) = \Gamma + \tilde{\eta} + \xi^2 \frac{\Gamma^2 - 1}{\Gamma + \tilde{\eta}}, \tag{B.6}$$

$$A_1(\Gamma) = \frac{\tilde{\eta}}{1 + \tilde{\eta}\Gamma} + \xi^2 \frac{\tilde{\eta}\Gamma}{(\Gamma + \tilde{\eta})(1 + \tilde{\eta}\Gamma)}, \tag{B.7}$$

$$A_2(\Gamma) = -\xi \frac{\tilde{\eta}}{\Gamma + \tilde{\eta}}, \tag{B.8}$$

$$A_3(\Gamma) = \xi \frac{1 + \tilde{\eta}\Gamma}{\Gamma + \tilde{\eta}}, \tag{B.9}$$

$$A_4(\Gamma) = \xi \frac{1 - \tilde{\eta}^2 + \xi^2}{(\Gamma + \tilde{\eta})(1 + \tilde{\eta}\Gamma)}, \tag{B.10}$$

$$A_5(\Gamma) = -1 - \xi^2 \frac{\Gamma}{\Gamma + \tilde{\eta}}. \tag{B.11}$$

The derivatives of the above coefficients, to be plugged into Eq. (4.45), are

$$\dot{A}_0(\Gamma) = 1 + \xi^2 \frac{1 + \Gamma^2 + 2\tilde{\eta}\Gamma}{(\Gamma + \tilde{\eta})^2}, \tag{B.12}$$

$$\dot{A}_1(\Gamma) = -\frac{\tilde{\eta}^2}{(1 + \tilde{\eta}\Gamma)^2} - \xi^2 \frac{\tilde{\eta}^2(\Gamma^2 - 1)}{(1 + \tilde{\eta}\Gamma)^2(\Gamma + \tilde{\eta})^2}, \tag{B.13}$$

$$\dot{A}_2(\Gamma) = \xi \frac{\tilde{\eta}}{(\Gamma + \tilde{\eta})^2}, \tag{B.14}$$

$$\dot{A}_3(\Gamma) = \xi \frac{\tilde{\eta}^2 - 1}{(\Gamma + \tilde{\eta})^2}, \tag{B.15}$$

$$\dot{A}_4(\Gamma) = -\xi \frac{(1 - \tilde{\eta}^2 + \xi^2)(1 + \tilde{\eta}^2 + 2\tilde{\eta}\Gamma)}{(\Gamma + \tilde{\eta})^2(1 + \tilde{\eta}\Gamma)^2}, \tag{B.16}$$

$$\dot{A}_5(\Gamma) = -\xi^2 \frac{\tilde{\eta}}{(\Gamma + \tilde{\eta})^2}, \tag{B.17}$$

and thanks to the above expressions the Jacobian of the electric field can be computed.

Acknowledgements

I would like to express my gratitude to my main advisor, Prof. Luca Del Zanna for his help and advice with this thesis and to Dr. Matteo Bugli who patiently assisted and guided me in the development of some parts of the code.

Niccolò Tomei, Florence, December 2021